Doctoral Dissertations

Graduate School

8-2013

The Development of Lithium Tetraborate Compounds for Thermal Neutron Detection

John David Auxier II

University of Tennessee - Knoxville, jauxier@utk.edu

Recommended Citation

To the Graduate Council:

I am submitting herewith a dissertation written by John David Auxier II entitled "The Development of Lithium Tetraborate Compounds for Thermal Neutron Detection." I have examined the final electronic copy of this dissertation for form and content and recommend that it be accepted in partial fulfillment of the requirements for the degree of Doctor of Philosophy, with a major in Chemistry.

George K. Schweitzer, Major Professor

We have read this dissertation and recommend its acceptance:

David M. Jenkins, Laurence F. Miller, Jimmy W. Mays

Accepted for the Council:

<u>Carolyn R. Hodges</u>

Vice Provost and Dean of the Graduate School

(Original signatures are on file with official student records.)

The Development of Lithium Tetraborate Compounds for Thermal Neutron Detection

A Dissertation

Presented for the

Doctor of Philosophy

Degree

The University of Tennessee, Knoxville

John David Auxier II

August 2013

Dedication

This doctoral thesis is dedicated to my family, specifically my parents John and Ruby Auxier, who gave me the utmost support, love, and guidance throughout my entire educational experience and my life as a whole. To my sister, Eva S. Auxier, who was always willing to listen, provide valuable input, and demonstrate what a model student is supposed to be. To my brother, Jerrad P. Auxier, who not only contributed data to the following pages, but has provided invaluable support during the development of this project and in my entire life. And finally, I thank Jesus Christ, the Creator of this world Who knows "the laws of the heavens" (Job 38:33, NIV) and that "By faith we understand that the universe was created by the Word of God…" (Heb. 11:3, ESV). A portion of that universe is studied in this dissertation.

Acknowledgements

I would like to thank Dr. George K. Schweitzer for his friendship, leadership, and advice throughout this project, without his help this project would be utterly deficient in its scientific content, its organization, and its completeness. I would also like to thank the members of my committee, Dr. David Jenkins, Dr. Laurence F. Miller, and Dr. Jimmy W. Mays for their time and commitment. I would also like to thank Andrew Mabe for his significant contributions to this project: technical discussions, insightful ideas, and relentless pursuit of perfection, which have made this project much more than it would have been without his efforts. I would also like to thank Stephen Young for his efforts in characterizing samples, writing, and for sharing insightful opinions throughout the duration of the project. I would like to thank Matthew Urffer and Jerrad P. Auxier in Nuclear Engineering for measuring responses of the samples, performing the necessary modeling calculations that made this project much more complete. I would like to thank the members of my committee for reading my submissions, offering helpful suggestions, and providing valuable scientific input. Finally, I would like to thank the members of lab: Anne Smalley, Brittany Miner, Jake Stewart, and Deborah Penchoff for providing moral support, scientific insight, and listening to outbursts concerning projects that failed and ideas that went awry. Without the contributions of the aforementioned individuals, this work would be incomplete and lacking in every facet, so I again thank you all for every effort you have made on my behalf.

Abstract

Due to the shortage of ^{3}He [helium-3], the goal of this project was to develop replacement materials for slow neutron detection in mixed radiation fields. The U.S. Department of Homeland Security (DHS) indicated that replacement materials should have an absolute neutron efficiency of 2.5 cps/ng of ^{252}Cf (Californium-252) and a neutron/gamma discrimination intrinsic efficiency of 1 x 10^{-6} [one gamma-ray response in a million counts]. In this work, the use of amorphous lithium tetraborate ($Li_2B_4O_7$:Ce) is analyzed as a thermal neutron detector. Also discussed is the synthesis of the lithium tetraborate, using ^{6}Li [lithium-6], to form a crystalline powder that is heated simultaneously with cerium oxide (CeO_2) and excess boric acid to produce an optically clear glass. In this study, the structure of glass was probed, the abnormal reduction of Ce^{4+} [tetravalent cerium] to Ce^{3+} [trivalent cerium] observed in the fluorescence peak at 360 nm, and irradiation studies with alpha particles, beta particles, gamma-rays, and neutrons were performed. The resulting material was shown to have a light yield of 550 photons/neutron, which is 8% the light output of GS-20, a lithiated glass.

Table of Contents

List of Figures

List of Tables

Appendix 1 List of Acronyms and Symbols

MLLD   Mathematical Lower Level Discriminator

P-XRD   Powdered X-Ray Detraction

Z   Impedance

Q   Energy of Reaction

NMR   Nuclear Magnetic Resonance

SSNMR   Solid State Nuclear Magnetic Resonance

SSNMR-MAS   Solid State Nuclear Magnetic Resonance – Magic Angle Spinning

SEM   Scanning Electron Microscope

UV-vis   Ultra Violet Visible Spectroscopy

CPMAS   Cross Polarization – Magic Angle Spinning

CLSM   Confocal Laser Surface Microscopy

EDS   Energy Dispersive X-Ray Spectroscopy

TEM   Tunneling Electron Microscope

MCNPX   Monte Carlo N-Particle eXtended

FT-IR   Fourier Transform – Infrared Spectroscopy

FT-IR-ATR   Fourier Transform – Infrared Spectroscopy, Attenuated Total Reflectance

ICP-OES   Inductively Coupled Plasma – Optical Emission Spectroscopy

PMT   Photo Multiplier Tube

Wt%   Percentage of Weight

cm   centi-meter

nm   nano-meter

mm   milli-meter

μm	micro-meter
sec	second
deg	degrees
˚C	degrees Celcius
PDMS	Poly – dimethylsiloxane
DTA	Differential Thermal Analysis
TGA	Thermogravimetric Analysis
cps	Counts per Second
MeV	million electron Volts
keV	kilo electron Volt
eV	electron Volt
V	Volt
G	Gain
mol	molar quantity
DNDO	Department Nuclear Detection Office
PNNL	Pacific Northwest national Laboratory
DHS	Department of Homeland Security
ppm	parts per million
HDPE	High Density Polyethylene
mR/h	milli-REM/ Hour
REM	Roentgen Equivalent Man
GARR	Gamma Absolute Rejection Ratio
ADC	Analog to Digital Converter
MCB	Multi Channel Buffer

PHD	Pulse Height Discriminator
REE	Rare Earth Element
Eqn	Equation
ng	nano-gram
N.T.P.	Normal Temperature and Pressure
σ	cross section
σ_{abs}	Abxolute Cross Section
USD	United States Dollar
$\varepsilon_{abs\ n}$	Absolute Neutron Detection Efficiency
$\varepsilon_{int\ \gamma n}$	Intrinsic gamma-neutron detection efficiency
barns	unit of nuclear cross section, equal to 10^{-24} square centimeter
μCi	micro-curie
mCi	milli-curie
mL	milli-liter
μL	micro-liter
g	gram
W	watt
soln	solution
MHz	mega hertz
β	Beta Particle
α	alpha particle
n	neutron
γ	gamma ray
(n, γ)	neutron – gamma reaction

(n,p)   neutron – proton reaction

(n,α)   neutron - alpha reaction

(n,t),   neutron – triton reaction

RC   radiative capture

CPPR   charged particle production reactions

SNM   Special Nuclear Material

Z   Proton Number

atm   Atmosphere

PS   Polystyrene

PVX   Polyvinylxylene

PVT   Polyvinlytoluene

P2VN   2-vinyl naphthalene

PPO/POPOP 2,5-diphenyloxazole/ 1,4-bis(5-phenyl-2-oxalozolyl)benzene

PS-*co*-PLiMAn   poly(styrene-*co*-lithium maleate)

PEN   ethylene naphthalate

THF   Tetrahydrofuran

HF   Hydrofloric Acid

AIBN   2,2'-azobisisobutyronitrile

DMSO-d$_6$ deuterated dimethylsulfoxide

CTA   cetyl trimethyl ammonium chloride

MEHQ   monomethyl ether of hydroquinone

BWXTY-12   Babcox and Wilcox Technical Services Y-12, LLC

LMCT   Ligand Metal Charge Transfer

Chapter 1

1.1   Introduction

1.1.1   Prologue

It has been shown by Bothe and others that beryllium when bombarded by α-particles of polonium emits a radiation of great penetrating power, which has an absorption coefficient in lead of about 0.3 cm^{-1}. Recently, Mme. Curie-Joliot and M. Joliot found, when measuring the ionisation produced by this beryllium radiation in a vessel with a thin window, that the ionisation increased when matter containing hydrogen was placed in front of the window. The effect appeared to be due to the ejection of protons with velocities up to a maximum of nearly 3 x 10^9 cm per sec. They suggested that the transference of energy to the proton was by a process similar to the Compton effect, and estimated that the beryllium radiation had a quantum energy of 50 x 10^6 electron volts.

I have made some experiments using the valve counter to examine the properties of the radiation excited in beryllium. The valve counter consists of a small ionisation chamber connected to an amplifier and the sudden production of ions by the entry of a particle, such as a proton or an α-particle, is recorded by the deflexion of an oscillograph. These experiment have shown that that radiation ejects particles from hydrogen, helium, lithium, beryllium, carbon, air, and argon. The particles ejected from hydrogen behave, as regards range and ionising power, like protons with speeds up to about 3.2 x 10^9 cm. per sec. The particles from the other elements have a large ionizing power, and appear to be in each case recoil atoms of the elements.

If we ascribe the ejection of the proton to a Compton recoil from a quantum of 52 x 10^6 electron volts, then the nitrogen recoil atom arising by a similar process should have an energy not greater than about 400,000 volts, should produce not more than about 10,000 ions and have a range in air at N.T.P. of about 1-3 mm. Actually, some of the recoil atoms in nitrogen produce at least 30,000 ions. In collaboration, with Dr. Feather, I have observed the recoil atoms in an

expansion chamber, and their range, estimated visually, was sometimes as much as 3 mm. at N.T.P.

These results, and others, I have obtained in the course of the work, are very difficult to explain on the assumption that the radiation from beryllium is a quantum radiation, if energy and momemtum are to be conserved in the collisions. The difficulties disappear, however, if it be assumed that the radiation consists of particles of mass 1 and charge 0, or neutrons. The capture of the α-particle by the ^9Be nucleus may be supposed to results in the formation of a ^{12}C nucleus and the emission of the neutron. From the energy relations of the process the velocity of the neutron emitted in the forward direction may well be about 3 x 10^9 cm. per sec. The collisions of the neutron with the atoms through which it passes give rise to the recoil atoms, and the observed energies of the recoil atoms are in fair agreement with this view. Moreover, I have observed that protons ejected from hydrogen by the radiation emitted in the opposite direction to that of the exciting α-particle appear to have a smaller range than those ejected by the forward radiation. This is a simple explanation on the neutron hypothesis.

If it be supposed that the radiation consists of quanta, then the capture of the α-particle by the ^9Be nucleus will form a ^{13}C nucleus. The mass defect of ^{13}C is known with sufficient accuracy to show that the energy of the quantum emitted in this process cannot be greater than about 14 x 10^6 volts. It is difficult to make such a quantum responsible for the effects observed.

It is to be expected that many of the effects of a neutron in passing through matter should resemble those of a quantum of high energy, and it is not easy to reach the final decision between the two hypotheses. Up to the present, all the evidence is in favour of the neutron if the conservation of energy and momentum be relinquished at some point.

J. Chadwick

Cavendish Laboratory,

Cambridge, Feb. 17 1932

1.2 Detector Background and Material Criteria

The detection of thermal neutrons is important to many areas of nuclear science including nuclear physics, nuclear medicine, particle accelerator experiments, and homeland security applications. Neutrons are emitted from elements such as uranium or plutonium as fission products and have energies >1 MeV. These neutrons can be thermalized using materials with low Z numbers, such as high density polyethylene (HDPE), to reduce the energy to 0.025 eV.

In the past, ^{3}He has been used to detect[1–3] thermal neutrons and has been used in applications as portal monitors. In recent years, there has been a shortage of this rare isotope (0.00014%) and there have been many efforts to develop replacement materials to meet this growing demand for detectors. The U.S. Department of Homeland Security (DHS), working through the Domestic Nuclear Detection Office (DNDO) and Pacific Northwest National Laboratory (PNNL), has developed a set of criteria that the detectors must satisfy to meet border applications. The requirements that detectors must meet in order to be considered for ^{3}He replacement materials are 1) thermal neutron detection efficiency and 2) gamma insensitivity requirements. The criteria are as follows:

1. The detectors must not alarm when exposed to a 10 mR/h gamma-ray exposure rate.
2. Absolute neutron detection efficiency, $\varepsilon_{abs\,n} \geq 2.5$ cps/ng ^{252}Cf at 2 m for a source in a specific moderated form (also 1.2 x 10^{-3})
3. Intrinsic gamma-neutron detection efficiency, $\varepsilon_{int\,\gamma n} \leq 10^{-6}$
4. Gamma absolute rejection ratio (GARR) for neutrons, $0.9 \leq GARR \leq 1.1$ at 10 mR/h exposure
5. Detectors must be produced at $30,000 (USD) per unit.

Neutrons present a unique challenge in detection given that they have no charge and have little interaction with matter. Therefore, it is necessary to use elements that have a large probability, or cross section (denoted σ), for interaction with these particles. Interactions with thermal neutrons can be categorized into absorption and elastic scattering functions, with elastic scattering contributing little to the detection processes.

Furthermore, when these elements interact with neutrons, they must produce secondary particles that can be easily detected. The elements chosen for this project are ^{6}Li (7.4%

naturally abundant (σ_{abs} = 940 barns) and [10]B (20% naturally abundant, σ_{abs} = 3835 barns) given their high thermal neutron absorption cross sections[4] and their production of charged particles with no secondary gamma-rays. Their interactions[5] with thermal neutrons are shown in the following equations:

$$^6_3Li + {}^1_0n \ \rightarrow {}^4_2He \ (2.05 \ \text{MeV}) + \ {}^3_1H \ (2.73 \ \text{MeV}) \ (Q = 4.78 \ \text{MeV}, 100\%) \qquad \text{Eqn. 1.1}$$
$$^{10}B + n \rightarrow {}^7Li \ (0.84 \ \text{MeV}) + {}^4He \ (1.47 \ \text{MeV}) \ (Q = 2.792 \ \text{MeV}, 94\%) \ \textit{excited state} \quad \text{Eqn. 1.2}$$
$$^{10}B + n \rightarrow {}^7Li \ (1.01 \ \text{MeV}) + {}^4He \ (1.78 \ \text{MeV}) \ (Q = 2.310 \ \text{MeV}, 6\%) \ \ \textit{ground state} \quad \text{Eqn. 1.3}$$
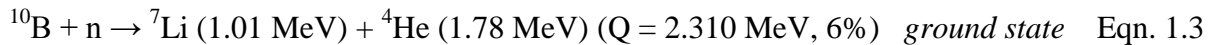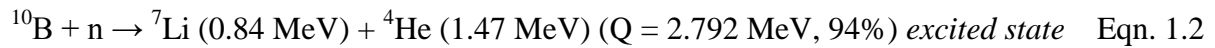
The resulting charged particles from either reaction can be used to produce a current in a semi-conducting device or can be used to produce light in a scintillating device. For this project the goal will be to develop scintillating materials that incorporate both [6]Li and [10]B for the replacement of [3]He detectors for homeland security applications (the reaction of [3]He with a thermal neutron is shown in Eqn. 1.4.

$$^3_2He + \ {}^1_0n \ \rightarrow \ {}^3_1H + \ {}^1_1H \ (\sigma_{abs} = 5,333 \ \text{barns}) \qquad \text{Eqn. 1.4}$$
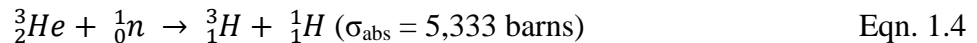
1.3   Current Detectors

In recent years, there have been a number of replacement technologies that have used liquid organic scintillators, inorganic scintillators[6], polymeric thin-film scintillators[7], [8], semi-conductors, and glass detectors[9–11].

1.3.1   Detection Mechanism

All of the above detectors rely on the isotopes of [6]Li and [10]B to detect thermal neutrons due to their high absorption cross sections and their high energy fission products as shown in Eqns. 1.1-1.3. All of the listed isotopes produce charged fission products or photon (gamma-rays or X-rays) as a result of their interaction with thermal neutrons. The charged particles will produce excitations and ionization in the detection matrix, which can be described by the Bethe-Bloch[12] equations. Similarly, the photons will pass through the detector matrix and produce ionizations and excitations. These ionizations and excitations can be used to produce a current

in a semi-conductor detector to produce a detectable signal; or the excitations can be used to excite a fluor or scintillation center in a scintillating device to produce a detectable signal.

1.3.2 Bridge to Proposal Problem

Of all the listed detectors, most rely upon the use of a single isotope, such as ^{6}Li, ^{10}B, ^{155}Gd, or ^{157}Gd instead of incorporating multiple neutron-sensitive isotopes into the same matrix. Recently, it has been of interest to develop materials that incorporate multiple neutron-sensitive isotopes to increase the neutron detection sensitivity. Some groups have attempted to use lithium borate phosphate glasses that are doped with Ce^{3+}, and have reported limited success with neutron/gamma discrimination.

1.3.3 Use of Lithium and Boron Glass Substrates

Lithium tetraborate ($Li_2B_4O_7$:Ce) has been reported in the literature for use as a thermal neutron detector, however there are reports of the polycrystalline material. This material lends itself to the problem of neutron detection given the high loading of Li and B per each molecule. This material also has high optical transparency in the wavelength range of interest, and unlike many detector materials, it is not hygroscopic and is highly stable across a wide range of temperatures.

1.4 Proposed Problem

In summary, the detection of thermal neutrons provides unique challenges due to the difficultly in detecting neutrons and meeting the requirements as specified by DHS/DNDO. In addition to the neutron/gamma discrimination criteria, the materials developed for this purpose must also be able to fit within the existing platforms (e.g. portal monitors). For scintillation materials, such as the current ^{3}He portal monitors, the light produced is at a wavelength range of 390 – 420 nm; hence, replacement technologies would be required to also produce light in this wavelength range to ensure compatibility with existing technologies.

To address this problem, this project will investigate the usefulness of lithium tetraborate doped with Ce to address the problem of thermal neutron detection. The focus of this work will be three-fold: 1) to characterize the elemental composition morphology of Ce doped amorphous lithium tetraborate, 2) to determine the effect of boric acid on the reduction of

rare earths (e.g. Ce) in a borate matrix, and 3) to determine the feasibility of using this material to detect thermal neutrons while meeting the DHS criteria.

There have been a number of similar studies with crystalline lithium borate and rare earths[13–25], such as Eu and Tb, their effects on light output, morphology and sample composition. Similarly, there have also been a number of reports[18], [26–34] as to the elemental composition and morphology of amorphous and vitreous alkali borate matrices. A focus of this work will be to use a variety of techniques to probe the element composition and morphology of Ce doped lithium borate.

A number of individuals[35] have noted that the rare earth elements undergo a reduction (i.e. $Eu^{3+} \rightarrow Eu^{2+}$) when they are heated to temperatures $> 850°C$ in the presence of boric acid and alkali borate matrices. However, these reports are usually involved with highly crystalline materials and not vitreous species. It will be a focus of this work to attempt to determine the cause of this effect, and whether or not it can be used to incorporate a rare earth element, such as Ce, to be used as a scintillation center in this matrix. Work will also be performed to determine if experiments can be done to enhance this effect through co-doping the material with other elements, such as Pr, to enhance this reduction effect.

Final work will be done to irradiate this material with neutrons via a 0.59 μCi ^{252}Cf source, gamma-rays from a 100 mCi ^{60}Co source, alpha radiation from an ^{241}Am source, and beta radiation from a ^{36}Cl source. The alpha and beta irradiation will be used to determine the ability of the matrix to transfer the energy of the impinging particle to the scintillation center. The neutron and gamma irradiation will be used to determine if these samples will meet the neutron/gamma discrimination criteria outlined by DHS. Experiments with varying sample thicknesses will be performed to attempt to maximize neutron detection efficiency and minimize gamma sensitivity.

Chapter 2: Literature Survey

2.1   Thermal Neutron Detection

2.1.1   Detection Background

       Thermal neutrons[36] have an energy of 0.025 eV and due to their inherent charge neutrality, these particles must be detected via indirect means. As mentioned earlier, neutron detection begins when the neutron interacts with a nucleus to initiate the release of charged particles. These charged particles can produce ionizations and excitations facilitating detection. Detection is performed via two methods: 1) the charged particles produce electron/hole pairs, or current, in a semiconductor which is converted to a signal, or 2) the charged particles can interact with a fluorescent molecule and produce light, which is subsequently detected and converted to a signal.

       Neutron interaction with matter is divided into two categories: scattering, both elastic or inelastic, and nuclear reactions. In the case of scattering, the neutron will undergo inelastic scattering, by which kinetic energy is transferred from the neutron to the nucleus of another atom. If enough kinetic energy[5], [12] is transferred, the second, or recoiling, nucleus will ionize the surrounding matrix and can be used to produce light. This method is only effective with very light nuclei, such as hydrogen or helium, which have been used to make practical neutron detectors. In the case of nuclear reactions, the reaction products of alphas, protons, gamma rays, and fission fragments are used to initiate the detection process.

       Detectors that use the inelastic scattering/recoil mechanism are typically only useful for fast neutrons (E > keV), and are therefore beyond the scope of this project[37]. Hence most thermal neutron detectors are based around nuclear reactions, which can be classified according to three separate categories as seen in Table 2.1.

Table 2.1-1 Thermal Neutron Reaction Categories		
Reaction Types	**Reaction Products**	**Nuclei of Interest**
Radiative Capture (n,γ)	γ-rays	^{113}Cd, ^{155}Gd, ^{157}Gd, etc.
Charged Particle Production Reaction (n,p), (n,α), (n,t), etc.	^{7}Li, α, ^{3}H, ^{2}H, or other light nuclei fission products.	^{10}B, ^{6}Li, ^{3}He, etc.
Neutron-Capture Induced Fission	fission products of U, Pu, or other heavy elements	^{235}U, ^{239}Pu, etc.

Detectors that employ neutron reactions can be divided neatly into two separate categories: semi-conductors and scintillators, with scintillation detectors representing the gross majority of detector types. Scintillation detectors generally rely upon radiative capture (RC) or charged particle production reactions (CPPR) for light production mechanism, and have generally been developed to employ the isotopes of ^{155}Gd, ^{157}Gd, ^{3}He, ^{6}Li, and ^{10}B. Given the impending shortage of ^{3}He, this project will focus on the development of ^{6}Li and ^{10}B into scintillation detection devices.

2.1.2 *Gamma-Ray Sensitivity*

For all detector types, the sensitivity to gamma-rays often becomes a deciding factor in the design of neutron detectors. Special nuclear material (such as uranium or plutonium) often emits 10 times the number of gamma-rays per every neutron emitted, thus a detector's sensitivity for gamma-ray must be small. The criterion for gamma-ray sensitivity of thermal neutrons is outlined by Kouzes[1], [2], *et al*. in PNNL report 18903.

Like neutrons gamma-rays only interact with matter via elastic and inelastic collisions, and will also produce excitations and ionization in the detection medium. These ionizations will produce a response from both the semi-conductor based detectors as well as the scintillation based detectors. Depending on the energy of an incoming gamma-ray and the average Z (proton

number) of the material, the interaction of the impinging gamma-ray will vary. This effect is shown in Fig. 2.1-1, which is taken from Knoll[5].
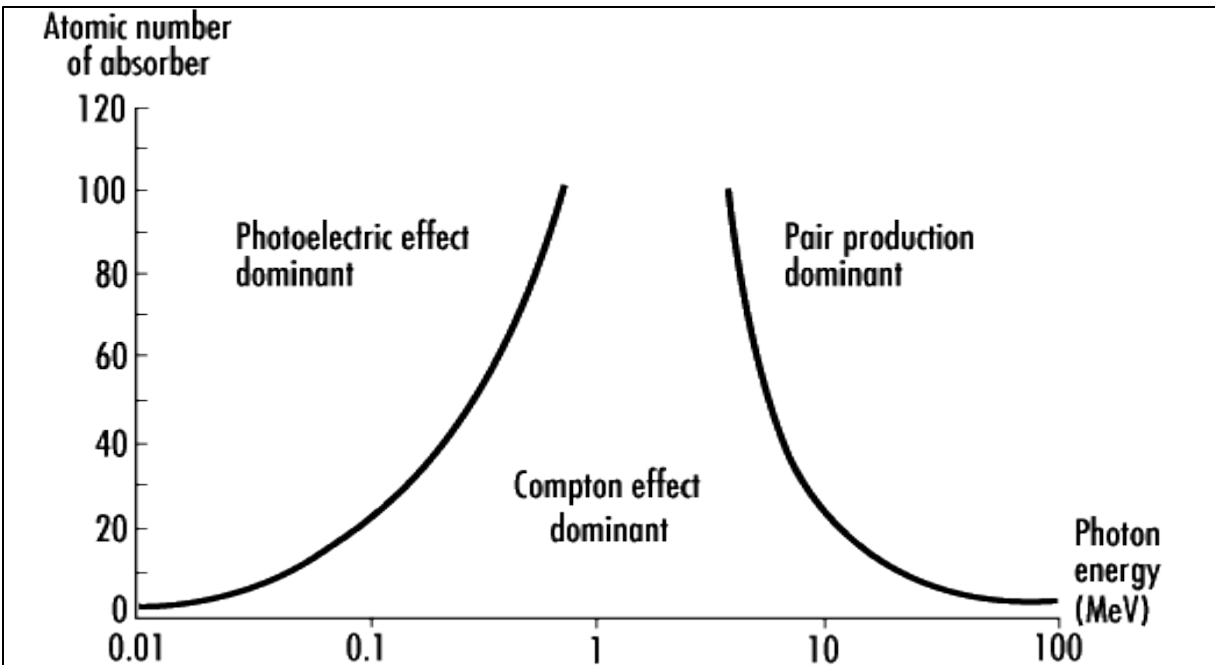
Figure 2.1-1: The interaction of gamma-rays with matter as a function of the impinging gamma-ray energy and the Z of the absorber.

As described by Knoll and Anderson [5], [12], gamma-ray sensitivity to photoelectric effect can be lowered by reducing the average Z number of the material. This effect can be approximated by the following expression:

$$\tau \cong constant \times \frac{Z^n}{E_\gamma^{3.5}}$$ Eqn. 2.1

In Eqn 2.1, τ is the probability of photoelectric absorption per atom over all ranges of energy, Z is the average proton number of the material, E_γ is the energy of the impinging gamma-ray, the *constant* is given as correction factor, and *n* is a constant that has values of 4

and 5. Therefore, a reduction in the average Z will reduce the probability of photoelectric interaction in the detector. Gamma-ray sensitivity can also be reduced by decreasing the thickness of the detector. The gamma-ray photon can be characterized by its mean free path (λ), which is the mean distance the photon travels before an interaction.

$$\lambda = \frac{\int_0^\infty x e^{-\mu x} dx}{\int_0^\infty e^{-\mu x} dx} = \frac{1}{\mu} \qquad \text{Eqn. 2.2}$$

In Eqn 2.2, μ is the linear attenuation coefficient and x is the distance traveled by the gamma-ray. By reducing the thickness of the material, the likelihood of gamma-ray interaction will be decreased.

2.2 Gas-filled Detectors

Gas filled thermal neutron detectors, such as the current ^{3}He detectors, were reported[38–40] as early as 1962, and have continued to be the technology employed in a variety of applications. Gas-filled detectors that employ ^{10}B have been reported[41] and they fall into two separate categories. The first design uses ^{10}BF$_3$ instead of ^{3}He, however this material has a large drawback due to the toxicity of BF$_3$. The second design involves coating the inside of the tube with solid substances, including boron oxide (B_2O_3), boron nitride (BN), and boron phosphide (BP)[41]. Like the ^{3}He tubes, the ^{10}B detectors are susceptible to inefficiencies and long response times.

2.3 Liquid Thermal Neutron Detectors

There have been some reports of thermal neutron detectors that used a liquid medium[42–45]. The majority of these reports indicate the use of scintillation liquids such as Saint-Gobain BC-501A or Perkin-Elmer Ultima-Gold scintillating cocktail. Other thermal neutron detectors using liquid medium for detection are the bubble detectors, which use viscous gels[46–48]. These detectors consist of a gas (similar to Freon) suspended in a polymeric matrix[49] and have been used in a variety of applications in dosimetry applications and dark matter searches. These detectors have virtually no gamma-ray response.

2.4   Solid State Detectors

To overcome the inefficiencies and long response times of the gas detectors, solid state detectors[50–54] were developed[55]. Solid state detectors can be divided into two separate categories: semi-conductors and scintillators. Since the focus of this project is to develop scintillators, a brief mention of the variety of semi-conductors will be listed. A. J. Peurrung[56] provides an excellent review of neutron detectors including those specifically related to thermal neutrons.

2.4.1   Semiconducting Detectors

Semi-conducting detectors for thermal detectors involve a number of detector types including: 1) silicon based detectors [55], [57] and 2) diamond-based devices[58–61], and 3) solid state devices, such as CdZnTe (CZT). Given the focus of this project on amorphous scintillator detector development, further discussion of semi-conductors would be beyond the focus of this work.

2.4.2   Scintillating Detectors

Solid-state scintillating detectors for thermal neutrons are the largest class of detectors and have a number of subcategories including: 1) inorganic, crystalline scintillators[6], [62], [63], such as CLYC (Cs_2LiYCl_2:Ce) , 2) Li Foils[57], [64], and 3) polymer thin films[7], [8], [65], and 4) inorganic glass scintillators [9–11], [26], [66], [67]. The focus of this project will be on inorganic glass scintillators for thermal neutron detection.

2.4.3   Early Glass Scintillators

Some of the earliest reports (1959) of glass scintillators for thermal neutrons were reported by Birks *et al.* [68] that used alumino-silicate glass composites. They employed both lithium and boron as neutron capture centers, and used lithium and boron oxides to introduce the neutron sensitive elements into the matrix. Cerium (III) was employed as the scintillation center in the matrix, and the bulk matrix was comprised of alumino-silicate oxides melted into a homogeneous mixture. Later work in 1976 by Spowart *et al.* used a similar compound, but did

11

not include boron as the neutron capture element [9–11]. This glass is commercially marketed as GS20 and was used as the detector standard for this project. The Nuc-Safe[69] company has made fibers that are similar in composition to GS20 that are amorphous scintillators.

2.4.4   Sol-Gel Glass Scintillators

Sol-gels are a solution-based method that can be catalyzed either by acid or base[70], [71]to produce vitreous materials. These materials have been reported to be used as waveguides[72], scintillators[73], [74], and thermal neutron detectors[74–77]. Wallace *et al.* [75], [76] has reported on the high optical clarity of these materials, which allows them to be loaded with Ce(III) cations and ^{6}LiF to be used as thermal neutron detectors. The drawback to this material was the lack of mechanical integrity and the inability of the material to prevent oxidation of the Ce(III) center to Ce(IV). Therefore, some references[78–81] have reported chemical methods to attach the Ce(III) center to the Si-O backbone of this material allowing for greater resistance to oxidation. This class of material has shown susceptibility to phase separation of the LiF from the gel and have a tendency to become very brittle when dried.

2.4.5   Current Lithium Tetraborate Based Detectors

In recent years, the use of lithium tetraborate single crystals as a potential neutron detection material has been proposed by Katagiri *et al.*[82], [83] and Ishii *et al.* [84], [85]. Both groups have used Ce as the scintillation center by using Ce_2O_3 to incorporate the Ce(III) into the matrix. The materials were heated at a variety of temperatures ranging from 850 ˚C to 1050 ˚C at different heating and cooling rates. The Ce(III) center is kept in the trivalent oxidation state by cooling and heating the material in a reducing atmosphere, such as 95% nitrogen and 5% hydrogen. These material types have been evaluated with mixed results for meeting the absolute neutron detection and neutron/ gamma discrimination criteria set forth by the DHS.   Ishii's work was primarily focused on using lithium tetraborate doped Ce as a crystalline material, and Katagiri's work focused on using a lithium tetraborate phosphate material, where they reported using both the crystalline and amorphous material.

It is known that the polycrystalline form of this material is opaque and would therefore have to be dispersed in a matrix to collect the light produced due to charged particles. Hence

the advantage of the lithium tetraborate as an amorphous substance is that it is highly transparent in the region from 300 nm to 800 nm. Unlike the crystalline form, the vitreous form of this material would not have to be dispersed in a secondary matrix to conduct the light, but would have the optical transparency to transport the light produced.

The amorphous lithium glass detectors doped with Ce have been further analyzed by Zadneprovski[86], where they used a $Li_2B_4O_7$ system doped with Cu, Ce, Eu, and a number of other rare earths. However, all the materials were introduced into the material in their lower oxidation states.

2.4.6   Experiments to Develop Lithium Tetraborate

The production of amorphous lithium borate is largely related to the maximum temperature that the material is heated to and the rate of cooling of the material. The amount of crystallinity is also related to the amount of other substances, such as boric acid and rare earth oxide present in the matrix.   In this work, amorphous lithium borate will be explored as a potential thermal neutron scintillation material and will also explore the use of boric acid as a reducing agent for the rare earth oxides.

2.4.6.1   Reduction of Rare Earths

In the proposed work, the development of Ce doped amorphous lithium tetraborate will use boric acid as a reducing agent. The abnormal reduction of rare earths has been reported by Stump *et al*[87] and Hao [35] *et al.* In these reports, the authors use alumino-borate or calcium borate matrices instead of the lithium tetraborate matrix that will be explored in this work. Similar reports[21], [23], [88–93] have studied similar occurrences in a number of alkali or alkaline metaloborates, as well as a strontium and aluminum borates. These reports indicated that the aliovalent doping of the material causes a reduction of the rare earth and requires the formation of a tetrahedral boron oxide $(BO_4)^{4-}$. It has been proposed that in the crystalline forms of these materials, the borate rings (B_3O_3) will donate electrons from the ring structure to the *s*-orbital of the metal atom. The structure of the Ce doped matrix is shown in more detail in Section 4.2.3.   This electronic contribution to the rare earth provides the reduction mechanism

that is essential for light output. Hence the focus of this project will be to explore a variety of concentrations of boric acid and cerium(IV) oxide to determine the optimum concentration needed to achieve maximum light output

2.4.7   Subtraction of $^6Li/^7Li$ or $^{10}B/^{11}B$

It has been shown in a number of references[46], [94–99] that utilization of the difference in cross-sections between the ^{6}Li and ^{7}Li isotopes gives a much higher efficiency for solid-state neutron detectors. In a mixed radiation field containing gamma-rays, fast neutrons, and thermal neutrons, the response of the ^{6}Li and ^{7}Li will be the same for the fast neutrons and gamma-rays. However, the higher thermal neutron cross-sections, as reported by NIST (National Institute of Standards and Technology) [4], [100] for ^{6}Li as seen in Fig. 2.4-1 will dominate at lower energies, which will increase the efficiency of the detector.
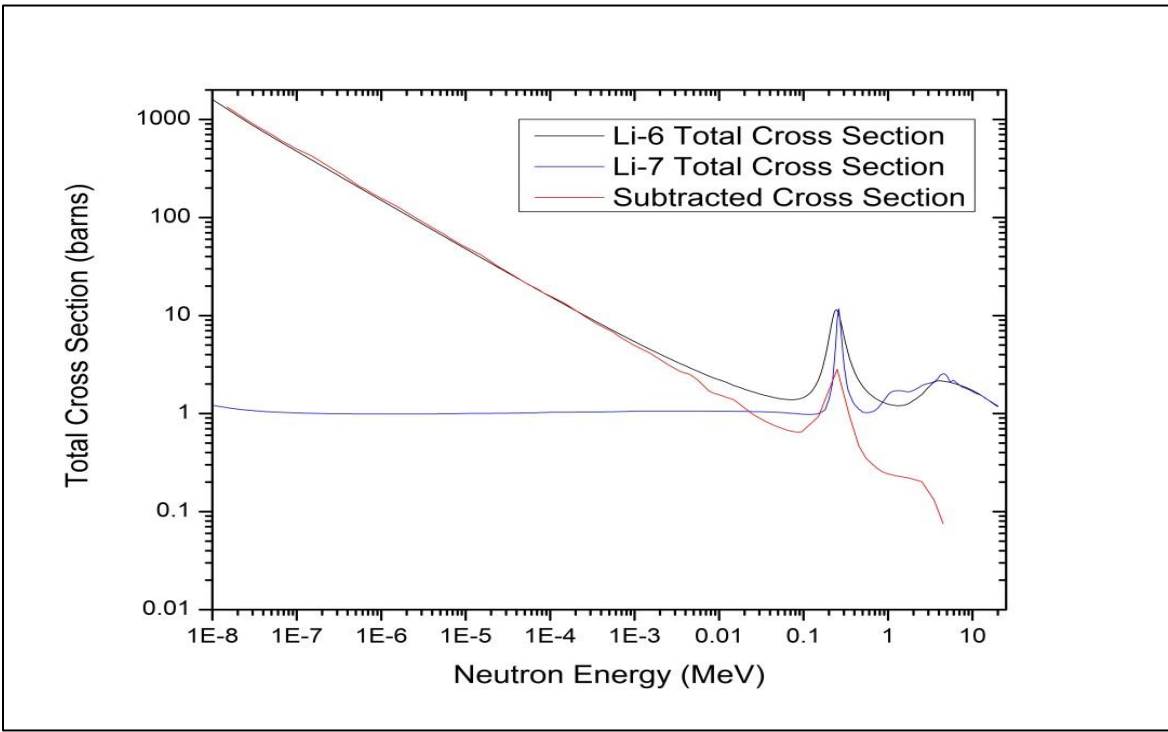
Figure 2.4-1: The total thermal neutron cross sections of ^{6}Li and ^{7}Li isotopes.

A similar analysis for $^{10}B/^{11}B$ can be made and the total neutron cross sections[4], [100] are shown in Fig. 2.4-2.
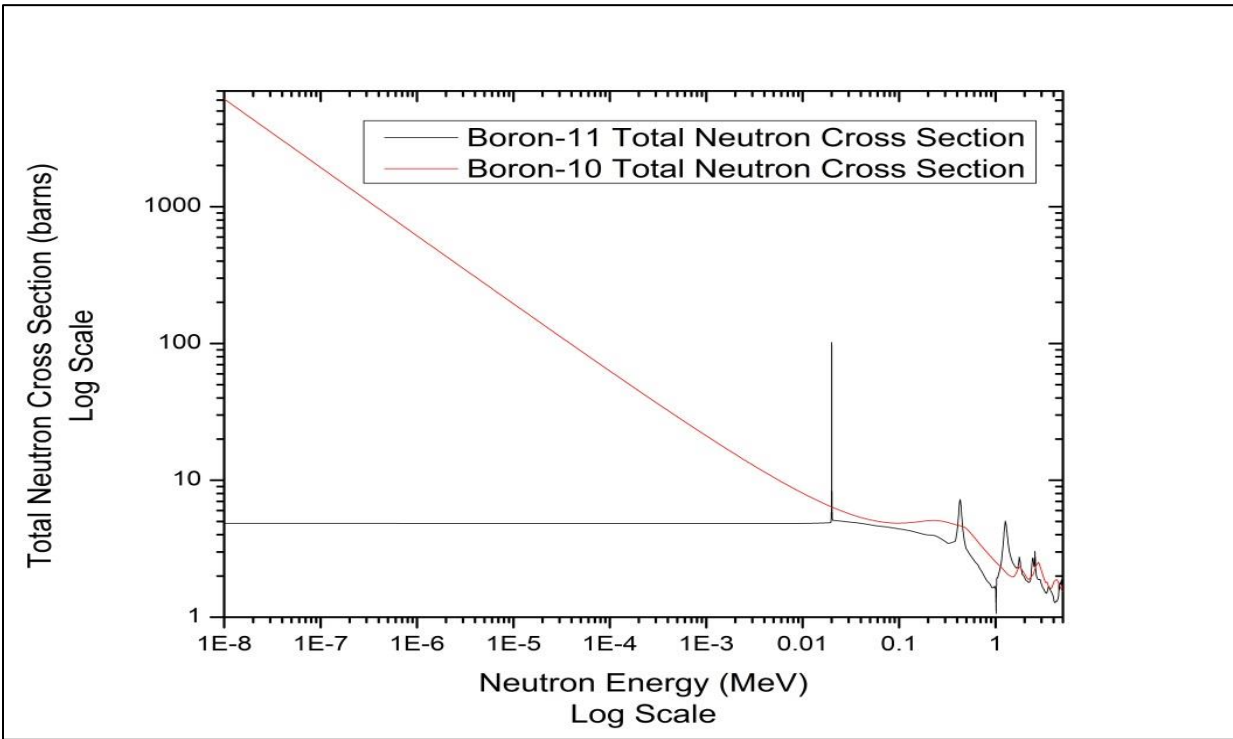
Figure 2.4-2 : ^{10}B and ^{11}B Total Neutron Cross Section.

When samples are made containing both isotopes of boron, the resulting material can be placed in a mixed field of fast neutrons, thermal neutrons, and gamma-rays, and by subtracting the ^{11}B spectrum from the ^{10}B spectrum, the thermal neutron response can be obtained. Therefore, the use of the large differences in cross sections can be used to increase the efficiency of the detectors. Although a number of groups have used this method to increase efficiency in lithium based detectors, there have not been a number of examples that used the subtraction of both lithium and boron to improve efficiency.   Thus, this could be a focus of the work that would be useful if the lithium borate material could not be synthesized to have inherent neutron/gamma discrimination qualities.

Chapter 3: Experimental Approach

3.1   Preparation of Lithium Tetraborate

A number of methods[101], [102] for the preparation of alkali (e.g. Li) borate species have been reported. However, in the synthesis of these alkali species, it is important to control the stoichiometry of the reactants. Otherwise the formation of the metaborate ($LiBO_3$), tetraborate ($Li_2B_4O_7$), and the pentaborate (LiB_5O_8) species will form as a mixture of crystalline products in the reaction vessel.

The lithium borate synthesis took a three-fold approach; with the first approach being to develop or optimize a synthesis method to produce an exclusive lithium tetraborate product. The second task was to determine the effect, if any, of the addition of the meta-, or penta-borate species into the lithium tetraborate, on the transparency of the glass. The final portion of the experiment was to determine the best loading of Ce into the matrix to achieve the highest optical clarity of the sample and maximize the light output of the sample.

3.1.1   Synthesis of Lithium Meta, Tetra, Pentaborate

Lithium meta-, and tetraborate are sold commercially as pure substances or as mixtures by companies such as Claissen® for XRF matrices. Although meta-, tetra-, and penta-borate materials can be purchased directly from manufacturers, the isotopic enrichments necessary for this work are not readily available. The ^{6}Li (97.6% enriched) is only available as ^{6}LiOH.   In this research, the ^{6}LiOH was provided by B&W Technical Services Y-12, LLC (formerly BWXT Y-12). Similarly, the ^{10}B (99.9%) is only available as boric acid (^{10}B(OH)$_3$) as purchased from Acros organics. Thus the meta-, tetra-, and penta-borate must be synthesized from the lithium hydroxide and boric acid precursors in order to achieve the necessary isotopic enrichment. The synthesis methods are described in sections 3.1.2 – 3.1.3.

3.1.2   Synthesis of Lithium Pentaborate

The synthesis of lithium pentaborate was performed by reacting lithium hydroxide with boric acid in aqueous medium to produce lithium pentaborate according to the following reaction:

$$\text{LiOH}_{(aq)} + 5\ \text{H}_3\text{BO}_{3(s)} \rightarrow \text{LiB}_5\text{O}_{8(s)} + 8\ \text{H}_2\text{O}_{(aq)} \qquad\qquad \text{Reaction 3.1}$$
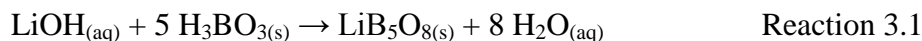
The reaction products were dried at 120°C to remove the water, producing a fine white powder. The products were characterized by P-XRD and ICP-OES. For ICP-OES analysis the lithium pentaborate was dissolved in conc. nitric acid and diluted to 2% in trace metal grade nitric acid (Fisher Scientific).

3.1.3   Synthesis of Lithium Tetraborate

3.1.3.1   Synthesis of Lithium Tetraborate (Ge Method)

Ge *et al.* proposed a method for making lithium tetraborate into thin films on a Si substrate for the purpose of thermal neutron detection. This was accomplished by coupling the material directly to the semiconductor. The advantage of this method was that it could be performed by a solution method at lower temperatures. The method required LiOH was reacted with glacial acetic acid at 50 °C to produce lithium acetate ($\text{LiC}_2\text{H}_3\text{O}$), which was dried to a solid. Similarly, boric acid was dissolved in 100% ethanol, according to the following reaction:

$$\text{H}_3\text{BO}_{3(s)} + 3\ \text{C}_2\text{H}_5\text{OH}_{(s)} \rightarrow (\text{C}_2\text{H}_5\text{O})_3\text{B}_{(s)} + 3\ \text{H}_2\text{O} \qquad \text{Reaction 3.2}$$

The resulting reaction produced a clear liquid, to which the solid lithium acetate was added in stoichiometric quantities according to the chemical formula of $\text{Li}_2\text{B}_4\text{O}_7$. According to Ge, 1 mol% boric acid was added to the mixture to compensate for boric acid loss during Rxn 3.2. The reaction mixture was stirred for 1 hr. to make a homogeneous solution. The reaction was then heated to 200 °C to remove the water. Upon heating to temperatures of 500 – 700 °C, the resulting product became a black color indicating that the acetate had decomposed into a carbon impurity. Since this method was originally intended for thin film coating onto a silicon substrate and not for bulk production of lithium tetraborate, this method was not successful for use in the bulk preparation of lithium tetraborate. Analysis of the final product was performed using P-XRD.

17

3.1.3.2   Synthesis of Lithium Tetraborate (Kaylan Method)

A second method was reported by Kayhan and Yilmaz. Solid Li_2CO_3 and H_3BO_3 were combined in a 1:4 ratio by grinding with a mortar and pestle. The powders were then placed in an alumina crucible and heated to 400 ˚C for 3 hr. under a normal atmosphere. The resulting white solid was ground again with a mortar a pestle, and heated to 750˚C for 1 hr. under normal atmosphere. The resulting powder was analyzed with P-XRD.

3.2   Experimental

Lithium tetraborate has been used in a number of applications, as mentioned in the previous chapter, but its primary use has been as a fluxing component for X-Ray Fluorescence (XRF) samples[103]. As is shown in Fig 4.2-17, it has excellent optical properties, particularly in the region from 350-430 nm, where photomultiplier tubes (PMT) used in portal monitors or other detection applications are sensitive. This material possesses no natural fluorescence center, and therefore must be doped with a metal ion such as Ce^{3+}, Eu^{2+}, or Cu^{2+} to provide the necessary fluorescence capability.

All samples were prepared in a Thermolyne 1400 series oven with a normal atmosphere at 1050 ˚C for a heating time of 1-2 hr. The heating rate was 40 ˚C/min and the cooling rate was immediate quenching to room temperature. Samples of 500 mg and 5.0 g of total mass were prepared under the aforementioned criteria and were heated in graphite crucibles. The 500 mg samples were prepared in graphite crucibles purchased from Leco®, and were then placed in ceramic crucibles to slow the reaction of the atmosphere with the crucible. The 5.0 g samples were prepared in reactor grade graphite supplied by the University of Tennessee Department of Nuclear and Radiological Engineering which was modified for this purpose.

3.3   Compositional Experiments

There are a number of reports[30], [33], [104], [105] concerning the production of lithium borate glass that discuss a number of parameters including the heating temperature, rate of heating, rate of cooling, and concentrations of the components. In this work, a study of how

the lithium borate composition affects the optical clarity and fluorescent capabilities of the glass samples was performed.

The first studies involved mixtures of lithium meta-, tetraborate ranging from 100% tetraborate to 100% metaborate and all samples were characterized by P-XRD. It was determined that 100% tetraborate produced the most optically clear glass.

3.4 Boric Acid Loading

A number of sources[35], [82], [84–86], [101], [106] have presented methods for incorporation of Ce and Eu into LBO and other matrices. Most methods involve heating the material to temperatures greater than 850˚C under N_2 and varying amounts of H_2 to produce a reducing atmosphere. The hydrogen/nitrogen atmosphere reduces Ce or Eu to the tri- or divalent state, which is necessary to create a fluorescent center.

Other sources have noted that Ce^{4+} or Eu^{3+} can be reduced using excess boric acid (H_3BO_3), although the mechanism of reduction is still somewhat disputed in the literature. Based on the reports[35], [87] of using excess boric acid to reduce the rare earth, a series of experiments were performed to determine how much boric acid can be added to achieve maximum reduction of the rare earth, while simultaneously maintaining maximum optical clarity.

The experiments that were performed with boric acid involved varying the weight percentage of boric acid in the lithium borate matrix loaded with 0.5 wt% CeO_2. Further experiments were performed by varying the amount of CeO_2 to maximize the light output. Finally, some researchers have indicated that co-doping the borate matrix with metallic ions such as Tb, Ca, Al, or Mg can improve the light output of the samples.

A series of experiments involved loading a lithium tetraborate matrix with increasing amounts of boric acid from 10 wt% to 20 wt%. It was determined that 17 wt% boric acid produced the most optically clear glass, and higher loadings produced highly crystalline

samples that were optically opaque. The samples were analyzed with P-XRD to determine crystallinity.

3.5   Ce Loading Experiments

After determining the maximum amount of boric acid, the weight percent of CeO_2 was varied from 0.5 wt% to 5.0 wt%, and the samples were analyzed by fluorescence and P-XRD. It was determined that the 0.5 wt% samples produced optically clear and colorless glass samples that had low crystallinity. Some experiments were performed (results are shown in Sec. 4.2.5.1) where cerium(III) was introduced into the matrix as the cerium(III) silicate ($Ce_4(SiO_4)_3$) and as $Ce_3(NO_3)$, such that the amount of Ce^{3+} was equivalent to that of the 0.5 wt% CeO_2 (or 0.04 at% Ce).

The Ce is loaded into the matrix as CeO_2, where Ce is in the tetravalent oxidation state. Upon heating, the Ce is converted from Ce^{4+} to Ce^{3+}, which populates the $4f$ orbital[107] allowing for the $5d$ to the $4f$ transition state, that occurs near 360 nm. It is theorized that the B_3O_3 rings that are formed in the LBO matrix will donate an electron into the lowest lying orbital of the rare earth in a ligand metal charge transfer (LMCT) type of mechanism.

3.6   Co-doping Loading Experiments

Sources[35], [87], [106] have highlighted the abnormal reduction of rare earth elements when heated in the presence of boric acid. They indicated that this reduction effect could be enhanced when other metal ions were added to the matrix. These metal ions should have accessible oxidation states of higher valency, such that they can serve as electron donors, to aid in the reduction of the Ce center. These metal ions must also have a colorless upper oxidation state, such that the final vitreous product is both clear and colorless. In this study, Tb^{3+} and Pr^{3+} were selected[108], since both have an accessible tetravalent oxidation state.

In these experiments, the lithium borate glass was loaded with 17 wt% boric acid, loaded with 0.5wt% CeO_2 (0.04 at% Ce), and doped in a 1:1 at% ratio with either the Pr or Tb. The Tb was mixed into the matrix as Tb_6O_{11}, and the Pr was mixed into the matrix as Pr_2O_3. In later work, the Tb was used exclusively in the trivalent state as Tb_2O_3 , since the Tb_6O_{11} consists as a

mixed oxide containing both Tb^{4+} and Tb^{3+}. The theory behind the co-doping was that once the sample was made, the Pr or Tb would serve as an electron donor to the Ce to increase the population of Ce^{3+} ions in the matrix, thus increasing the light output of the sample. See Figure 4.2-16 for florescence data.

3.7   General Characterization Methods

3.7.1   Inductively Coupled Plasma – Optical Emission Spectroscopy

Inductively Coupled Plasma-Optical Emission Spectroscopy is a powerful technique to determine the elemental composition of a number of samples. The experiments were performed using a Perkin Elmer Optima 2100DV ICP-OES spectrometer.

The samples were dissolved in hydrofluoric acid (50%, Acros) and diluted with 2% HF in polyethylene volumetric flasks. The challenge in dissolving the samples was the loss of boron via the reaction of boron with HF as shown in Reaction 3.3.

$$Li_2B_4O_{7(s)} + 14\ HF_{(aq)} \rightarrow 4\ BF_{3(g)} + 2\ LiF_{(s)} + 7\ H_2O_{(aq)} \qquad \text{Reaction 3.3}$$
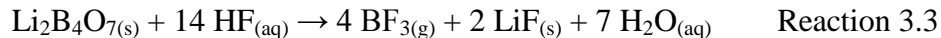
The liberation of boron trifluoride as a gas reduces the accuracy of the ICP-OES experiments due to the loss of boron from the matrix.

3.7.2   Powder-X-Ray Diffraction (P-XRD)

Powder X-Ray Diffraction (P-XRD) is a highly useful tool for characterizing the borate reactants as well as determining the amount of crystallinity in the final vitreous lithium borate glasses. All experiments were performed using a Panalytical Empryean X-ray diffractometer using a Pixcel 3D detector. The x-ray source was a Cu anode set at 10 mA and 45 kV, respectively, using a slit window of 1/4˚ 2θ. All samples were measured using a silicon (001) no-background sample holder and were set to spin at 4 revolutions/sec.   All spectra were acquired from 5˚ 2θ to 70 ˚ 2θ.

21

All spectra were analyzed using the X'Pert HighScore Plus (PW3212) software, ver. 3.0, and all structure determination were solved using the "SuperFlip" algorithm as part of this software.

3.7.3 Solid State Nuclear Magnetic Resonance (SSNMR)

Like P-XRD, SSNMR-Magic Angle Spinning (MAS) was useful in determining the products formed from the preparation of the lithium meta-, tetra-, and pentaborate. Once the borate products were sufficiently dry, it became very difficult to re-dissolve them so as to obtain solution NMR data from the samples, thus warranting the use of SSNMR-MAS. Similarly, the final glass was highly insoluble in any solvents except for concentrated hydrofluoric acid, thus requiring this material to be analyzed by SSNMR-MAS.

The SSNMR-MAS experiments were all performed using a Varian Inova 400 MHz instrument with a Varian-Chemagnetics 5 mm double resonance MAS probe. The boron experiments were performed[27], [30], [31], [109] using B-11 NMR and used boric acid as a standard. The Li-7 NMR experiments were performed using a lithium chloride standard.

3.7.4 Fourier Transform – Infrared Spectroscopy, Attenuated Total Reflectance (FT-IR-ATR)

Fourier Transform – Infrared Spectroscopy was another method to determine the structure of the lithium tetraborate materials, FT-IR-ATR spectroscopy was used. This spectroscopy allows the user to probe the structure of the B-O structure[110] as reported by Pekpak *et al.*

The instrument was a Perkin-Elmer Frontier FT-IR-ATR Spectrum 100 with each spectrum being acquired after a 12-scan background and 32 scans for the sample. The background and the samples were acquired using PDMS (poly-dimethylsiloxane) to couple the sample to the lens of the detector.

3.7.5 Fluorescence Spectroscopy

In order to measure the effectiveness of the reduction of the rare earth elements, fluorescence measurements were performed. All fluorescence measurements were obtained on a Perkin-Elmer LS-55 fluorescence instrument. The emission and excitation experiments were performed using a slit width of 5 nm and a detector gain of 750 kV.

Fluorescence was a very important technique to this work due to the similarity in fluorescence and scintillation. While scintillation requires high energy particles (e.g. alpha, tritons, etc.) to pass through the matrix and deposit energy which is converted to photons via a fluorescence center, fluorescence requires photons of specific energies to excite the fluorescent center to produce photons. While the mechanism for scintillation is different, without a fluorescent center, the sample will not scintillate.

3.7.6   UV-vis Spectroscopy

UV-vis spectroscopy was performed using a Perkin-Elmer Evolution 600 UV-vis spectrometer and was measured using a 5 nm slit width.

3.7.7   Confocal Laser Surface Microscopy (CLSM)

All of the confocal laser surface microscopy (CSLM) measurements were made using a Leica SP2 CSLM equipped with a 488 nm argon ion laser. Prior to performing the imaging, the samples were all polished using 400, 600, 800, and 1200 grit silicon carbide paper to improve the smoothness of the surface. This polishing also improved the coupling of the sample to face of the PMT during irradiation testing. The measurements were made at both the surface of the samples and at a variety of depths in the matrix.

3.7.8   Scanning Electron Microscopy (SEM)

All of the scanning electron microscopy (SEM) imaging was performed using a LEO 1525 microscope with an accelerating voltage of 10 kV.

3.7.9   Energy Dispersive X-Ray Spectroscopy (EDS)

Energy Dispersive X-ray Spectroscopy (EDS) uses high energy electrons to remove core electrons from atoms in the sample. The ejected electrons leave "holes" in the vacant electron levels, which are filled by electrons in higher orbitals falling down to fill the empty positions. In this transition, x-rays are emitted and have specific energies that correspond to the element from which they are ejected. This technique is limited to elements with $Z > 3$, hence it is not useful for lithium measurements, where Z is the proton number of the element. All EDS measurements were made using the LEO 1525 microscope and were measured after the SEM measurements were taken.

3.8   Nuclear Irradiation Characterization

All of the samples that were made were irradiated by alpha, beta, gamma, and neutron sources. The neutron and gamma data were evaluated to determine if they met the DHS criteria for neutron/gamma discrimination and for intrinsic neutron efficiency. The following section provides all of the experimental details pertaining to these irradiation experiments. Due to geometry difficulties, the absolute neutron efficiency and GARR were not determined for the samples.

3.8.1   Neutron Characterization

The characterization of the samples by neutron irradiation was performed using a 0.59 μg ^{252}Cf source (purchased on July 2, 2009). The source was encased in 0.5 cm of stainless steel and was further encased in 6 cm of HDPE (high density polyethylene) as depicted in Fig. 3.8-1. The total number of neutrons passing through through the samples was 284 neutrons/sec/cm^2 based on a sample with a diameter of 5.16 cm and 50 μm in thickness, as measured on April 4, 2013. The this number was calculated according to standard methods with MCNPX (Monte Carlo N-Particle eXtended) by Urffer [111].
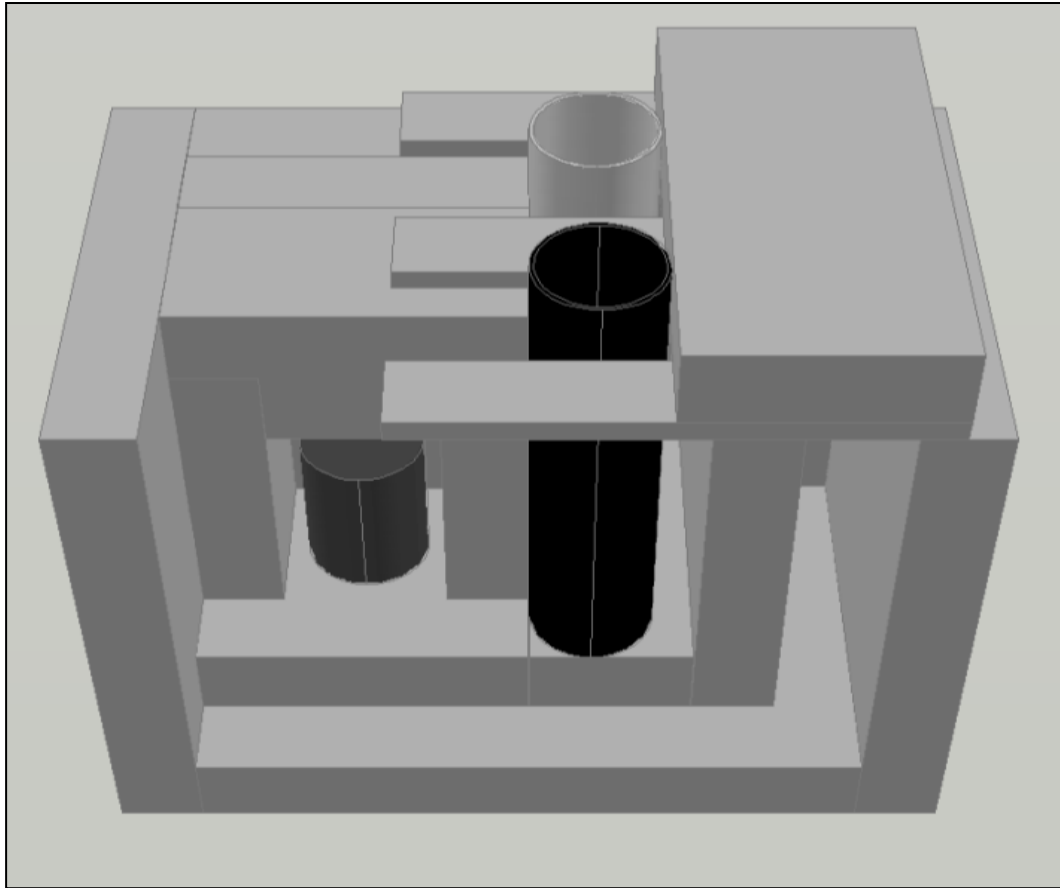
Figure 3.8-1: Neutron irradiator setup.

In figure 3.8-1, the small cylinder (on left) represents a 0.59 μg ^{252}Cf source (purchased July 2, 2009) encased in 0.5 cm of stainless steel and 1.25 cm of lead. The large gray enclosed cylinder (upper right) represents an acrylic tube with 0.5 cm of cadmium shielding. The black enclosed cylinder (lower right) represents the acrylic tube with 0.5 cm of lead shielding. A side of the irradiator is removed for better display of the structure.

The neutron spectrum was calculated according to standard methods with MCNPX (Monte Carlo N-Particle eXtended) by Urffer [111]. The neutron energy spectrum of the ^{252}Cf source prior to HDPE moderation was also calculated with MCNPX and is depicted in Fig. 3.8-2.
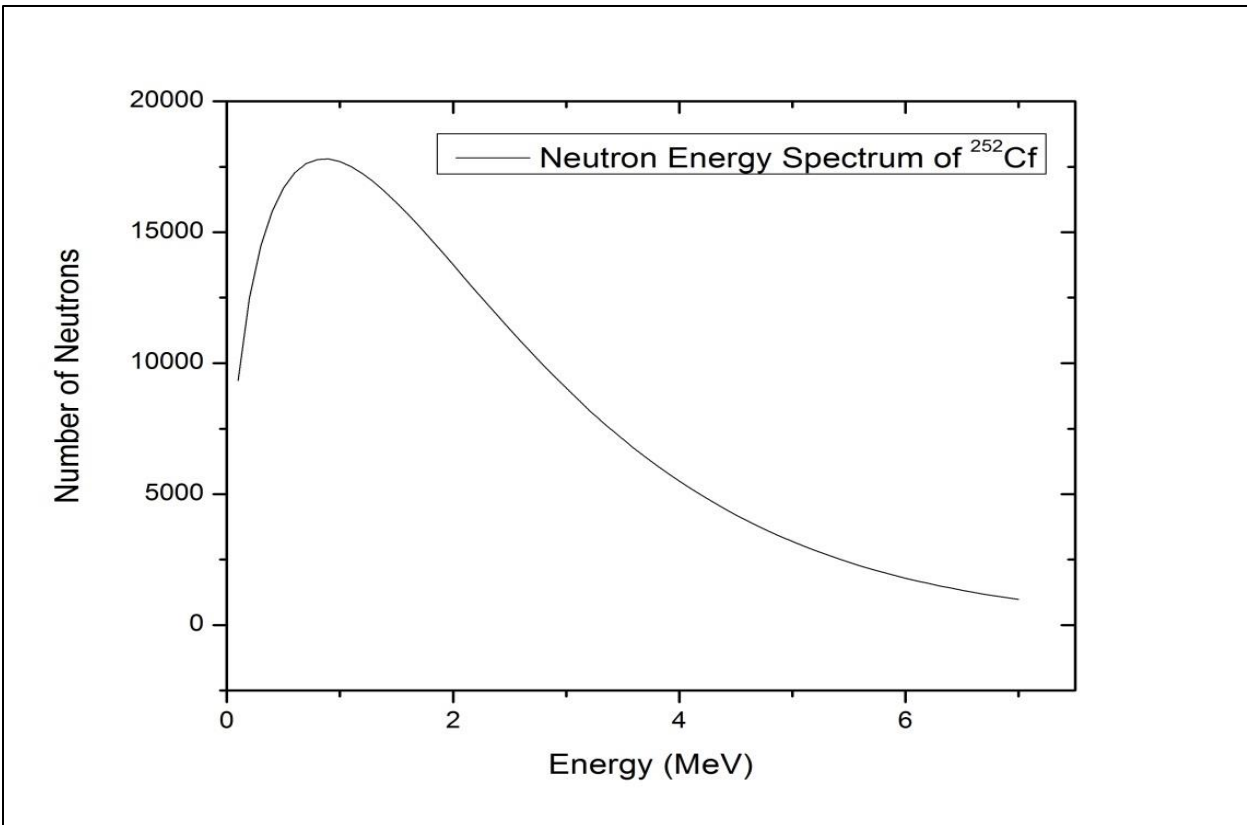
Figure 3.8-2: ^{252}Cf neutron energy spectrum prior to moderation through 6 cm of HDPE [111]. This is scaled by 0.59 ng of ^{252}Cf.

Also using MNCPX [111], the energy spectrum of neutrons interacting with a detector of 5.1 cm diameter and 50 μm thickness was calculated and is depicted in Fig. 3.8-3. The neutron energy spectrum is represented by the spectrum of neutrons coming through the lead cylinder.
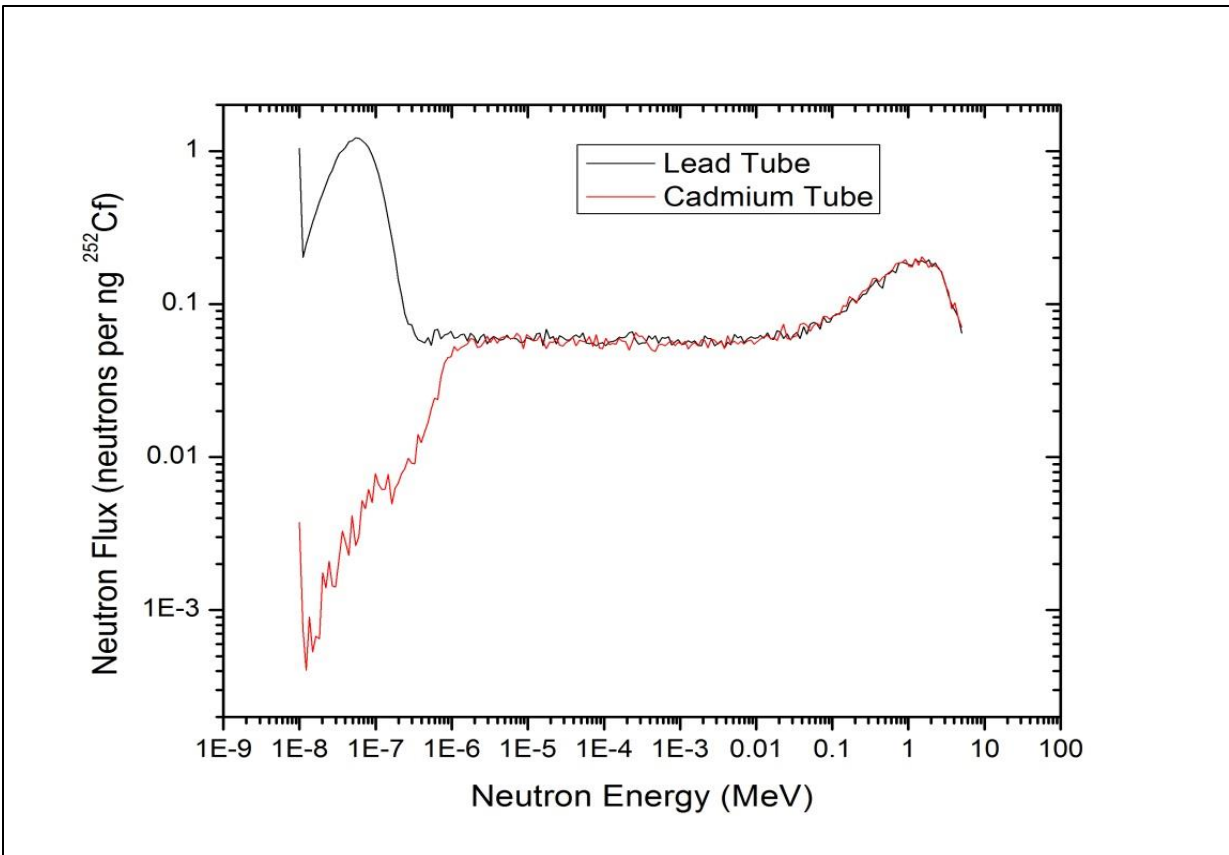
Figure 3.8-3 : Neutron energy spectrum as calculated by MCNPX based on the responses from GS-20 [111].

In figure 3.8-3, the black line (-) represents the neutron spectrum of [252]Cf after passing thought the lead tube, which contains thermal neutrons, fast neutrons, and gamma-rays. The red line (-) is the neutron spectrum through the cadmium tube with contains fast neutrons and gamma-rays.

During characterization, the samples were irradiated for 3600 sec. in both the lead cylinder and the cadmium cylinder, and the spectrum obtained from the irradiation tube was subtracted from the spectrum obtained in the lead cylinder. All samples were coupled to a photomultiplier (PMT) tube using optical grease and covered with a Teflon® tape reflector. The sample was irradiated inside the acrylic tube surrounded by lead to obtain the scintillation response to all gamma-rays and all-neutrons[111], [112]. The scintillation responses were

converted to electrical pulses using a Philips 2202B PMT mounted on a Canberra 2007P base powered by an ORTEC 556 high voltage power supply set at 1200V. The signals from the base were amplified using an ORTEC 572A amplifier set at 50G with a 2 μs shaping time. The amplified signal digitalized using an ORTEC 926 MCB with a 8192 channel ADC. The digitalized output was then saved using the MAESTRO-32 software from ORTEC. The light output was calibrated using known responses from GS20 lithiated glass. All glass samples were compared based upon their intrinsic neutron efficiency, which was given to be 1.2×10^{-3} or 2.5 cps/ng of ^{252}Cf at 2 m in moderated form[1–3]. All spectra acquired, whether alpha, beta, gamma-ray, or neutron are corrected for background, with an irradiation time of 1200 sec. The following is an excerpt from Urffer with regard to the calculations of intrinsic efficiency and solid angle.

The intrinsic efficiency is defined[5] in Eqn. 3.1.

$$\epsilon_{int} = \frac{N_c}{N_i} \qquad\qquad Eqn.\ 3.1$$

In Eqn. 3.1, the ε_{int} is the intrinsic efficiency, N_c is the number of counts recorded by the detector, and N_i is the quanta (number of particles) of radiation incident upon the detector. The quanta of radiation incident upon the detector (N_i) can be subdivided into two components: the source strength and the solid angle. The composition of N_i is shown in Eqn. 3.2.

$$N_i = \Omega S_0 \qquad\qquad Eqn.\ 3.2$$

In Eqn. 3.2, the S_0 is the source strength and Ω is the solid angle. The source strength of the ^{252}Cf is defined according to Eqn. 3.3.

$$S = S_0 e^{\frac{-ln(2)}{t_{1/2}}t} \qquad\qquad Eqn.\ 3.3$$

In Eqn. 3.3, S represents the strength of the source at the current time, $t_{1/2}$ represents the half-life of ^{252}Cf (2.65 years), and t represents the age of the source. The solid angle was calculated using MCNPX, as performed by Matthew Urffer. A F1 tally is used over the detector surface with two cosine bins, $-1 < \cos\theta < 0$ and $0 < \cos\theta < 1$. As macro-bodies are used for the surfaces of the detector, $-1 < \cos\theta < 0$ represents the particles that cross into the surface and $0 < \cos\theta < 1$ represents the particles that leave the surface. The MCNPX simulation was bench marked against GS20 and against polymer films.

The number of counts upon a detector is measured using the neutron irradiator facility. The quanta of radiation incident upon the detector is found from MCNPX calculations. This consists of two parts: 1) determining the number of neutrons crossing the detector surface in the lead and cadmium wells and, 2) determining the source strength. The source strength of the ^{252}Cf source, obtained July 2, 2009, and has a spontaneous neutron emission rate of 2.3 x 10^6 neturon/s/μg. Thus the source strength at any time can be calculated using Eqn. 3.3, as shown below.

$$S = S_0 e^{\frac{-\ln 2}{t_{1/2}}t}$$

$$S = 0.59\ \mu g\ {}^{252}_{98}Cf \times \left(\frac{2.3 \times 10^6\ neutron/s}{\mu g\ {}^{252}_{98}Cf}\right) \times\ e^{\frac{-\ln 2}{2.65\ yr}t}$$

$$S = 1.357\ \times 10^6 neutron/s \times e^{\frac{-\ln 2}{2.65\ yr}t}$$

Table 3.1: Simulated Neutron Solid Angle for Various Film Radii		
Thickness	*1 cm*	*1.27 cm*
0.5	8.03 x 10^{-4}	
0.2	6.34 x 10^{-4}	9.87 x 10^{-4}
0.1	5.77 x 10^{-4}	9.31 x 10^{-4}

3.8.2   Gamma-ray Characterization

Gamma-ray characterization was performed using a 97 μCi ^{60}Co source encased in 1.27 cm of stainless steel, thus providing a beam like geometry. The samples were counted for 600 s. The ^{60}Co produces two gamma photons[113] of 1.17 MeV and 1.33 MeV, respectively. The calculation for the number of incident gamma-rays is detailed in the following section by Urffer.

The gamma-ray intrinsic efficiency is calculated by a combination of simulations to determine the solid angle that the detector subtends and radioactive decay. The gamma

irradiator consists of the 97 μCi ^{60}Co (obtained January 1, 2012, $t_{1/2}$ = 5.27 yr). The incident quanta of gamma-rays is calculated using Eqn 3.3.

$$S = S_0 e^{\frac{-\ln 2}{t_{1/2}}t}$$

$$S = 97 \; \mu Ci \; {}^{60}_{27}Co \times \left(\frac{1.3 \times 10^{10} \; decay/s}{Ci}\right) \times \left(\frac{2 \; photon}{decay}\right) \times \; e^{\frac{-\ln 2}{5.27 \; yr}t}$$

$$S = 7.187 \times 10^6 \frac{photon}{s} \times \; e^{\frac{-\ln 2}{5.27 \; yr}t}$$

The sample was mounted to the PMT and the signal was processed according to the description found in Section 3.4.1.

3.8.2.1   *Neutron/Gamma-ray Discrimination Characterization*

Due to equipment limitations and counting geometry constraints, it was not possible to determine if the samples met all of the criteria specified by DHS[1], [2] as presented in Section 1.1. Of the mentioned criteria, the intrinsic gamma-neutron detection efficiency ($\varepsilon_{int, \gamma n}$) and the intrinsic neutron detection efficiency were determined. In practice the gamma and neutron spectra are obtained as per the methods described in Section 3.8.1 and 3.8.2. Representative gamma and neutron spectra are shown in Fig. 3.8-4.
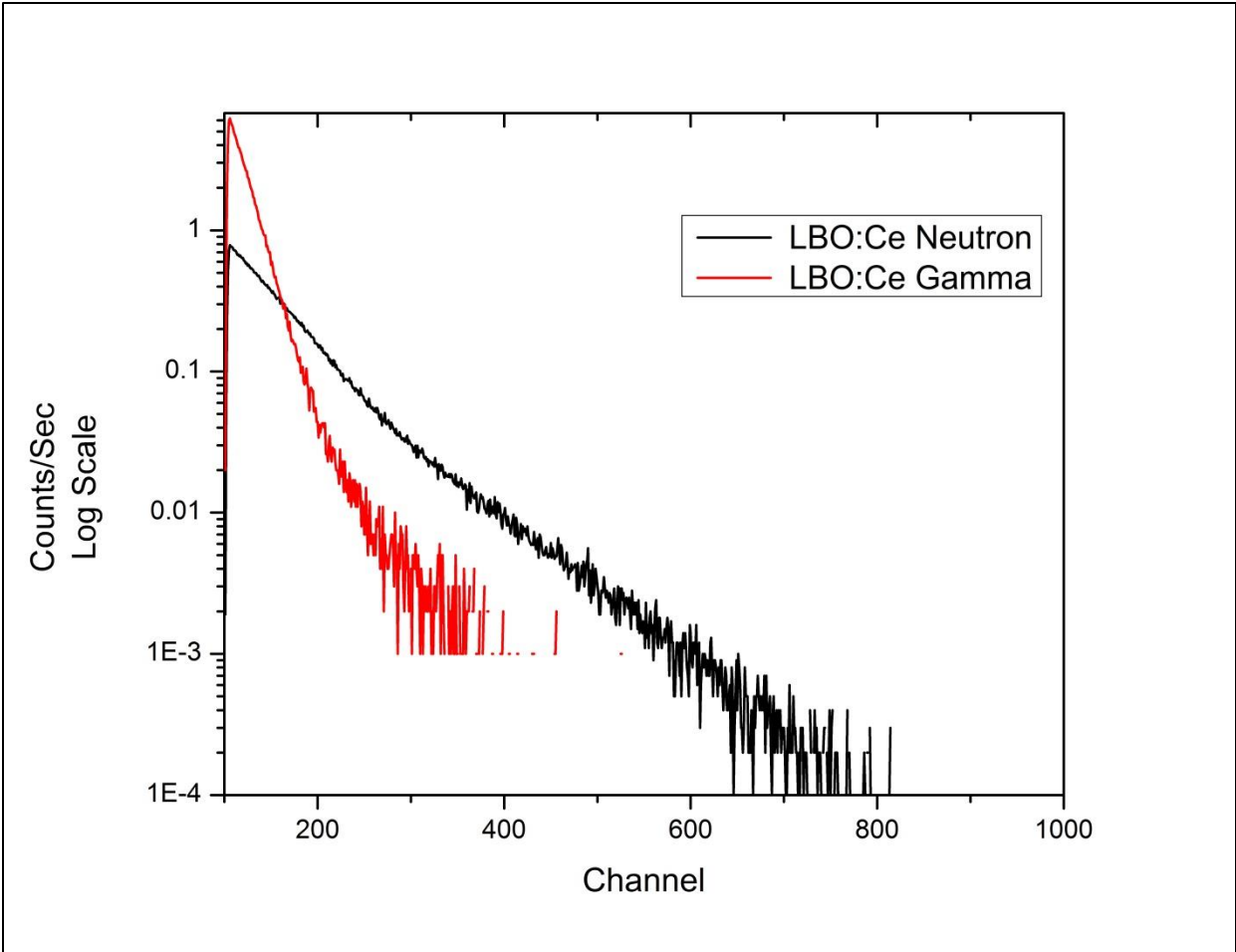
Figure 3.8-4: Representative neutron and gamma spectrum. The count time of the gamma-ray spectrum was 600 sec, and the count time for the neutron spectrum was 3600 sec.

In Fig. 3.8-4, the lack of data for the gamma-ray spectrum below 1 x 10^{-3} is a result of the count time of 600 sec. Since the spectrum is plotted on a log scale any counts that are zero or negative (as a result of background) correction will not be plotted on the logarithmic scale. Since the glass samples (Fig 3.8-4) do not have clearly defined features[111], spectral averages are used to create a defined feature. The spectral average is obtained using Eqn. 3.4.

$$\langle \mu \rangle = \frac{\int_0^\infty x \cdot f(x)\,dx}{\int_0^\infty f(x)\,dx}$$
Eqn. 3.4

In Eqn. 3.4, $\langle \mu \rangle$ is the average of the spectra, f(x) is the spectra (actual data), and x is the channel number.

The mathematical lower level discriminator (MLLD) is set to be the channel at which $\varepsilon_{int,\gamma} \leq 10^{-6}$ and the MLLD is applied to the neutron spectrum. Equation 3.5 is used to mathematically determine the gamma intrinsic efficiency.

$$\epsilon_{int,\gamma} = \frac{\int_{MLLD}^{\infty} f(x)\, dx}{Particles\ Incident} = 10^{-6} \qquad\qquad \text{Eqn. 3.5}$$

In Eqn. 3.5, MLLD is the mathematical lower level discriminator, f(x) is the spectra (actual spectral data acquired), and Particles Incident is the number of incident particles through the sample. The particles incident were calculated using MCNPX and were performed by Urffer[111]. In Fig. 3.8-5 a graphical representation of the MLLD discriminator is presented for a lithium tetraborate glass doped with 1.0 wt % CeO_2.
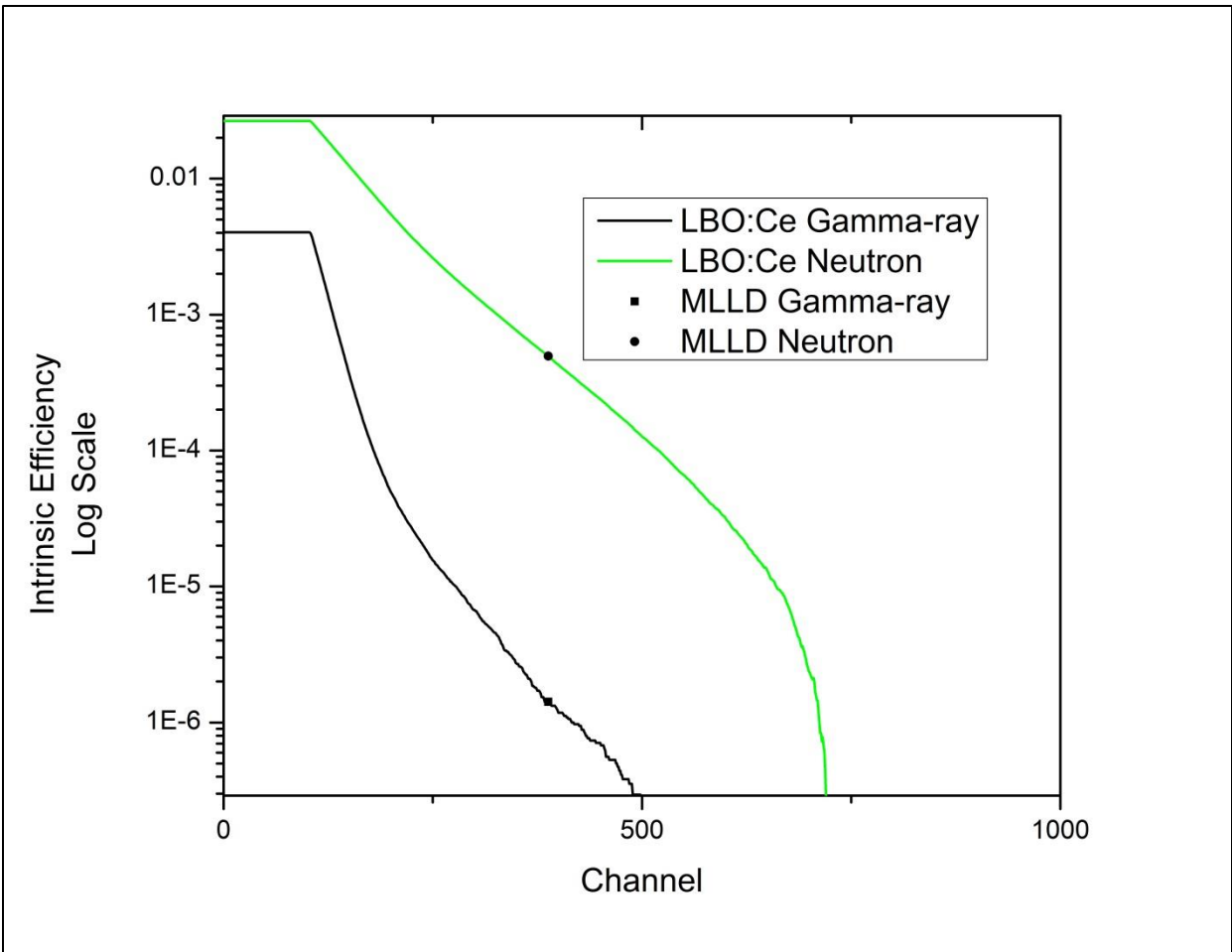
Figure 3.8-5: Representation of the MLLD setting as applied to the thermal neutron response.

In Fig. 3.8-5, the flat region (channel 0 to 100) corresponds to the physical LLD of the counting system. In this region, all of the counts are zero, hence the sum of the spectrum at all of these points is equivalent, giving rise to the flat line.

Once the gamma-ray intrinsic efficiency has been determined, the neutron spectrum must be integrated starting at the MLLD channel setting determined from the gamma spectrum. The equation for integration is shown in Eqn. 3.6.

$$\epsilon_{int,n} = \frac{\int_{MLLD}^{\infty} f(x)\, d(x)}{\text{Neutron Particles Incident}} \qquad \text{Eqn. 3.6}$$

3.8.2.2   Comparison to GS20

In Eqn. 3.3, Neutron Particles Incident is the number of thermal neutrons crossing the sample, MLLD is the mathematical lower level discriminator determined from the gamma spectrum, and f(x) is the actual neutron spectrum.

After the gamma-ray/neutron discrimination is MLLD is calculated, the peak from the neutron spectrum (Fig. 3.8-4) can be calibrated to the GS20 spectrum (Fig. 3.8-6).
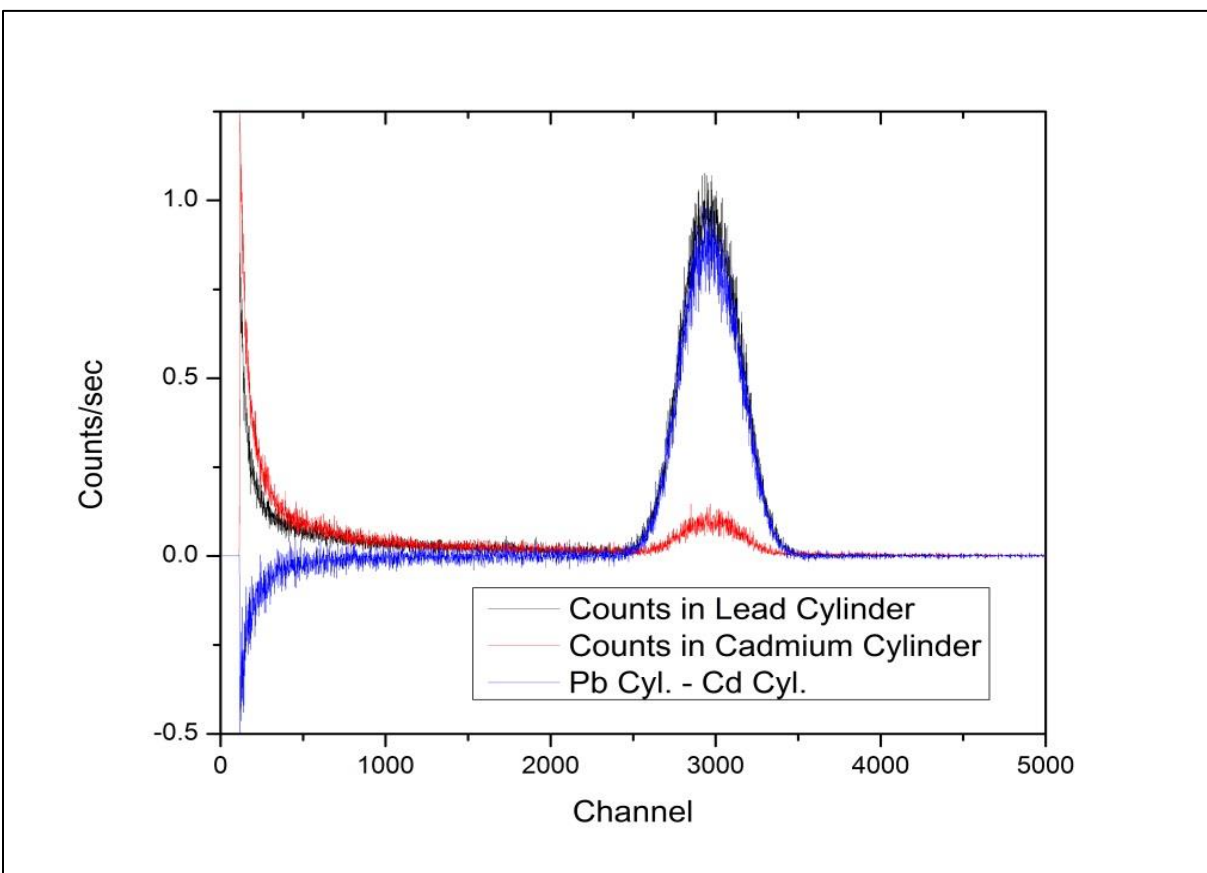
Figure 3.8-6: The neutron and gamma-ray irradiation spectrum of GS20. GS20 is reported to have 6250 photons/neutron[10], and a peak at channel number 3100, with a gain setting of 20, and a PMT voltage of 1180 V.

In figure 3.8-6, the irradiation in the lead cylinder is shown by the black line (-), and irradiation by gamma-rays and fast neutrons from the ^{252}Cf source are observed when irradiated in the cadmium cylinder as is shown in the red line (-). When the cadmium cylinder spectrum is subtracted from the lead cylinder spectrum the resulting spectrum, shown in the blue line (-), is observed. By subtracting the cadmium spectrum from the lead spectrum, the thermal neutron response is approximately obtained. The spectra are normalized to 1.0. The number of photons per neutron event is given by the following calculation.

$$\frac{6250 \; photons}{1 \; neutron} \times \frac{1 \; neutron}{3100 \; channel} = 2.01 \; photons/channel \qquad \text{Eqn 3.4}$$

When scaled to a gain of 50, this results in a 0.8 photons/channel. This results will be used for the comparison calculation of the lithium tetraborate glass are compared to that of GS-20 in Section 4.4.1.

3.8.3   Alpha Characterization

The alpha response was carried out by irradiation using a 0.1 µCi ^{241}Am source placed in direct contact with the sample. The sample is mounted to the PMT and the signal was processed according to the description found in Section 3.4.1.

3.8.4   Beta Characterization

The beta characterization was carried out using a 0.1062 µCi ^{36}Cl source placed in direct contact with the surface of the sample. The sample was mounted to the PMT and the signal was processed according to the description found in Section 3.4.1.

3.9   Acknowledgements

I would like to thank Dr. Carlos Steren and Matthew Dembo for their help in performing the SSNMR experiments. I would like to thank Brittany Miner, John Cadotte, Kristin Forsberg, and Jake Stewart for their help in performing the ICP-OES experiments. I would also like to

Chapter 4: Experimental Results

The following sections provide the data resulting from the experiments discussed in Chapter 3 and are presented in the order of discussion given in Chapter 3. This chapter is divided into three separate sections: 1) characterization results of precursor materials, 2) characterization results of glass samples, and 3) irradiation results of glass samples.

4.1 Characterization Results of Precursor Materials

4.1.1 Lithium Pentaborate Synthesis Results

The synthesis of lithium pentaborate is discussed in Section 3.1., and the ICP-OES (Table 4.1-1) and P-XRD (Fig. 4.1-1) are presented.

The P-XRD spectra were taken using the instrument described in Section 3.3.2, and the results of the lithium pentaborate are shown in Fig. 4.1-1.
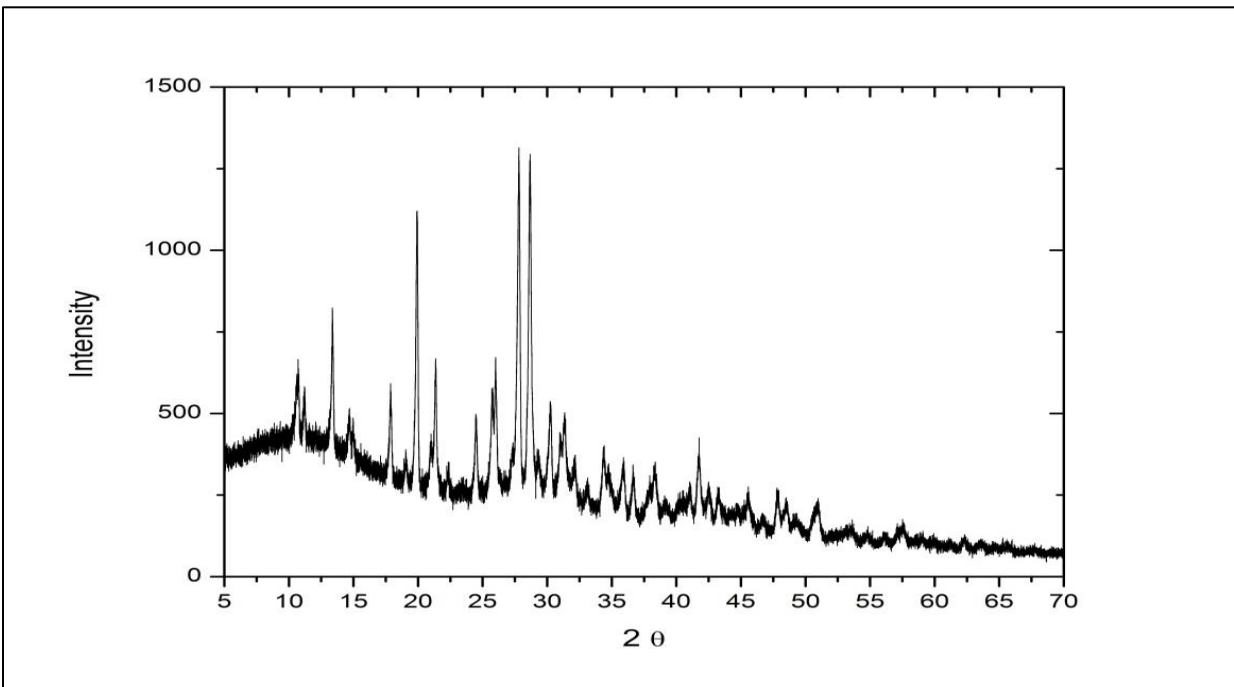
Figure 4.1-1: P-XRD of lithium pentaborate.

The HighScore analysis of this compound confirmed the identity of this diffraction pattern to be lithium pentaborate (LiB_5O_7). This was verified by the ICP-OES analysis results shown in Table 4.1-1.

Table 4.1-1 ICP-OES Results of Lithium Pentaborate Synthesis			
Analyte	Analysis Wavelength (nm)	Conc. (ppm)	Resulting Molar Ratio
Li	670.8	0.0986	LiB_5O_7
B	249.7	4.883	

It should be noted that ICP-OES cannot perform hydrogen and oxygen analysis, and therefore is not reported. There is excellent agreement in the data from both methods confirming synthesis for lithium pentaborate.

4.1.2   *Lithium Tetraborate Synthesis (Ge Method) Results*

The synthesis of lithium tetraborate using the Ge method is discussed. The resulting products were analyzed using P-XRD methods and a variety of products were observed. Since Ge[101] had originally intended this method to be used for coating lithium tetraborate on silicon wafers, the subsequent heating methods were performed on silicon wafers. After heating the solid to 200°C to drive off the water, from the white particles, the results were analyzed with P-XRD and are shown in Fig. 4.1-2.
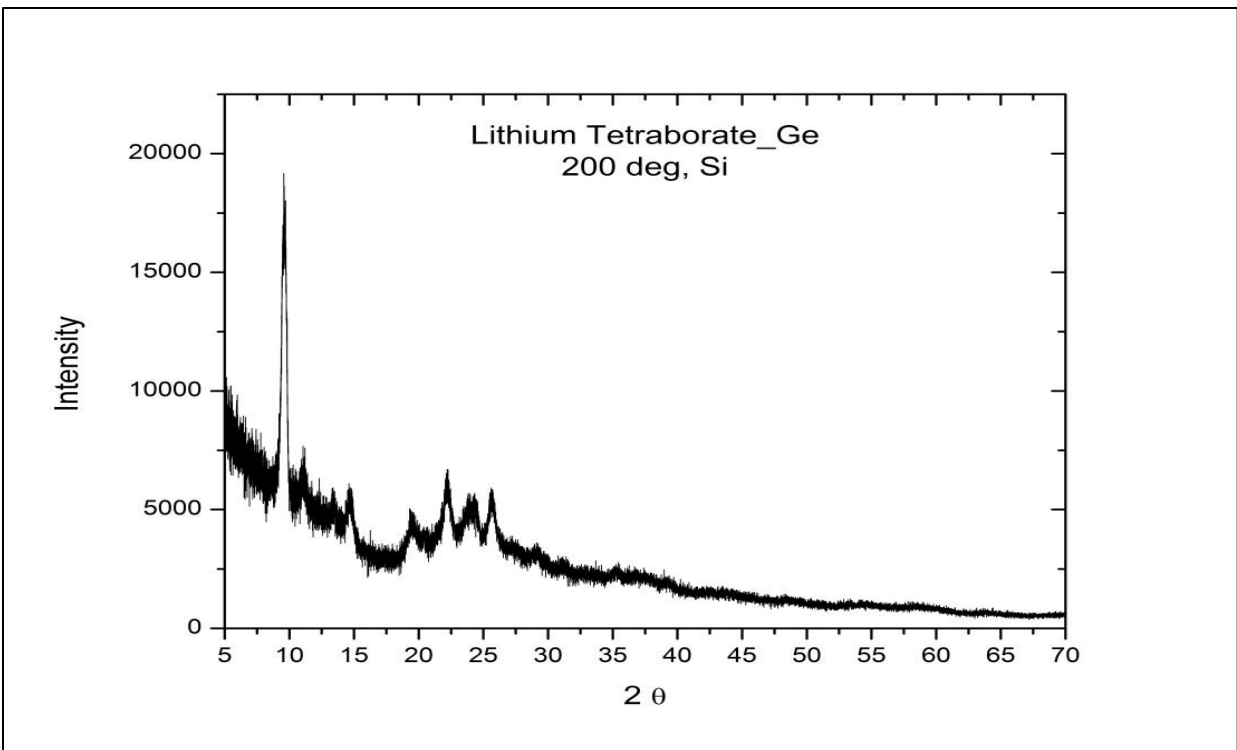
Figure 4.1-2: P-XRD of product formed after heating solid at 200 ˚C on a silicon wafer.

The diffraction pattern was analyzed and the results were given to be lithium di-hydroxoborate (LiBO$_2$·2 H$_2$O); a result that was consistent throughout all the experiments. This was indicative that too little boric acid was added in the initial reaction; in later heating trials, excess boric acid was added as a solid to increase the boron to lithium stoichiometric ratios. The samples were heated to 550 ˚C and the P-XRD results are shown in Fig. 4.1-3.
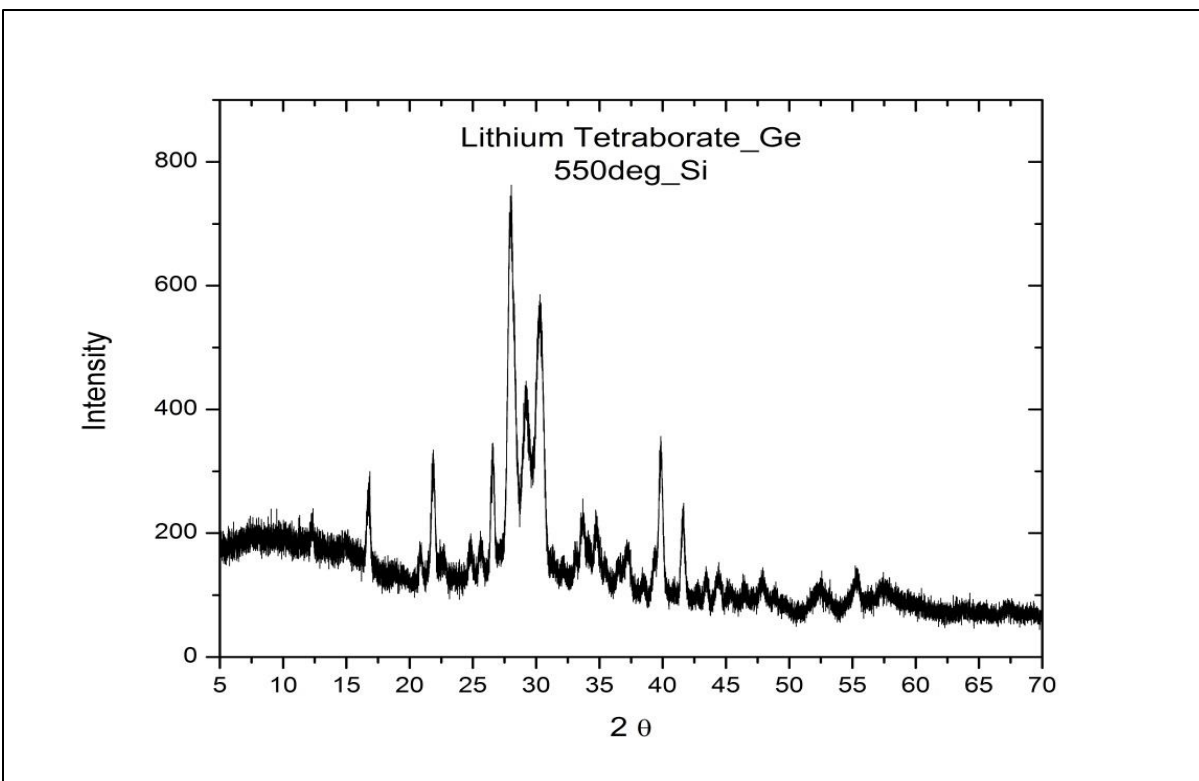
Figure 4.1-3: P-XRD pattern of product after heating to 550 ˚C on silicon wafer.

The analysis of this solid revealed that lithium metaborate ($LiBO_2$), lithium tetraborate ($Li_2B_4O_7$), and silicon dioxide (SiO_2) were formed. However, the resulting product was black in color, indicating that the removal of the carbon from the matrix was not successful. Thus the product was heated in a crucible to 850˚C to remove the excess carbon impurities, and the P-XRD pattern is shown in Fig. 4.1-4.
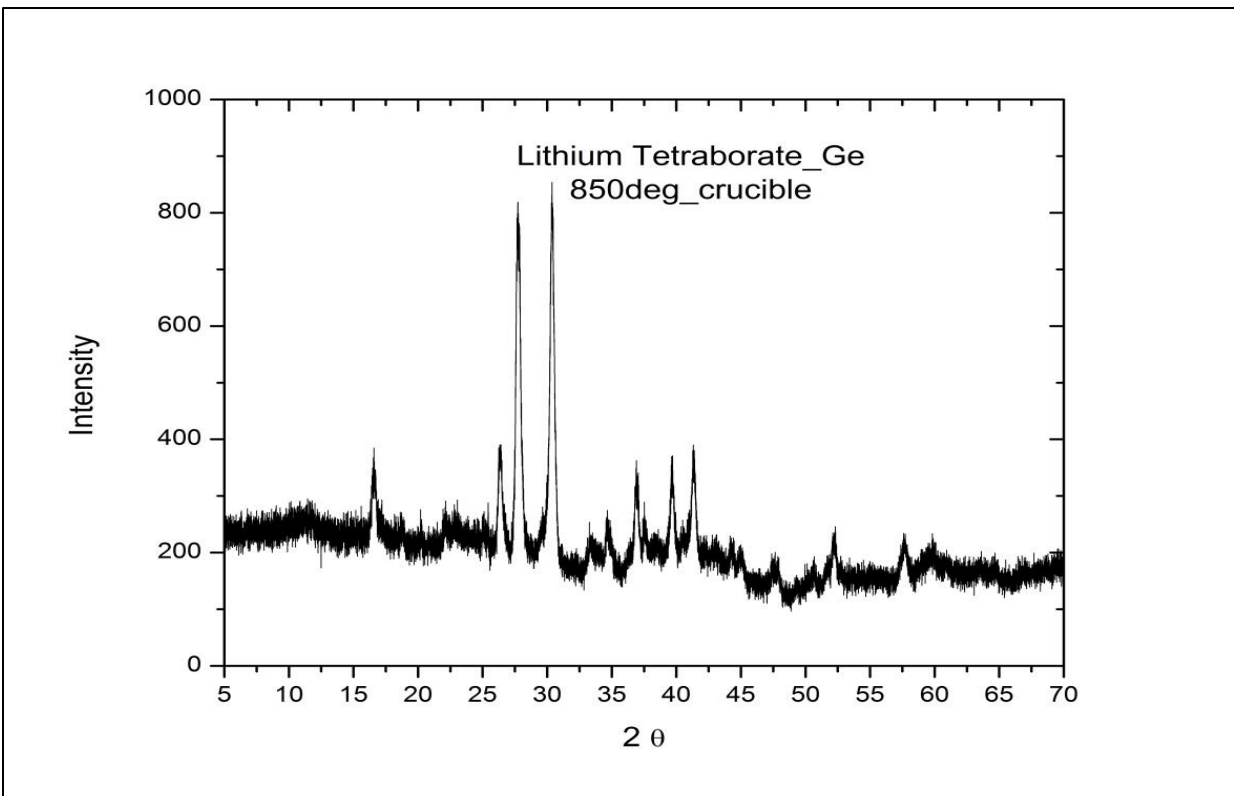
Figure 4.1-4: P-XRD of product after heating the product to 850 ˚C in crucible.

The P-XRD results indicated that lithium metaborate and lithium tetrahydridoborate (LiBH$_4$) were formed. In an attempt to improve product purity, a Pyrex petri dish was substituted for the silicon wafer, and the solutions of lithium acetate and boron ethoxide were poured into the dish and heated to 550˚C. The results are shown in Fig. 4.1-5.
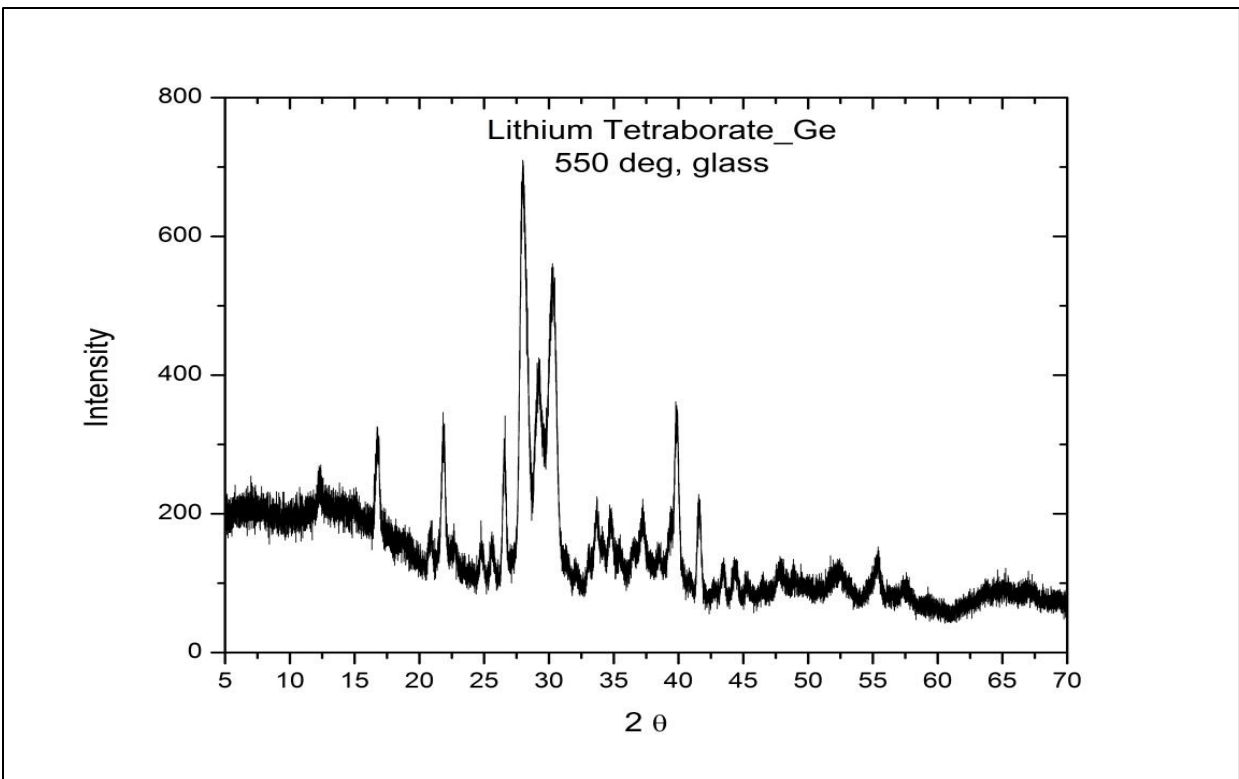
Figure 4.1-5: P-XRD of product after heating at 550 ˚C in a glass crucible.

The analysis of the results gave lithium metaborate ($LiBO_2$) and lithium tetraborate ($Li_2B_4O_7$) with SiO_2 impurities. Since this method could not be tuned to produce lithium tetraborate with high purities, it was not used to form the [6]Li enriched form of lithium tetraborate.

4.1.3   Lithium Tetraborate Synthesis (Kaylan Method)

The method by Kaylan[102] was used for the synthesis of enriched lithium tetraborate and the synthesis is described in Section 3.1.3.2. After heating for 3 hr. at 400 ˚C, a resulting white powder was formed. The P-XRD pattern is shown in Fig. 4.1-6.
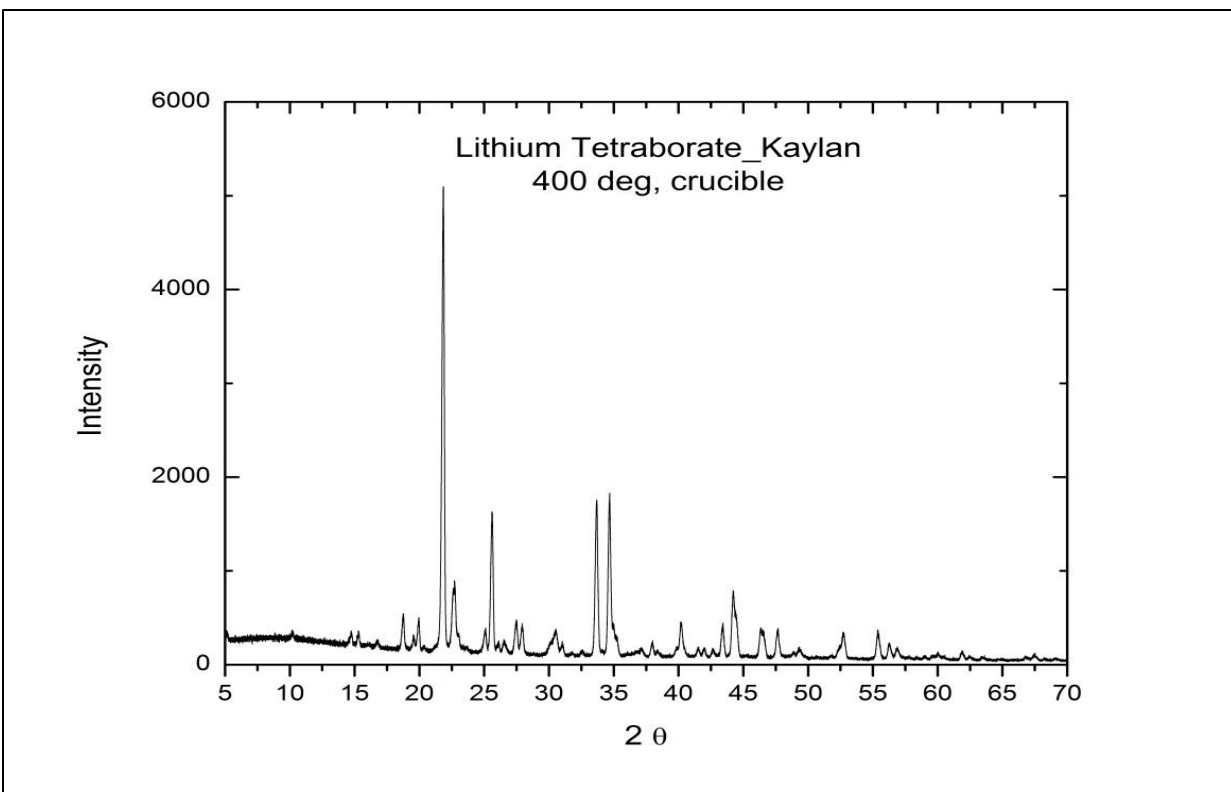
Figure 4.1-6: P-XRD pattern of product after heating at 400 ˚C in a crucible.

The HighScore analysis (Section 3.7.2) of the powder pattern indicated that lithium tetraborate ($Li_2B_4O_7$) had been produced. After heating to 800˚C, the product formed was analyzed by P-XRD and the results are shown in Fig. 4.1-7.
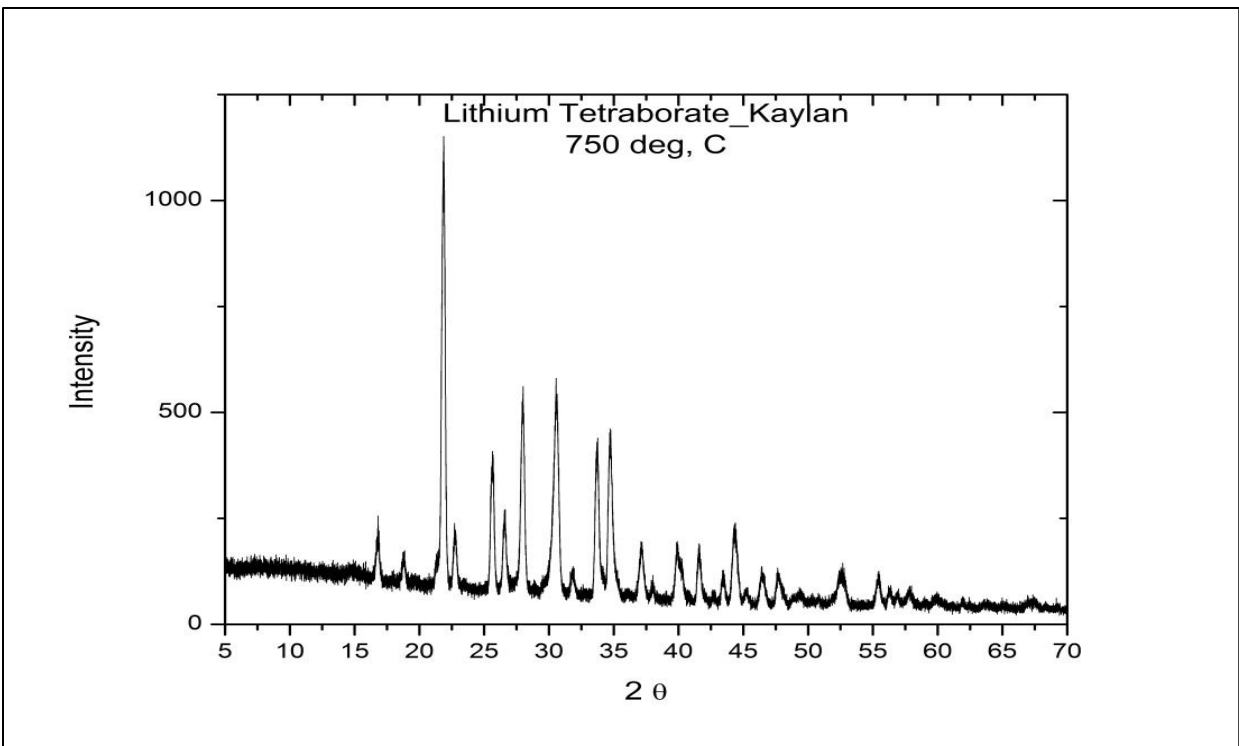
Figure 4.1-7: P-XRD pattern of product after heating at 800 ˚C for 1 hr.

The HighScore (Sec. 3.7.2) analysis of the powder pattern indicated that lithium closo-dioxoborate (LiBO$_2$) and lithium tetraborate (Li$_2$B$_4$O$_7$) were formed in this process.

4.2   Characterization Results of Glass Samples

4.2.1   Inductively Coupled Plasma – Optical Emission Spectroscopy

In order to determine the elemental composition of the samples, ICP-OES was performed and the results are presented in Table 4.2-1. The glass analyzed was lithium tetraborate with 17 wt% boric acid and 0.5wt% CeO$_2$.

Table 4.2-1 Elemental Composition of Lithium Borate Glass			
Element	*Wavelength (nm)*	*Conc. (mg/L)*	*Moles*
B	249.7	4.056	2.19×10^{-4}
Li	610.4	1.374	9.89×10^{-5}

The ratio of lithium and boron as presented in Table 4.2-1 is 1:2.21. This ratio is in agreement with a mixture of lithium tetraborate ($Li_2B_4O_7$) and lithium borate ($Li_3B_5O_9$). Henceforth, the glass is referred to as lithium borate. Since excess boric acid was added to the matrix, the excess of 10.5% is in good agreement with the ICP-OES data.

4.2.2 *Powder X-ray Diffraction (P-XRD) Results*

Because P-XRD was relied upon so heavily in this project, this section is divided into three sections: 1) boric acid loading sections, 2) meta- and tetra-loading experiments, and 3) glass samples.

4.2.2.1 *Boric Acid Composition*

Since boric acid is the component required to reduce the Ce^{4+} to the Ce^{3+} state, the amount of boric acid was varied from 10 wt% loading to 20 wt%. The resulting glass material was analyzed with P-XRD to determine the amount of crystallization present in the matrix. Increased crystallinity leads to a decrease in optical clarity, hence it is important to make a highly amorphous material. All samples were loaded with 1 wt% Ce for comparison. The P-XRD results for the 10 wt% loading samples are shown in Fig. 4.2-1.
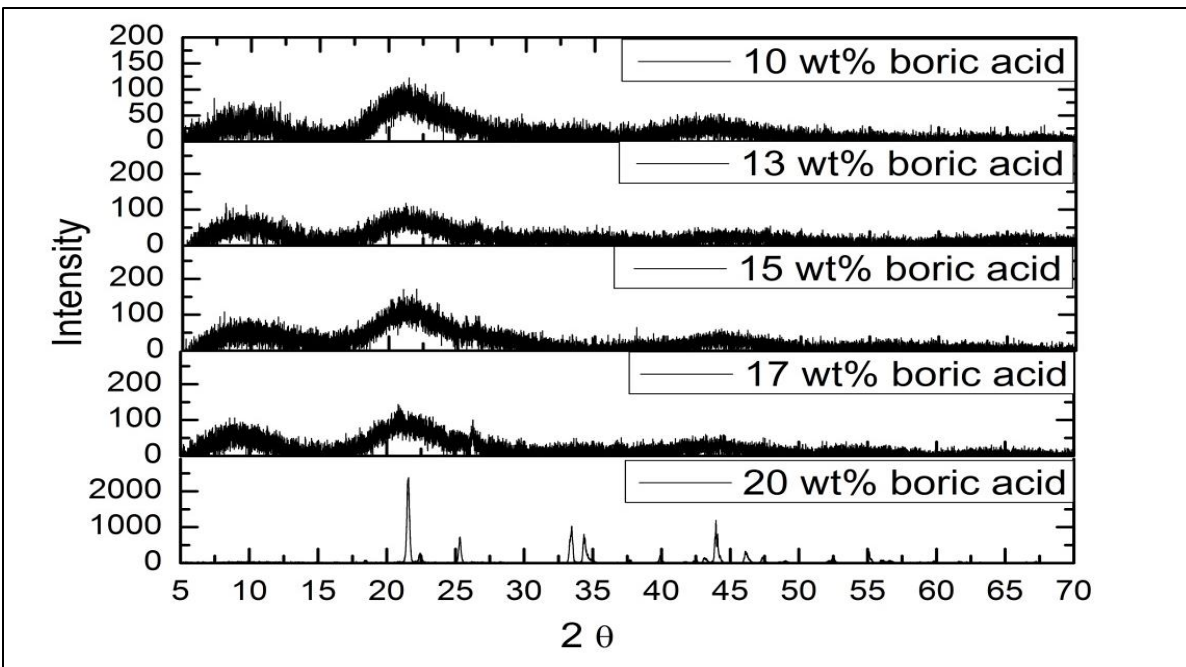
Figure 4.2-1: P-XRD pattern of lithium tetraborate loaded with 1 wt% Ce.

The boric acid loading is varied from 10 wt% to 20 wt% and the crystallinity is measured.

The results of the 10 wt% boric acid sample were amorphous with no recognizable material selected from the HighScore database. The 13 wt%, 15 wt%, and 17wt% boric acid results indicated that the resulting materials were totally amorphous, with no matching results selected from the HighScore database. The result from lithium tetraborate glass with 20 wt% loading of boric acid was exclusively lithium tetraborate, as reported from the HighScore database. From these experiments, it was determined that all future glass would use 17 wt% boric acid. This would give a glass with maximum optical clarity and optimum reduction of the Ce scintillation center.

4.2.2.2 Meta- and Tetra-loading experiments

According to companies such as Claissen[103], who make fluxes from varying lithium borate compounds, depending on the oxide to be dissolved mixtures of alkali borates (e.g. meta- and tetraborate) should be used. The amount of lithium tetraborate and lithium metaborate

46

should be mixed at different ratios to achieve maximum optical clarity for XRF (X-ray Fluorescence) experiments. In this set of experiments the mol% of lithium metaborate was adjusted from 25 mol% to 99 mol% with 1.0 mol% CeO_2, and the amount of crystallinity was analyzed with P-XRD. The P-XRD results are shown in Fig. 4.2-2.
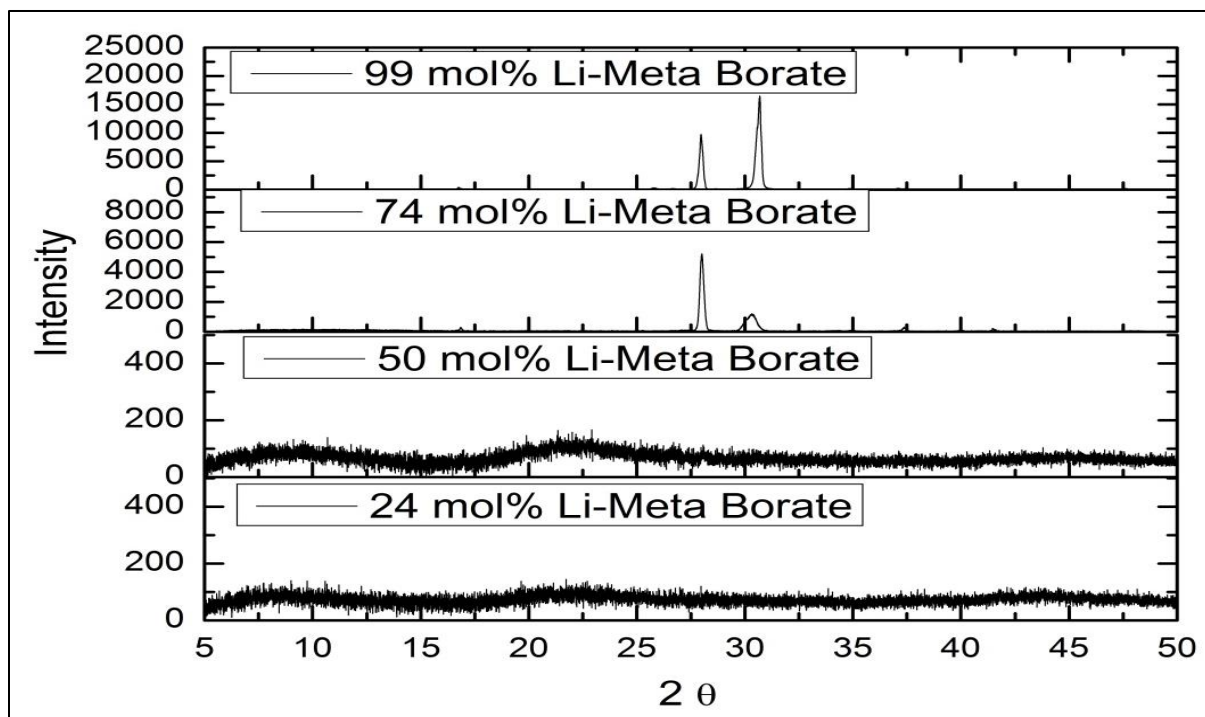
Figure 4.2-2: P-XRD patterns of the varying amount of crystallinity as a function of the amount of lithium metaborate.

The lowest crystallinity was observed from samples with a lower amount of lithium metaborate. The UV-vis experiments (Section 4.2.6) revealed that the highest optical clarity was obtained from samples with 0 mol% lithium metaborate. Thus, no lithium metaborate was incorporated into the final glass.

4.2.2.3 Glass Samples

The actual glass samples were also analyzed with P-XRD, fluorescence (see section 4.2.5), and UV-vis (see section 4.2.6). A blank glass of Lithium Tetraborate with no rare earth doping containing only 17 wt% boric acid is shown in Fig. 4.2-3.
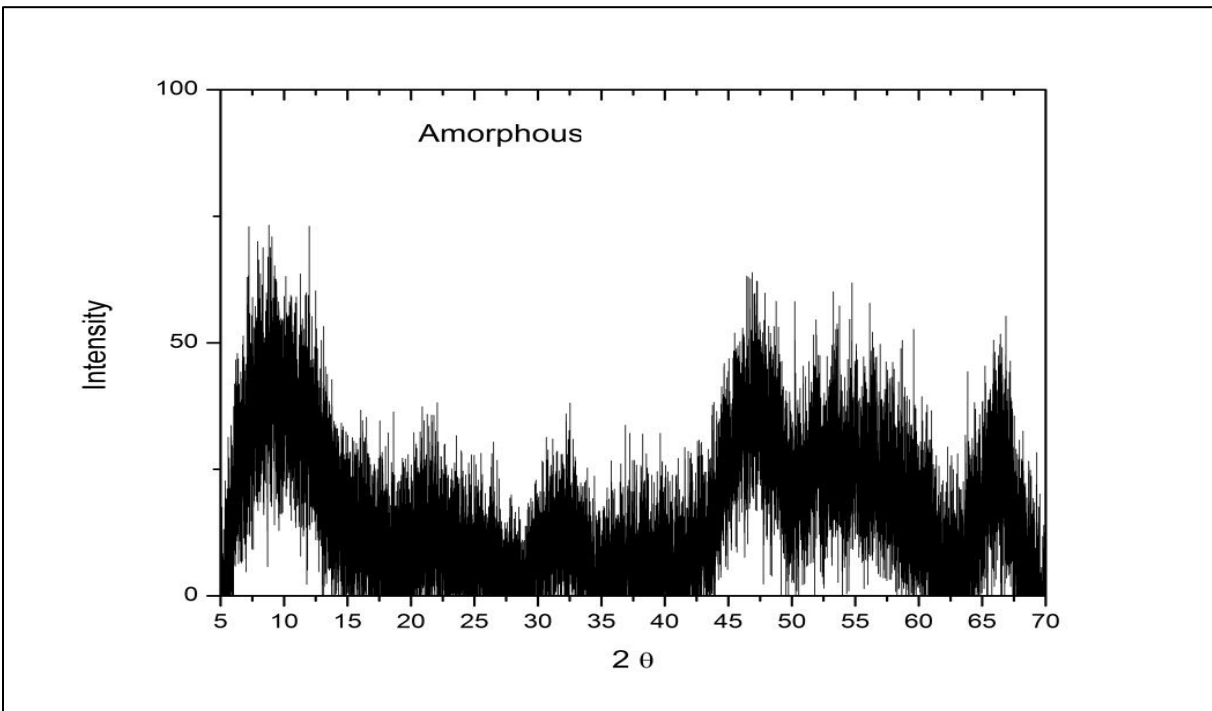
Figure 4.2-3: P-XRD pattern of amorphous lithium tetraborate.

The results in Fig. 4.2-3 were totally amorphous, with no material selected from the HighScore database.
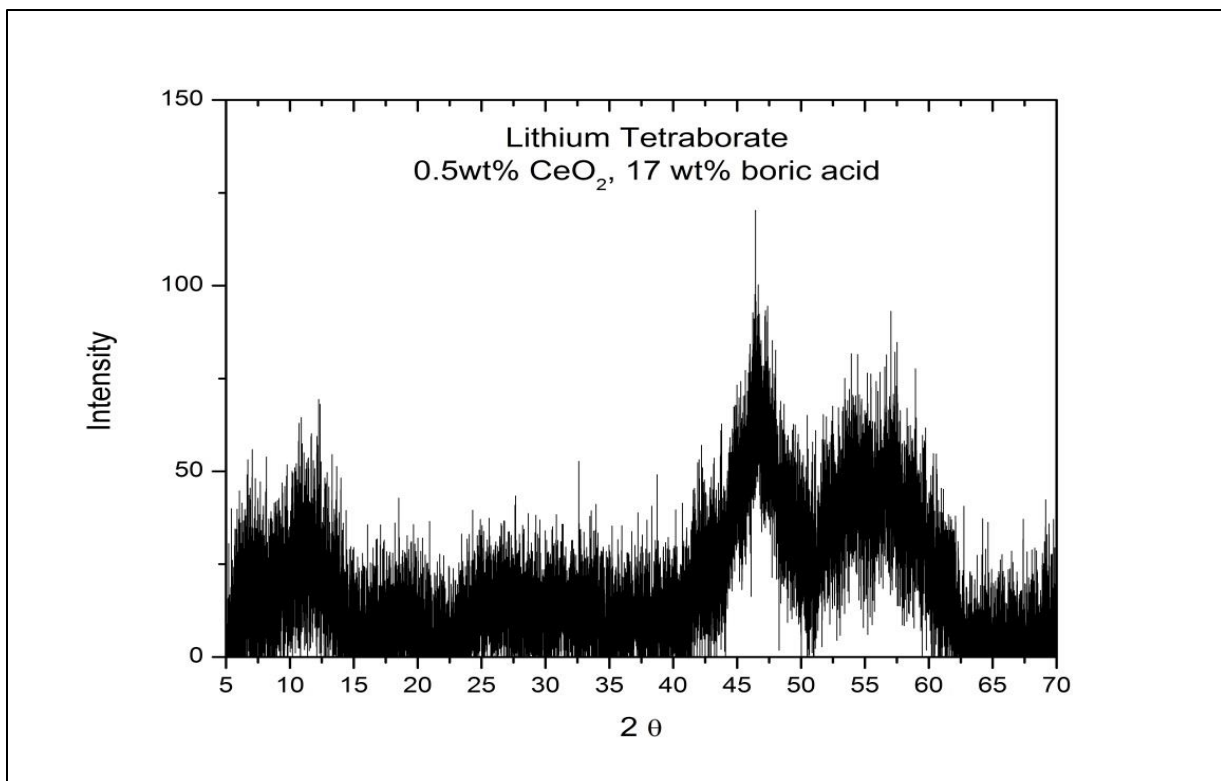
Figure 4.2-4: P-XRD pattern of lithium tetraborate doped with 0.5 wt% CeO_2 and 17 wt% boric acid.

The P-XRD pattern of a vitreous lithium tetraborate doped with 17 wt% boric acid, 0.5 wt% Ce in lithium tetraborate are shown in Fig. 4.2.4. The HighScore Database results showed trace lithium catena-dihydroxopentaborate ($LiB_5O_9 \cdot H_2O$), which is consistent with the highly hygroscopic nature of boron oxides.

4.2.3 Solid State Nuclear Magnetic Resonance (SSNMR) Results

The SSNMR results provide insight into the chemical structure of the LBO:Ce matrix. The ^7Li, ^{11}B, and ^1H nuclei were studied using H_3BO_3 and LiCl as standards[27], [30], [31], [114–117] for the NMR[118], [119] experiments. The boric acid has a trigonal boron that is connected to three –OH groups. The solid state NMR of boric acid is shown in Fig. 4.2-5.
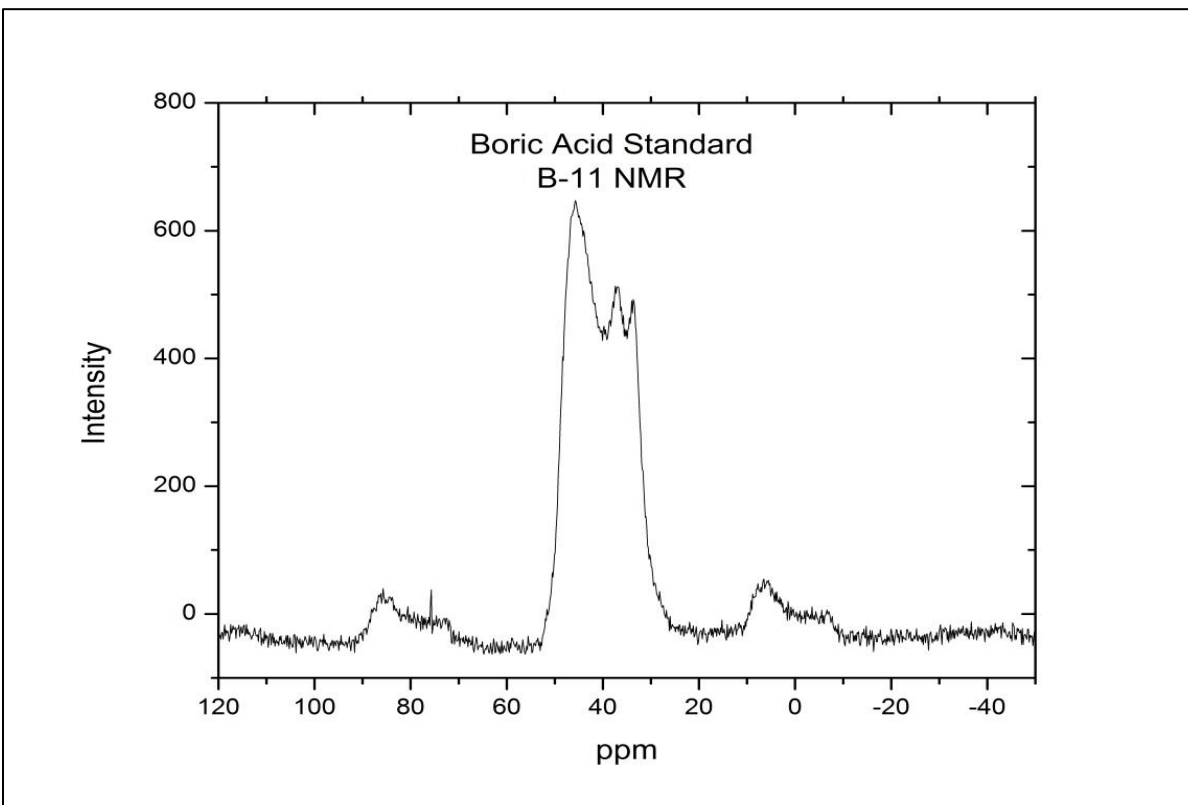
Figure 4.2-5: SSNMR (B-11) of boric acid.

The results of the B-11 NMR show a triplet feature centered between 45 and 30 ppm. To reduce the effect of the nearby hydrogens, the Cross Polarization – Magic Angle Spinning (CPMAS) NMR was performed. The CPMAS experimental results are shown in Fig. 4.2-6. The ^{1}H groups were excited and the energy was transferred to the ^{11}B nucleus, eliminating the observed splitting. The CPMAS-SSNMR is shown in Fig. 4.2-6.
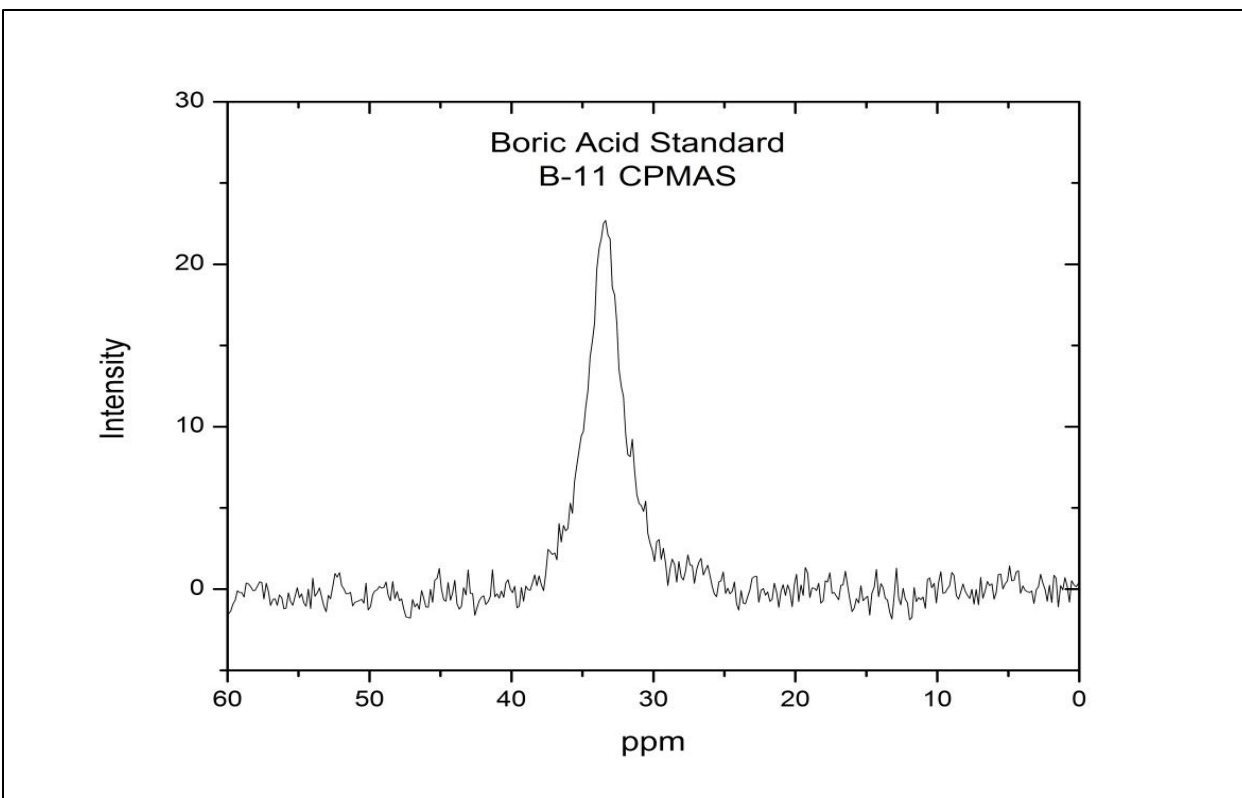
Figure 4.2-6: SSNMR of boric acid standard using a CPMAS, a singlet is observed at 33 ppm.

Based on the results in Figs. 4.2-5 and 4.2-6, the trigonal boron species bonded to 3 oxygen groups and gives a peak centered near 33 ppm. Mackenzie *et al.*, and Sen *et al.* report the boric acid isotropic chemical shift (δ_{iso}) should be at ~19 ppm, however their measurements were made using a boron trifluoride etherate ($BF_3 \cdot Et_2O$) standard (δ_{iso} = 3.2 ppm). These experimental methods were used to interpret the SSNMR information of the lithium tetraborate spectrum.

Work by Byrappa[104], [120] *et al.*, Touboul[32] *et al.*, and Bray *et al.*[121] indicated that lithium borate, upon heating and cooling, will form an optically opaque crystalline matrix and an amorphous matrix, both with the chemical formula of $Li_2B_5O_9$. The amorphous motif is thought to have the structural form of a single tetrahedral boron connected to 4 oxygen atoms. The oxygen atoms are connected to trigonal boron species to form a ring with the chemical formula of B_3O_3. This structure is shown on left in Fig. 4.2-7.   Single crystal work by Senyshyn *et al.* [122] and Chen *et al.*[123] have proposed that the single crystal structure and

51

that of the amorphous substance is more likely to take the structure that is proposed (on right) in Fig. 4.2-7.
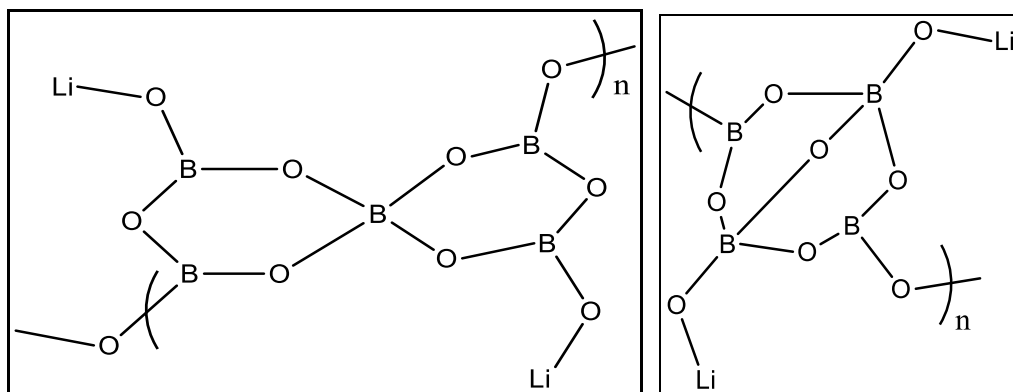
Figure 4.2-7: The proposed monomer unit of lithium borate. The structure thought to be obtained by Byrappa and Bray is the left. The structure proposed by Senyshyn is shown on right.

The amorphous structure, when doped with CeO_2 is comprised of these $Li_2B_5O_9$ repeat units. This structure is observed in the SSNMR spectra shown in Fig. 4.2-8.
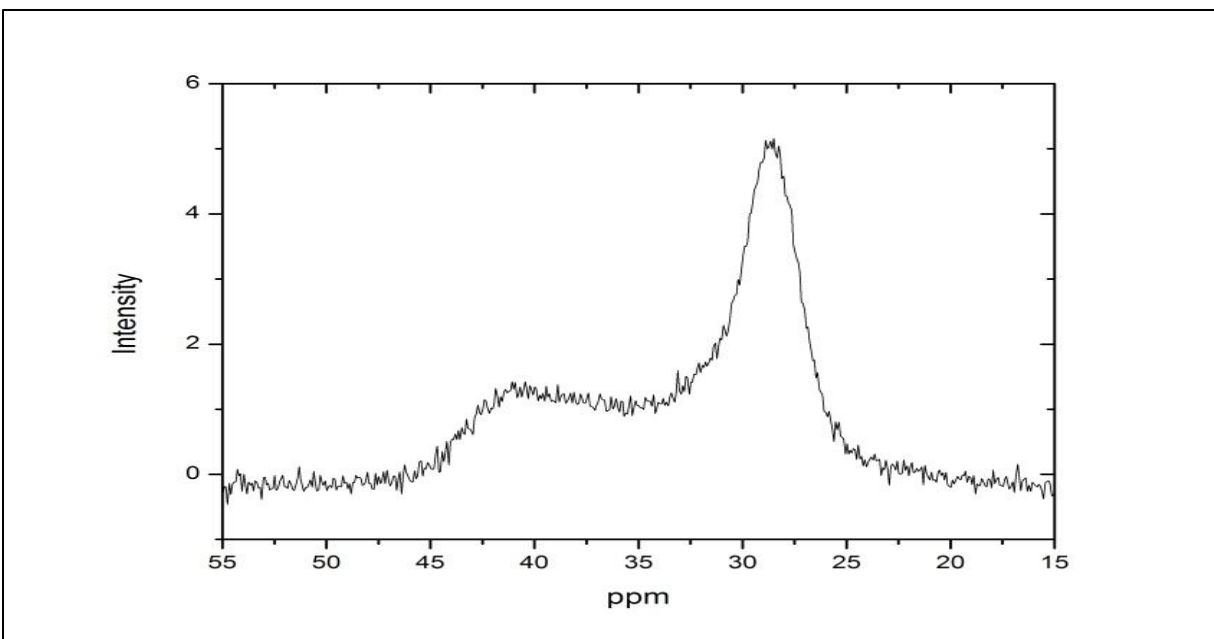
Figure 4.2-8: Lithium borate glass, doped with 0.5 wt% Ce and 17 wt% boric acid, B-11 SSNMR result.

The trigonal boron species is observed at 29 ppm and the tetragonal species is observed at 41 ppm. Integration of these peaks gives a resulting ratio of trigonal boron to tetragonal species of 3.95:1, which is in agreement with the predicted stoichiometry of trigonal boron to tetragonal boron of 4:1.

However, another explanation for the spectrum in Fig. 4.2-8 is also present in the literature. Mackenzie *et al.* points out that the peak 29-30 ppm corresponds to a $(BO_3)^{3-}$ or $(BO_4)^{4-}$ species that does not form the boraxol rings as shown in Fig. 4.2-7, and would correspond to the tetragonal boron. They further discuss that the peak at 42 ppm would correspond to the trigonal boron species in the boraxol rings. Both explanations agree with the data acquired from the FT-IR-ATR experiments (Sec. 4.2.4) and the ICP-OES experiments (Sec. 4.2.1).

When Ce is introduced into the matrix, it is thought to be stabilized by two B_2O_3 rings, which creates a Ce atom assumed to have an 8 (shown) or 9 coordinate atoms as seen in Fig. 4.2-9. To maintain electro-neutrality, the Ce^{3+} will replace 3 lithium atoms in the matrix, whereupon the borate rings (B_3O_3) will stabilize the Ce^{3+}. It is theorized[35] that the *s* electrons from the borate ring will be donated to the 4*f* shell of the Ce. In this way[107], the Ce will have the fluorescent capability of the 5*d* to 4*f* transition as shown in section 4.2.5.
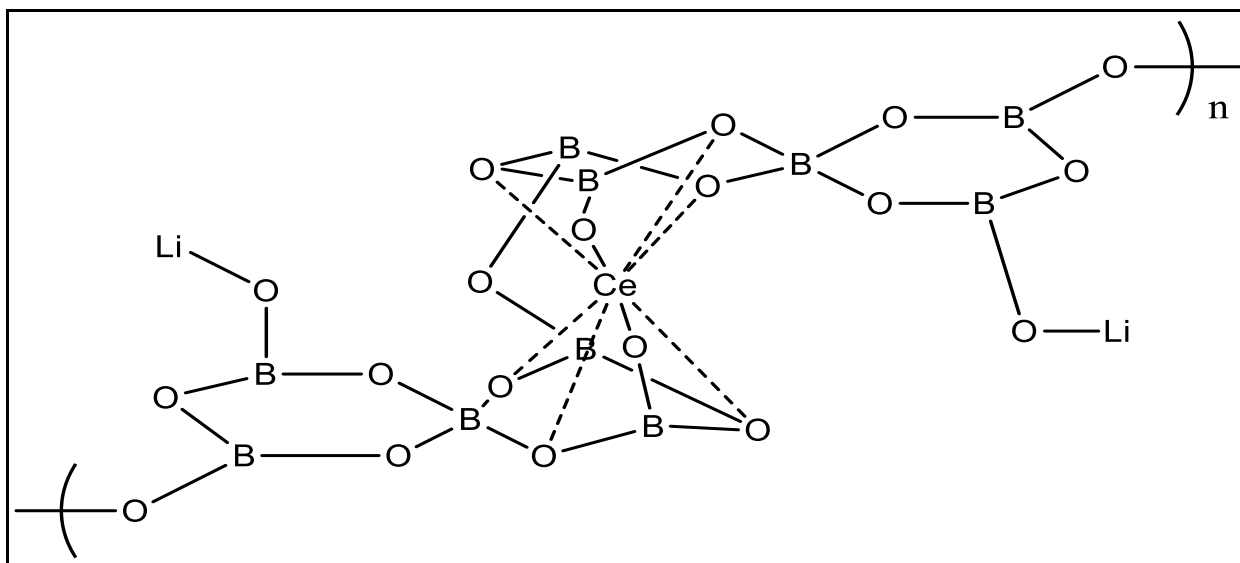
Figure 4.2-9: Ce^{3+} stabilized in amorphous lithium tetraborate matrix.

To verify the presence of a single lithium environment, ^{7}Li SSNMR was performed and the results are shown in Fig. 4.2-10. The lithium NMR was taken of the species, and a single peak at 0.4 ppm was observed.
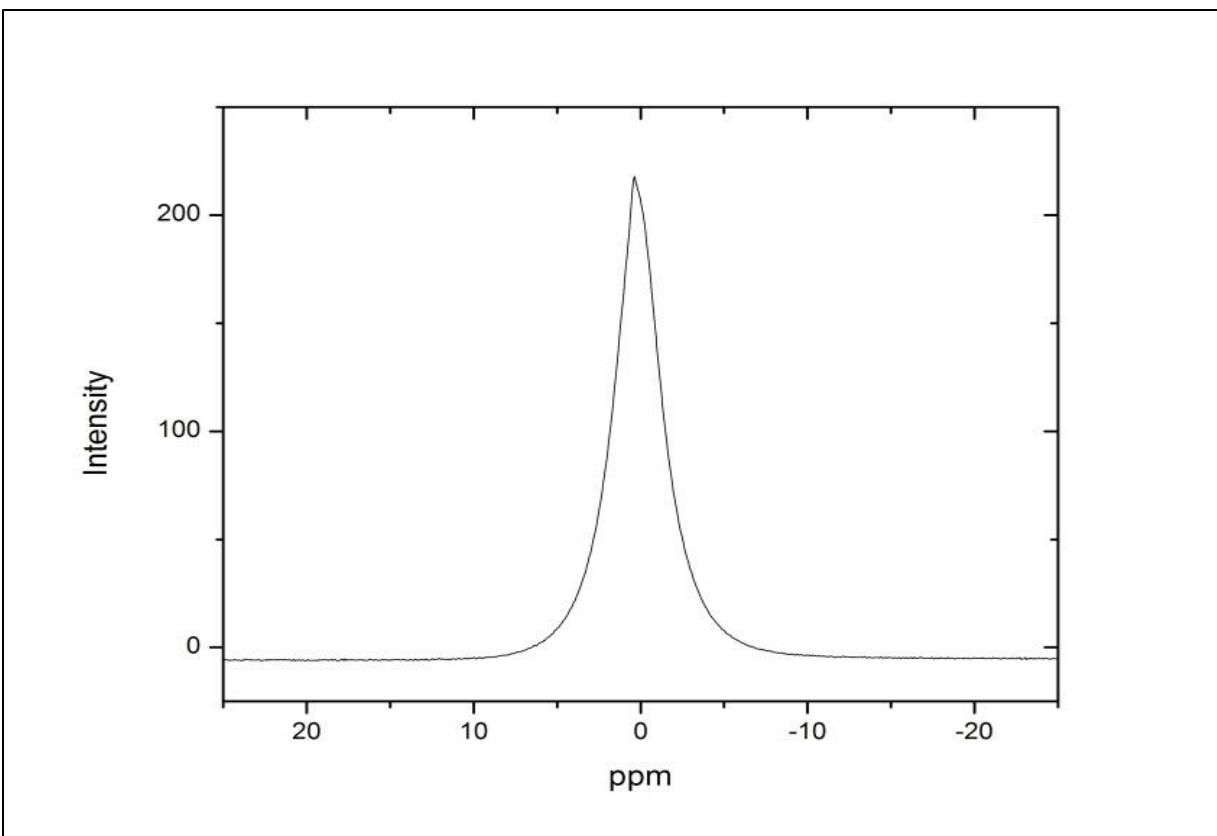
Figure 4.2-10: The SSNMR (^{7}Li) spectrum for lithium borate (0.5 wt% CeO_2, 17 wt% boric acid) doped glass.

A ^{1}H-NMR was also taken of this compound, although the final matrix should not have free protons. However the SSNMR ^{1}H spectrum, shown in Fig. 4.2-11, indicates the presence of a single ^{1}H environment.
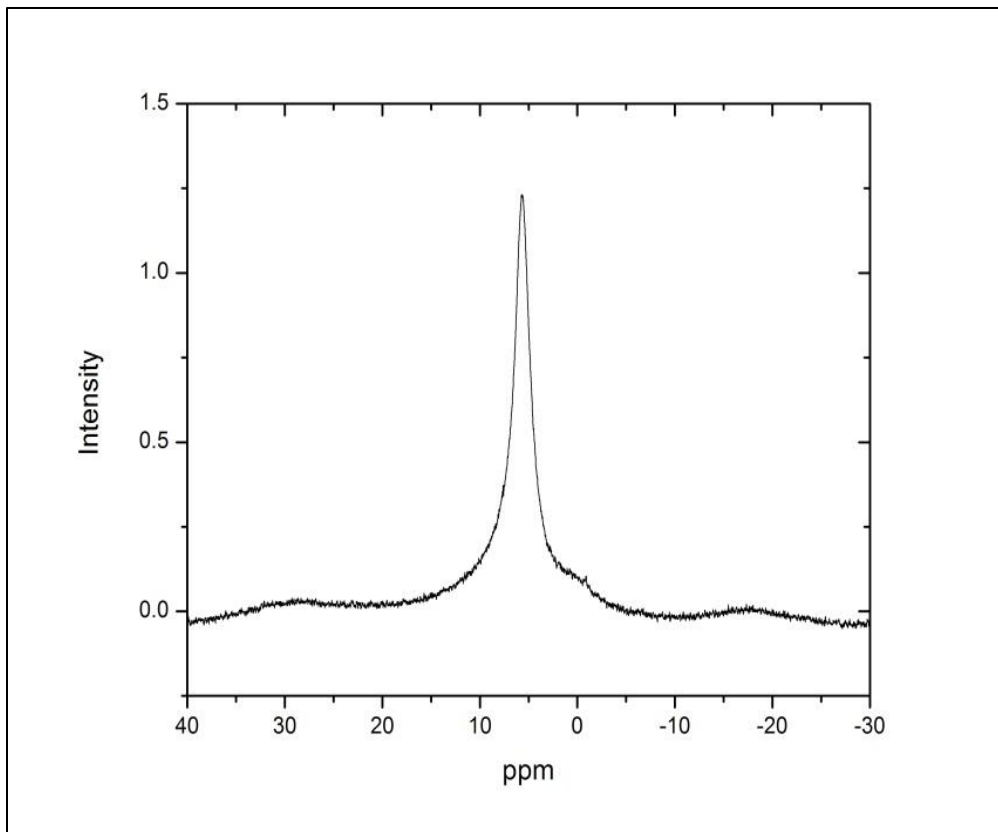
Figure 4.2-11: The SSNMR (^{1}H) spectrum for lithium borate glass, doped with 0.5 wt% Ce and 17 wt% boric acid.

According to Sevim[124] *et al*, boric acid decomposes via the following reactions:

$$2\ H_3BO_3 \rightarrow 2\ HBO_2 + 2\ H_2O \quad (118\text{-}162\degree C) \qquad \text{Eqn 4.1}$$

$$2\ HBO_2 \rightarrow B_2O_3 + H_2O \quad (162\text{-}300\degree C) \qquad \text{Eqn. 4.2}$$
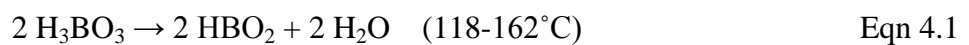
This decomposition was verified by thermogravimetric analysis (TGA) and differential thermal analysis (DTA) with fittings by both the Suzuki and Coats-Redfern methods. Smolanoff[125] *et al* reported that although this decomposition occurs, boron oxide (B_2O_3) is highly hydroscopic and is difficult to prevent water interaction to produce the metaborate (HBO_2) species. From the ^{1}H SSNMR results shown in Fig. 4.2-11, there appears to be a single hydrogen environment, as evidenced by the peak at 5.6 ppm. This result indicates that boron oxide on or near the surface of the film would uptake water.

4.2.4   *Fourier Transform – Infrared –Attenuated Total Reflectance Spectroscopy*

Infrared spectroscopy was useful in combining the results from the SSNMR and the P-XRD results. It also has the potential to probe the possible IR transition due to the loading of the Ce(III) into the material.
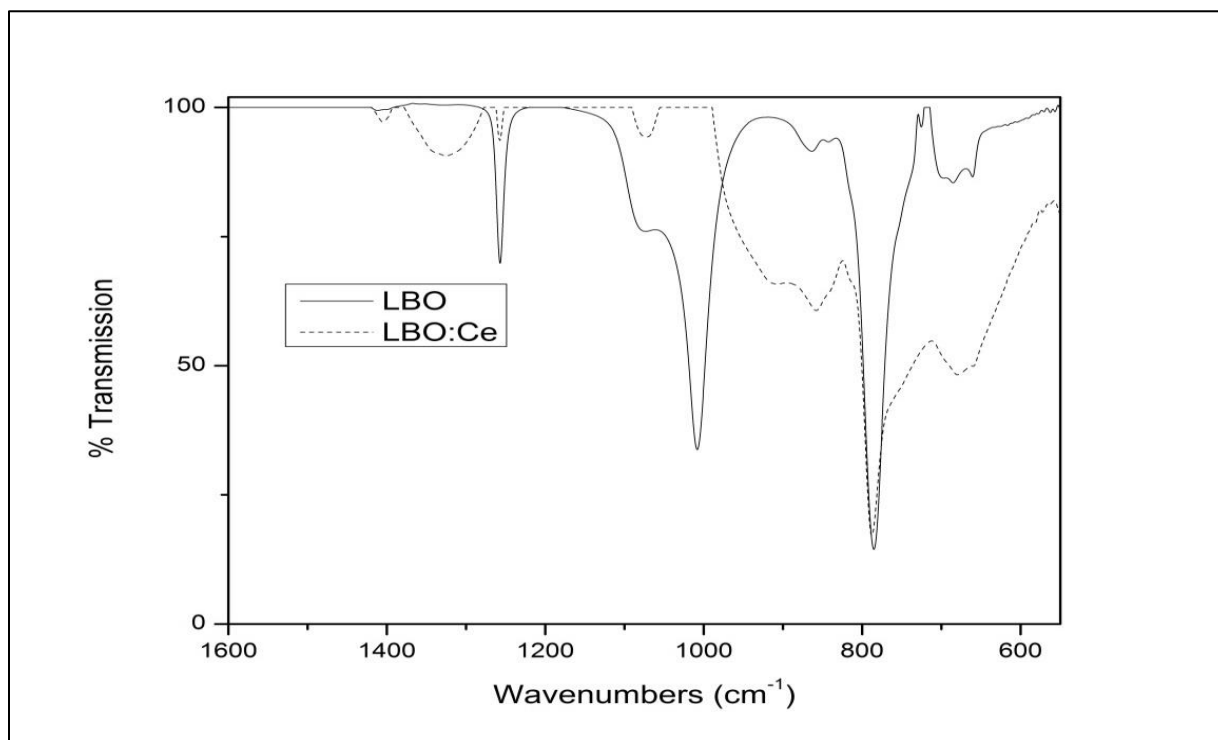
Figure 4.2-12 The FT-IR-ATR Spectra of blank lithium borate glass (denoted LBO) and the lithium glass doped with 0.5 wt% CeO_2 and 17 wt% boric acid (denoted LBO:Ce).

In Fig. 4.2.12, the peaks at 540-580 cm^{-1} correspond to the plane bending of boron oxygen triangles. The peaks between 850-865 cm^{-1} corresponds to the stretching vibrations of tetrahedral $(BO_4)^{4-}$, the peaks between 1245 -1807 cm^{-1} correspond to the stretching vibrations of $(BO_3)^{3-}$, and the peaks between 1248-1343 cm^{-1} correspond to the B-O stretching vibrations in the trigonal units.[110] A list of the peaks are shown in Table 4.2-2.

In the spectrum (Fig 4.2-12), the plane bending motions in the of the boron-oxygen plane are greatly intensified by the presence of the Ce doping, since the peak at 582 cm^{-1} is greatly increased. The (BO$_4$) stretching vibrations, peak 858 cm^{-1}, are also more intense in the doped sample than in the un-doped sample. Also the peaks at 1324 cm^{-1} and 1404 cm^{-1} are observed in the doped spectrum, but are not observed in the un-doped sample.

Table 4.2-2 The FT-IR vibrations observed in doped and undoped lithium tetraborate sample		
*Occurrence**	*Li$_2$B$_4$O$_7$*	*Li$_2$B$_4$O$_7$, 0.5 wt% CeO$_2$*
Plane Bending of Boron Oxygen (580-590 cm^{-1})	582	582
	685	787
Stretching vibrations of Tetrahedral (BO$_4$)$^{4-}$ (860-900 cm^{-1})	863	858
Stretching vibrations of (BO$_3$)$^{3-}$ (1240-1807 cm^{-1})	1008	1072
		1141
		1212
B-O stretching vibrations in trigonal units (1248 – 1348 cm^{-1})	1257	1257
	1411	1324
		1404

* the FT-IR bands are assigned using the approximate ranges outlined by Pekpak *et al.* [110]

4.2.5   *Fluorescence*

Fluorescence was a crucial technique in determining the effectiveness of varying the concentration of rare earth oxide and boric acid in the lithium tetraborate matrix. By improving

the light output of fluorescence, it is assumed that light output by scintillation will also be improved.

A series of experiments was performed to determine the effect of boric acid loading on the samples. A set of 3 samples were loaded with 17 wt%, 15 wt%, and 13 wt% boric acid with 0.5 wt % Ce in the lithium tetraborate matrix. The results are shown in Fig. 4.2-13.
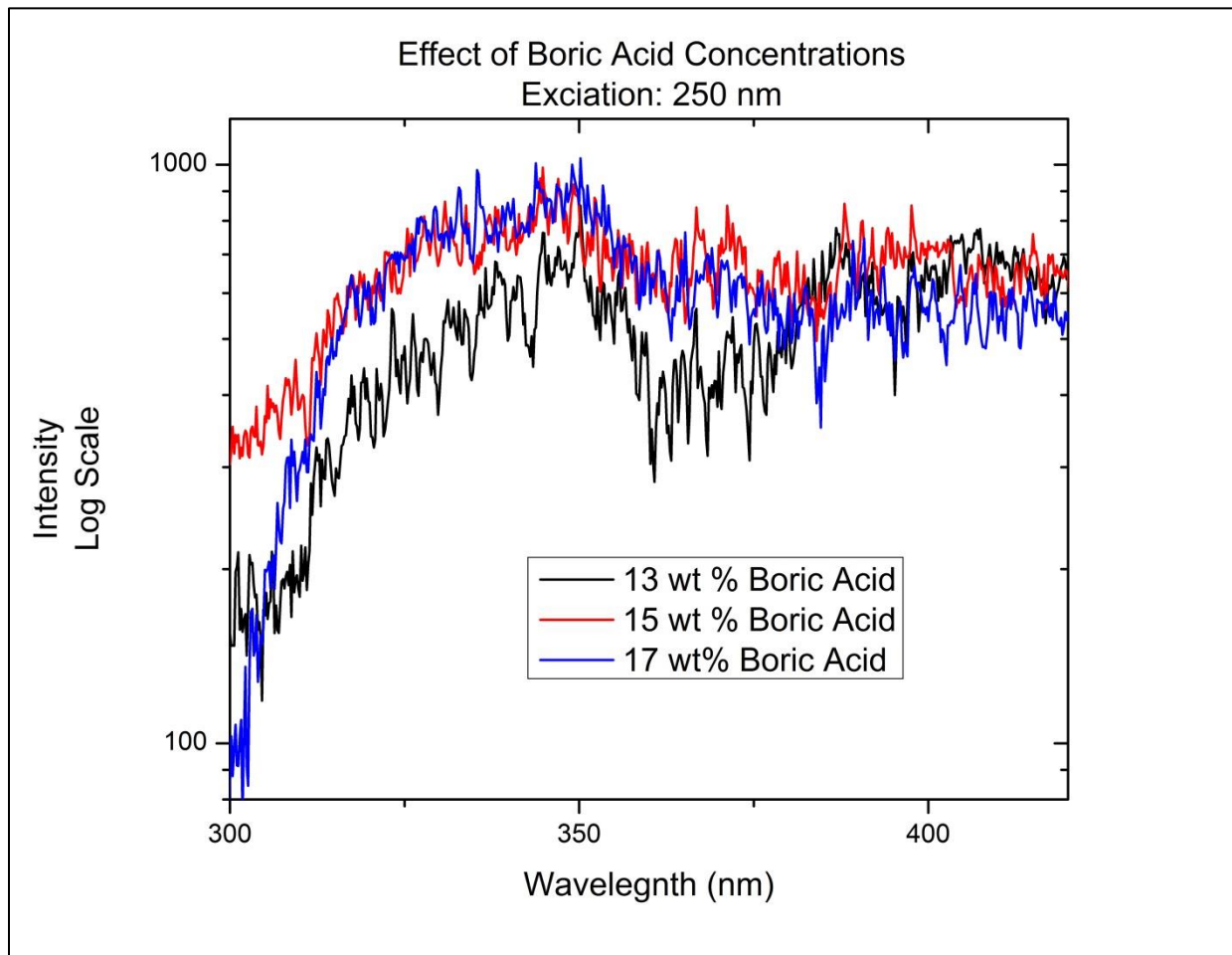
Figure 4.2-13: Lithium borate glass doped with 0.5 wt% CeO_2 with varying concentrations of boric acid. All samples were excited at a wavelength of 250 nm.

The amount of boric acid improves the intensity of the light output as the boric acid concentration increases from 13 wt% to 15 wt%, however little improvement in light intensity is observed with an increase from 15 wt% to 17 wt%.

Once the amount of boric acid to achieve maximum reduction was determined, a series of experiments was also performed to vary the concentration of Ce in the matrix. The variation in the concentration of Ce(IV) was used to determine the optimum amount of Ce to achieve the maximum light output for fluorescence. A set of glasses were prepared using lithium borate, 17 wt % boric acid, and 0.5 wt%, 1.0 wt%, 2.0 wt%, 3.0 wt%, and 5.0 wt% CeO_2. The results are shown in Fig. 4.2-14.
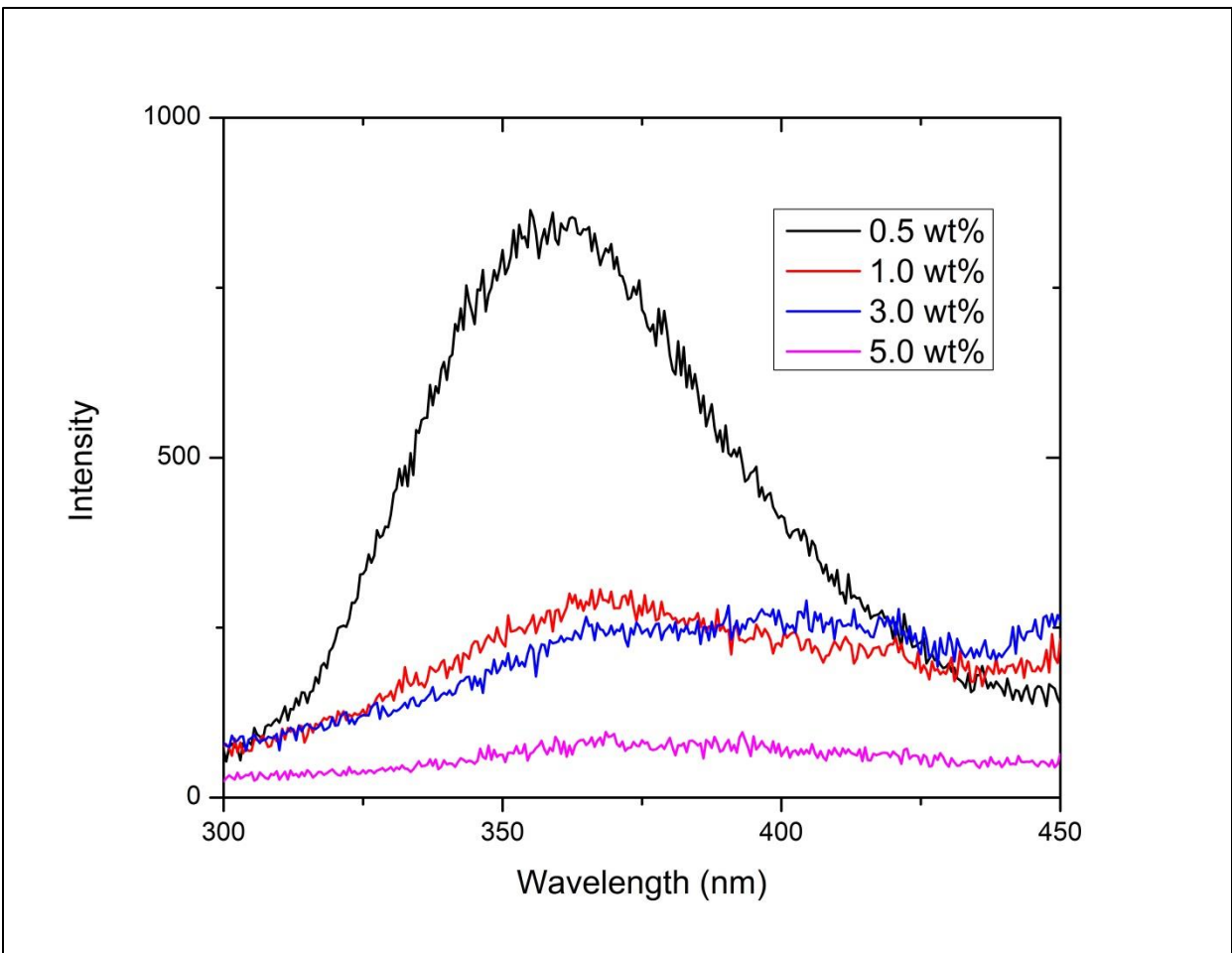
Figure 4.2-14: Fluorescence of lithium tetraborate glass at varying concentrations of CeO_2 in the matrix. All samples contained 17 wt% H_3BO_3 and were heated for 1 hr.

The results from Fig. 4.2-14 indicated that at 5.0 wt% CeO_2 there is little reduction of the Ce^{4+} to the Ce^{3+} state. At lower concentrations of CeO_2, the reduction becomes more effective, which is evidence by the increase in the fluorescence intensity. This increase in fluorescence intensity is directly related to the increase in Ce^{3+} centers in the matrix. The fluorescence profile of the final material is shown in Fig. 4.2-15.
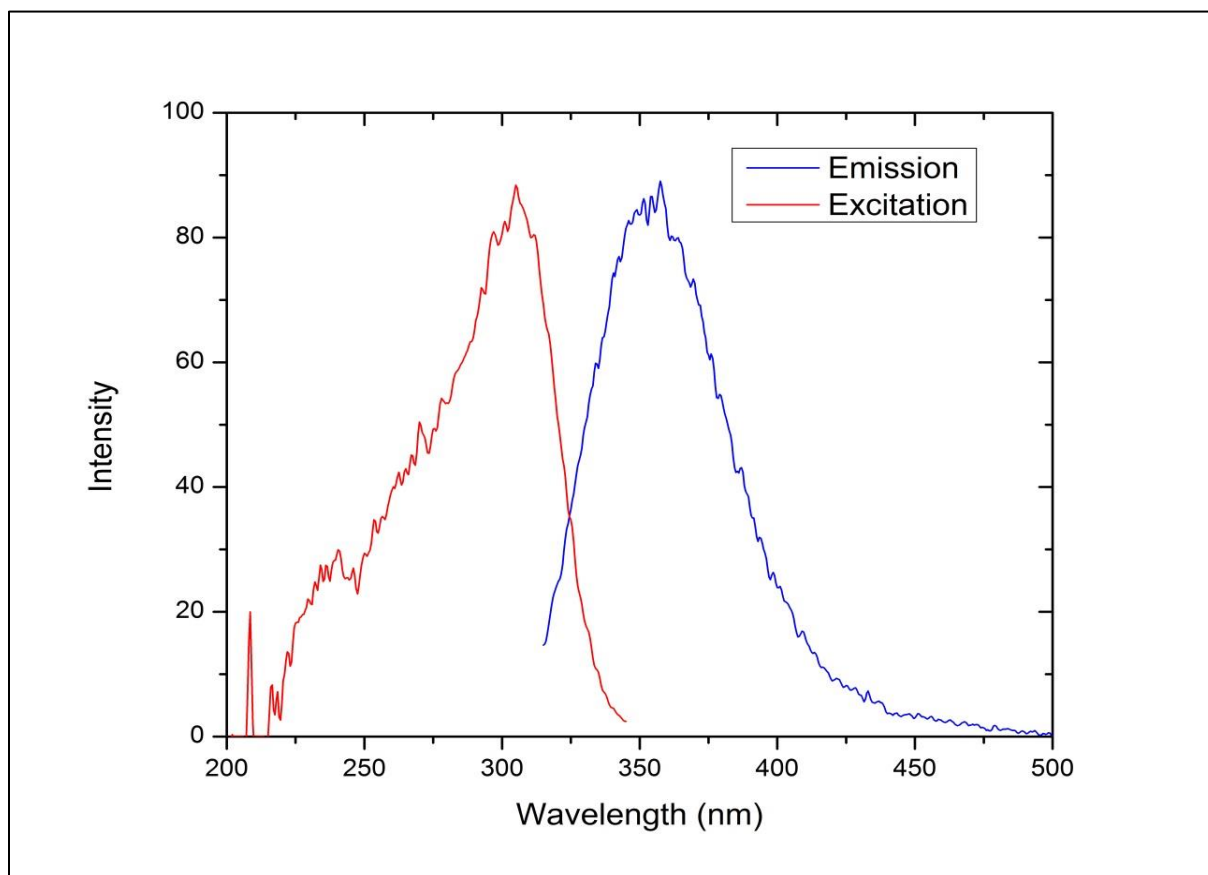
Figure 4.2-15: The fluorescence profile of lithium tetraborate doped with 0.5 wt% CeO_2.

The final material was observed to have strong absorption near 310 nm with a maximum emission near 355 nm. According to Elias[93], the trivalent Ce has a ground state that is split by spin-orbit coupling to give 2 ground states, the $^2F_{7/2}$ and the $^6F_{5/2}$. The $^2F_{7/2}$ state is 2253 cm^{-1}

(4439 nm) above the $^2F_{5/2}$ ground state. Upon excitation, by high-energy particles or photons, the single $4f$ electron is excited to the $5d$ shell, where the spin-orbit coupling splits the excited level into the $^2D_{3/2}$ and $^2D_{5/2}$ state. There is a further excited state, where the single $5f$ electron is excited to the $6s$, however this de-excitation is not observed.

A number of individuals have reported the reduction of lanthanoid oxides (e. g. Ln_2O_3) by using excess boric acid and alkaline earth borates (e.g. MB_4O_7). This effect was first reported on in 1993 by Pei et al.[126]. In this study, the author effectively reduced Eu^{3+}, Sm^{3+}, and Yb^{3+} to their divalent states using strontium borate (SrB_4O_7) with excess boric acid in a non-reducing atmosphere. Similar reports by Zeng et al. [127] and by Hao et al.[35] have used both strontium borate and calcium borate (CaB_4O_7 to achieve similar results. Other reports by Sanchez-Benitez et al.[128], Hirao et al.[129], and Holsa et al.[130] have reported the effective reductions of some rare earth ions in aluminum borates and have offered similar mechanisms to that originally proposed by Pei [126].

The proposed mechanism for this reduction process was first provided in the Pei et al. In Pei's work, it is proposed that two Eu^{3+} ions will replace three Sr^{2+} ions in the matrix to maintain electroneutrality. The defect that is created by the absence of one of the Sr^{2+} ions will donate two electrons to two of the Eu^{3+} species effectively reducing the valency from Eu^{3+} to Eu^{2+}. Later work by Sidorenko et al.[131–133] involved doping a strontium borate halide (e.g. Cl or Br) matrix with Ce^{4+} ions, and observing a similar reduction. All reports have discussed that the reduction comes as a result of the vacancy created by the displacement of the Sr^{2+} ions in the matrix[134], [135]. In the case of lithium tetraborate being doped with Ce^{4+}, a similar mechanism is assumed to take place. A single Ce^{4+} ion will replace four Li^+ ions in the matrix creating defect sites, and these defect sites will donate single electrons to the Ce^{4+} ions. In the discussion of the defect site that is created, there is disagreement as to the types of ions produced is as shown in the possible equations below.

$$2\ Ce^{4+} + O^{2-} \rightarrow 2\ Ce^{3+} + O \qquad\qquad \text{Eqn. 4.3}$$

Using the Kroger-Vink notation[135] to represent equation Eqn 4.3,

$$Ce^{\bullet} + O_{Li}{}' \rightarrow 2\ (Ce{\cdot}O_{Li})^{x} \qquad\qquad \text{Eqn. 4.4}$$

62

In Eqn. 4.4, the symbols $^{\bullet}$, $'$, and ^{x} represent +1, -1, and 0, respectively. In this way, the vacancy created by the 4 Li^{+} ions is replaced by a $(Ce \cdot O_{Li})^{x}$ association, thereby by achieving the desired reduction of Ce^{4+} to the Ce^{3+} form. It theorized that the $(Ce \cdot O_{Li})^{x}$ association is stabilized by the formation of tetrahedral (BO_4)- sites that are present in the $Li_2B_4O_7$ diborate framework[31]. According to El-Damrawi *et al.*[20] and Tsvetkov *et al.*[136] the addition of CeO_2, or other alkaki oxides, and Li_2CO_3 promotes the depletion of these $(BO_4$-$)$ sites in favor of the boraxol ring motif presented by Bray *et al.*[121]. Hence , the 17 wt% addition of boric acid is added to replenish the boron lost as boraxol rings and to promote the formation of $(BO_4$-$)$ sites rather than the B_3O_3 rings.

4.2.5.1   *Co-Doping Results*

Co-doping the sample with rare-earth ions was performed in an effort to improve the light yield of the sample. As discussed in Sec. 3.6, a number of samples were made with varying amounts of rare earth oxides, which are presented in Table 4.2-3 and the normalized fluorescence results are shown in Fig. 4.2-16.

Table 4.2-3 Sample Compositions and Fluorescence Intensity of Lithium Borate Glass				
at% Ce	*Material*	*at% REE**	*Material*	*Summed Fluorescence Intensity*
0.04	CeO_2	N/A	N/A	2.78×10^5
0.04	$Ce_4(SiO_4)_3$	N/A	N/A	1.06×10^4
0.04	CeO_2	0.03 (Tb)	Tb_6O_{11}	5.26×10^4
0.04	CeO_2	0.03 (Tb)	$Tb_2(CO_3)_5$	2.77×10^4
0.04	CeO_2	0.03 (Tb)	Pr_2O_3	2.94×10^4

*Rare Earth Element (REE)
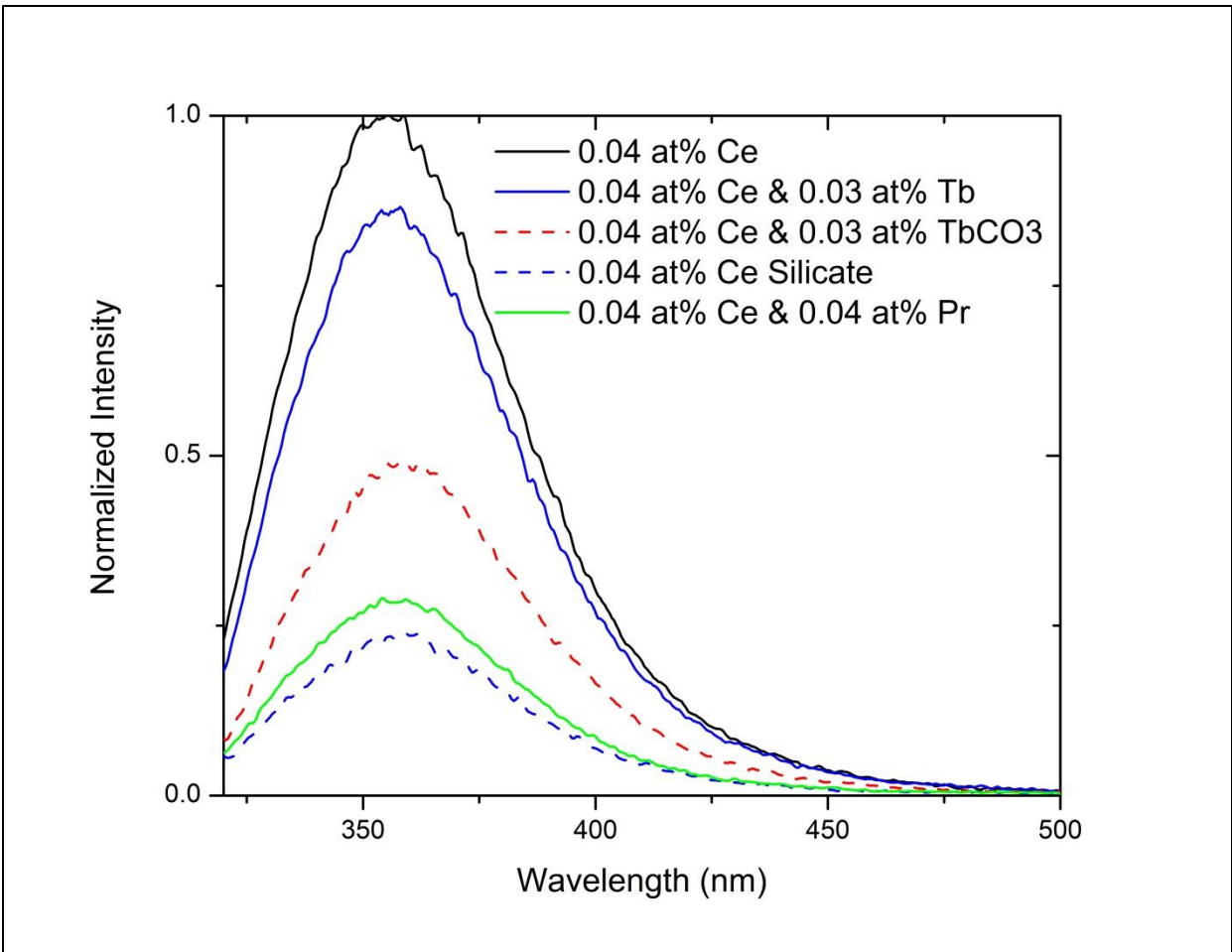
Figure 4.2-16 Normalized florescence of co-doped lithium borate glass

Figure 4.2-16 shows the normalized florescence of the co-doped lithium borate glass. The glasses were doped with 0.04 at% Ce (equivalent 0.5 wt% CeO_2). The glasses were also doped with metal ions of terbium and praseodymium. After polishing, all samples were analyzed by fluorescence spectroscopy (Fig. 4.2-16) and the results indicate that the maximum light output is obtained by loading the sample using only CeO_2 with no other rare earth ions present.

4.2.6   UV-vis Spectroscopy (UV-Vis)

UV-vis spectroscopy serves as an excellent way to measure the optical clarity of the samples as well as providing a way to measure the band-gap of the material. The band-gap of this material is especially important to determine the ability of the energy to migrate in the

matrix from the fission center to the scintillation center.   The UV-vis spectrum is shown in Fig. 4.2-17, and reveals that the samples have high optical transparency in the range from 400-800 nm with a decrease at 330 nm.
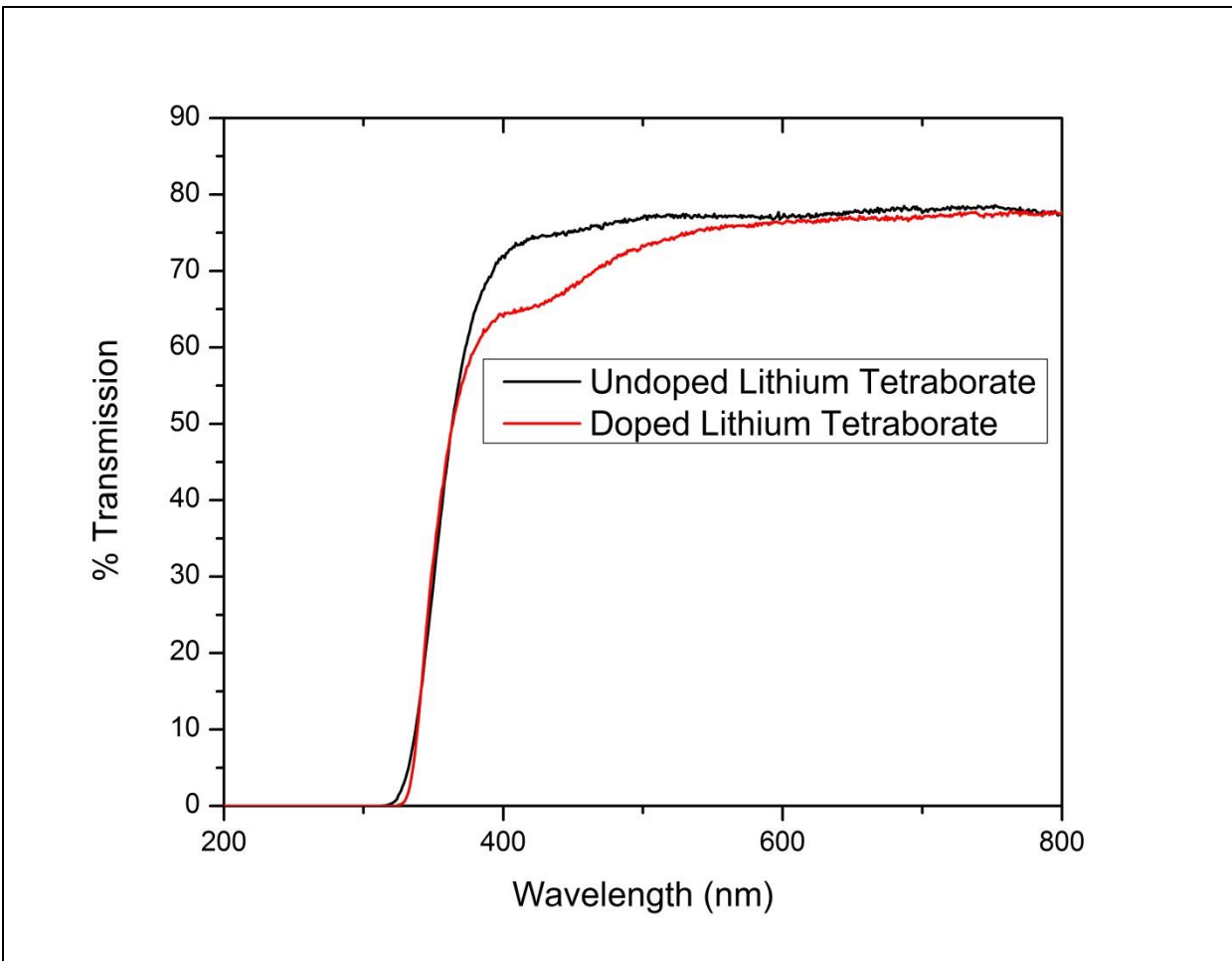
Figure 4.2-17: UV-vis spectra of lithium borate doped with 0.5 wt% CeO_2 glass and 17 wt% boric acid.

The determination of the band-gap is defined in more detail by Perkin-Elmer[137] and provides an analysis of the data to give a band-gap of approximately 3.74 eV for both the doped and un-doped material. To determine the band-gap, the wavelength is converted to eV using Eqn. 4.5.

$$E = \frac{hc}{\lambda}$$

In Eqn. 4.5, E is the energy (in J), h is Planck's constant, c is the speed of light, and λ is the wavelength (in m). The energy (in J) is readily converted to eV and the % transmission is plotted as a function of the wavelength in eV. A straight line can be drawn from the upper point of inflection to the lower point of inflection as shown in Fig. 4.2-18. The point at which the line intersects the x-axis is the band-gap.
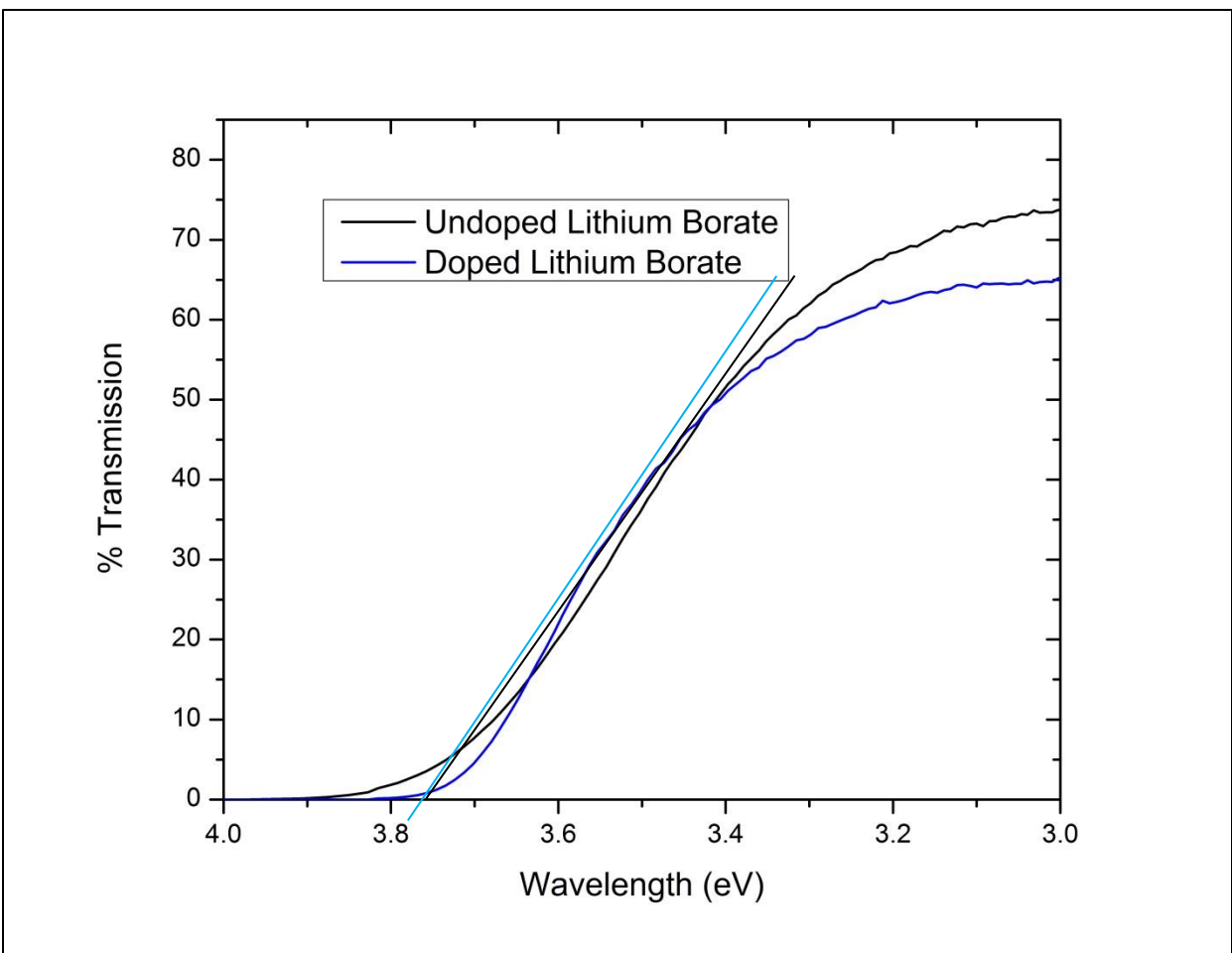
Figure 4.2-18: Band-gap determination of lithium borate glass doped with 0.5 wt% CeO_2 and 17 wt% boric acid.

4.2.7   Confocal Laser Surface Microscopy (CLSM)

The CLSM spectroscopy is an excellent technique to determine the morphology and homogeneity of the samples. The CLSM images of the blank lithium borate glass (Figure 4.2-19) and lithium borate doped with 0.5 wt% CeO_2 (Figure 4.2-20) are presented in the figures below.
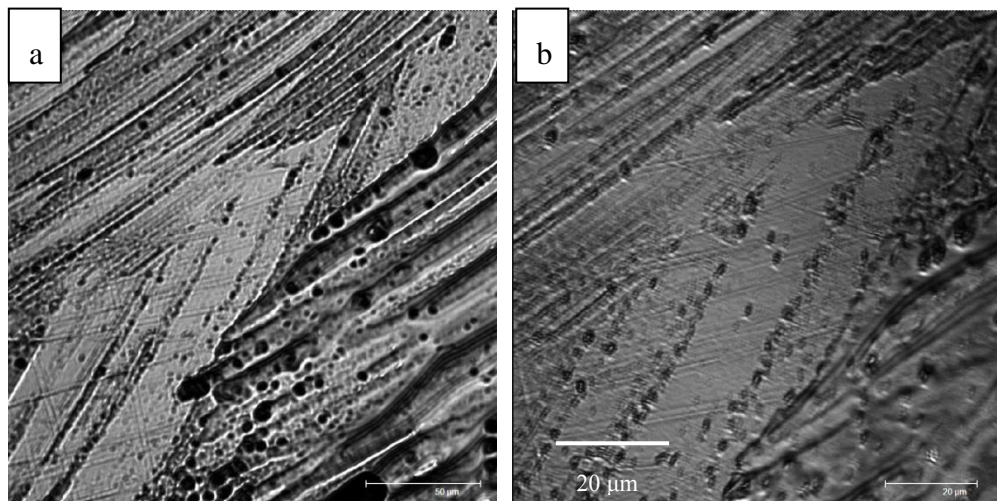
Figure 4.2-19: CLSM microscopy image of a blank (a & b) lithium borate glass containing 17 wt% boric acid. The measurement bar is at 20 um.

The CLSM images of the blank glass not only reveal the effects of polishing in the grooved surface of the glass, but also reveal highly homogeneous materials. Like the blank material (Figure 4.2-19), the 0.5 wt % CeO_2 and 17 wt% boric acid samples also demonstrated high homogeneity as is seen in Fig. 4.2-20.
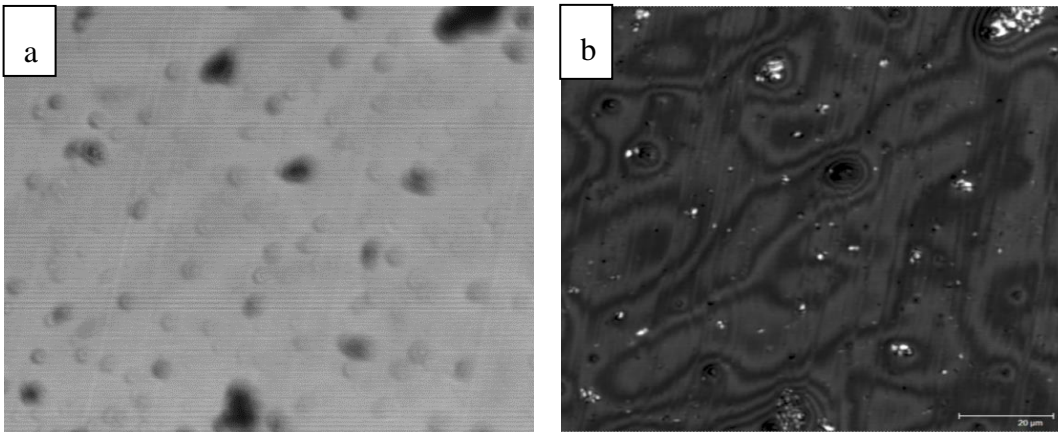
Figure 4.2-20: CLSM microscopy image of lithium borate glass doped with 0.5 wt% CeO_2 and 17 wt% boric acid. The measurement bar is set at 20 um. Image a) taken at 20μm depth in the sample and b) is taken at the surface of the sample.

The CLSM images reveal highly homogeneous samples, with trace amounts of polishing artifacts on the surface. These samples also have trace areas that appear to be crystalline regions, which could be partially crystallized lithium tetraborate, hydrated boron oxide, or a mixture of these species. These regions appear to be dispersed throughout the entire matrix. To determine the identity of these regions, a sample was made containing lithium borate and 17 wt% boric acid and cooled slowly to allow crystallization of the sample. The CLSM images of this crystalline sample are presented in the following figures.
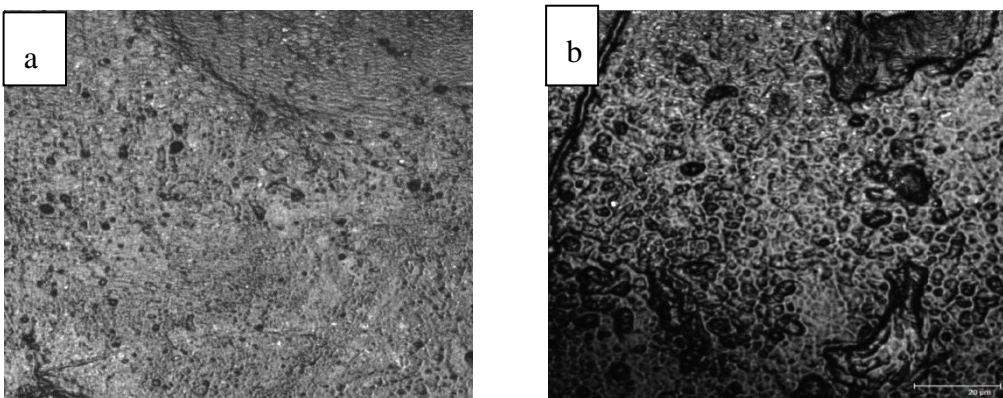
Figure 4.2-21: CLSM microscopy image of a lithium borate glass doped with 5.0 wt% CeO_2 and 17 wt% boric acid. The measurement bar is set at 20 μm.

4.2.8   Scanning Electron Microscopy (SEM)

SEM provides an excellent technique that is complimentary to the CLSM measurements and is used to examine the morphology and homogeneity of the samples. The samples are highly homogeneous as is observed in the following figures. A sample containing 0.5 wt % CeO_2, 17 wt% boric acid, in a lithium borate glass is shown in Fig. 4.2-22.
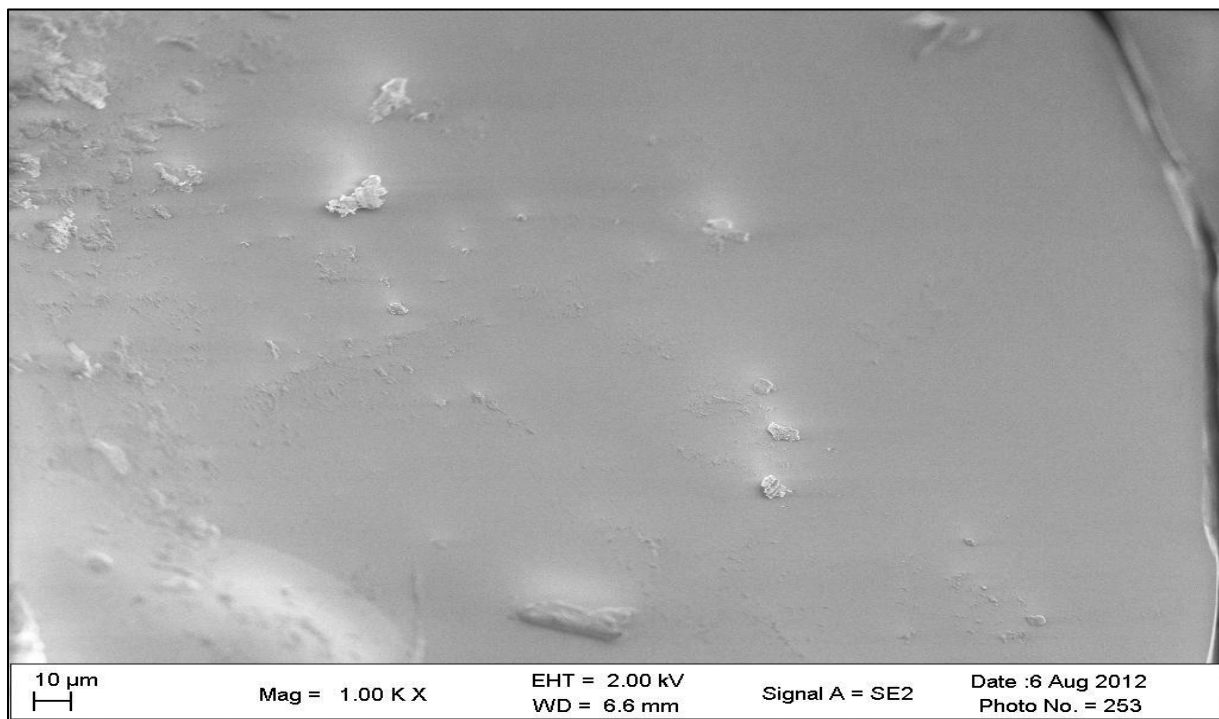
Figure 4.2-22: SEM image of lithium borate glass doped with 0.5 wt% CeO_2 and 17 wt% boric acid. Image is of the surface.

The large particles that are embedded in this matrix may be boron oxide that has crystallized in the matrix. In Fig. 4.2-23, a lithium borate glass (doped with 3.0 wt% CeO_2 and 17 wt% boric acid) is presented, and as with the 0.5 wt% CeO_2 doped sample, high homogeneity is observed.
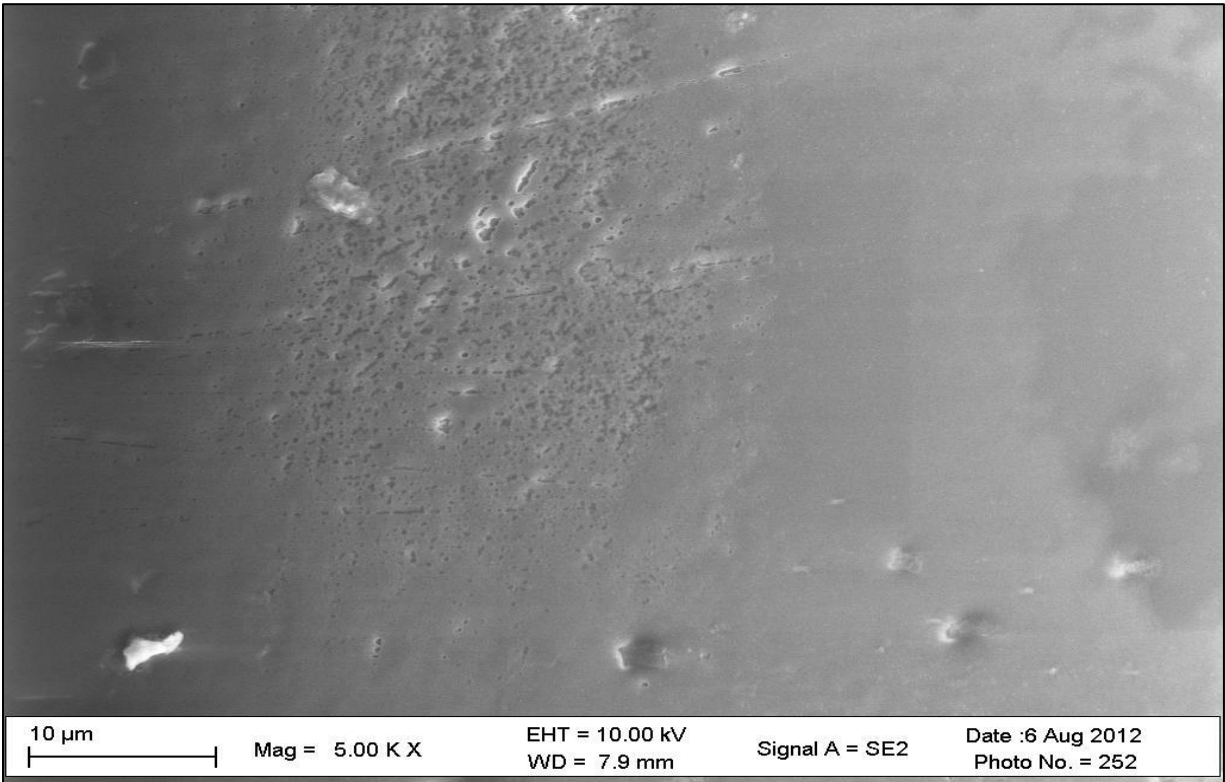
Figure 4.2-23: SEM image of a 3.0 wt% CeO2, 17 wt% boric acid in a lithium borate glass.

As with the 0.5 wt% sample, the 3.0 wt% sample (Figure 1.2-23) also has small areas of crystallization that may be crystallized boric acid. In Fig. 4.2-24, the 5.0 wt% CeO$_2$ sample is shown.

Unlike the 0.5 wt% CeO$_2$ and 3.0 wt% CeO$_2$ samples, the 5.0 wt% CeO$_2$ sample (Figure 4.2-24) will crystallize regardless of the rate of temperate decrease. The sample in crystalline form shows high homogeneity.
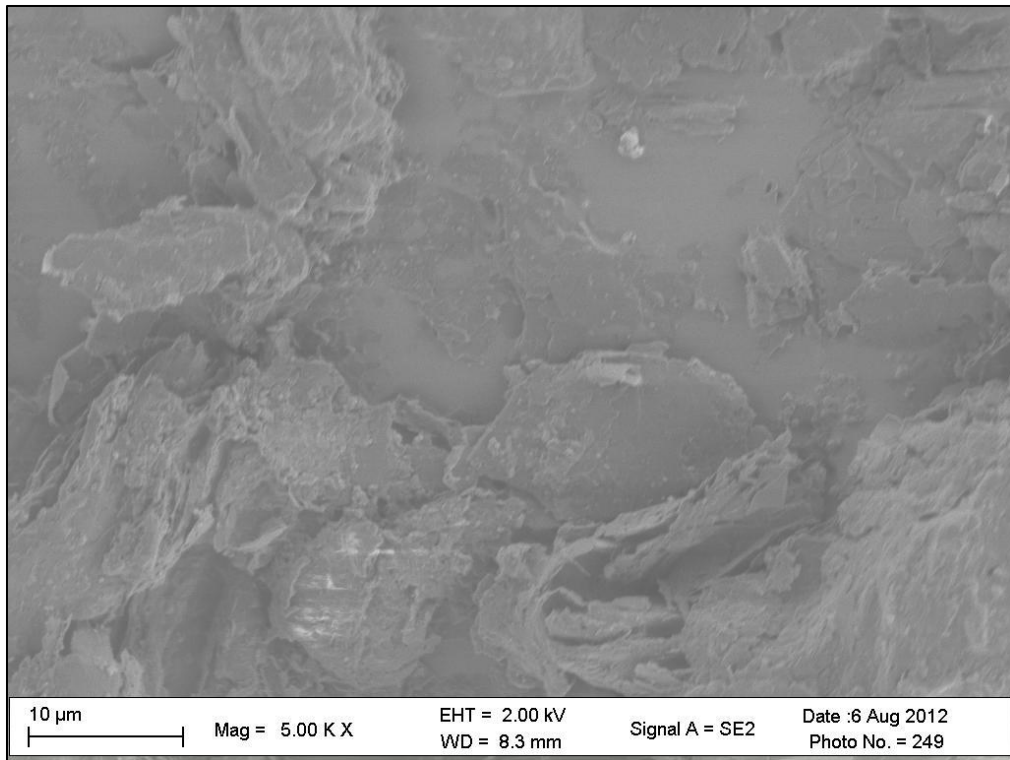
Figure 4.2-24: SEM image of the lithium borate glass doped with 5.0 wt% CeO_2 and17 wt% boric acid.

4.2.9   *Energy-dispersive X-ray Spectroscopy (EDS)*

During the SEM experiments, the EDS experiments were also performed and all experiments confirmed oxygen and boron as being present. However, none of the experiments revealed Ce as being present, which is likely due to the low amount (0.04 at%) or that the dwell time on the surface was insufficient to observe these signals. A representative spectra of the lithium borate doped with 0.5 wt% CeO_2 and 17wt% boric acid is shown in Fig. 4.2-25.
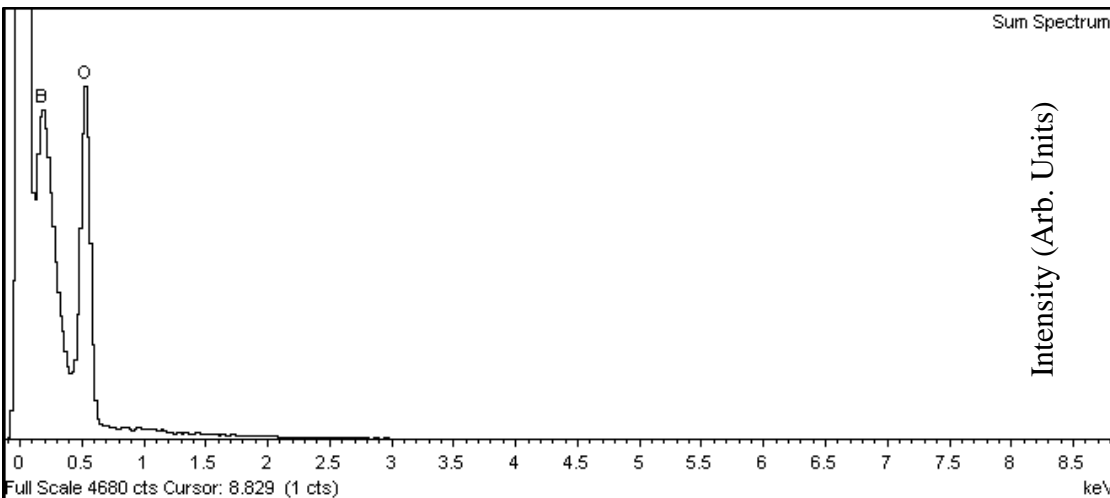
Figure 4.2-25: EDS spectrum of lithium borate glass doped with 0.5 wt% CeO_2 and 17 wt % boric acid.

The lack of Ce observed in the spectrum may be a result of the Ce being deeper in the matrix, or that the dwell time of the sample was too short to determine its presence. EDS is a surface technique and would therefore not have the ability to probe deeper to determine the presence of the Ce.

4.3   Nuclear Irradiation Results

After the structural, optical, and morphological characterization is performed, the sample was irradiated as per the description given in Section 3.8.1.

4.3.1   Neutron Irradiation Results

The neutron irradiation results are shown in Fig. 4.3-1; the glass was irradiated for 3600 s. and the peak centroid was determined to be at channel number ~550, as determined from the spectrum obtained by the lead minus cadmium results (not shown).
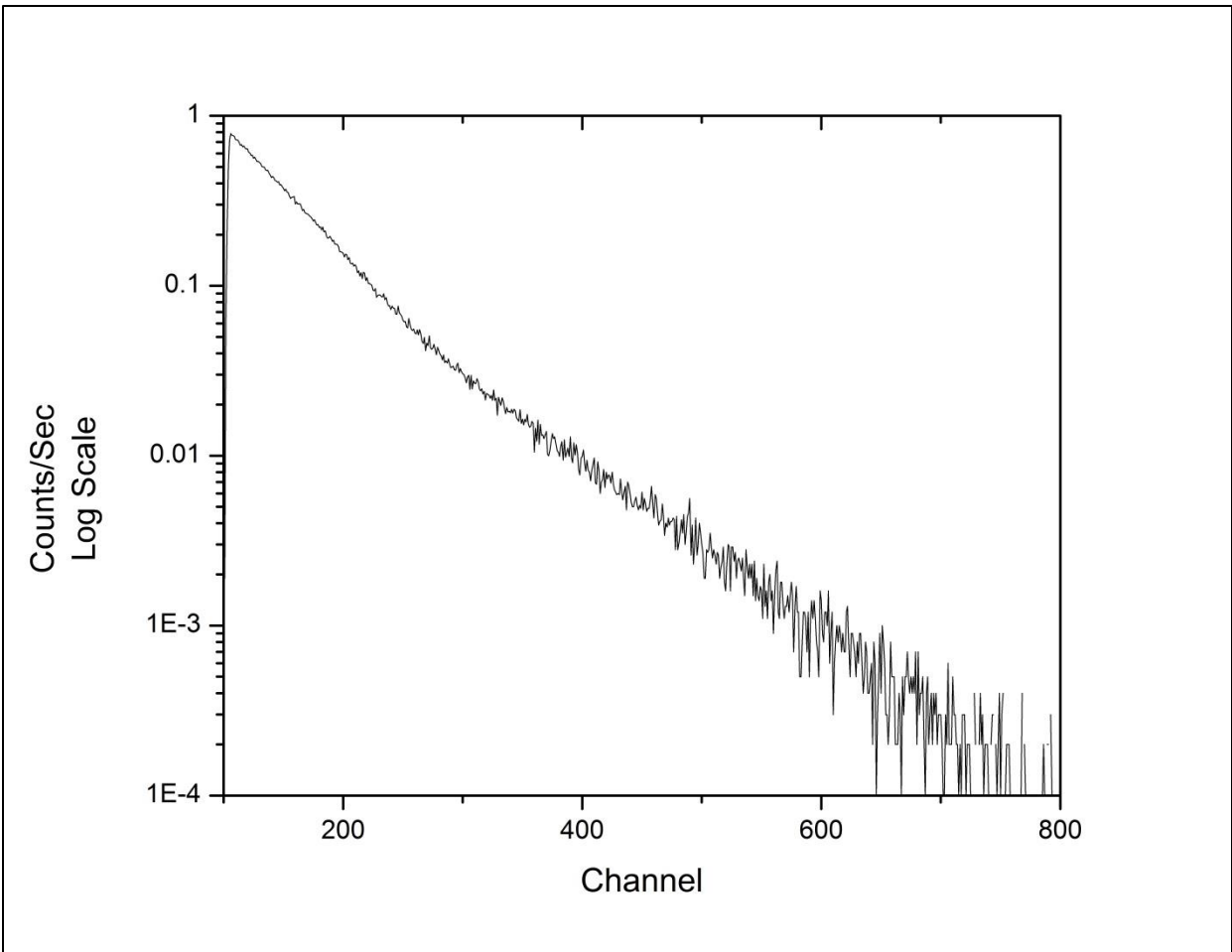
Figure 4.3-1: Neutron irradiation results for irradiation of lithium borate doped with 0.5 wt% CeO_2 and 17 wt% boric acid. The count time for the neutron spectrum was 3600 sec.

4.3.2   *Neutron/Gamma Irradiation Results*

After the characterization, experiments were performed on the glass samples; a sample containing 0.5 wt% CeO_2, 17 wt% boric acid and enriched lithium tetraborate ($^6Li_2B_4O_7$) was prepared for neutron, gamma, alpha, and beta irradiation. The neutron results are shown in Figure 4.3-1.

The neutron and gamma irradiation results of the 0.5 wt% CeO_2 sample are presented in Fig. 4.3-2. The gamma sensitivity requirements of 1 x 10^{-6} counts/sec were met at channel 410, which is the channel setting for the mathematical lower level discriminator (MLLD). At

channel 410, the intrinsic neutron efficiency was 3.7 x 10^{-4}counts/sec (cps) which is lower than the DHS requirement of 1.2 x 10^{-3} counts/sec/ng of ^{252}Cf at 2 m in moderated form.   The neutron peak for this sample was given found at channel ~550. The sample was calibrated to the GS20 spectrum (observed in Fig 3.8-6), and the result was 1.33 x 10^{3} photons/neutron event.
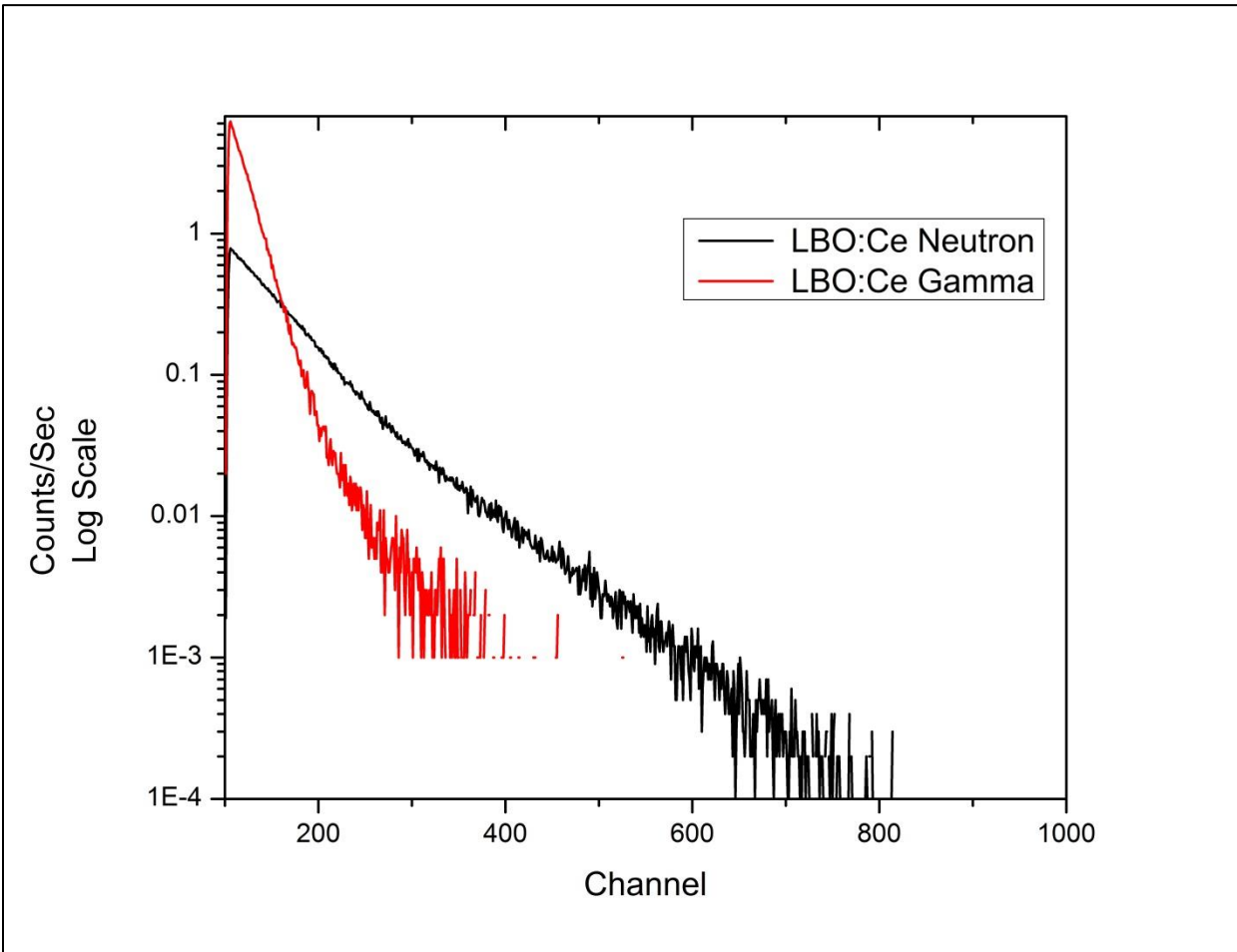
Figure 4.3-2: The neutron and gamma irradiation results of the lithium borate, 0.5 wt% CeO$_2$, 17 wt% boric acid sample. The count time for the gamma spectrum was 600 sec and the count time for the neutron spectrum was 3600 sec.

For Figure 4.3-2, the count time was 3600 sec for the neutron spectrum, and 600 sec for the gamma-ray spectrum, hence the appearance of the data cutoff for the gamma spectrum. A 1.327 g sample of lithium borate glass is used in the following calculations. The sample

discussed had a thickness of 2.7 mm, and was roughly rectangular in shape (1.3 cm by 2.2 cm). The sample was measured on April 4, 2013. The neutron intrinsic efficiency is calculated according to Eqn. 3.1 and Eqn. 3.3, by calculating the source strength at the time of measurement. The following equations were provided by Matthew Urffer.

$$S = 1.357 \times 10^6 \frac{neutron}{s} \times e^{\frac{-ln\,2}{2.54\,yr}3.76\,yr}$$

$$S = 4.86 \times 10^5 \; neutrons/s$$

To calculate the number of particles crossing the surface of the detector, the sample is approximated to be a cylinder, using Eqn. 4.6.

$$r = \sqrt{\frac{1.3\,cm \times 2.2\,cm}{\pi}} \qquad\qquad \textit{Eqn. 4.6}$$

$$r = 0.95 \; cm$$

In Eqn. 4.6, r is the radius of the cylinder in cm. Linear interpolation is used to calculate the expected solid angle at a thickness of 0.27 cm, and the ratio of the areas is used to calculate the solid angle. The linear interpolation is calculated from the data presented in Table 3.1, where the closest radius value is 1 cm. The calculation of the linear interpolation is shown in Eqn. 4.7.

$$\frac{A_1}{A_2} = \frac{\Omega_{1,n}}{\Omega_{2,n}} \qquad\qquad \textit{Eqn. 4.7}$$

$$\Omega_{2,n} = \frac{r_2^2 \Omega_{1,n}}{r_1^2}$$

$$\Omega_{2,n} = \frac{0.95 \; cm^2 \times 6.73 \times 10^{-4}}{1 cm^2} = 6.07 \times 10^{-4}$$

In Eqn. 4.7, $\Omega_{1,n}$ is the solid angle for neutrons of a film with a radius of 1 cm, Ω_2 is the solid angle for neutrons through the actual sample, r_1 is the radius of 1 cm, r_2 is the radius of the sample. Using Eqn. 3.2, the number of neutrons passing though the sample (N_i) can be determined as shown in the following calculation.

$$N_i = \Omega_{2,n} S$$

$$N_i = (6.07 \times 10^{-4}) \times (4.86 \times 10^5 neutron/s)$$

$$N_i = 284 \ neutrons/s$$

In a similar fashion the number of gamma-rays from the ^{60}Co source must also be calculated to determine the intrinsic efficiency of the sample with respect to gamma-rays. The source has aged 1.26 since January 1, 2012. Hence Eqn. 3.3 can be used to determine the number of gamma-rays.

$$S_\gamma = 7.178 \times 10^6 \frac{photon}{s} \times e^{\frac{-\ln 2}{5.27 \ yr} 1.26 \ yr}$$

$$S_\gamma = 6.08 \times 10^6 \ photon/s$$

A linear interpolation approach is used to calculate the solid angle, using Eqn. 4.7.

$$\frac{A_1}{A_2} = \frac{\Omega_{1,\gamma}}{\Omega_{2,\gamma}}$$

$$\Omega_{2,\gamma} = \frac{r_2^2 \Omega_{1,\gamma}}{r_1^2}$$

$$\Omega_{2,\gamma} = \frac{0.95 \ cm^2 \times 6.17 \times 10^{-3}}{1 \ cm^2} = 5.57 \times 10^{-3}$$

As with the calculation for the number of neutrons, the solid angle is multiplied by the source strength (6.08 x 10^6 photon/s), to determine the rate of gamma-rays crossing the surface, using Eqn. 3.2.

$$N_i = \Omega_\gamma S_\gamma$$

$$N_i = 5.57 \times 10^{-3} \times 6.08 \times 10^6 photon/s$$

$$N_i = 3.39 \times 10^6 \ photon/s$$

In Fig. 4.3-3, the integrated gamma-ray and neutron results are shown with the calculated LLD setting to achieve the neutron/gamma sensitivity requirements.
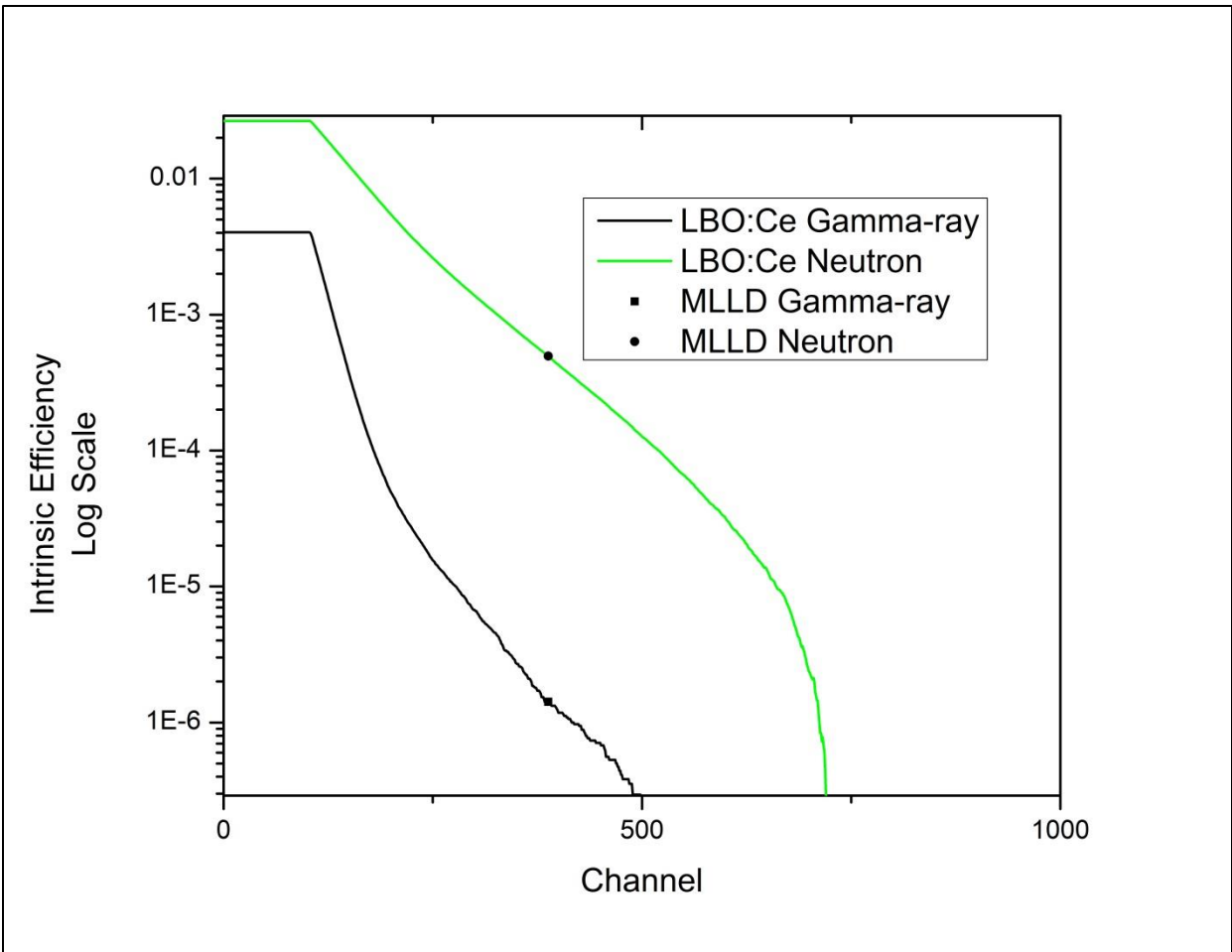
Figure 4.3-3 The integrated gamma and neutron data for the lithium borate (doped with 0.5 wt% Ce, and 17 wt% boric acid), using ^{6}Li enriched lithium borate.

In Fig. 4.3-3, the flat region from channel 0 to 100 (hence these channels have zero counts) is a results of the physical LLD of the count setup. When the spectra are summed, the summed count rate is equivalent at the lower channels and the spectra appear flat. The count rate at the calculated LLD setting at channel 388 gives a count rate of 0.9 cps for the neutron irradiation results. This translates into a count rate of 11.5 cps/mg of ^{6}Li. The count time was 3600 sec for the neutron spectrum, and 600 sec for the gamma-ray spectrum. Improvements to the gamma sensitivity could be made by reducing the thickness of the sample as has been attempted by a number of groups[5], [8], [65].

4.3.3   Gamma Scintillation Efficiency

   In conjunction with the co-doping experiments, the related fluorescence measurements were performed. Table 4.3-1 gives the gamma-ray irradiation intensity of 0.04% cerium glass loaded with different rare earth elements. A number of samples were prepared, and Fig. 4.3-4 shows the scintillation intensity for the different glass compositions using the 97 μCi ^{60}Co source (purchased on January 1, 2012).

Table 4.3-1 Sample Compositions and Gamma-ray Irradiation Intensity of Lithium Borate Glass				
at% Ce	*Material*	*at% REE**	*Material*	*Sum of counts using the ^{60}Co gamma-ray source*
0.04	CeO_2	N/A	N/A	8.43 x 10^5 (shown in Fig. 4.3-2)
0.04	$Ce_4(SiO_4)_3$	N/A	N/A	1.22 x 10^6
0.04	CeO_2	0.03 (Tb)	Tb_6O_{11}	2.22 x 10^6
0.04	CeO_2	0.03 (Tb)	$Tb_2(CO_3)_5$	2.22 x 10^6
0.04	CeO_2	0.03 (Pr)	Pr_2O_3	2.02 x 10^6

*Rare Earth Element
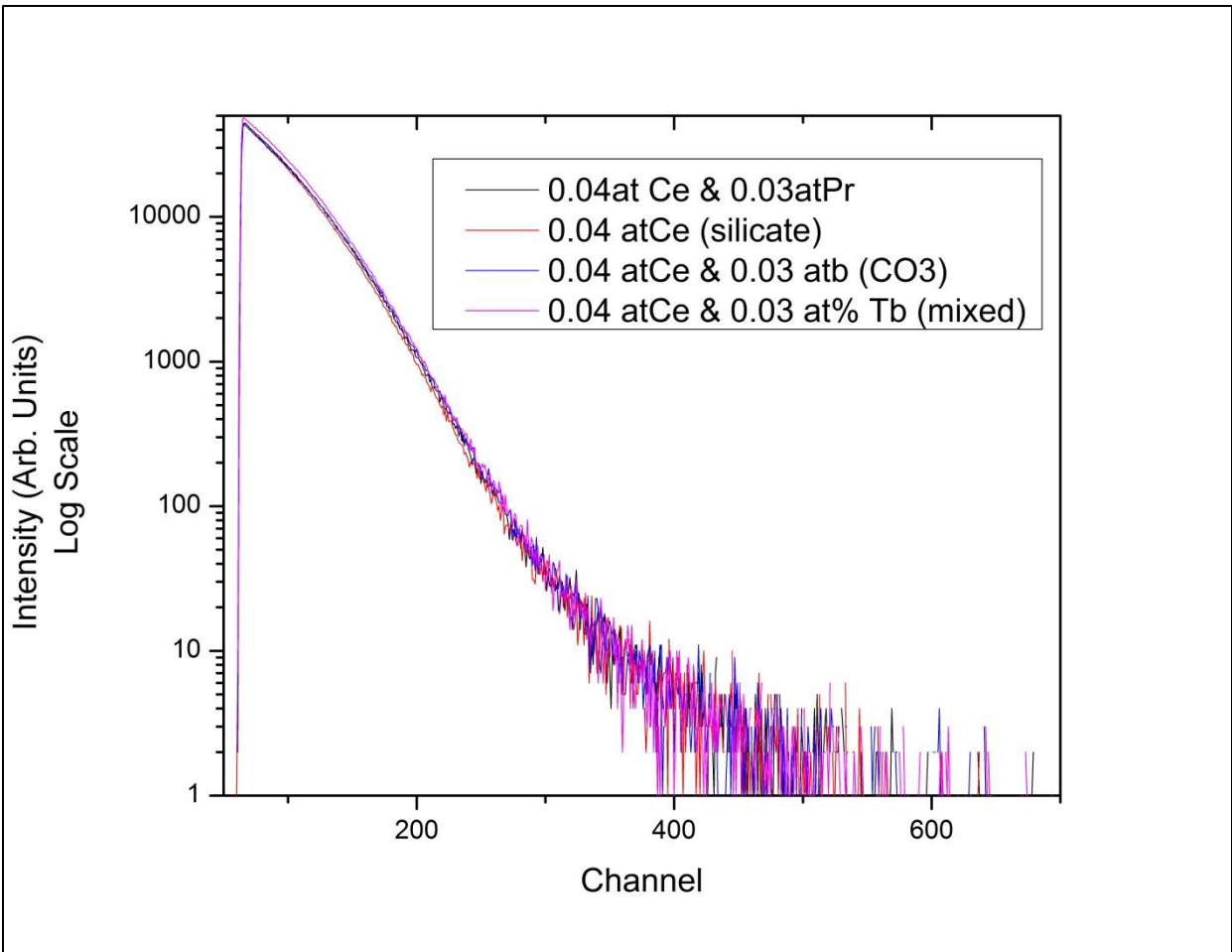
Figure 4.3-4: Gamma-ray irradiation results of the co-doped glass.

These experiments indicate that the scintillation efficiency are nearly equivalent regardless of the elements that are co-coped into the matrix. The exception is the sample containing only Ce^{3+} as the scintillation center, which had a lower light output, than the other samples. This is in agreement with Eqn. 2.1, which predicts that gamma-ray interaction will increase with an increase in the average Z number of the material.

4.3.4 Alpha Radiation Results

The alpha particle irradiation results were obtained using a 1 μCi ^{241}Am source mounted to the surface of the sample. The results are shown in Fig. 4.3-5.
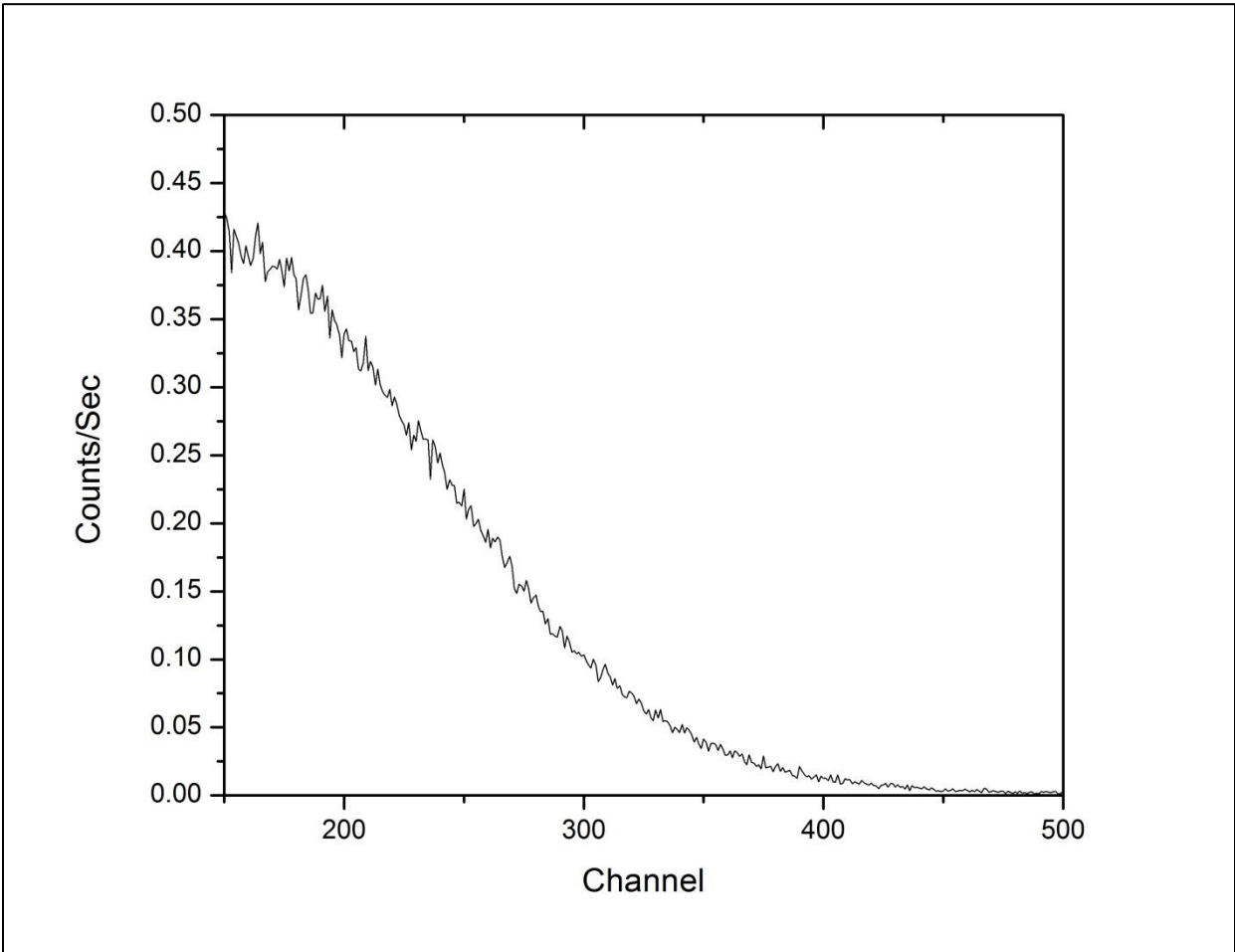
Figure 4.3-5: The alpha particle irradiation results for lithium borate 0.5wt% CeO_2, 17 wt% boric acid. The count time for this spectrum was 600 sec, with a peak at channel ~190.

The range of the alpha particle in the sample is 2.18 x 10^{-3} cm; hence the particles are not likely to deposit energy at enough depth to produce excitation of the Ce^{3+} center. Similarly, the range of the proton (or triton) is calculated[138] to be 3.81 x 10^{-3} cm.

4.3.5   Beta Radiation Results

The beta particle irradiation results were obtained using a 1 μCi ^{36}Cl source mounted to the surface of the samples. The results are shown in Fig. 4.3-6.
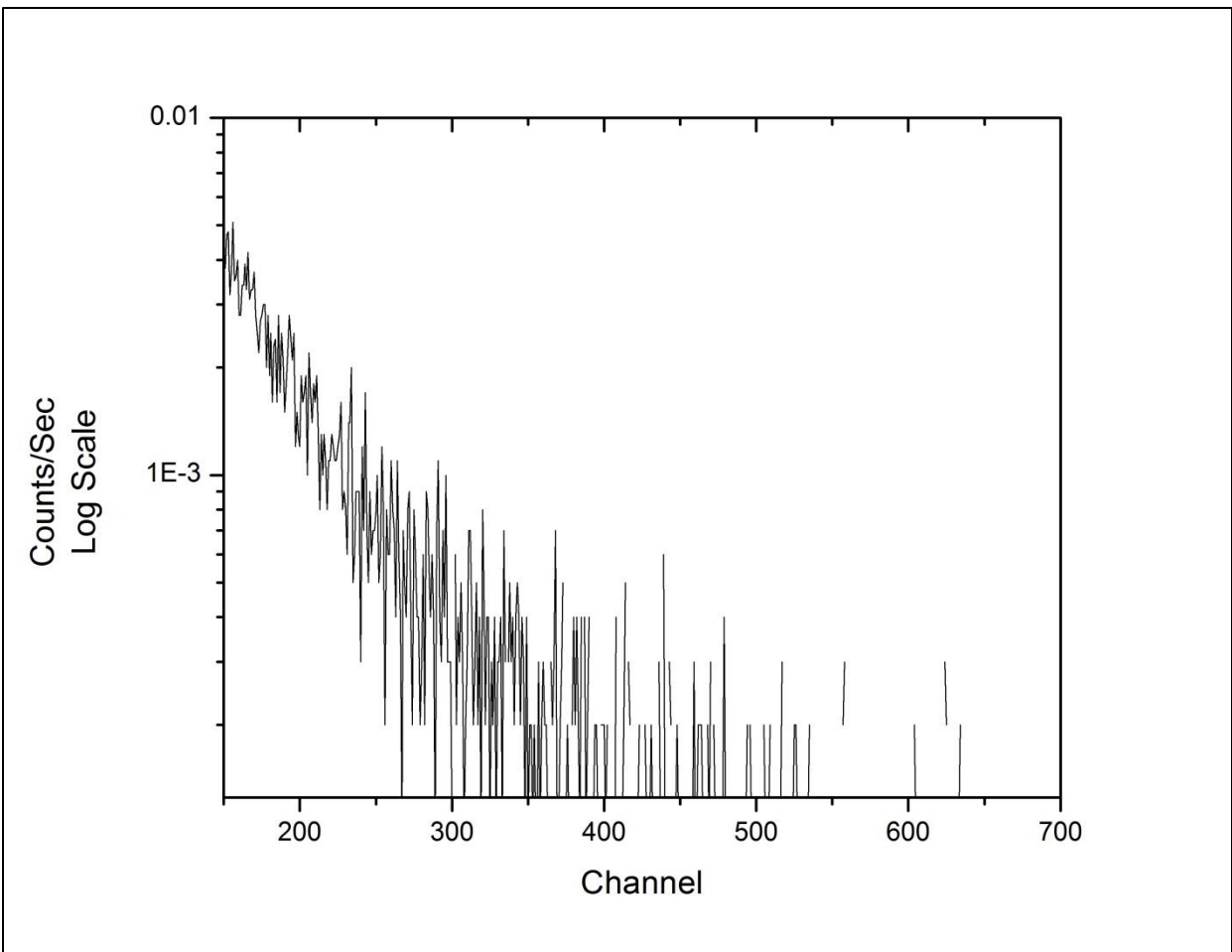
Figure 4.3-6: Beta particle irradiation results for lithium borate with 0.5 wt% CeO_2, 17 wt% boric acid. The count time for this spectrum was 10,000 sec.

The range of the beta particle is 0.13 cm, the endpoint is observed at channel ~400. This endpoint is derived by extrapolating from the slope of the spectrum to the x-axis. The large increase in light output from the beta particle irradiation spectrum as compared to the alpha particle irradiation spectrum is a result of the small range of the alpha particle in the material[5]. The alpha particle does not penetrate deeply into the sample matrix and therefore has a lower probability of interacting with the scintillation center. Furthermore, once the alpha particle interacts with the scintillation center (e.g. Ce^{3+}), the energy of the particle is severely degraded such that it has low energy for excitation. The beta particle has a much higher penetration depth and therefore interacts more effectively with the scintillation center, which is observed by the

higher light output.   The pulse height deficit (PHD) that is calculated in Sec. 3.8.4 is determined to be 4.93 for the 0.5 wt% CeO_2 and 17 wt% boric acid doped sample.

4.4   Comparison to GS-20

The standard neutron detector for this project was GS-20, which is noted by Kouzes *et al.*[3] as being a standard references material by which to compare neutron detectors. This material was developed by Spowart *et al.*[9–11] and was based on earlier work mentioned by Birk[68].   In Section 4.4.1-3, a comparison of light output of the lithium borate glass to GS-20 will be reported. The comparisons will be with respect to the alpha particle, beta particle, neutron, and gamma-ray response.

4.4.1   Neutron and Gamma-Ray Comparison

In Fig. 4.4-1, the neutron and gamma-ray responses of the lithium borate glass are plotted with those of GS-20.
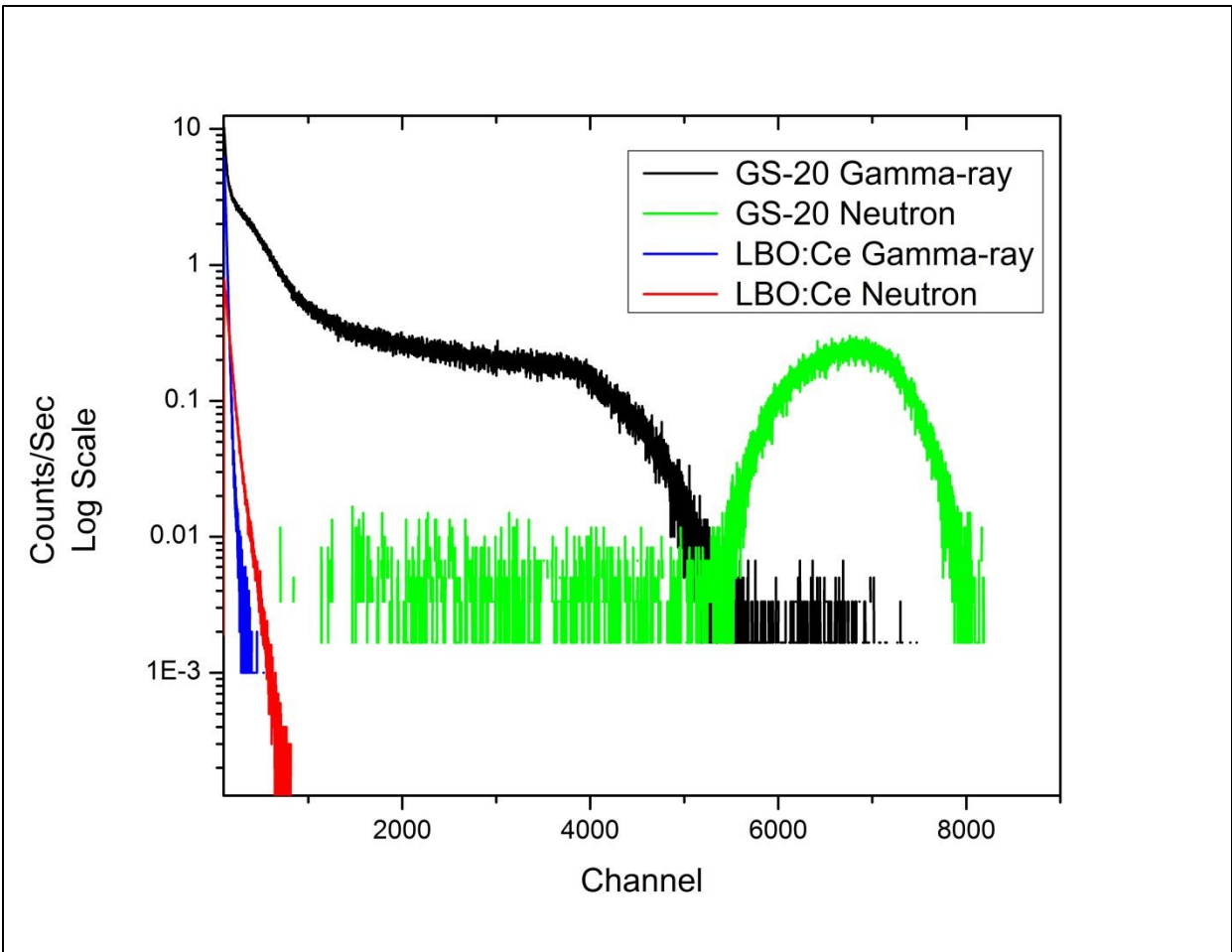
Figure 4.4-1: Comparison of the lithium borate gamma-ray and neutron response to the GS-20 gamma-ray (count time of 300 sec) and neutron (count time of 300 sec.) response. The neutron spectrum for both samples was 3600 sec. and the gamma-ray acquisition time was 600 sec.

The comparison of the sample to GS20 is performed by the following protocol. The neutron peak position is noted from the linear plot (Fig. 4.3-1 and is determined to be at channel ~550. The following calculation is used to determine the number of photons/neutron calculated for GS20 in Eqn. 4.8.

$$\frac{550\ channel}{1\ neutron} \times \frac{0.8\ photons}{1\ channel} = \frac{440\ photons}{1\ neutron} \qquad \text{Eqn 4.8}$$

Using this calculation the number of photons/neutron for the lithium borate glass sample was determined to be 440 photons/neutron. This light yield is approximately 8% of that of GS-20. Ishii *et al.* [85] reported that a boron oxide phosphate glass of similar composition was approximately 9.2 % lithium glass standard that was used in their work. In Ishii's work, Ce fluorescence center was introduced into the glass in the trivalent oxidation state (e.g. Ce^{3+}). Hence the aliovalent doping method used in this project is effect at reducing the Ce^{4+} to the Ce^{3+} state, using these light yield calculations.

4.4.2 *Alpha Particle Comparison*

As with the neutron/gamma measurements, a comparison of the alpha particle irradiation results of the lithium borate glass to the GS-20 results was performed. The alpha particle irradiation results of the lithium borate glass and GS-20 are shown in Fig. 4.4-2.
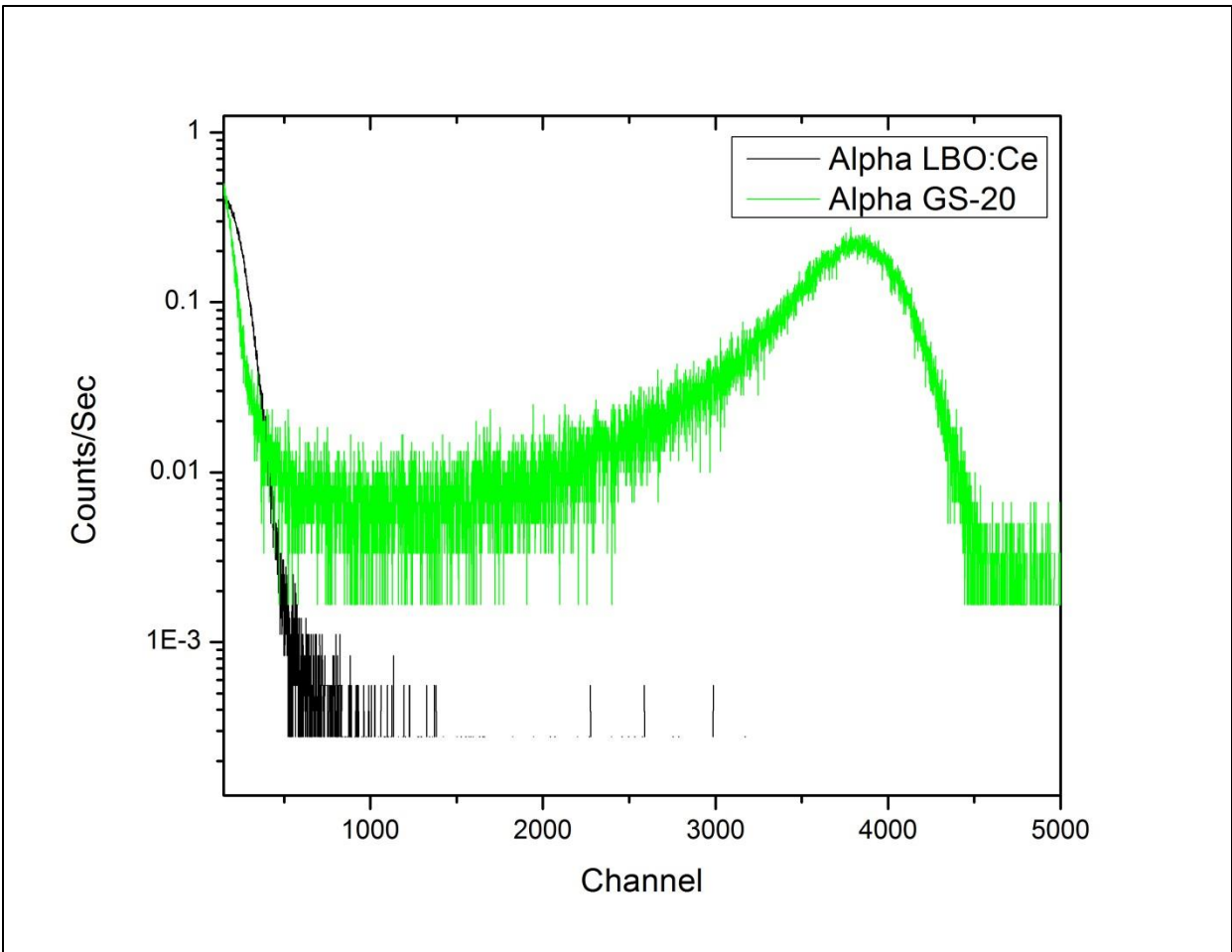
Figure 4.4-2: The comparison of the alpha irradiation responses of lithium borate glass and GS-20 are shown. The irradiation time was 300 sec for both GS-20 was 300 sec. and the count time for the LBO:Ce was 3600 sec.

The alpha analysis can be used to determine the pulse height deficit (PHD) of the alpha response. When the alpha response is measured, the channel number of the peak is recorded. The photons/MeV can be determined using the photon/channel ratio of GS20 (Section 3.8.2.2). Using Eqn 4.8 it is possible to determine the number of photons per α particle, where the peak position (in channel number) is 190 (refer to Fig. 4.3-5).

$$Apha\ Peak\ (channel) \times \frac{0.8\ photons}{1\ channel} = \frac{152\ photons}{1\ \alpha\ particle} \qquad \text{Eqn. 4.9}$$

Then by using the energy[139] of the ^{241}Am source (5.41 MeV):

$$\frac{152 \; photons}{1 \; \alpha \; particle} \times \frac{1 \; \alpha \; particle}{5.48 \; MeV} = \frac{28 \; photons}{1 \; MeV}$$ Eqn. 4.10

This value for photons/MeV from alpha particle irradiation will be compared to the photons/MeV as determined from the beta particle irradiation (Sec. 4.4.3).

4.4.3   Beta Particle Comparison

To complete the PHD analysis of the sample, the beta particle irradiation of the lithium glass sample and GS-20 are compared. The beta particle irradiation results of lithium borate glass and GS-20 are shown in Fig. 4.4-3
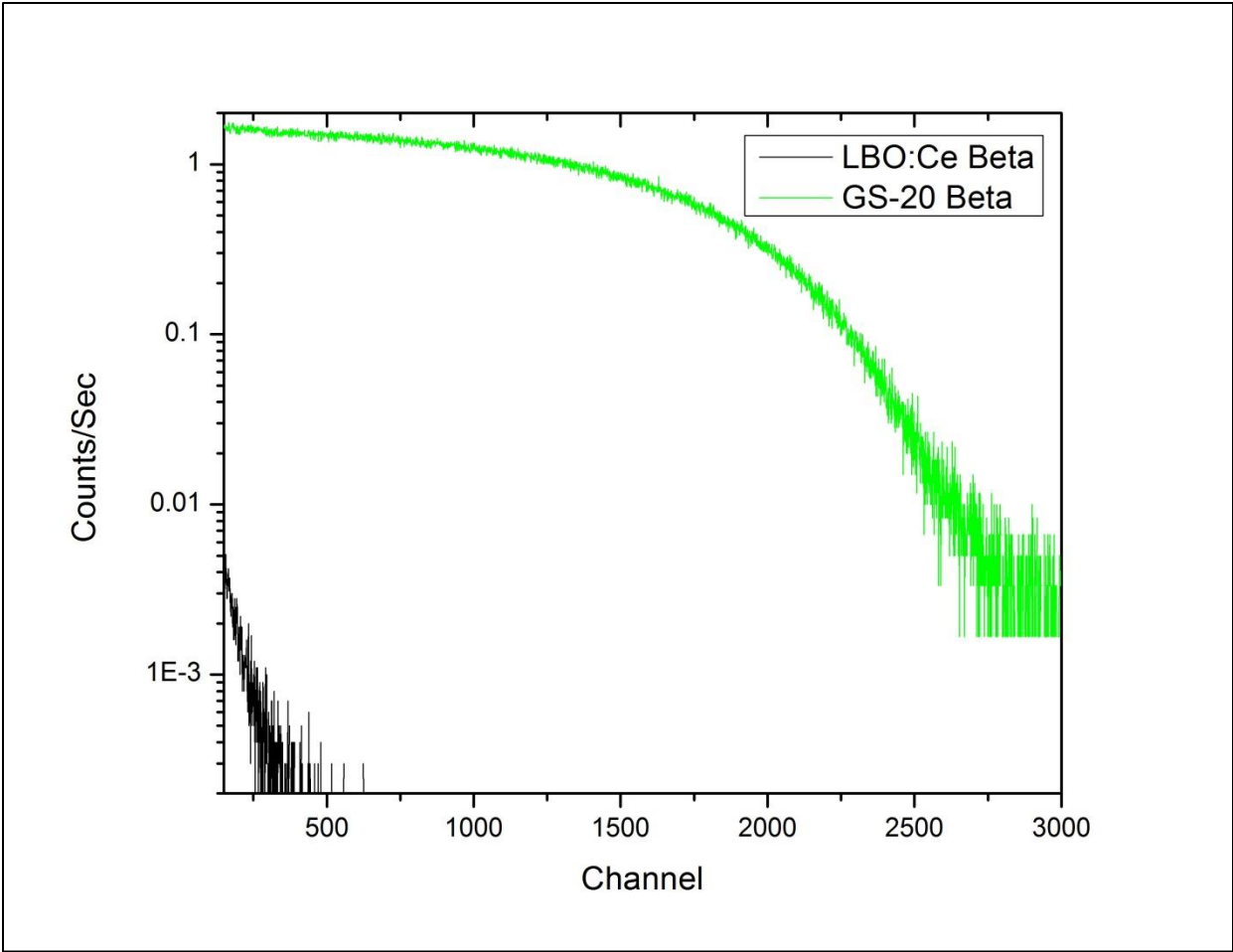
Figure 4.4-3: The beta particle irradiation results of the lithium borate glass and GS-20 are compared. The irradiation time for both samples was 300 sec. for the GS-20 and 3600 sec. for LBO:Ce.

The beta particle spectrum was analyzed to determine the end-point, and from the collected data (Sec. 4.3.5) it was determined to be at channel ~400. The ^{36}Cl has a 0.709 MeV beta energy[113], [139]. Like the calculation for the alpha particle energy, the resulting photons/MeV can be calculated using Eqn. 4.11.

$$\frac{400 \; channel}{1 \; \beta \; particle} \times \frac{1 \; \beta \; particle}{0.709 \; MeV} \times \frac{0.8 \; photons}{1 \; channel} = \frac{451 \; photons}{MeV} \qquad \text{Eqn. 4.11}$$

From these calculations it is possible to calculate the PHD or β/α ratio in terms of photons/MeV. By dividing the 451 photons/MeV (for β particles) by the 28 photons/MeV alpha, the resulting PHD is determined to be 16.1.

4.5   Acknowledgements

Chapter 5 Conclusions and Future Work

5.1   *What Was Obtained*

As mentioned in Section 1.2, the DHS criteria are specified[1], [2].

1.   The detectors must not alarm when exposed to a 10 mR/h gamma-ray exposure rate.
2.   Absolute neutron detection efficiency, $\varepsilon_{abs\ n} \geq 2.5$ cps/ng ^{252}Cf at 2 m for a source in a specific moderated form (also 1.2×10^{-3})
3.   Intrinsic gamma-neutron detection efficiency, $\varepsilon_{int\ \gamma n} \leq 10^{-6}$
4.   Gamma absolute rejection ratio (GARR) for neutrons, $0.9 \leq GARR \leq 1.1$ at 10 mR/h exposure
5.   Detectors must be produced at \$30,000 (USD) per unit.

In this study, the intrinsic gamma-neutron detection efficiency could be directly measured, and the absolute detection efficiency can be estimated from the measured data by modeling a particular configuration with a radiation transport code, such as MNCPX.

The result obtained from the experiments was a highly transparent amorphous lithium borate glass. This glass was successfully synthesized using the appropriate heating and cooling treatment cycles. Furthermore, this amorphous material was doped with Ce(III) by way of reducing Ce(IV) with excess boric acid at high temperatures.

While amorphous lithium tetraborate has been used as a fluxing agent for X-Ray Fluorescence (XRF) experiments, the problems associated with the ^{3}He shortage provide a good impetus for the development and use of this material as a thermal neutron detector. As discussed in Chapter 2, there have been reports of both crystalline and amorphous lithium materials being used as thermal neutron detectors. Similarly, Chapter 2 discussed some of the solid-state physics literature related to the *in situ* method of reducing rare earth oxides in the presence of boric acid, particularly in alkaline earth borates and strontium or aluminum borates. However, the literature did not address this abnormal reduction of rare earths using alkali borates, such as sodium or lithium borate.

Therefore, this project explored the development of lithium borate doped with Ce(III) using the *in situ* boric acid method. This project accomplished a number of studies to determine the elemental composition, structure, and morphology of this material, in addition to analyzing its response to mixed radiation fields of alpha particles, beta particles, gamma-rays, and neutrons. The results were presented in Chapter 4.

5.2   Conclusions

As presented in the literature, a number of individuals have explored lithium borate as a thermal neutron detector, since the material has high optical transparency, is not hygroscopic, and has a high loading capacity for lithium and boron. During the course of the experiments, a lithium tetraborate material was developed to which lithium and boron were added; the weight percent of loading in the final material was ^{6}Li (6 wt%) and ^{10}B (4.41 wt%).

The P-XRD, UV-Vis, and fluorescence experiments performed on the material indicated that a glass with 0.5 wt% CeO_2 (0.04 at% Ce) and 17 wt% boric acid provided the optimum optical clarity and maximum fluorescence intensity. The P-XRD results showed that at these weight percentages the material was a highly amorphous, transparent, polymeric material.

This material was studied by SSNMR and FT-IR-ATR to determine the bonding mechanisms. The experiments revealed that the trigonal boron species formed six-membered rings that were tethered at the center by a single tetragonal boron species. These structural results were confirmed by the FT-IR-ATR spectroscopy.

The elemental composition of this material was identified by ICP-OES and EDS. The results indicated that the lithium to boron ratio was 1:2.21. This ratio is in good agreement with the supposed lithium to boron ratio of 1:2, with excess boric acid in the matrix. The fluorescence and UV-vis data showed that maximum light output occurs at 359 nm, with a decrease in intensity at 400 nm.   The samples have high optical clarity from 330 nm to 800 nm, and a band-gap of 3.52 eV, indicating the material has semiconducting properties and little self-absorption in the fluorescent region. The SEM, TEM, and CLSM work revealed that the

samples were highly homogeneous, indicating that the fission products produced in the matrix have a high likelihood of interacting with the scintillation centers. A picture of the sample is shown in Fig. 5.2-1
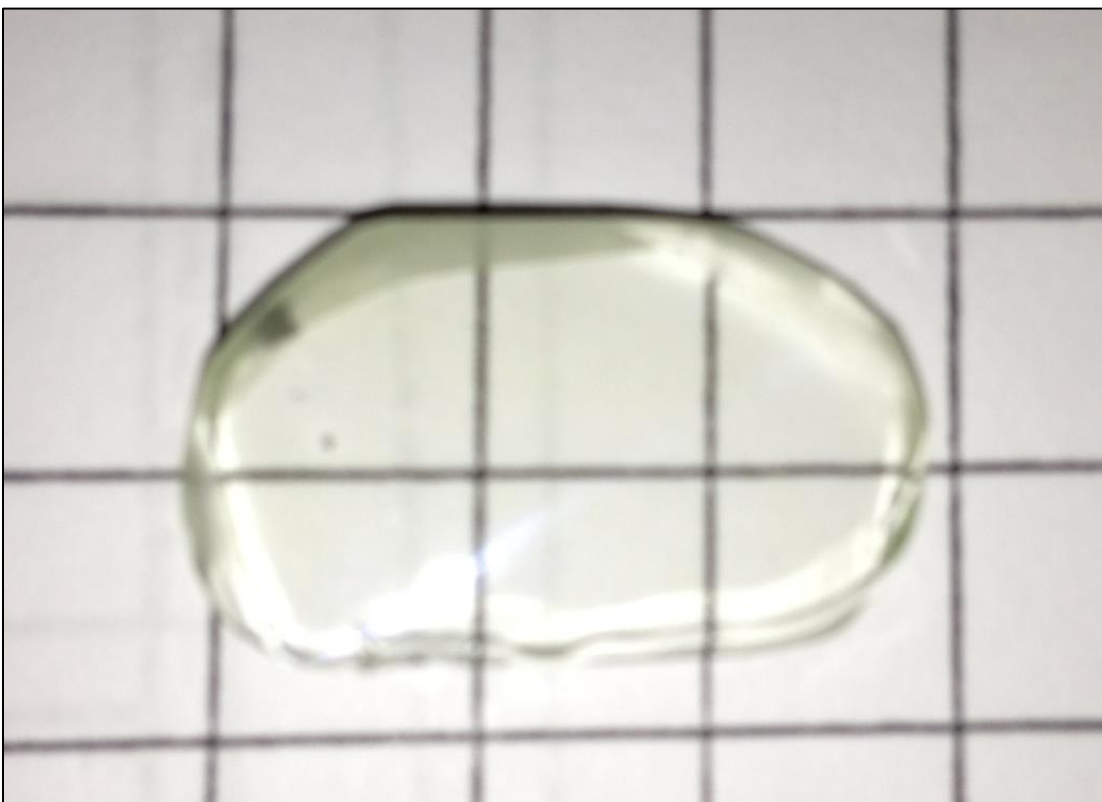
Figure 5.2-1: A picture of the lithium borate glass, doped with 0.5wt% Ce and 17 wt% boric acid.

The sample is transparent, and very lightly colored. The edges were not completely polished, thus they appear dark.

One goal for the material was adequate gamma discrimination. The samples were irradiated with gamma-rays, alpha particles, beta particles, and neutrons as specified. The gamma-ray irradiation results indicated that the material had a neutron/gamma-ray discrimination of $\varepsilon_{int, n\gamma} = 10^{-6}$ at channel 388. When this MLLD setting was applied to the neutron irradiation results, the sample had a count rate of 0.9 cps or an efficiency of 5.06×10^{-4}. Since a portion of the neutron spectrum extends beyond the gamma-ray MLLD setting, this material shows some promise of meeting the absolute neutron count rate described by the DHS. In the appropriate geometry and size, this material could be used for the purpose of neutron

detection, but further work would need to be performed to improve the light yield of this material. These possible methods are given in Section 5.3.

5.3   Future Work

Future work on this project would continue in two directions, both directed at increasing the efficiency of the material. The first direction would be to improve the quantum efficiency of the material by co-doping the material with other metal ions, such as Tb or Pr. Although some experiments have been presented using co-doping metal ions such as Tb(III) or Pr(III), the effect of varying the concentration of the co-dopant has not been explored any further than simply using ratios 1:1 at% ratios of Ce(III) to the other rare earth ions.

Further experiments would explore co-doping the lithium tetraborate glass by varying at% ratios of Tb(III) or Pr(III) to Ce(III) to determine the effect on the light output, band-gap, optical transparency, and fluorescent intensity of this material. After optimizing the at% ratios of these doping materials, the samples would be subject to gamma-ray and neutron irradiation to determine the effects, if any, on the brightness of scintillation response.

The second objective of the future work of project would be to determine the effect of annealing or heat treatment of these samples. Annealing experiments[140], [141] would be performed to determine the effect of heating the glass to a variety of temperatures to determine the effect on the optical clarity and fluorescence intensity. As with the co-doping experiments, gamma-ray and neutron irradiation would be performed to determine the effect of this annealing on the scintillation light output. In the proposed experiments, a variety of annealing temperatures, annealing times (also called hold time), and rates of heating and cooling would be explored.

Chapter 6 Additional Projects Involving Thermal Neutron Detection

Section 6.1 and subsequent sections are the text of a paper submitted to *Nuclear Instruments and Methods A*, and was co-authored by Andrew Mabe, Matthew Urffer, Dr. Dayakar Penumadu, Dr. Laurence F. Miller, and Dr. George K. Schweitzer.

6.1   Synthesis of Lithiated Polymers

As discussed in the candidacy research proposal (CRP), one of the projects to be developed was the synthesis of lithiated polymers. This project was performed in conjunction with Andrew Mabe, and the following section is the discussion of the work from this project.

6.1.1   Introduction

The development of effective thermal neutron detectors is relevant to the fields of nuclear physics, nuclear power generation, imaging, and homeland security. ^{3}He filled proportional counters are widely used to detect fissile materials by detection of low-energy neutrons in radiation portal monitors and in neutron scattering experiments. Due to the recent expanded use and reduced production of ^{3}He, it is of interest to national security and basic scientific research to develop a technology to replace ^{3}He for neutron sensing devices[1].

Conventional research in the area of polymer scintillation detector development usually involves the use of common aryl vinyl polymers such as polystyrene (PS), polyvinyltoluene (PVT), and polyvinylxylene (PVX) or their modifications. The use of these polymers stems from the relatively low cost, facile synthesis, and intrinsic luminescent properties of the aromatic pendant groups. These polymers can be blended with appropriate fluors to improve the overall quantum efficiency of fluorescence and to move the wavelength of maximum emission to regions where common bialkali photomultiplier tubes (PMTs) are most sensitive (400 – 450 nm). In order to function as a thermal neutron scintillation detector, a neutron capture nuclide such as ^{6}Li, ^{10}B, or ^{157}Gd must be mixed with an aryl vinyl polymer and a fluor[7], [8], [142]. In this study, ^{6}Li was chosen as the neutron capture nuclide because it has a high absorption cross section (940 b) and a large reaction energy (Q = 4.78 MeV). On capture of a thermal neutron,

^{6}Li fissions into an alpha particle (2.05 MeV) and a triton (2.78 MeV). These charged particles generate ionizations and excitations in the surrounding matrix which are then harvested by appropriate fluors that subsequently emit photons at longer wavelengths.

Scintillation light is generated inside the material and must escape the surface in order to be detected; hence, the ideal scintillation detector is completely transparent such that it does not scatter or absorb its own scintillation light[68]. In our previous works, we investigated poly(2-vinyl naphthalene) (P2VN) containing lithium-6 salicylate (^{6}LiSal) and organic dyes[7] as well as poly(ethylene naphthalate) containing lithium-6 fluoride (^{6}LiF) and organic dyes[8] as potential thermal neutron detectors. ^{6}LiSal was chosen because it contains ^{6}Li to capture neutrons and salicylate (Sal$^-$) to function as a fluor and ^{6}LiF was chosen because it has a high atom density of ^{6}Li and is not hygroscopic. However, the resulting composites were not transparent due to phase separation of the organic and inorganic components. There are a few examples of transparent composites that have been reported in the literature. For example, PVT can be loaded with either o-carborane[142] or gadolinium(III) isopropoxide[143] to result in transparent composites. An independent previous report of a transparent lithiated scintillation detector utilized a styrene-lithium methacrylate copolymer[144]. The present work intends to circumvent the issue of phase separation and concomitant reduction in optical clarity by providing chemical bonds between the ^{6}Li and the polymer matrix.

The polymer chosen for this work is poly(styrene-co-lithium maleate), abbreviated as PS-co-PLiMAn, shown in Fig. 1. Styrene was selected because it is relatively inexpensive, it is easy to purify and polymerize, and it contains aromatic pendant groups which facilitate scintillation. Under free radical conditions, styrene and maleic anhydride form an alternating copolymer which has been used in a variety of applications[145], [146]. The alternating nature of the resulting copolymer ensures that the sizes of the phases are approximately of molecular size and will therefore cause negligible scattering of scintillation light. The maleic anhydride groups can be hydrolyzed to generate two acid groups per monomer unit, each of which can be titrated to form a dilithium salt, permitting a maximum loading of ^{6}Li of 5.24% by mass. PS-co-PLiMAn is insoluble in common organic solvents which precludes its use with common fluors used in polymer scintillators. It is, however, soluble in water, permitting the use of salicylic acid (HSal) as a fluor.
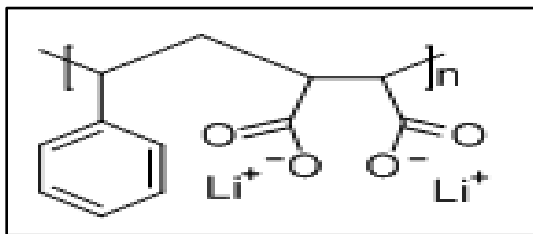
Figure 6.1-1 Chemical structure of PS-*co*-PLiMAn.

6.1.2 *Materials and Methods*

6.1.2.1 *Materials*

[6]LiOH · H_2O, enriched to 97.6% [6]Li, was dissolved in methanol at 10 g/L at room temperature, then filtered with a 1 μm filter. The methanol was evaporated from the filtrate at 150°C to give anhydrous [6]LiOH with >95% purity, as determined by inductively coupled plasma-optical emission spectroscopy (ICP-OES). Tetrahydrofuran (THF) (Fisher), diethyl ether (Fisher), and toluene (Fisher) were fractionally distilled from anhydrous calcium chloride and passed through a 200 nm filter immediately before use. Styrene (Acros) was purified immediately before use by passing the monomer through a column containing activated basic alumina on top of silica gel to remove t-butyl catechol inhibitor and other impurities. Free radical initiator 2,2'-azobisisobutyronitrile (AIBN) (Aldrich), was recrystallized from methanol and stored at 5°C under argon until needed. Acrylic disks 1 mm thick with a diameter of 50.8 mm (Eljen Technologies) were cleaned with ethanol immediately prior to use. Maleic anhydride 99% (Acros), deuterated dimethylsulfoxide (DMSO-d[6]), HSal (Fisher), ethanol (Fisher), methanol (Fisher), and Optima® LC/MS grade water (Fisher) were used as received.

6.1.2.2 *Synthesis of PS-co-PMAn*

Maleic anhydride (4.168 g, 42.5 mmol), styrene (4.426 g, 42.5 mmol), 33 mL toluene, 5 mL diethyl ether, and a magnetic stir bar were added to a flame-dried round bottom flask and sealed with a rubber septum. The flask was evacuated with a high vacuum and refilled with argon three times to degas the solution. The flask was suspended in an oil bath at 60°C under

magnetic stirring, then purified AIBN (36.6 mg, 0.223 mmol) was dissolved in 2 mL toluene and injected into the flask through the septum using a syringe to initiate the polymerization. Polymerization was carried out for 45 minutes, during which time the polymer precipitated from the solution. The white precipitate was collected by filtration, then washed with toluene and diethyl ether to remove unreacted monomers, initiator, and homopolymers. The resulting polymer was then dried to constant weight under vacuum at 60°C.

6.1.3   Lithiation of PS-co-PMAn and Film Fabrication

A mass of 399.7 mg PS-*co*-PMAn was dissolved in 10 mL THF. In a separate beaker, an appropriate mass of ^{6}LiOH was dissolved in 10 mL H_2O and heated to 90°C with stirring. The copolymer solution was added to the ^{6}LiOH solution dropwise. The solution was stirred at 90°C for one hour to permit completion of the hydrolysis reaction and evaporation of the THF. The solution was then cooled to 40°C, then an appropriate mass of HSal was added. This solution was stirred for one hour at 40°C to ensure complete dissolution of the HSal. The clear viscous solution was pipetted onto an acrylic disk and dried to constant mass at 40°C. The cast solution was covered with a beaker to slow solvent evaporation rate and to increase the solvent vapor pressure directly above the film to promote uniformity of film drying. This method afforded an optically clear film free of cracks or crazing, as shown in Fig. 2. To determine the maximum amount of ^{6}Li that could be incorporated into the polymer, a series of films containing 25%, 50%, 75%, 82.5%, 90%, and 100% lithiation of the maleic anhydride units were cast. The films at 90% and 100% lithiation were cloudy, so the composition of 82.5% lithiation was used throughout all further experiments. On drying, 82.5% lithiation yields a total ^{6}Li loading of 4.36% by mass for the neat polymer, assuming complete hydrolysis of the anhydride units.
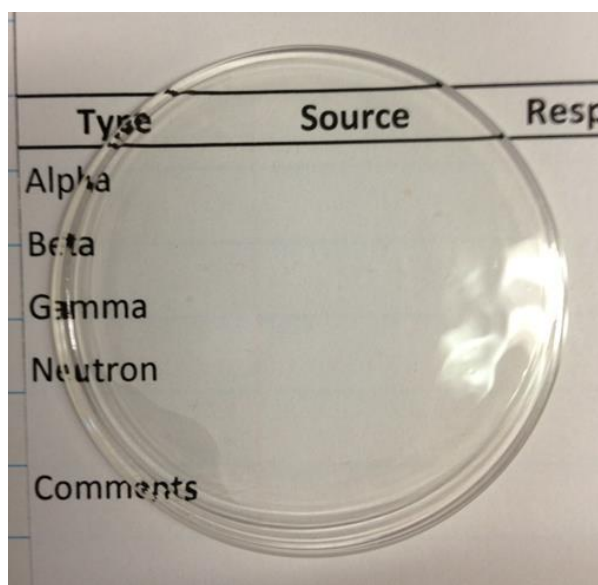
Figure 6.1-2 Transparent PS-*co*-PLiMAn film containing 11.7% HSal by mass mounted on an acrylic disk. The film thickness is approximately 200 μm. The film is placed on a card containing text to illustrate the optical clarity.

6.1.4   *Characterization Methods*

The purified ^{6}LiOH was monitored for hydration and formation of carbonates by powder x-ray diffraction on a Panalytical Emperean powder X-ray diffractometer and by analyzing ^{6}Li content using ICP-OES on a Perkin Elmer Optima 2100 DV Optical Emission Spectrometer at 670.781 nm in axial detection mode. The degree of isotopic enrichment of ^{6}Li was determined by mass spectrometry using a QSTAR® XL Hybrid LC/MS/MS System. The mass distribution of the neat copolymer was determined by gel permeation chromatography in THF against PS standards using a Tosoh EcoSEC GPC system in refractive index mode. The resulting mass distribution was M_N = 96,800 g/mol, M_w = 303,700 g/mol, and PDI = 3.14. The composition of the copolymer was determined by ^{1}H NMR using a Bruker Avance 400 MHz spectrometer. The copolymer was dissolved in DMSO-d$_6$ for analysis. The ^{1}H spectrum indicated that the copolymer was alternating with a 1:1 ratio of styrene to maleic anhydride. Optical transmission measurements were conducted using a Thermo Scientific Evolution 600 UV-Vis Spectrophotometer. Fluorescence measurements were conducted using a PerkinElmer LS55

Fluorimeter equipped with a xenon flash lamp as the excitation source. Both excitation and emission spectra were collected with 5.0 nm spectral bandwidths.

Scintillation measurements were conducted as previously described[7]. Briefly, samples cast on acrylic disks were coupled to a PMT using optical grease with the sample side facing away from the PMT, then covered with a teflon tape reflector. A moderated ^{252}Cf source was used to generate neutrons. The sample was first measured in an acrylic tube surrounded by lead to obtain the scintillation response to gamma-rays and all neutrons. The sample was then measured in an acrylic tube surrounded by a 1.6 mm thick sheet of cadmium to shield thermal neutrons. The net thermal neutron response was then obtained by subtracting the response in the cadmium tube from the response in the lead tube. The alpha and beta responses were measured with an ^{241}Am source and a ^{36}Cl source, respectively. Gamma-ray responses were obtained using a 97 μCi ^{60}Co source. The light pulses from the samples were converted into electrical pulses using a Philips 2202B PMT mounted on a Canberra 2007P base powered by an ORTEC 556 high voltage power supply set at 1200V. The signals from the base were amplified using an ORTEC 572A amplifier set at a gain of 50 with a 2 μs shaping time. The amplified signal was digitalized using an ORTEC 926 MCB with an 8192 channel ADC. The digitalized output was then saved using the MAESTRO-32 software from ORTEC. The instrumentation was calibrated using scintillation responses from GS20 lithiated glass.

6.1.5 Results

6.1.5.1 Optical Transmission and Fluorescence

The optical transmission of PS-*co*-PLiMAn containing 11.7% HSal is shown in Fig. 3. The cutoff wavelength is at 360 nm and the average percent transmission between 360 and 600 nm is 78.5%. The spectrum has not been corrected for reflection off of the sample surfaces.
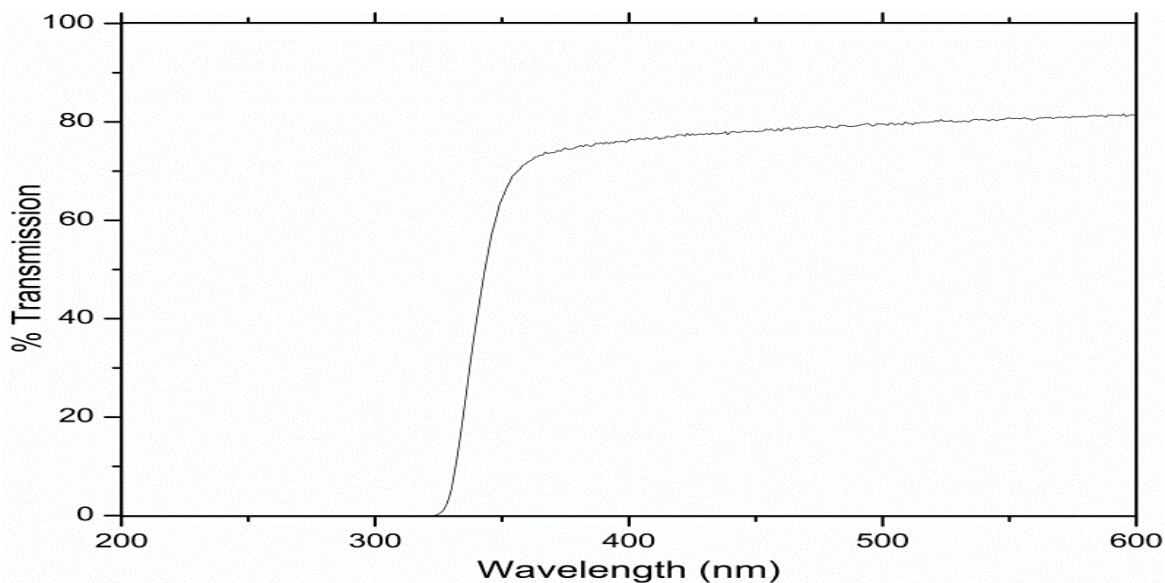
Figure 6.1-3 Transmission spectrum of PS-*co*-PLiMAn containing 11.7% HSal.

Photoluminescence spectra are shown in Fig. 4. The wavelength of maximum excitation for neat PS is at 278 nm and the wavelength of maximum emission is at 310 nm (excimer emission) with a quantum yield for fluorescence (φ_f) of about 0.16. HSal has an emission wavelength at 450 nm ($\varphi_f = 0.02$) whereas the salicylate ion (Sal$^-$) has an emission wavelength at 408 nm ($\varphi_f = 0.36$)[147]. Previous experiments have indicated that the emission characteristics of Sal$^-$ and LiSal are nearly identical. The photoluminescence experiment was designed to excite the PS subunits and record emissions at 310 nm, 408 nm, and 450 nm in order to determine the relative amounts of light emitted from PS excimers, Sal$^-$, and HSal, respectively. The photoluminescence spectra indicate that the maximum intensity excitation wavelength is at 278 nm, indicative of styrene excitation. When excited at 278 nm, the primary emission wavelength is at 408 nm with emissions at 310 nm (PS excimer) and 450 nm (HSal) essentially absent. The absence of emission at 310 nm indicates that the excitations on the PS subunits are completely harvested. The emission at 408 nm and absence of emission at 450 nm indicate that Sal$^-$ is the primary emitter rather than HSal. By considering that the the acid form of the polymer and HSal are both weak acids that are subject to acid-base equilibrium, the emission results indicate that some of the lithium ions have been removed from the maleate groups by HSal resulting in maleic acid and LiSal. It should be noted that in this sample, there

are 1.98 mmol maleate groups (3.96 mmol carboxyl groups), 0.433 mmol HSal, and 3.27 mmol Li$^+$ ions. Thus, even if the HSal were to be completely converted to LiSal, the majority of the Li$^+$ would still be associated with the polymer chain.
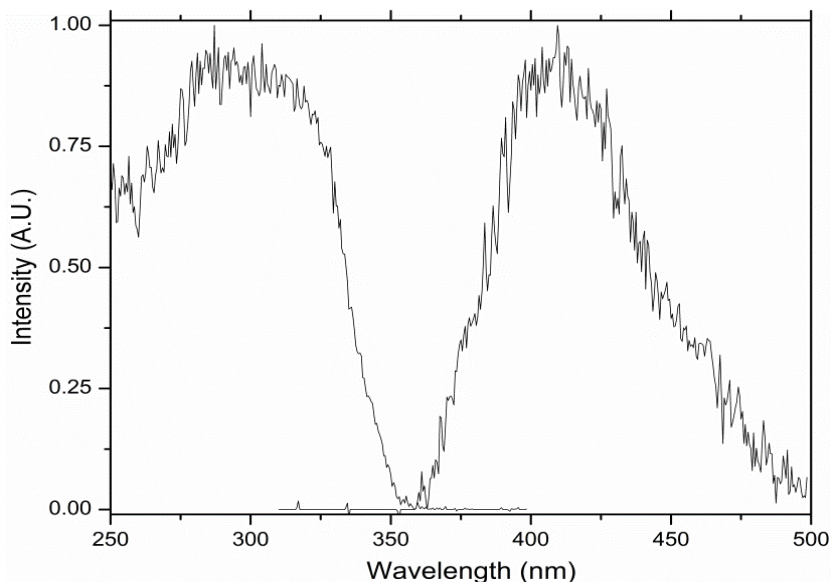
Figure 6.1-4 Excitation (left) and emission (right) spectra of PS-*co*-PLiMAn containing 11.7% by mass HSal.

To determine the concentration of HSal required to obtain the maximum fluorescence yield, a series of PS-*co*-PLiMAn films containing 2% - 26% HSal were fabricated and the fluorescence emission of each was measured. Each film was excited at 278 nm and the resulting emission spectrum was integrated from 350 – 500 nm to obtain a value proportional to the number of photons emitted from each film. It should be noted that the shape of the emission curves are nearly identical for all samples. The results are shown in Fig. 5 and indicate that increasing the amount of HSal initially increases the fluorescence response up to 11.7%, after which the emission intensity is significantly reduced. This can be reasoned by considering that the primary emission is from Sal$^-$. It is presumed that at and below 11.7%, the primary component is the Sal$^-$, most likely in the form of LiSal. Above 11.7%, acid-base equilibrium between the HSal and the maleic acid becomes important. This would convert some of the LiSal to HSal. The quantum efficiency of HSal is much lower than that of Sal$^-$, resulting in a

reduction in the overall emission intensity. Incorporation of 11.7% HSal into the PS-*co*-PLiMAn film results in a material that is 3.85% ^{6}Li by mass.
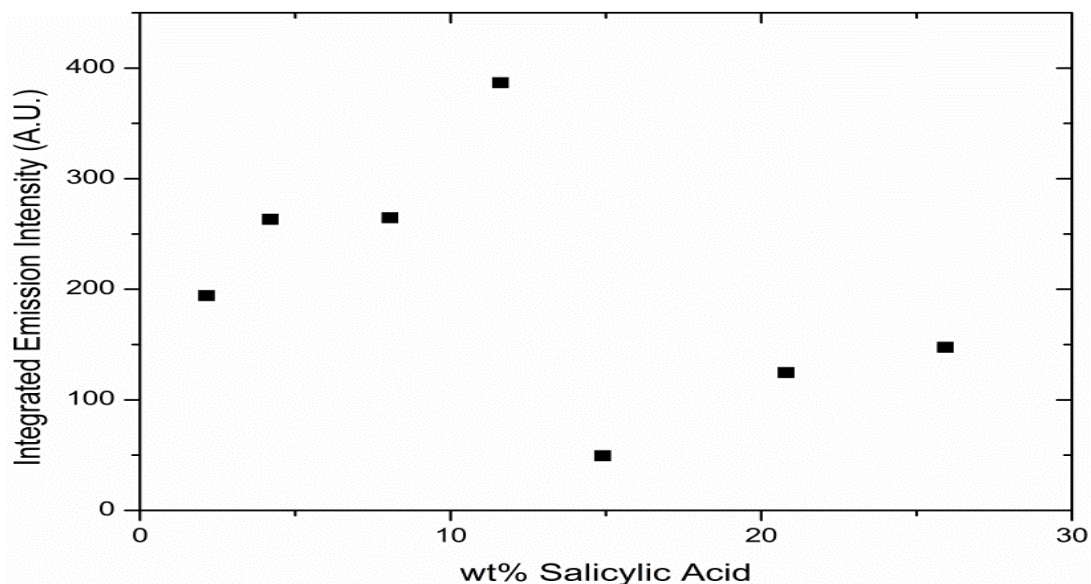
Figure 6.1-5 Integrated fluorescence emission intensity as a function of wt% HSal.

6.1.5.2 Scintillation Responses

Calibration of scintillation responses was accomplished by using the responses of GS20 lithiated glass. It is known that GS20 glass emits 6250 photons per neutron capture event. In our setup, the neutron peak for GS20 glass was located at channel 7390. These values permit calibration of absolute light yields by using the relationship shown below. The value 0.846 photons/channel can be used as a conversion factor to convert channels to photons in our configuration.

$$\frac{6250\ photons/neutron}{7390\ channels/neutron} = 0.846\ photons/channel$$

Scintillation responses were obtained for a film approximately 200 μm thick cast onto an acrylic disk. This thickness was chosen in order to reduce the sensitivity to gamma-rays relative to charged particles resulting from ^{6}Li fission. The alpha response from ^{241}Am is shown in Fig.

6. The peak is at channel 441. Multiplying this value by 0.846 photons/channel gives 373 photons, indicating that an average of 373 photons are collected from each alpha event. The beta response from ^{36}Cl is shown in Fig. 7. The spectral average is at channel 165 and the endpoint is at channel 310, indicating that an average of 139 photons are collected per beta event and a maximum of 262 photons are collected per beta event. It is difficult to estimate a pulse height deficit for this material from this data because the film of interest was fabricated to be 200 μm thick which is thick enough to stop the alpha particles but not thick enough to permit complete energy deposition from the ^{36}Cl beta particles.

The responses to thermal neutrons and to gamma-rays are shown in Figs. 8 and 9, respectively. The thermal neutron peak is at channel 434, indicating that the material emits approximately 367 photons per neutron capture event. The intrinsic efficiency for gamma-rays reaches 10^{-6} at channel 369. Setting a lower level discriminator at this channel and discarding all signals below it enables the possibility of eliminating any signal that would occur from 99.9999% of the incident gamma-rays. Above this discriminator setting, the film gives 12.4 counts per second for thermal neutrons, indicating that this material can be used for thermal neutron detection in the presence of a strong gamma-ray field by using only pulse height discrimination techniques.
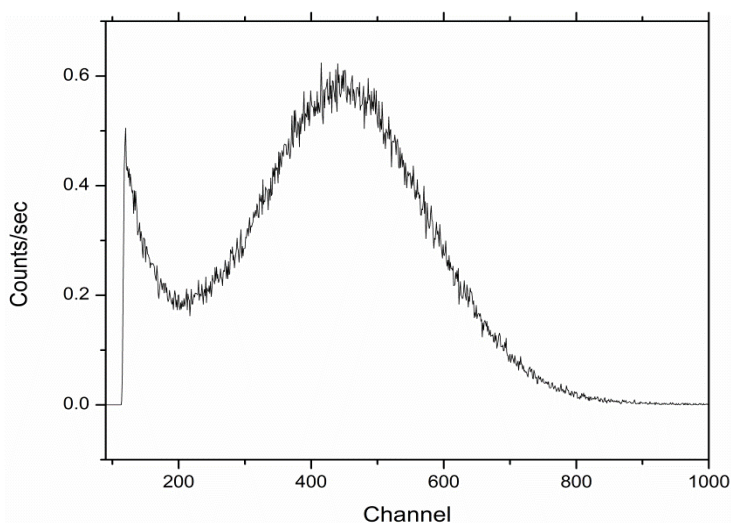
Figure 6.1-6 ^{241}Am alpha response. The peak is at channel 441, indicating that the material emits an average of 373 photons per incident alpha particle. The count time was 600 seconds.
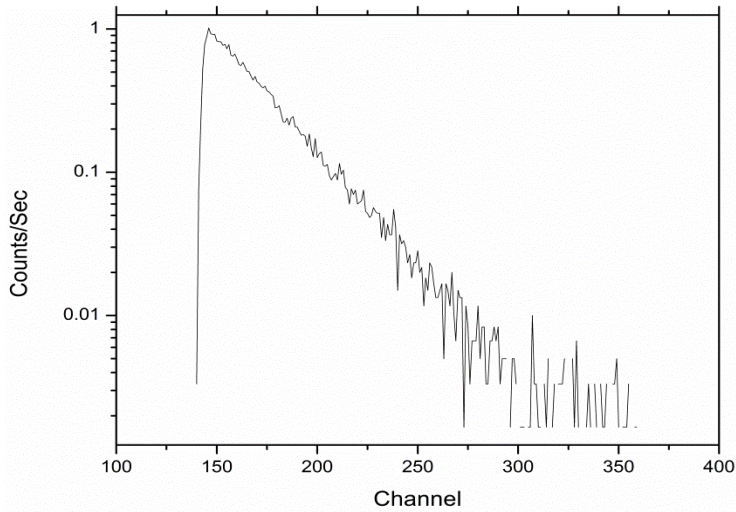
Figure 6.1-7 ^{36}Cl beta response. The y-axis is on a log scale to improve the visibility of the endpoint.

The spectral average is at channel 165 and the endpoint is at channel 310, indicating that the material emits an average of 139 photons and a maximum 262 of photons per incident beta particle. The count time was 600 seconds.
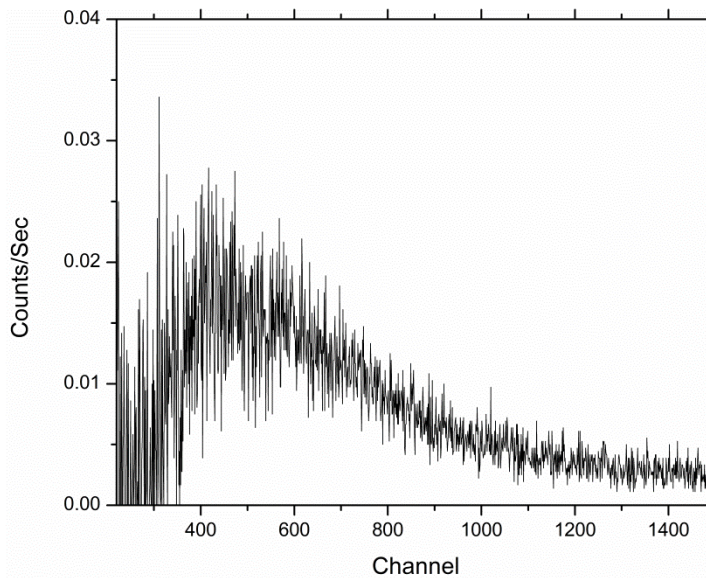
Figure 6.1-8 ^{252}Cf thermal neutron response. The peak is at channel 434, indicating that the material emits an average of 367 photons per captured neutron. The count time was 3600 seconds.
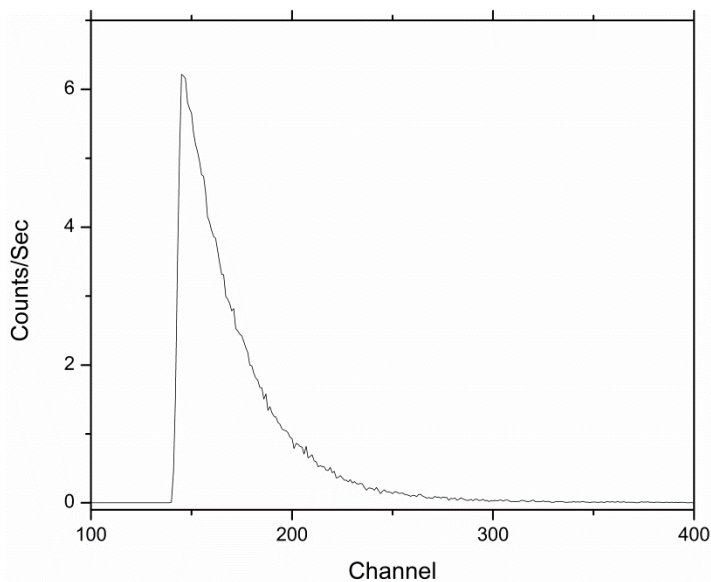
Figure 6.1-9 ^{60}Co gamma-ray response. The intrinsic efficiency for gamma-rays decreases to 10^- ^{6} at channel 369. The count time was 600 seconds.

6.1.6 Conclusions

The application of a new copolymer to the field of scintillation materials has resulted in an optically transparent water-soluble ^{6}Li loaded polymeric thermal neutron scintillation detector. A novel, robust, and repeatable synthesis procedure for PS-*co*-PLiMAn containing 3.85% ^{6}Li and HSal is reported. Photoluminescence measurements indicate that incorporation of 11.7% HSal into the polymer results in the optimum emission characteristics, presumably due to the formation of LiSal. The average light yield of a 200 μm thick film was 373 photons per alpha particle (^{241}Am), an average of 139 photons and a maximum of 262 photons per beta particle (^{36}Cl), and 367 photons per thermal neutron capture event. The low sensitivity to gamma-rays indicates that the material can be used for thermal neutron detection in the presence of a strong gamma-ray field using only pulse height discrimination methods.

6.2 Synthesis of Lithium Fluoride Particles

This section, Section 6.2, discusses a project regarding the synthesis of lithium fluoride particles for incorporation into a variety of plastic matrices. This work was performed jointly with Rohit Uppal, Idraneel Sen, Stephen Young, and Dr. Dayakar Penumadu.

As discussed in the CRP, another focus of work would be the synthesis of lithium fluoride (LiF) particles that were 450 nm or less in order to be incorporated into polymer matrices, such as polystyrene (PS) or poly (ethylene naphthalate) (PEN). The following section is a discussion that provides the synthesis methods and SEM imaging of the resulting particles. After preparation of these particles, it was found that they could not readily be dispersed into the PS matrix, since this material is produced using a solution casting method as discussed in Section 6.3.

These particles were, however, readily dispersed into the PEN matrix, since it is made through melt processing, fiber processing, and other heat-based methods. The work described below was performed in conjunction with Stephen Young and Rohit Uppal and will be submitted for review.   The following discusses the varying methods that were used to produce lithium fluoride for ease of dispersion into the PEN matrix.

The following report is an attempt to provide all of the experimental details and results associated with the synthesis of very small (>300 nm) LiF particles. The purpose of this set of experiments was to determine the effect of surfactant and solvent upon the size of the particles. The following surfactants were tested with acetone as the solvent: 1) Sodium Dodecyl Sulfate,

2) Sodium Dioctyl Sulfosuccinate, 3) Cetyl Trimethylammonium Chloride. Dr. Sen had the original idea of using acetone as the solvent, it was tested with the aforementioned surfactants.

The need for small lithium fluoride particles is important when attempting to load thin film plastics, such as polystyrene (PS) and polyvinyl toluene (PVT), with lithium fluoride. The smaller particle allows for greater transparency, thus will improve the light output due to a decrease in Rayleigh and Mie scattering inside the sample.

After initial results to make particles of LiF on the order of 200-300 nm was successful on a small scale (1-30 mg of LiF) using acetone as a solvent, it became necessary to change solvents to THF (tetrahydrafuran); PS and PVT are not easily dissolved in acetone, but are easily dissolved in THF. Thus later experiments attempted to modify the size of the particles using THF as the solvent. The following experiments produced mixed results, and when a polymer (such as PS) was added to the reaction vessel, the particles agglomerated to a larger size. Due to the agglomeration, work in this area was discontinued. However, using hot-press melting methods, it might be possible to overcome this agglomeration issue.

6.2.1   Synthesis Standard Titration

In a teflon beaker, 4.5872 g of $6LiOH \cdot H2O$ was dissolved in 50 mL deionized water with stirring and heated to 80°C. A volume of 3.9696 mL 48% HF was diluted to 20 mL with deionized water and added to the LiOH solution until pH = 7. The white precipitate was collected by vacuum filtration, washed with deionized water, then dried. The mass of the collected LiF was 2.451 g to give a percent recovery of 89.73%.

6.2.2   Characterizations

6.2.2.1   Scanning electron microscopy

A scanning electron microscope image of the resulting particles is shown in Fig. 1 below. Particle sizes were Mean = 2.6 µm, Range = 1.2 µm – 3.5 µm.
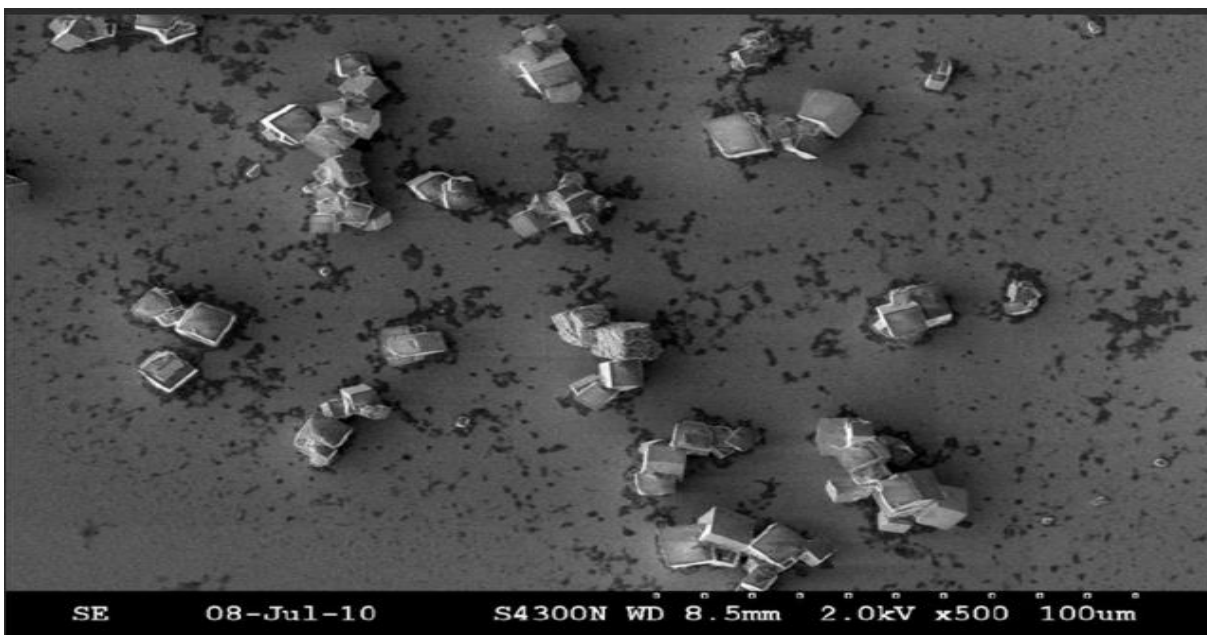
Figure 6.2-1 SEM image of Lithium Fluoride particles synthesized by simple titration

6.2.2.2 *Powder X-ray Diffraction*

X-ray powder diffraction of the particles was taken to determine crystallinity. The resulting diffraction pattern (Fig. 2) was analyzed using the HighScore ® software. Peaks at 38.5, 44.8, 65.3, 78.5, and 82.8 are in agreement with values reported in the literature for LiF.
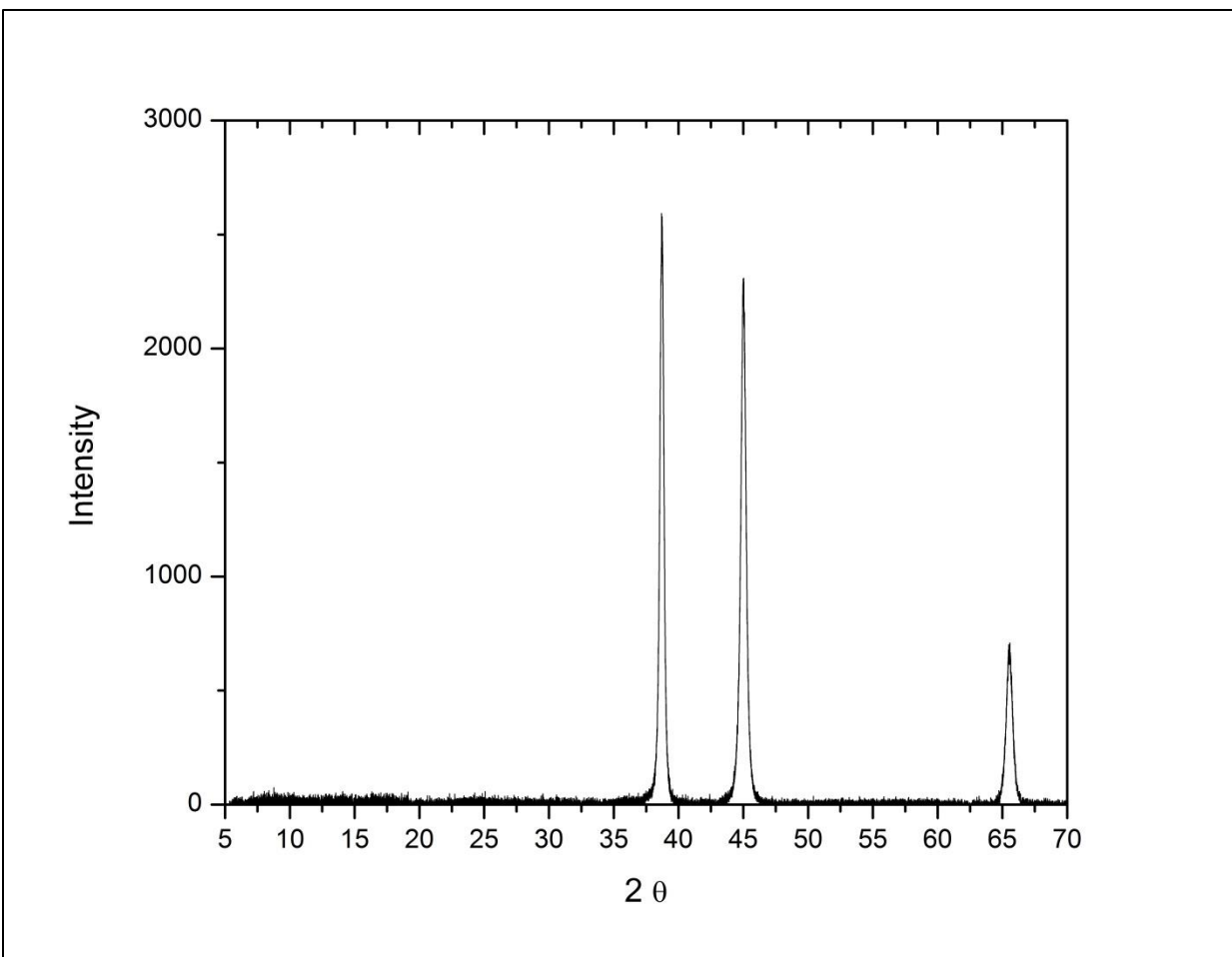
Figure 6.2-2 P-XRD results for LiF particles synthesized by simple titration.

6.2.2.3   Conclusions

When synthesized by standard titration, LiF forms cubic particles with sizes Mean = 2.6 μm, Range = 1.2 – 3.5 μm. This method would not be used to produces particles of 200-300 nm.

6.2.3   Synthesis Stragegy 2: Addition of Excess HF and Quenching (July 8, 2010)

In a teflon beaker, 500 mg of 6LiOH · H2O was dissolved in 14.2 mL of water with stirring. A volume of 819 μL of HF (48% in H2O) was then added to the solution to bring the pH to 2.2. The reaction was permitted to proceed for 10 seconds, then the solution was filtered

by vacuum filtration using Fisher Scientific P8 filter paper, washed with DI water, and air-dried on a vacuum filter. When the solution was poured through the filter, very little material was collected on the filter paper and the solution that went through the paper was still cloudy. Upon a second filtration, using Fisher Scientific Q2 paper, very little material was collected and the solution that went through the filter paper was still cloudy. The cloudy solution was collected and the solvent was evaporated under vacuum at 75°C. The resulting solid material was brown, indicating that the HF had attacked the glass evaporation dish and liberated poisonous brown SiF_4 gas. This process was repeated, but the reaction was quenched by pouring it into 45mL of acetone after 5 seconds. The solvent was evaporated in a Teflon dish, then the material was dried at 90°C under a vacuum.

6.2.4 Characterizations

6.2.4.1 Scanning electron microscopy

An SEM image of the resulting particles is shown in Fig. 3 below. The particle size distribution was bimodal. Larger particles were in the range of 1.5 µm – 3.3 µm; smaller particles were in the range of 104 nm – 700 nm.
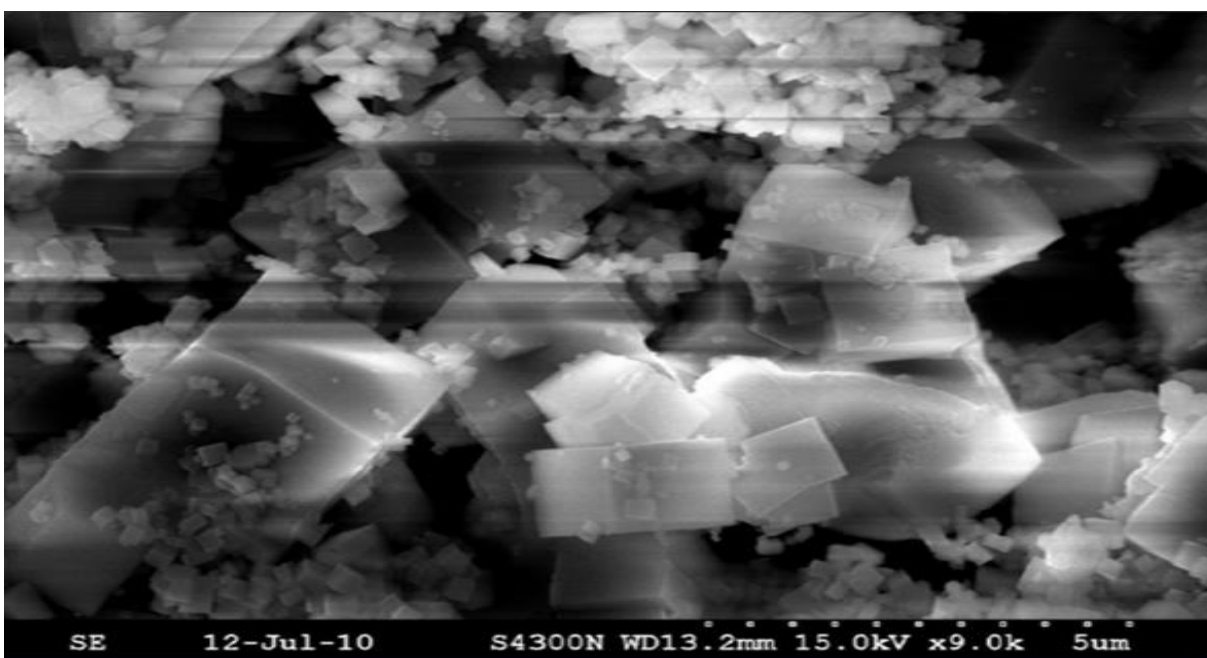
Figure 6.2-3SEM image of lithium fluoride synthesized by using excess HF and quenching the reaction after 5 seconds.

A small amount of the LiF particles were dissolved by heating in THF, then the solvent was evaporated. An SEM image of the resulting particles is shown in Fig. 4 below. The smaller particles are now absent, but the large particles are still present. This indicates that Ostwald ripening has occurred, in which the smaller particles dissolve and deposit onto the larger particles. Particle sizes were in the range 1.2 µm – 3.0 µm.
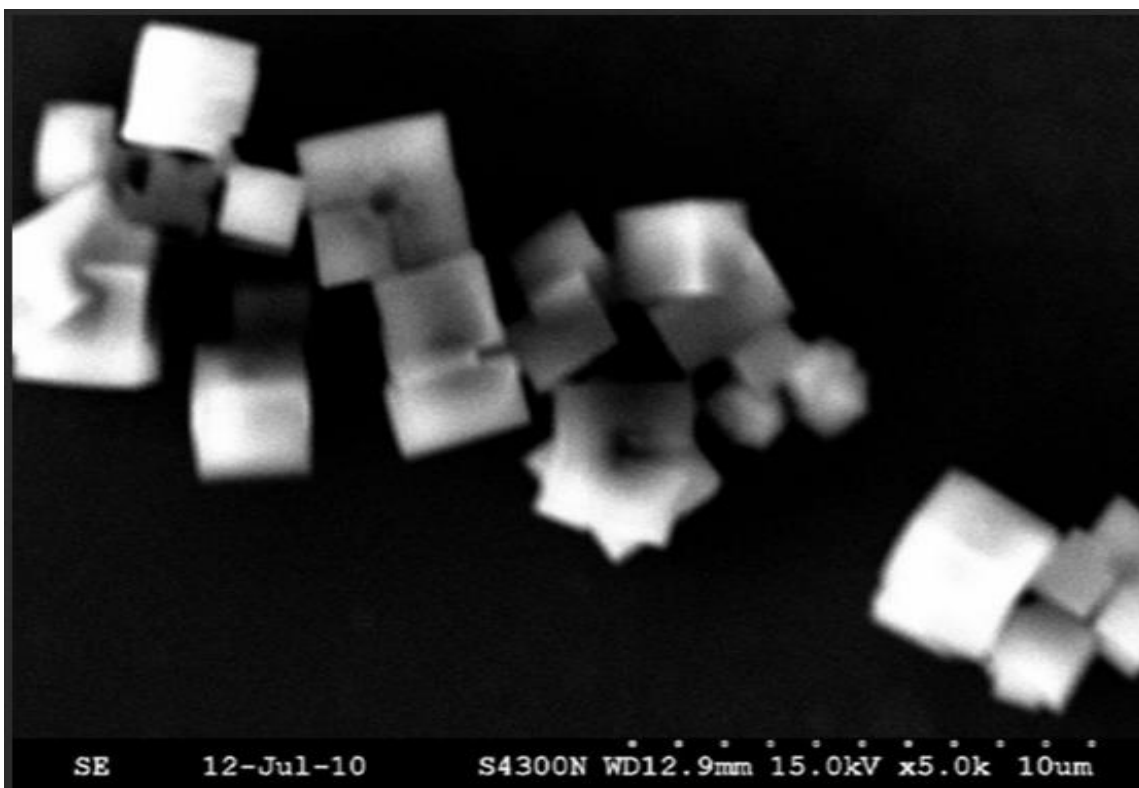
Figure 6.2-4 Lithium fluoride particles after dissolution in THF. Size: 1.2 – 3.0 μm. The disappearance of the smaller particles indicates Ostwald ripening has occurred.

6.2.5   Conclusions

Average particle size can be reduced by using excess HF and quenching the reaction after 5 seconds by pouring it into acetone. Dissolution in THF results in Ostwald ripening and the average particle size becomes approximately the same as the simple titration method. This indicates that the nanometer-sized particles are not thermodynamically stable relative to the

micron-sized particles. Thus, it may be necessary to use an appropriate surfactant to reduce the surface energy of the smaller particles and prevent dissolution.

6.2.6   Synthesis Strategy 3: Sodium Dodecyl Sulfate

A mass of 3.0137 g LiOH · H_2O was dissolved in 15 mL deionized H_2O with stirring at 80ºC. The solution was filtered using a 400 nm filter then 9.3 mg sodium dodecyl sulfate was added. A mass of 2.98 g HF(aq) was added to 50 mL acetone. The HF/acetone solution was then added to the LiOH/surfactant solution until pH = 6 to precipitate LiF. The resulting suspension was filtered using a 200 nm nylon filter to collect the particles.   The resultant was collected at 3 separate times, with the solution being filtered through Whatman qualitative grade filter paper having a pore size of 200 nm. The first aliquot was collected after 1 mL of solution had been passed through the solution, where the filter paper was set aside for SEM imaging. The process was repeated for aliquot volumes of 2 mL and 5 mL of solution. The resulting SEM images are shown in the following figures.

The percent yield and total mass was not calculated, as not all of the particles were harvested from the filter, the mass would have been difficult to determine. This procedure was repeated and similar results were obtained.

6.2.7   Characterizations

6.2.7.1   Scanning electron microscopy

Characterization with scanning electron microscopy was used to determine particle size and shape. Particle size statistics are: Mean = 115 nm, Range = 37 nm – 212 nm, Standard deviation = 46 nm. The particles are primarily cubic.
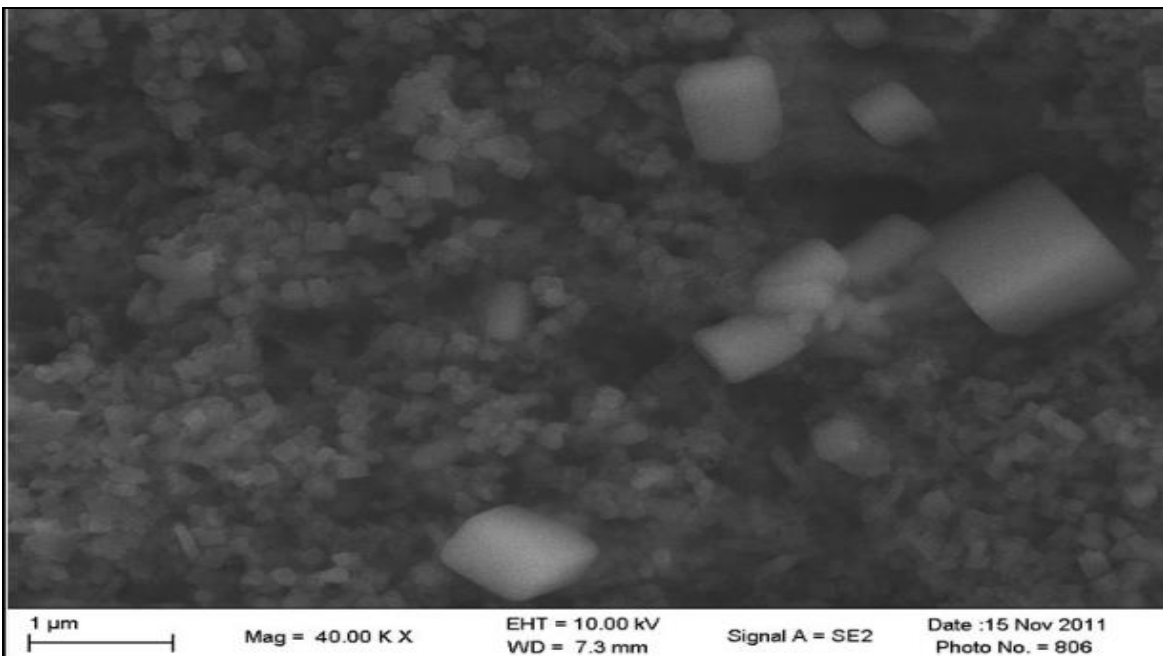
Figure 6.2-5 SEM images of particles collected after 1 mL of solution was filtered.
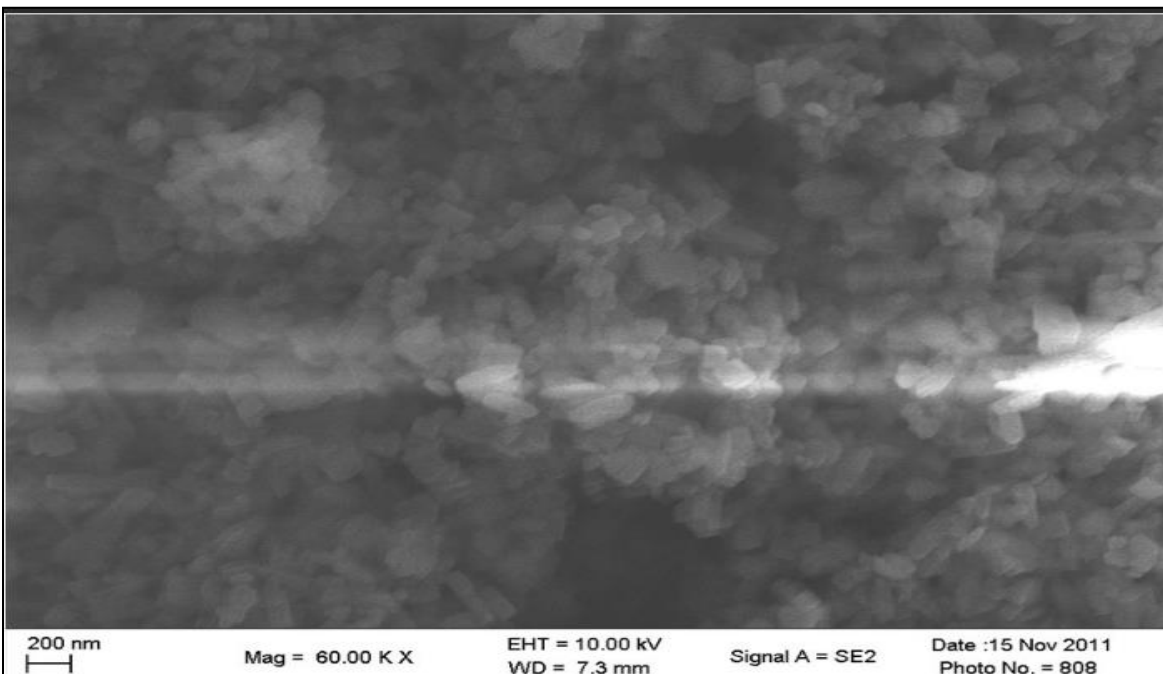
Figure 6.2-6 SEM image of particles collected after 2 mL of solution was filtered.
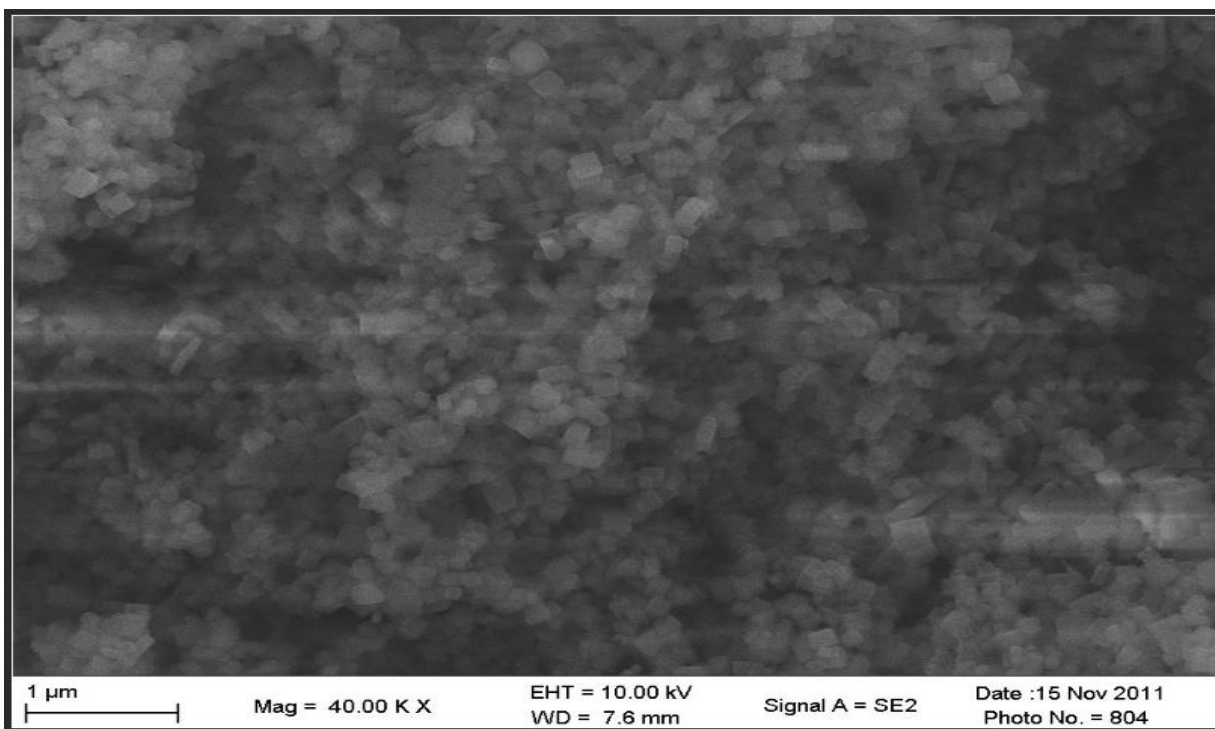
Figure 6.2-7 SEM Image of particles collected after 5 mL solution was filtered.

The mean particles size (with the exception) of some very large particles, appears to be between 200 and 300 nm.

6.2.7.2   X-ray powder diffraction

X-ray powder diffraction was performed on the particles to confirm the identity and provide another measurement of particle size. Average particle size obtained by XRD and 157 nm, as determined using the Scherrer equation.

6.2.8   Conclusions

The presence of sodium dodecyl sulfate and acetone affected the final particle size. It is thought that the factors involved could be one or a combination of the following: 1.) Presence of surfactant, 2.) Presence of Na+ on the surfactant, 3.) Concentrations of Li and surfactant, or 4.) Presence of acetone

Strategy 4: Sodium Dioctyl Sulfosuccinate with Acetone

6.2.9 *Synthesis Strategy 4: Sodium Dioctyl Sulfosccinate with Acetone*

The synthesis method as used in the previous section was used, and the procedure was scaled back a factor of 10. A solution was made using a mass of 0.2978 g of LiOH and 2.6 mg of surfactant in 25 mL of DI water was used. This was titrated with a solution of 0.300 mL of HF in 5 mL of acetone. The solutions were stirred vigorously and the HF/acetone was added in 200 uL amounts until 2 mL had been added. The cloudy solution was filtered through a 200 nm filter, however only SEM characterizations were performed.

6.2.10 *Characterizations*

6.2.10.1 *Scanning electron microscopy*

After 2 mL of the cloudy solution was passed through the 200 nm Whatman filter paper, the following SEM images were obtained.
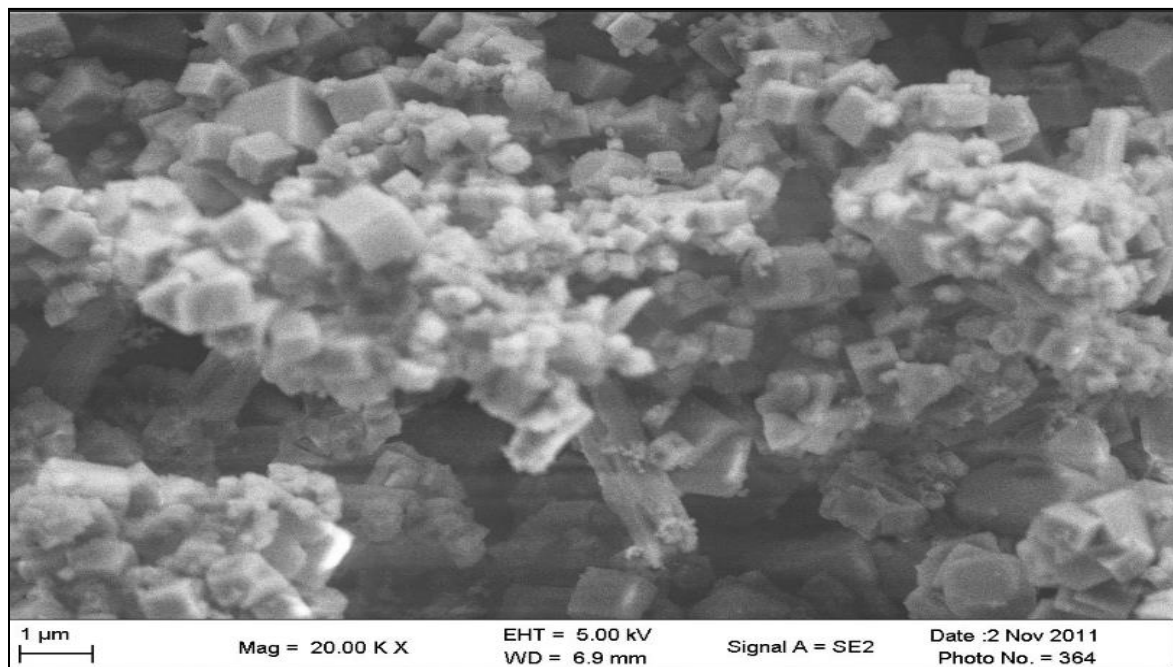
Figure 6.2-8 SEM Image of LiF particles produced using Sodium Dioctyl Sulfosuccinate
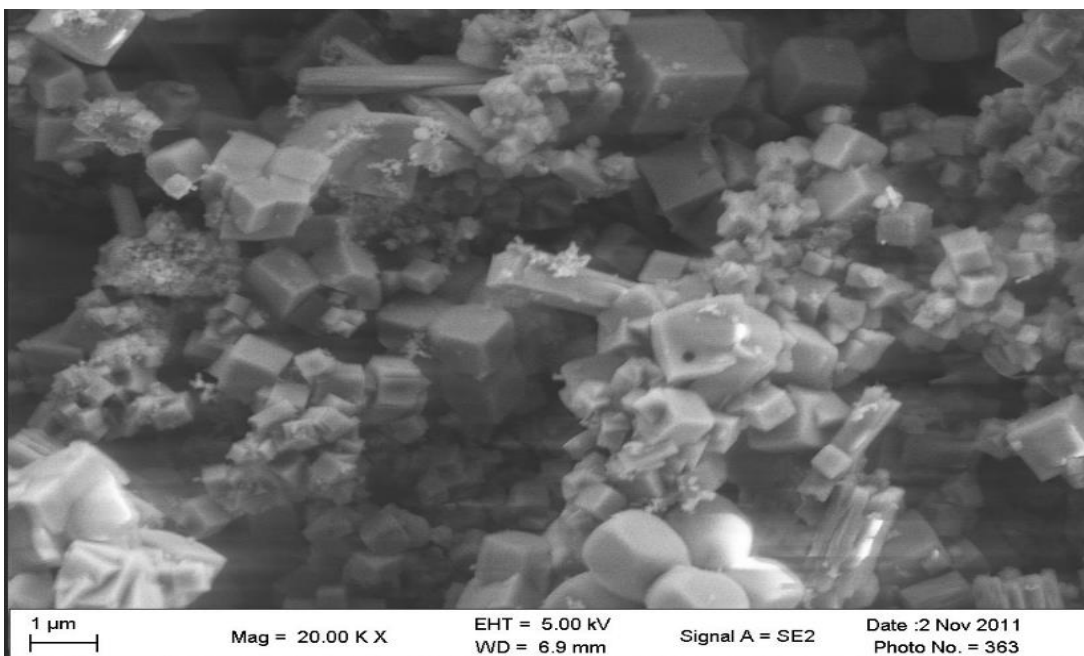
Figure 6.2-9 SEM image of LiF particles produced using Sodium Dioctyl Sulfosuccinate.

6.2.11   Conclusions

The results from this method were not as good as those obtained from using the Cetyl Trimethylammonium Chloride with acetone (see section 5) or the results obtained from using the sodium dioctyl sulfosuccinate with acetone (see section 3).

6.2.12 Synthesis Strategy 5: Cetyl Trimethylammonium Chloride

A mass of 292.6 mg LiOH was dissolved in 25 mL deionized water at 80ºC while stirring the solution. After dissolution, 4.83 g cetyl trimethylammonium chloride was added. A solution of 250 μL HF in 5 mL acetone was added to the solution. After addition of 1 mL HF/acetone, 1 mL of the solution was removed and centrifuged, the supernatant was decanted, then the resulting precipitate was stored in a vacuum oven at 60ºC at 125 Torr for 2 days. The remainder of the solution was filtered through a 200 nm filter to collect the precipitate. SEM image of the particles on the filter are shown in Fig. 10.

6.2.13 Characterizations

6.2.13.1 Scanning electron microscopy

SEM image of the resulting particles is shown in the Fig. 10 below. The particles are primarily cubic and in the micron size range. It is interesting to note that the cubic geometry is slightly different than previous samples. In these samples, there are pieces of the cubes missing either through the center or on the side of the particles. All pieces that are "missing" are rectangular in shape.
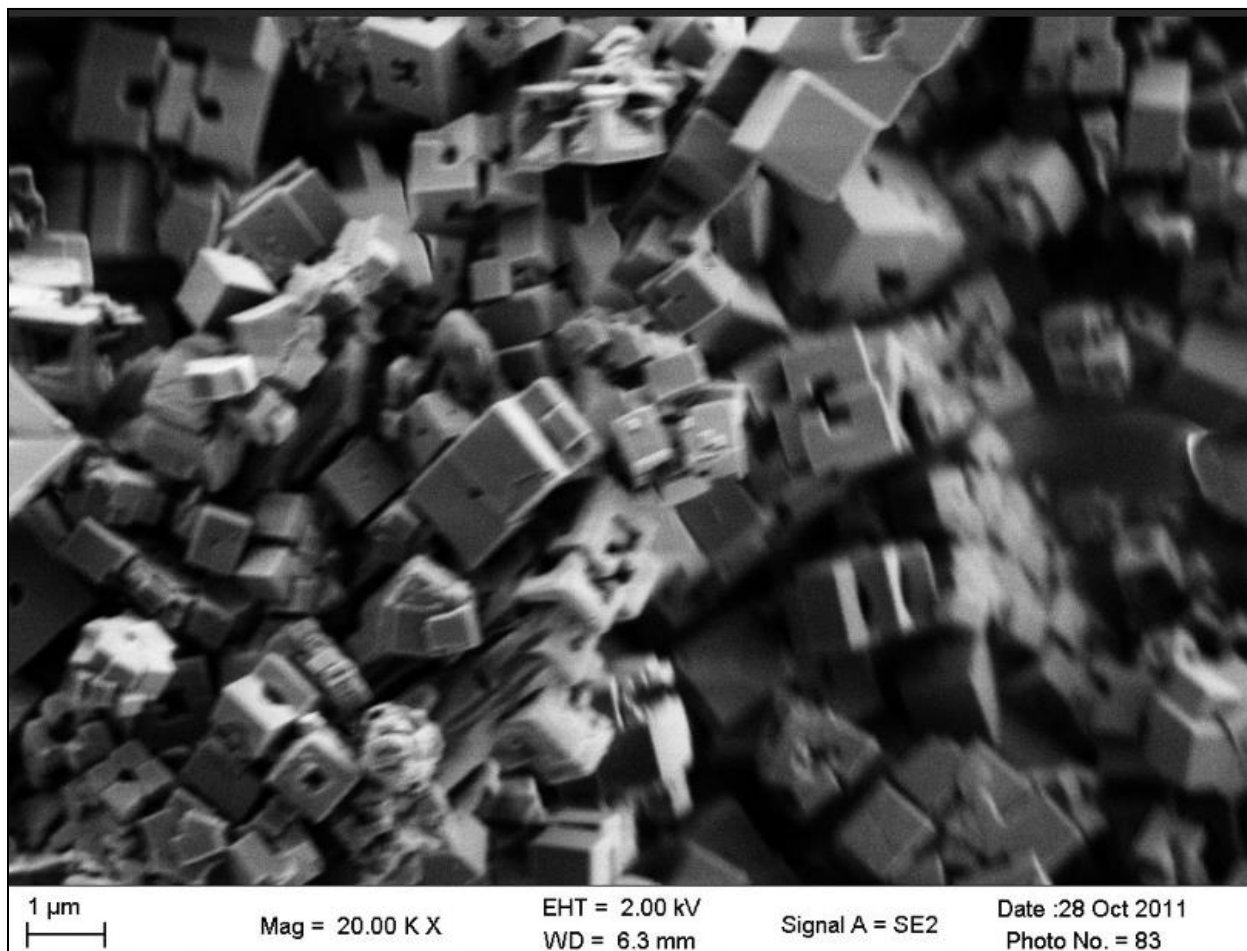
Figure 6.2-10 This image was taken on a 200 nm filter paper, and the surfactant was cetyl trimethyl ammonium chloride (CTA). The final pH was adjusted to 8, however this image was taken after only 1 mL of the HF soln was added.
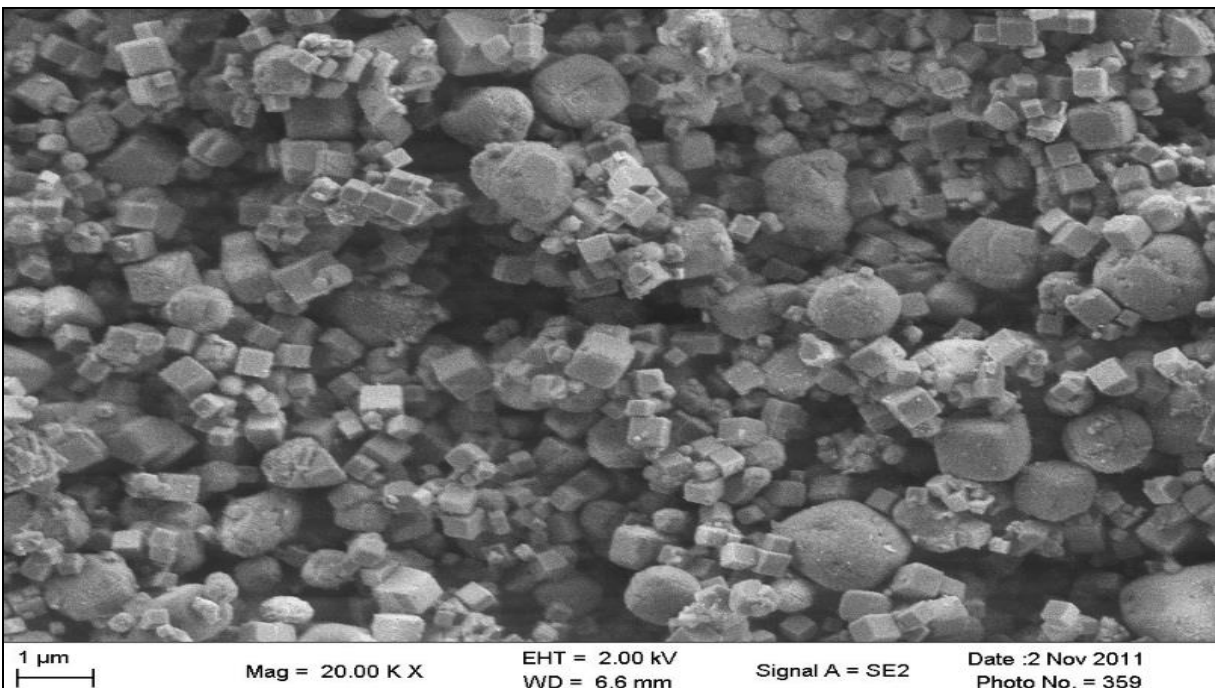
Figure 6.2-11 LiF particles on 200 nm filter paper after 2 mL of HF solution was added
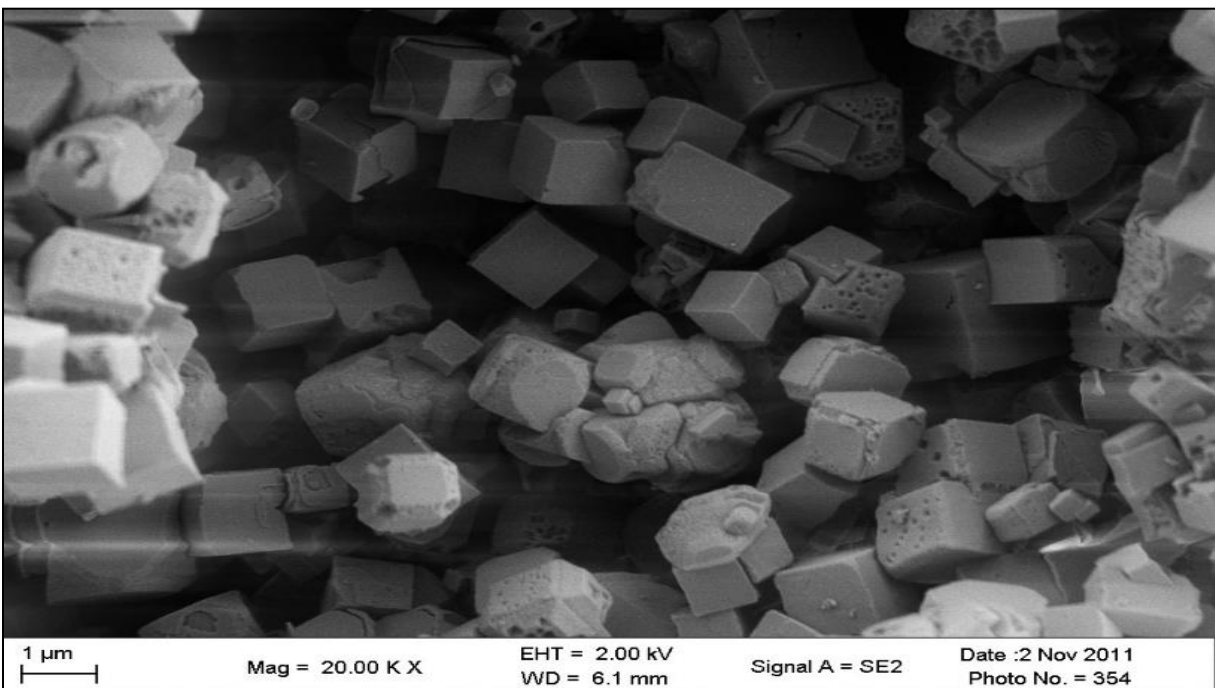
Figure 6.2-12 LiF particles on 200 nm filter paper after 5 mL of solution was added. Final pH =8.

From the above images, the sizes of the particles are clearly larger than the XRD data, which would indicate particle size of 70-80 nm. However, this may be a result were the particles are actually the 70-80 nm size. Due to agglomeration, however, the overall size is 1-1.5 μm. In Fig. 4-6, the "holes" or "pockets" in the crystals may be a result of the surfactant effects.

6.2.14 Conclusions

As confirmed by the SEM images, the Cetyl Trimethylammonium chloride did not interact with the LiF particles and the size is similar to that of the direct synthesis methods. This surfactant would not be used in future work.

6.2.15 Synthesis Synthesis 6: Use of Dioctyl Sodium Sulfosuccinate in THF

In a water solvent, 0.9647 g of dioctyl sodium sulfosuccinate (DSS) was added to 0.0986 g of LiOH, giving a 10:1 ratio of surfactant to LiOH. A 25 mL solution of HF (0.01208 g of 50% HF) and THF was also prepared. The DSS/LiOH/H_2O solution was added to the HF/THF solution in three separate additions. A 1 mL aliquot of the DSS/LiOH/H_2O solution was added and the solution was filtered through a 200 nm filter paper. The product and filter paper was analyzed with SEM. This procedure was repeated with a 3 mL and 5 mL aliquot, and all samples were analyzed with SEM.

6.2.16 Characterizations

6.2.16.1 SEM Imaging

The following SEM images, like the preceding figures, are of three separate filter paper samples after 1 mL of the LiOH/THF/Dioctyl Sodium Sulfosuccinate solution was added to the THF/HF solution.
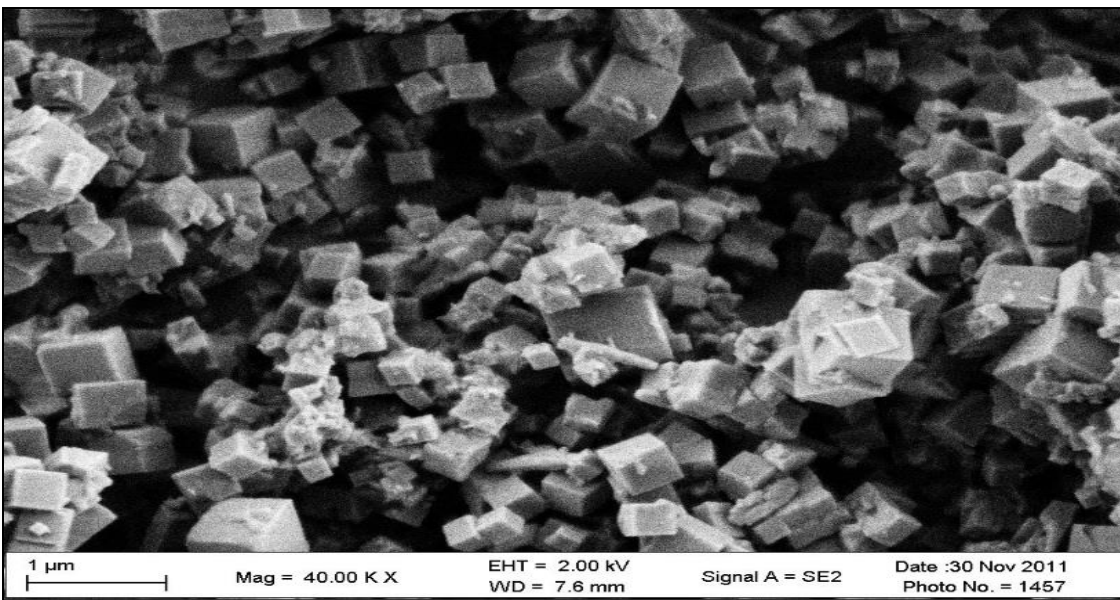
Figure 6.2-13 LiF particles on a 200 nm filter paper, after 1 mL of LiOH/THF/DSS is added to THF/HF solution.
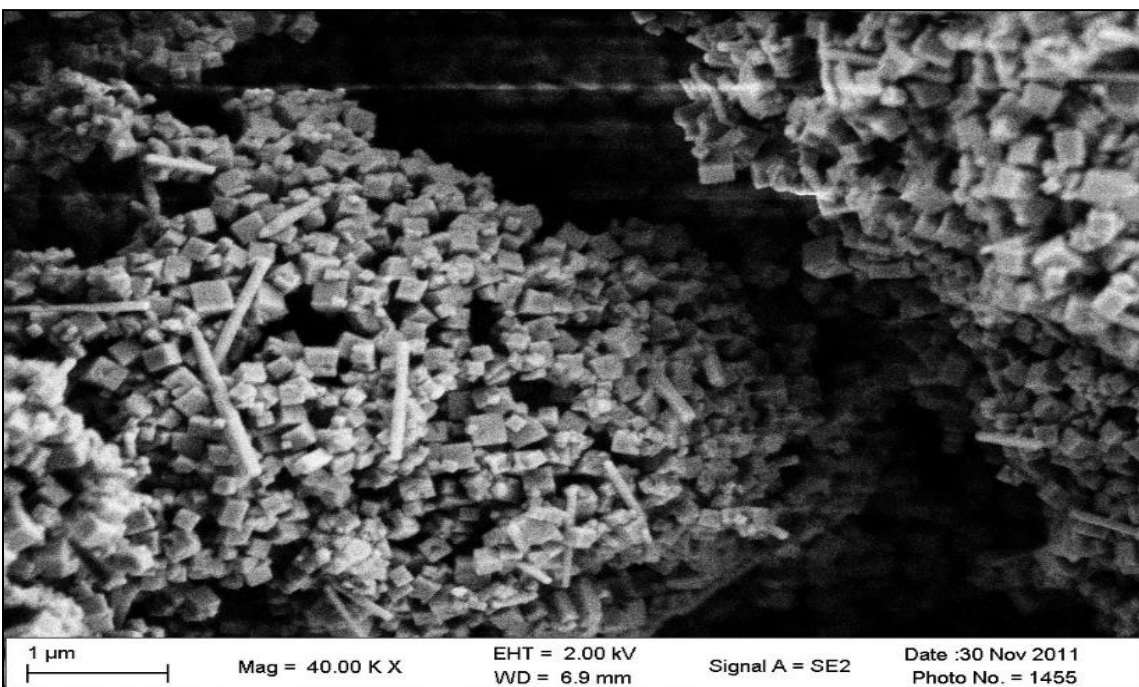
Figure 6.2-14 LiF particles on a 200 nm filter paper, after 3 mL of LiOH/THF/DSS is added to THF/HF solution.

6.2.17 Conclusions

Of all of the attempts, this process produced particles of the most consistent size range in a solvent that would be suitable for solution casting of polymer films. Futhermore, this synthesis method demonstrated that the surfactant had the largest effect upon the size of the particles and would be a suitable method for producing particles of >300 nm in size.

6.2.18 Synopsis

Based on the above conclusions, the effects of surfactant type and solvent system were explored, and the results indicated that Dioctyl Sodium Sulfosuccinate in THF produces small LiF particles. Unlike the acetone systems, all of the particles were similar in size, with no large particles observed in the system.

6.3 Thin Film Polymer Composite Scintillators for Thermal Neutron Detection

The final project discussed in my CRP was loading polystyrene (PS) samples with ^{6}LiF and casting the material as a film using a solution casting method. This project involved studying the effect to adding PPO/POPOP (2,5-diphenyloxazole/ 1,4-bis(5-phenyl-2-oxalozolyl)benzene), mixed at 97.13% PPO and 2.87% POPOP to the PS matrix to determine the effect of the loading of the fluor on light output. The project also explored the effect of loading the PS films with varying amounts of ^{6}LiF to determine the effect on optical clarity. Final experiments were involved with varying the thickness of the film to observe the effect on gamma-ray sensitivity. The results and discussion of Section 6.3 were submitted to the *Journal of Composites* for review, and a draft of the text is presented in the following section. This draft was co-authored with Andrew Mabe, Matthew Urffer, Stephen Young, Dr. Dayakar Penumadu, Dr. George K. Schweitzer, and Dr. Laurence F. Miller.

6.3.1 Introduction

The development of efficient thermal neutron detectors is relevant to the fields of nuclear physics, nuclear power generation, imaging, and homeland security. Helium-3 filled proportional counters are widely used in radiation portal monitors to detect illicit transport of fissile materials, in neutron scattering experiments, in medical imaging, and in well logging. Due to the recent expanded use and reduced production of He-3, the supply of He-3 dwindling such that the Department of Homeland Security has issued research funds to develop a replacement technology[1]. As described herein, efforts have been made to develop inexpensive and atmospherically stable polymeric composite materials to function as thermal neutron scintillation detectors that have low sensitivity to gamma irradiation.

The use of organic polymers as scintillators has many advantages over other scintillating materials such as single crystals and inorganic glasses in that selected polymers are air-stable, do not require high processing temperatures, have relatively low cost, are easy to fabricate in large areas in a wide range of geometries, and have fast response times[148]. Common commercially available polymeric scintillators are generally based on aryl vinyl polymers such as polystyrene (PS) and polyvinyltoluene (PVT). The aromatic pendant groups on these polymers have emission in the wavelength range 300 – 350 nm under both UV- and x-ray induced excitation[149], [150], so these polymers must be doped with wavelength shifters to shift the wavelength of scintillation to the region of sensitivity of common bialkali photomultiplier tubes (400 – 450 nm).

In order for organic polymers to function as thermal neutron detectors, they must be sensitized with neutron capture nuclides such as ^{6}Li, ^{10}B, or ^{157}Gd.[5] In this study, ^{6}Li was selected as the thermal neutron capture nuclide because of its large capture cross section (940 barns) and large reaction energy (Q = 4.78 MeV). On absorption of a thermal neutron, ^{6}Li fissions into an alpha particle (2.05 MeV) and a triton (2.73 MeV)[5]. These charged particles deposit their kinetic energy in the matrix primarily by Coulombic interactions with electrons to form ionizations and excitations. This energy is then harvested by antenna fluorophores and shifted to wavelengths suitable to be collected by a photomultiplier tube.

In our previous work, we evaluated poly(2-vinyl naphthalene) containing ^{6}lithium salicylate (^{6}LiSal) and conjugated organic dyes[7] and poly(ethylene naphthalate) containing

[6]lithium fluoride (^{6}LiF) and conjugated organic dyes[8] as potential thermal neutron detectors. In this study, ternary composite films comprising PS, ^{6}LiF, and glass-forming organic dyes were explored as potential thermal neutron scintillation detectors.

6.3.2 Materials and Methods

6.3.2.1 Component Selection

An ideal thermal neutron scintillation detector is stable in atmospheric conditions such that it is not significantly damaged through the course of common use. Incorporation of hygroscopic materials into a hydrophobic polymeric matrix causes water to be absorbed in the material which decreases the mechanical integrity of the composite over time. Many lithium salts are hygroscopic which sharply narrows the available lithiated materials that can be implemented as neutron sensitizers. In the present work, lithium fluoride was chosen because it is not hygroscopic, does not decompose in the presence of the atmosphere, is thermally stable, and is transparent in the wavelength region 300 – 450 nm. Moreover, it has an atom density of 6.117×10^{22} lithium atoms/cm^3 (corrected for 97.6% ^{6}Li enrichment) which is higher than most common lithium salts. Utilization of a higher atom density material decreases the volume fraction of neutron activator material required to achieve the desired neutron detection efficiency. PS was selected because it is commonly implemented as a matrix for polymer scintillators, it is comparably inexpensive, and it is easy to synthesize. ^{6}Lithium fluoride was synthesized in our laboratory rather than purchasing because the price of enriched starting materials is lower than that of the enriched lithium fluoride.

6.3.2.2 Materials

Lithium-6 hydroxide monohydrate enriched to 97.6% ^{6}Li was heated to 110°C for four hours to remove volatile impurities, dissolved in deionized water, and filtered with a 2.5 μm filter to remove insoluble impurities. The ^{6}Li/^{7}Li ratio was determined by QSTAR Mass Spectroscopy. Hydrofluoric acid (48%, Aldrich) and methanol (Fisher Scientific) were used without further purification. Tetrahydrofuran (Fisher Scientific) was fractionally distilled from calcium chloride immediately before use to remove water and butylated hydroxytoluene stabilizer. Styrene (Acros) was purified immediately before use by passing the monomer through a column containing activated basic alumina on top of silica gel to remove monomethyl ether of hydroquinone (MEHQ) inhibitor and other impurities. Free radical initiator 2,2'-

azobisisobutyronitrile (AIBN), obtained from Aldrich, was recrystallized from methanol immediately before use. A preblended fluor mixture comprising 2,5-diphenyloxazole (PPO) and 1,4-bis(5-phenyl-2-oxazolyl)benzene (POPOP) mixed as 97.13% PPO and 2.87% POPOP, obtained from Curtiss Laboratories, Inc., was used without further purification. This blend will be referred to as PPO/POPOP. Acrylic disks 3 mm thick with a diameter of 50.8 mm (Eljen Technologies) were cleaned with acetone immediately prior to use.

6.3.3   Synthesis

Lithium-6 fluoride was synthesized in a Teflon beaker by dissolving purified lithium hydroxide in deionized water and adding hydrofluoric acid until the solution was slightly acidic. The solution was stirred for 10 minutes to ensure no lithium hydroxide remained. The resulting precipitate was collected by vacuum filtration with a 2.5 µm filter, washed with deionized water to remove soluble impurities, then dried by washing with acetone. The resulting white powder was stored in a vacuum dessicator.

Polystyrene was synthesized by conventional free radical polymerization. Purified styrene (10 mL) and AIBN (60 mg) were placed in a vial containing a septum. The container was sealed, degassed three times with vacuum and argon, and placed in an oil bath at 90ºC to polymerize. After 60 hours, the resulting transparent polymer disk was dissolved in 150 mL purified tetrahydrofuran, precipitated by dropwise addition into 900 mL cold methanol, then collected by vacuum filtration and washed with methanol. The purified polymer was dried in air for at least 24 hours prior to use.

6.3.4   Film Casting

The compositions of interest, expressed in weight percentages, were 0% – 30% ^{6}LiF, 5% – 15% PPO/POPOP, and thicknesses over the range 15 µm – 2.6 mm. To fabricate film samples, measured amounts of PS, ^{6}LiF, and PPO/POPOP were placed in a small glass vial. Tetrahydrofuran (2.5 mL) was added and the solution was heated to 60ºC for 20 minutes to dissolve the polymer and fluors, then sonicated to suspend the ^{6}LiF. Each sample was then cast onto an acrylic disk, covered with a beaker to slow evaporation rate and prevent dust contamination and crazing due to drafts, then dried for 24 hours to give films of varying translucency as shown in Fig. 1. Samples were characterized without removal from the acrylic

disk to prevent stress crazing and mechanical failure of the film, to facilitate coupling to the photomultiplier tube, and to prevent direct contact of the material with optical grease.

Images demonstrating the relative optical clarity of some of the samples are shown in Fig. 1. At a constant concentration of [6]LiF, thicker samples are less transparent than thinner samples. Increasing the concentration of [6]LiF decreases the optical clarity as would be expected due to the difference in refractive index between the [6]LiF and the PS. This decrease in transmission is more highly dependent on the concentration of [6]LiF in thicker samples than in thinner samples. The 15 µm thick samples do not show much change in transmission over the concentration range of [6]LiF studied. The morphology and size distribution of the [6]LiF particles in the composites were examined by a Leica SP2 confocal laser-scanning microscope (CLSM) equipped with a 488 nm argon ion laser to probe the distribution of the particles in the interior volume of the sample. Image processing and measurements were performed with ImageJ software. Cubic [6]LiF particles with a mean size of 3.2 µm are clearly visible in the image. Several images in different places of the sample were obtained. The images demonstrate that the particles are randomly distributed in the matrix and not agglomerated.
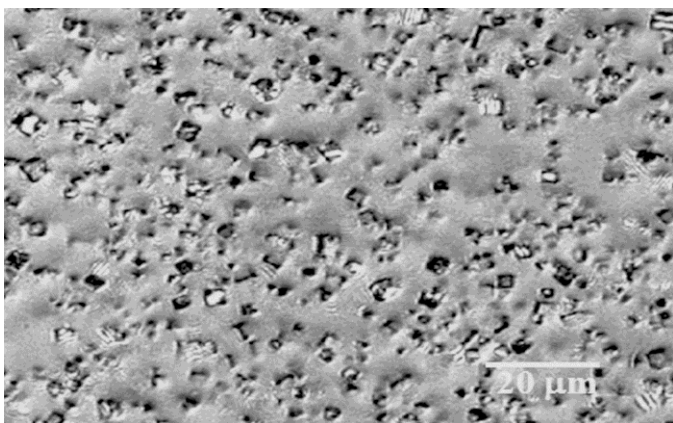
Figure 6.3-1 Bright-field CLSM image of [6]LiF particles distributed in a PS matrix. Mean particle size = 3.2 µm, range = 1.6 – 5.3 µm. The scale bar is 20 µm.
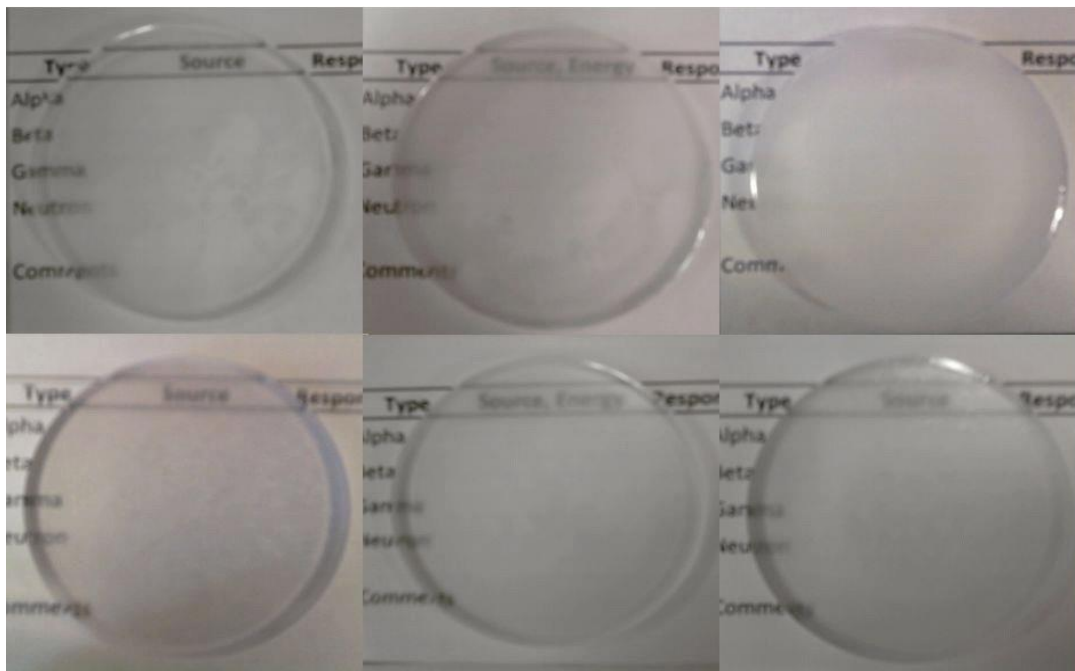
Figure 6.3-2 Representative images of PS composites containing ^{6}LiF and PPO/POPOP. Top row: Samples with varying thicknesses containing 20% ^{6}LiF and 5% PPO/POPOP. Left to right: 25 μm, 50 μm, 150 μm. Bottom Row: 15 μm samples containing 5% PPO/POPOP and varying concentrations of ^{6}LiF. Left to right: 10%, 20%, 30%.

6.3.5 Characterizations

Fluorescence measurements were conducted using a HORIBA Jobin Yvon Fluorolog-3 spectrofluorometer equipped with a 450 W Xe lamp as the excitation source. Both emission and excitation spectra were collected with 1 nm spectral bandwidth.

Scintillation measurements were conducted as previously described [8]. Briefly, samples cast on acrylic disks were coupled to a photomultiplier tube using optical grease with the sample side facing away from the PMT, then covered with a Teflon tape reflector. A moderated mass of 0.59 μg ^{252}Cf was used as the neutron source. Thermal neutron response was determined by first irradiating the sample inside an acrylic tube surrounded by lead to obtain the scintillation response to gamma rays and all neutrons. The sample was then irradiated in an acrylic tube surrounded by a 1.6 mm thick sheet of cadmium to shield thermal neutrons and measure the response to gamma rays and fast neutrons. Spectral subtraction was then used to obtain the net thermal neutron response. The alpha and beta responses were measured with an ^{241}Am source and a ^{36}Cl source, respectively. The peaks were recorded for the alpha responses

and the end points were recorded for the beta responses. Gamma responses were obtained using a 1 μCi ^{60}Co source. The light pulses from the samples were converted into electrical pulses using a Philips 2202B PMT mounted on a Canberra 2007P base powered by an ORTEC 556 high voltage power supply set at 1200V. The signals from the base were amplified using an ORTEC 572A amplifier set at 50G with a 2 μs shaping time. The amplified signal was digitalized using an ORTEC 926 MCB with an 8192 channel ADC. The digitalized output was then saved using the MAESTRO-32 software from ORTEC.

6.3.6   Results and Discussion

6.3.6.1   Fluorescence Characterizations

A typical normalized fluorescence spectrum of a sample containing PS, ^{6}LiF, and PPO/POPOP is shown in Fig. 3. The wavelength of maximum excitation (λ_{ex} = 274 nm) is characteristic of PS excitation. The wavelength of maximum emission (λ_{em} = 421 nm) is characteristic of POPOP emission. A photophysical mechanism for the possible routes of excitation enegy migration is shown in Scheme I, where φ_f is quantum efficiency of fluorescence[151], λ_i represents a photon with a wavelength characteristic of the process, and * indicates an electronically excited state. First PS is excited at 274 nm. Ideally, the excitation energy is harvested nonradiatively from PS by PPO, which then emits a photon with 100% quantum efficiency. This photon is then absorbed by POPOP and reemitted at 421 nm with a quantum efficiency of 93%.

<p align="center">Possible Mechanisms of Excitation Energy Transport</p>

1) *Excitation of Matrix*
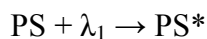
   $PS + \lambda_1 \rightarrow PS^*$

2) *Matrix Relaxation*

   $PS^* \rightarrow PS$

   $PS^* \rightarrow PS + \lambda_2$ $\qquad\qquad$ (φ_f = 0.16)

   $PS^* + PPO \rightarrow PS + PPO^*$

3) *PPO Excitation*

$PS^* + PPO \rightarrow PS + \quad PPO^*$

$PPO + \lambda_2 \rightarrow PPO^*$

4) *PPO Relaxation*

$PPO^* \rightarrow PPO + \lambda_3$ $\qquad (\varphi_f = 1.00)$

5) *POPOP Excitation*

$\lambda_3 + POPOP \rightarrow POPOP^*$

6) *POPOP Relaxation*

$POPOP^* \rightarrow POPOP$

$POPOP^* \rightarrow POPOP + \lambda_4$ $\quad (\varphi_f = 0.93)$
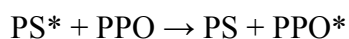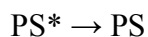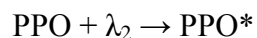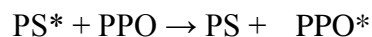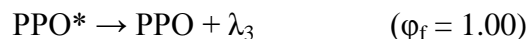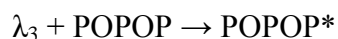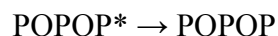
The efficiency of excitation of PS is dictated by the extinction coefficient at the wavelength of maximum excitation which is an intrinsic property of the material. After the PS is excited, there are three competing processes that determine the fate of the excitation energy: The excited monomer unit can 1) be quenched internally, 2) emit a photon at λ_2 (excimer emission), or 3) transfer the energy to PPO. Transfer of excitation energy between PS and PPO occurs by both radiative and nonradiative mechanisms; the fraction of nonradiative transfers increases with increasing concentration of PPO[152].
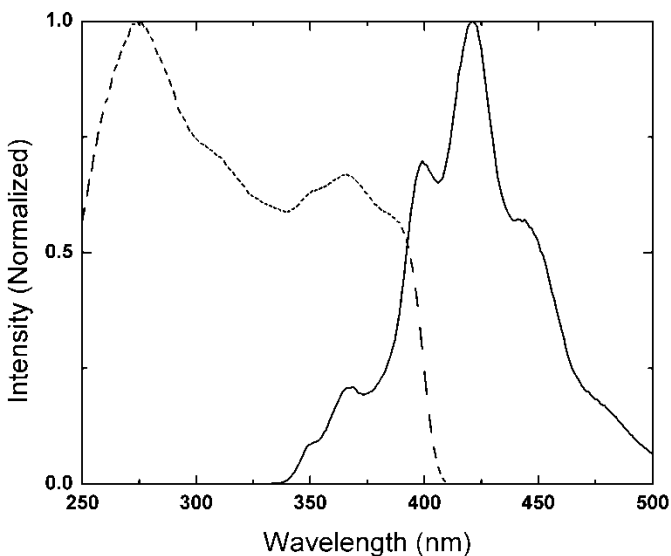
Figure 6.3-3 Excitation (– –) and emission (—) spectra of a typical sample. Spectra are normalized to maximum peak intensities.

Before incorporation of ^{6}LiF in the matrix, it was first necessary to optimize the concentration of PPO/POPOP to maximize the light yield. Fluorescence spectra of PS containing varying concentrations of PPO/POPOP (Fig. 4) were analyzed to determine the concentrations most suitable for use in these samples.

To maximize the light yield, it was first necessary to ensure that the maximum amount of excitation energy is harvested from PS. By measuring the excitation intensity that results in emission from PS (314 nm) as a function of PPO/POPOP concentration, the concentration at which no PS emission is observed can be determined. This should be the concentration where transfer to PPO should be optimum and no light is lost as emission from PS. The data in Fig. 4 show that the emission from PS decreases rapidly with the addition of low concentrations of PPO/POPOP. At 1.5% the emission from PS is reduced by approximately 96%.

The concentration at which sufficient antenna molecules are present to harvest the excitation energy from PS such that no emission from PS is observed should be optimized for use as a scintillation composition. However, considering that quantum efficiency of a pure PS film is about 0.16, it is possible that more excitation energy can be collected by further

129

increasing the concentration of the antenna molecule. To confirm this hypothesis, PS was excited at 274 nm and the emission from POPOP was measured as a function of PPO/POPOP concentration. It can be seen that although 96% of the PS emission is quenched at 1.5%, only 75% of the maximum emission intensity from POPOP is achieved at this concentration. Further addition of PPO/POPOP results in an increase in emission intensity up to approximately 5%. The emission levels off until 10%, then decreases thereafter due to self-absorption. This demonstrates that the optimum concentration of PPO/POPOP in this material is in the range 5 – 10%. It is interesting to note that at the concentration where nearly all PS emission is quenched, addition of more antenna molecules significantly increases the amount of excitation energy that can be collected from PS. This effectively increases the overall quantum efficiency of the system. It is thus determined that even though the overall quantum efficiency of the pure matrix is low, the quantum efficiency of the overall emission can be improved by utilization of an antenna molecule that efficiently harvests the excitation energy from the matrix before it can relax vibrationally.
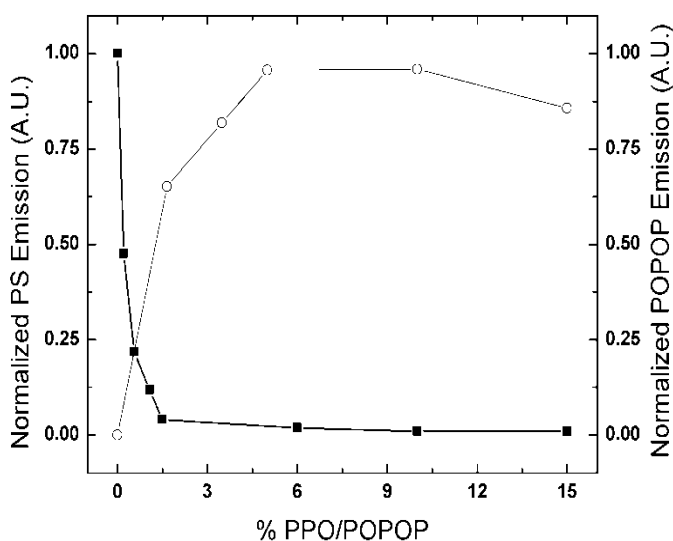
Figure 6.3-4 PS emission (■) and POPOP emission (○) for 150 μm samples as a function of wt% PPO/POPOP

In Figure 6.3-4, PS emission was obtained by measuring the excitation spectrum that yielded emission at 314 nm, then integrating the response over the region 250 nm – 300 nm. POPOP emission was obtained by measuring the emission spectrum resulting from excitation at 274 nm, then integrating over the region 390 nm – 500 nm.

It is generally agreed upon that effective scintillators must be transparent to their own scintillation light. To determine the effect of reduced optical transmission on fluorescence, emission spectra shown in Fig. 5 were measured for samples containing 10% PPO/POPOP with varying concentrations of ^{6}LiF. Comparison of the relative emission intensities demonstrates that increasing the amount of ^{6}LiF in the sample increases the emission intensity. This can be rationalized by considering that the PS/^{6}LiF composite is a mechanical mixture with 3.2 μm cubic lithium fluoride particles trapped inside the PS matrix. Because the refractive indices of lithium fluoride and polystyrene are different and the particles are sufficiently larger than the wavelength of incident light, each particle acts as a scattering site for the incident excitation photons. A greater the number of scattering sites in the matrix increases the overall path length of any given photon in the film. The Beer-Lambert law indicates that absorption of a photon by a material is dependent on both concentration and path length of the absorbing medium. It was shown in Fig. 4 that increasing the concentration of PPO/POPOP above 10% results in a decrease in the observed emission, so the observed phenomenon in Fig. 5 cannot be due to a higher probability of scattered photons emitted from PPO being captured by POPOP. This also cannot be attributed to the energy transfer between PS and PPO because this mechanism occurs primarily without emission of a photon. Thus, most probable explanation for this phenomenon is that the greater number of scattering sites increases the average path length of the photons in the excitation beam through the material, resulting in a greater probability that an incident photon will be absorbed by the PS. Because more photons are absorbed in PS matrices with higher loadings of ^{6}LiF, more excitations are available to be harvested by the antenna fluors.
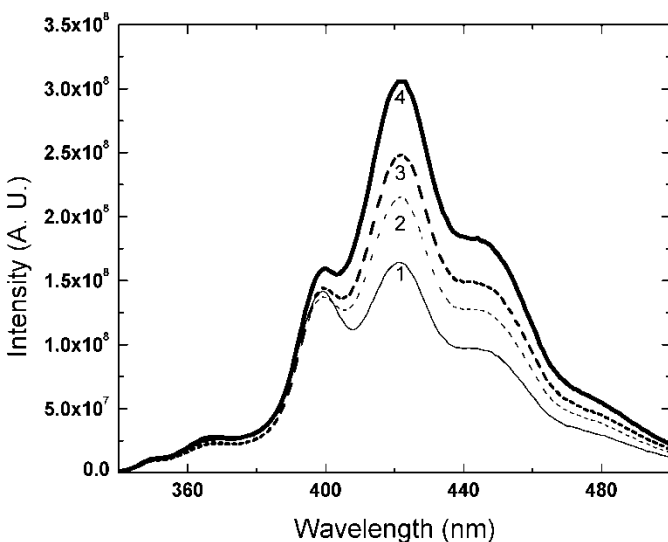
Figure 6.3-5   Emission spectra of 150 μm thick samples containing 10% PPO/POPOP at various loadings of ^{6}LiF. Spectra were obtained by excitation at 274 nm. Spectra are numbered according to the following percentages of ^{6}LiF: (1) 0%, (2) 10%, (3) 15%, (4) 20%.

6.3.6.2   *Scintillation Measurements*

The films were characterized by responses to alpha radiation from ^{241}Am. Alpha responses of films with different percentages of fluor (0.1 − 15%) were measured for 50 μm and 150 μm samples. Peak positions indicated that the optimum concentration of fluor was 5%, which is in agreement with the fluorescence data. This weight percentage was used throughout the rest of the experimentation. Alpha responses of samples containing 10% ^{6}LiF and 5% PPO/POPOP with thicknesses 15 μm – 150 μm are shown in Fig. 6. It is observed thinner samples have a decreased resolution and therefore a decreased average light output as characterized by the broad peaks whereas the thicker samples show a sharper peak and therefore a greater average light output. This is attributed to the fact that the range of the incident 5.48 MeV alpha is about 39.1 μm in PS, as shown in Table I, which exceeds the thicknesses of the 15 and 25 μm thick films. This indicates that the incident alphas are not completely stopped in the 15 and 25 μm films, whereas they are completely stopped in the 50 and 150 μm films. Thus, it is expected that the resolution should be poor in the 15 and 25 μm films and improved in the 50 and 150 μm films. It can also be seen that the light output is reduced in the 150 μm film relative to the 50 μm film. This is attributed to increased self absorption and increasing scattering

132

probability of the scintillation light in the 150 μm sample. The active volume is only about 39 μm deep as evidenced by the range of the alpha; thus, the scintillation light must travel a greater distance in the 150 μm film to reach the PMT as compared to the 50 μm film, increasing the probability that self-absorption or scattering will occur.
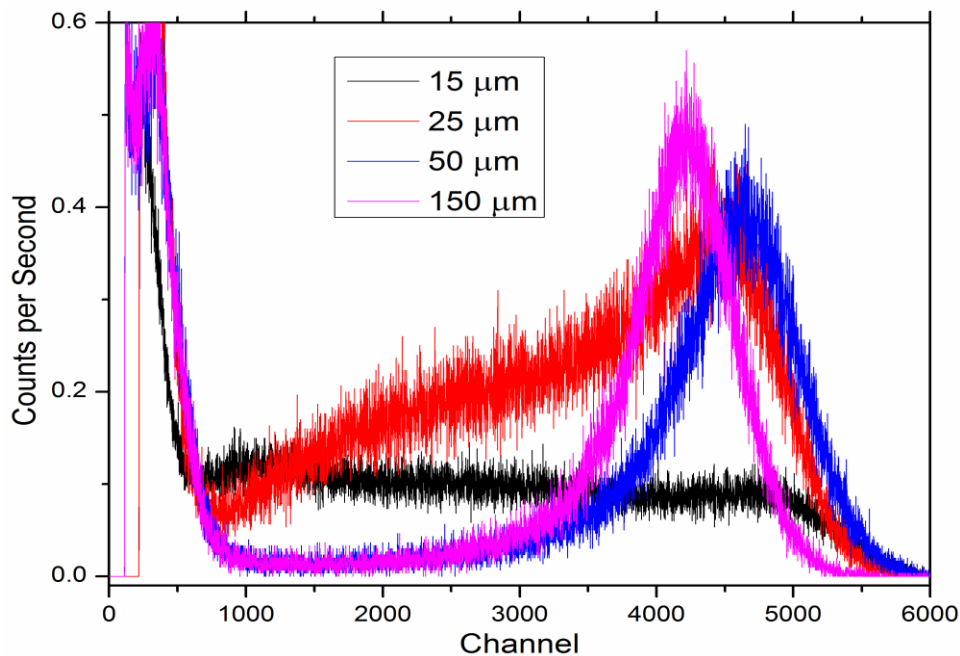
Figure 6.3-6 Alpha spectra for samples containing 10% ^{6}LiF and 5% PPO/POPOP for thicknesses over the range 15 – 150 μm.

Table 6.3-1 Ranges of Charged Particles

Material	α (5.48 MeV)	α (2.05 MeV)	t (2.73 MeV)
PS	39.1 μm	10.1 μm	61.8 μm
^{6}LiF [a]	20.8 μm	5.81 μm	33.1 μm

Ranges of charged particles calculated using SRIM-2011[153]. Reported values are averages from simulating 500 ion interactions.

[a]Density and molar mass of ^{6}LiF were adjusted for 97.6% ^{6}Li enrichment.

In order to estimate the repeatability in fabrication and measurement of these samples, four compositions were fabricated multiple times and the neutron count rates in counts per second (CPS) were recorded. The compositions were 25 µm and 50 µm samples each containing 20% and 30% ^{6}LiF with 5% PPO/POPOP. These results (Table II) are included to indicate the level of repeatability for net neutron count rates for identically prepared and counted samples. Differences in net neutron count rates are attributed to potential changes in dispersion of ^{6}LiF, inherent error in measuring sub-milligram quantities during sample fabrication, and small changes in the geometry among multiple measurements. The error values indicate that the measurement and fabrication protocols are repeatable.

Table 6.3-2 Repeatability of Neutron Count Rates

Thickness	wt% ^{6}LiF	Neutron Count Rate (CPS)
25 µm	20	20.9 ± 3.6
	30	46.9 ± 1.5
50 µm	20	52.2 ± 2.6
	30	91.4 ± 2.7

Neutron and gamma responses for a 50 µm thick sample containing 20% ^{6}LiF and 5% PPO/POPOP are shown in Fig. 7. The separation of the neutron and gamma spectra indicate that neutron/γ discrimination can be achieved in these samples using pulse height discrimination techniques. The absence of a clear peak can be attributed to the ranges of the fission products, shown in Table I, relative to the film thickness. The average range of the triton in PS is approximately 60 µm which is greater than the thickness of the film. Assuming that the neutron capture probability does not vary over the entire thickness of the film[7], it is likely that a significant fraction of the energy of the triton is not deposited in the film. This decreases the overall resolution of the composite material; however, thicker samples result in more overlap of the neutron and gamma spectra, thereby eliminating the possibility of discrimination.
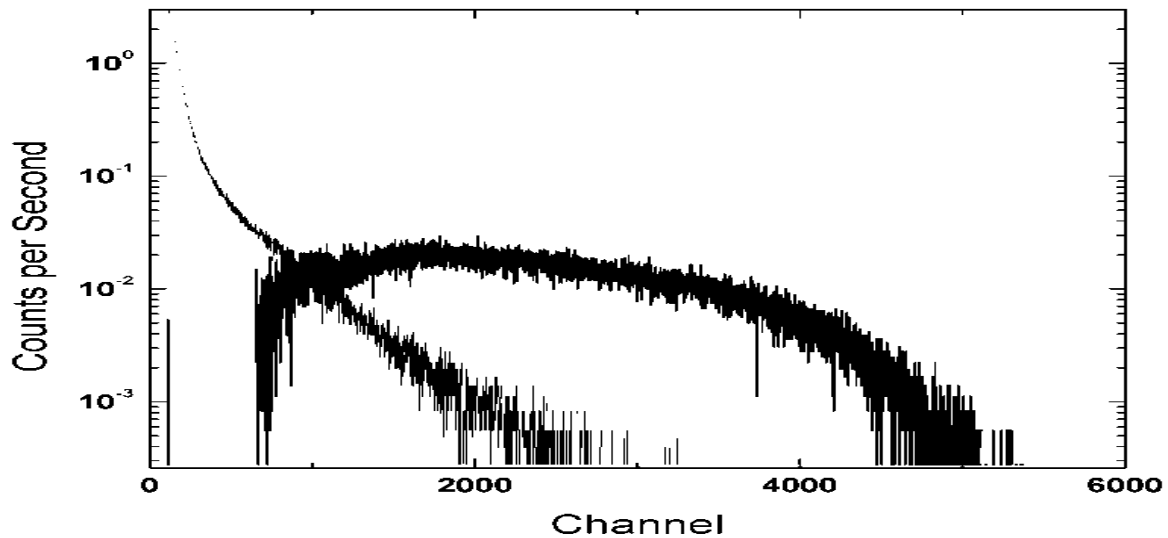
Figure 6.3-7 Neutron (thick line) and gamma (thin line) responses for a 50 μm sample containing 20% ^{6}LiF and 5% PPO/POPOP

Pulse height discrimination between neutron and gamma events is facilitated when the neutron count rates at higher channel numbers are increased, indicative of higher efficiency detection of charged particles. Samples containing higher loadings of ^{6}LiF have higher total count rates. However, at higher channels the samples with higher loadings become less efficient due to scattering. This can be rationalized by considering two factors present in the different samples. First, higher concentrations of ^{6}LiF result in a decrease in optical clarity of the samples. This increases the probability that the scintillation light will be scattered before reaching the photomultiplier tube, resulting in a lower observed efficiency. Additionally, it must be considered that lithium fluoride does not scintillate and energy deposited in the lithium fluoride particles is not efficiently transferred to the scintillating volume. Increasing the fraction of non-scintillating particles in the matrix thus decreases the overall kinetic energy available to be transduced into scintillation light.

Values for discriminator (PHD) settings were obtained by integrating the neutron and gamma spectra, dividing each point by the total number of particles the sample per unit area (1050 neutrons/s and 1850 γ/s), then finding the channel at which the neutron efficiency is 1.2×10^{-3} and the gamma efficiency is 1×10^{-6}, as shown in Fig. 8. The data in Fig. 9 indicate the pulse height discriminator level required to achieve intrinsic neutron efficiencies of 1.2×10^{-3}

135

and intrinsic gamma-neutron detection efficiencies of 1×10^{-6} for samples containing 10% ^{6}LiF and 5% PPO/POPOP over the thickness range $15 - 2600$ μm. It should be noted that the MCA used in this experiment only has 8192 channels; values reported above 8192 channels are the results of extrapolation. It is evident that the best neutron/gamma discrimination can be achieved with samples in the thickness range 25 μm – 150 μm. Above 150 μm, the material becomes more sensitive to gamma radiation and below 15 μm the range of the charged particles released from ^{6}Li fission greatly exceeds the thickness of the film such that a sharp reduction in the pulse height is observed. It should be noted that the values reported for neutron efficiencies and intrinsic gamma-neutron efficiencies are based on the test configuration in our laboratory. Monte Carlo calculations are in progress to estimate the bias introduced by this situation and these results will be reported in future work.
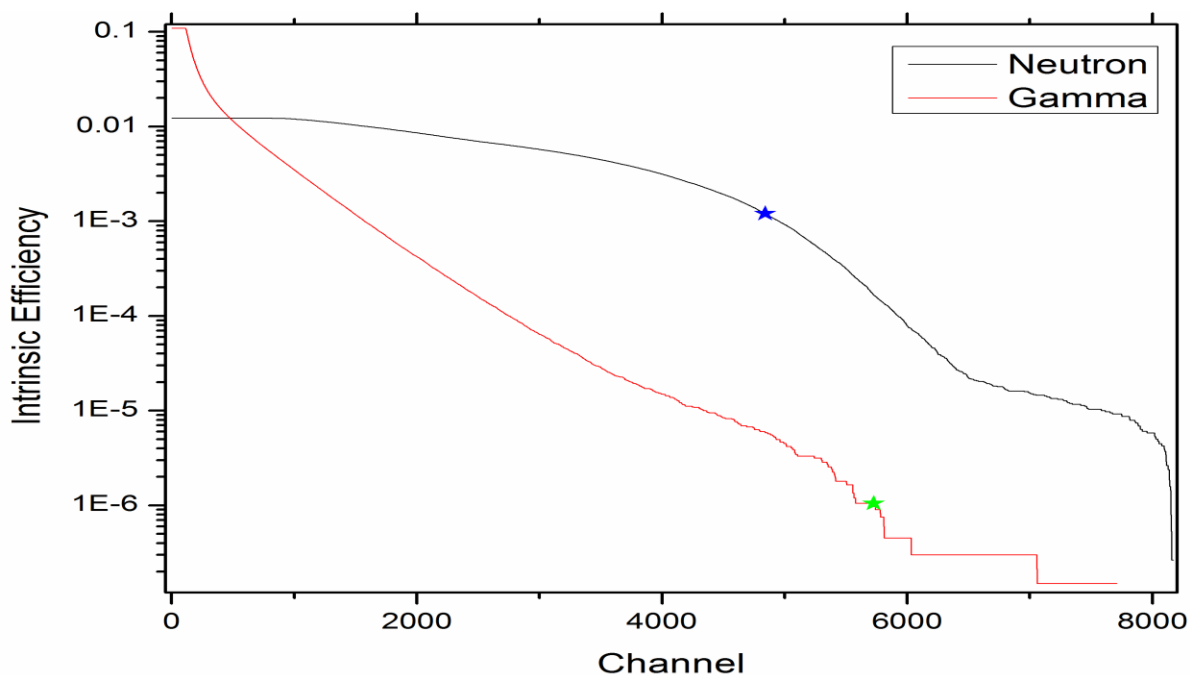
Figure 6.3-8 Intrinsic efficiency plotted against channel number for a 50 μm film containing 10% ^{6}LiF and 5% PPO/POPOP. Stars indicate the channels at which intrinsic efficiencies reach 1.2×10^{-3} for neutrons and 10^{-6} for gammas.
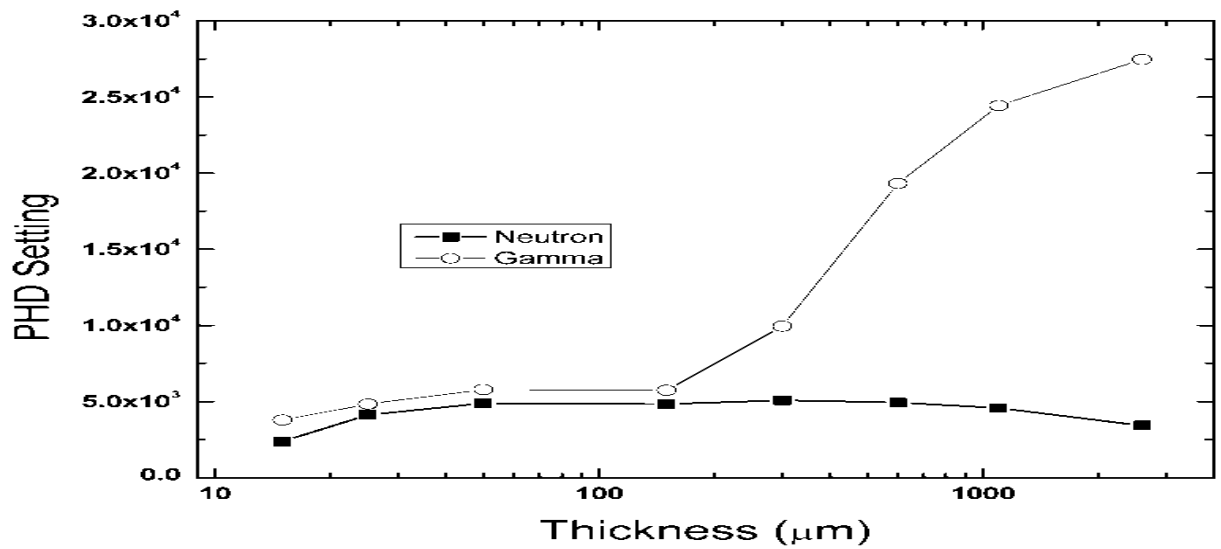
Figure 6.3-9 PHD levels required to achieve intrinsic neutron efficiencies of 1.2×10^{-3} and intrinsic gamma-neutron detection efficiencies of 1×10^{-6} as a function of thickness. The optimal discrimination capabilities can be achieved with materials in the range 25 μm – 150 μm.

Sample geometry required to achieve neutron/gamma discrimination is at the expense of neutron detection efficiency. Shown in Fig. 10 are the intrinsic efficiencies for the samples reported in Fig. 9. It is demonstrated that even though thinner samples demonstrate better neutron/gamma discrimination capabilities, it is achieved at the expense of intrinsic neutron detection efficiencies. Thicker samples can be fabricated to achieve detection efficiencies of up to 70% but this comes at the expense of the material to facilitate neutron/gamma discrimination.
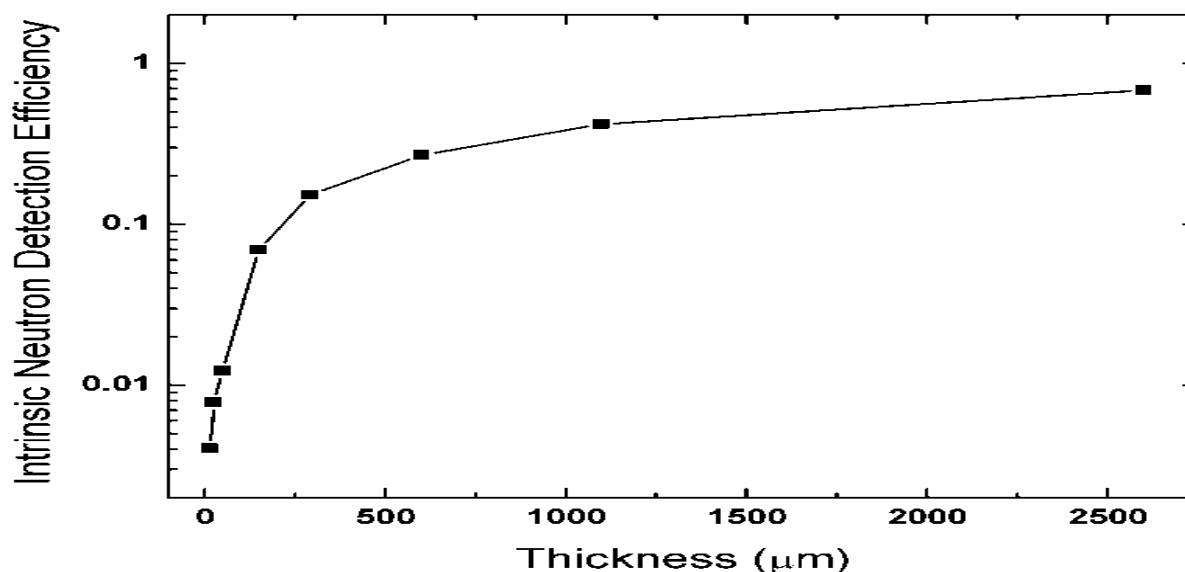
Figure 6.3-10 Intrinsic neutron detection efficiency as a function of thickness for samples containing 10% ^{6}LiF and 5% PPO/POPOP.

6.3.7   Conclusions

This work has demonstrated that effective composite thermal neutron scintillation detectors can be fabricated using PS, ^{6}LiF, and PPO/POPOP and cast as films by solution casting methods. Compositions of the films were varied to optimize responses. Fluorescence intensity for neat films was found to be optimum at 5% PPO/POPOP and was improved by adding ^{6}LiF to act as scattering sites for the incident excitation beam. The gamma response was unaffected by changing concentration of ^{6}LiF in the matrix. The best neutron/gamma discrimination capabilities were obtained in the film thickness range 25 − 150 μm. It is shown that for films containing 10% ^{6}LiF, intrinsic neutron detection efficiencies approach 70% but this comes at the expense of reduced neutron/gamma discrimination capabilities.

6.3.8   Acknowledgements

138

List of References

[1]   R. T. Kouzes, "The He-3 Supply Problem. PNNL-18388," *PNNL Report*, 2009.

[2]   R. T. Kouzes, J. R. Ely, A. T. Lintereur, and D. L. Stephens, "Neutron Detector Gamma Insensitivity Criteria. PNNL-18903," *PNNL Report*, 2009.

[3]   R. M. van Ginhoven, R. T. Kouzes, and D. L. Stephens, "PNNL-18471: Alternative Neutron Detector Technologies for Homeland Security," 2009.

[4]   A. Munter, "NIST Scattering Lengths and Cross Sections," 2012. [Online]. Available: http://www.ncnr.nist.gov/resources/n-lengths/.

[5]   G. F. Knoll, *Radiation Detection and Measurement*, 2nd ed. John Wiley and Sons, 1989.

[6]   C. W. E. van Eijk, A. Bessiere, and P. Dorenbos, "Inorganic thermal neutron scintillators," *Nuclear Instruments and Methods in Physics Research A*, vol. 529, pp. 260–267, 2004.

[7]   I. Sen, D. Penumadu, M. Williamson, L. F. Miller, A. D. Green, and A. N. Mabe, "Thermal Neutron Scintillator Detectors Based on Poly(2-vinylnapthalene) Composite Films," *IEEE Transactions on Nuclear Science*, vol. 3, no. 1386, 2011.

[8]   I. Sen, M. Urffer, D. Penumadu, S. A. Young, L. F. Miller, and A. N. Mabe, "Polyester Composite Thermal Neutron Scintillation Films," *IEEE Nuclear Science Symposuim & Medical Imaging Conference*, vol. 59, p. 1781, 2012.

[9]   A. R. Spowart, "Neutron Scintillating Glasses: Part II The effects of temperature on pulse height and conductivity," *Nuclear Instruments and Methods in Physics Research*, 1976.

[10]   A. R. Spowart, "Neutron Scintillating Glasses: Part I: Activation by external charged particles and thermal neutrons," *Nuclear Instruments and Methods*, vol. 135, 1976.

[11] E. J. Fairley and A. R. Spowart, "Neutron Scintillating Glasses Part III: Pulse Decay Time Measurements at Room Temperature," *Nuclear Instruments and Methods*, vol. 150, pp. 159–163, 1978.

[12] D. W. Anderson, *Absorption of Ionizing Radiation*, 1st ed. Baltimore, MD: University Park Press, 1984.

[13] P. Pascuta, G. Borodi, and E. Culea, "Influence of europium ions on structure and crystallization properties of bismuth borate glasses and glass ceramics," *Journal of Non-Crystalline Solids*, vol. 354, no. 52–54, pp. 5475–5479, Dec. 2008.

[14] R. E. Newnham, M. J. Redman, and R. P. Santoro, "Crystal Structure of Yttrium and other Rare Earth Borates," *Journal of the American Ceramic Society*, vol. 46, no. 6, pp. 253–256, Oct. 1963.

[15] G. Corradi, V. Nagirnyi, A. Watterich, A. Kotlov, and K. Polgár, "Different incorporation of Cu + and Cu 2+ in lithium tetraborate single crystals," *Journal of Physics: Conference Series*, vol. 249, p. 012008, Nov. 2010.

[16] M. Lafjiji, N. El Jouhari, L. Benarafa, A. Lautie, and G. Le Flem, "Caracterisation et approche structurale de verres du systeme La2O3-MgO-B2O3," *Spectrochimica Acta Part A*, vol. 59, pp. 1643–1653, 2003.

[17] T. Okajima, N. Umesaki, A. Konishi, T. Jin, I. Tanaka, and T. Yazawa, "An XAFS study of the local structure of europium ion in crystallised borosilicate glass," *Physics and Chemistry of Glasses: European Journal of Glass Science and Technology, Part B*, vol. 47, no. 4, pp. 558–562, 2006.

[18] S. Z. Smirnov, V. G. Thomas, S. P. Demin, and V. A. Drebushchak, "Experimental study of boron solubility and speciation in the Na2O–B2O3–SiO2–H2O system," *Chemical Geology*, vol. 223, no. 1–3, pp. 16–34, Nov. 2005.

[19]   Y. Shimizugawa, N. Umesaki, J. Qiu, and K. Hirao, "Local structure around europium ions doped in borate glasses.," *Journal of synchrotron radiation*, vol. 6, no. Pt 3, pp. 624–6, May 1999.

[20]   G. El-Damrawi and K. El-Egili, "Characterization of novel CeO2–B2O3 glasses, structure and properties," *Physica B: Condensed Matter*, vol. 299, no. 1–2, pp. 180–186, May 2001.

[21]   E. W. J. L. Oomen and A. M. A. van Dongen, "Europium (III) in Oxide Glasses: Dependence of the emission spectrum upon glass composition," *Journal of Non-Crystalline Solids*, vol. 111, pp. 205–213, 1989.

[22]   G. Corbel, M. Leblanc, and J. C. Krupa, "Luminescence analysis and subsequent revision of the crystal structure of triclinic L-EuBO 3," vol. 287, pp. 71–78, 1999.

[23]   Y. Shimizugawa, K. Handa, and J. R. Qiu, "X-ray and UV irradiation effects on Ce 3 + ion doped in UV sensitive glass," *Journal of Materials Science Letters*, vol. 22, pp. 15 – 16, 2003.

[24]   O. E. Raola and G. F. Strouse, "Synthesis and Characterization of Eu-Doped Cadmium Selenide Nanocrystals," *Nano Letters*, vol. 2, no. 12, pp. 1443–1447, Dec. 2002.

[25]   I. N. Ogorodnikov, V. A. Pustovarov, S. I. Omel'kov, A. V. Tolmachev, and R. P. Yavetskiĭ, "Luminescence VUV spectroscopy of cerium-and europium-doped lithium borate crystals," *Optics and Spectroscopy*, vol. 102, no. 1, pp. 60–67, Jan. 2007.

[26]   R. Engels, R. Reinartz, J. Schelten, and B. Czirr, "Thermal Neutron Detection with the Lithium Borate Scintillator," vol. 47, no. June, pp. 948–951, 2000.

[27]   M. P. Tabbey and J. R. Hendrickson, "NMR Study of Lithium Borate Glasses with Low Lithia Contents," *Journal of Non-Crystalline Solids*, pp. 51–56, Oct. 1980.

[28] H. Li, H. Lin, W. Chen, and L. Luo, "IR and Raman investigation on the structure of (100-x)[0.33B2O3–0.67ZnO]–xV2O5 glasses," *Journal of Non-Crystalline Solids*, vol. 352, no. 28–29, pp. 3069–3073, Aug. 2006.

[29] E. J. Reardon, "Dissociation Constants for Alkali Earth and Sodium Borate," *Chemical Geology*, vol. 18, pp. 309–325, 1976.

[30] P. Aguiar and S. Kroeker, "Boron speciation and non-bridging oxygens in high-alkali borate glasses," *Journal of Non-Crystalline Solids*, vol. 353, no. 18–21, pp. 1834–1839, Jun. 2007.

[31] S. A. Feller, W. J. Dell, and P. J. Bray, "10B NMR Studies of Lithium Borate Glasses," *Journal of Non-Crystalline Solids*, vol. 51, pp. 21–30, Nov. 1982.

[32] M. Touboul, E. Bétourné, and L. Seguin, "Crystal Structure of $LiB_5O_8 \cdot 5H_2O$," *Materials Science Forum*, vol. 228–231, pp. 741–746, 1996.

[33] J. Krogh-Moe, "The Structure of Vitreous and Liquid Boron Oxide," *Journal of Non-Crystalline Solids*, vol. 1, no. 4, pp. 269–284, 1969.

[34] S. E. Ashbrook and M. E. Smith, "Solid state 17O NMR-an introduction to the background principles and applications to inorganic materials.," *Chemical Society Reviews*, vol. 35, no. 8, pp. 718–35, Aug. 2006.

[35] J. H. Hao and J. Gao, "Abnormal reduction of Eu ions and luminescence in CaB[sub 2]O[sub 4]: Eu thin films," *Applied Physics Letters*, vol. 85, no. 17, p. 3720, 2004.

[36] T. W. Crane and M. P. Baker, *Thermal Neutrons*. 1982, pp. 379–406.

[37] "XI . Detection of Neutrons," *Nuclear Engineering 401 Class*, 2011. [Online]. Available: http://inst.nuc.berkeley.edu/NE104/Lectures/Neutron-Detection_NE104_Spring11.pdf. [Accessed: 05-Jan-2013].

[38] A. Doumas and G. C. Smith, "Comparison of various stopping gases for 3He-based position sensitive neutron detectors," *Nuclear Instruments and Methods in Physics Research Section A: Accelerators, Spectrometers, Detectors and Associated Equipment*, vol. 675, pp. 8–14, May 2012.

[39] L. V. East and R. B. Walton, "Polyethylene Moderated He-3 Neutron Detectors," *Nuclear Instruments and Methods*, vol. 72, pp. 161–166, 1969.

[40] B. Yu, G. J. Mahler, N. A. Schaknowski, and G. C. Smith, "A position-sensitive ionization chamber for thermal neutrons," *IEEE Transactions on Nuclear Science*, vol. 48, no. 3, pp. 336–340, Jun. 2001.

[41] K. P. Ananthanarayanan and P. J. Gielisse, "Boron Compounds for Thermal-Neutron Detection," vol. 118, pp. 45–48, 1974.

[42] K. Banerjee, T. K. Ghosh, S. Kundu, T. K. Rana, C. Bhattacharya, J. K. Meena, G. Mukherjee, P. Mali, D. Gupta, S. Mukhopadhyay, D. Pandit, S. R. Banerjee, S. Bhattacharya, T. Bandyopadhyay, and S. Chatterjee, "Variation of neutron detection characteristics with dimension of BC501A neutron detector," *Nuclear Instruments and Methods in Physics Research*, vol. 608, no. 3, pp. 440–446, Sep. 2009.

[43] S. Ait-Boubker, M. Avenier, G. Bagieu, J. F. Cavangnac, J. Collot, J. Favier, E. Kajfasz, D. H. Koang, A. Stutz, and B. Vignon, "Thermal Neutron Detection and Identification in a large volume with a new lithium-6 loaded liquid scintillator," *Nuclear Instruments and Methods in Physics Research A*, vol. 277, pp. 461–466, 1989.

[44] H. P. Chou and C. Y. Horng, "Integral test of a boron-10 loaded liquid scintillator for neutron detection," *Nuclear Instruments and Methods A*, vol. 328, no. 3, pp. 522–525, May 1993.

[45] Y.-C. Lo and R. E. Apfel, "Prediction and Experimental Confirmation of the response function for neutron detection using superheated drops," *Physical Review A*, vol. 38, no. 10, 1988.

[46] A. J. Peurrung, "Nuclear Instruments and Methods in Physics Research Section A: Accelerators, Spectrometers, Detectors and Associated Equipment," *Nuclear Instruments and Methods in Physics Research A*, vol. 443, no. 2–3, pp. 400–415, 2000.

[47] Frost (BTI Industries), "Bubble Detectors." pp. 17–18, 2009.

[48] H. Ing, R. A. Noulty, and T. D. Mclean, "Bubble Detectors - A Maturing Technology," *Radiation Measurements*, vol. 27, no. 1, 1997.

[49] C. Q. Tu, S. L. Guo, Y. L. Wang, X. H. Hao, C. M. Chen, and J. L. Su, "Study of Bubble Damage Detectors for Neutron Detection," *Radiation Measurements*, vol. 28, no. 97, pp. 159–162, 1997.

[50] J. Li, R. Dahal, S. Majety, J. Y. Lin, and H. X. Jiang, "Hexagonal boron nitride epitaxial layers as neutron detector materials," *Nuclear Instruments and Methods in Physics Research*, vol. 654, no. 1, pp. 417–420, Oct. 2011.

[51] V. A. Nikolaev, "Solid-state track detectors in radiometry, isotope analysis, and radiography," *Radiochemistry*, vol. 54, no. 1, pp. 1–17, Feb. 2012.

[52] A. N. Caruso, "The physics of solid-state neutron detector materials and geometries.," *Journal of Physics: Condensed Matter*, vol. 22, no. 44, p. 443201, Nov. 2010.

[53] A. Kreyssig, K. Irmer, and U. Hartung, "ZnS/6Li scintillation material as an alternative to 6Li-glass scintillators for neutron detection in time focusing geometry," *Nuclear Instruments and Methods in Physics Research*, vol. 349, no. 1, pp. 292–294, Sep. 1994.

[54] C. L. Wang, L. Gou, J. M. Zaleski, and D. L. Friesel, "ZnS quantum dot based nanocomposite scintillators for thermal neutron detection," *Nuclear Instruments and Methods*, vol. 622, no. 1, pp. 186–190, Oct. 2010.

[55] C. Petrillo, F. Sacchetti, O. Toker, and N. J. Rhodes, "Solid state neutron detectors," *Nuclear Instruments and Methods in Physics ResearchNuclear Instruments and Methods*, vol. 378, no. 96, pp. 541–551, 1996.

[56] A. J. Peurrung, "Recent developments in neutron detection," *Nuclear Instruments and Methods in Physics Research*, vol. 443, no. September 1999, pp. 400–415, 2000.

[57] K. A. Nelson, S. L. Bellinger, B. W. Montag, J. L. Neihart, T. A. Riedel, A. J. Schmidt, and D. S. McGregor, "Investigation of a lithium foil multi-wire proportional counter for potential 3He replacement," *Nuclear Instruments and Methods in Physics Research*, vol. 669, pp. 79–84, Mar. 2012.

[58] S. Almaviva, M. Marinelli, E. Milani, G. Prestopino, A. Tucciarone, C. Verona, G. Verona-Rinati, M. Angelone, and M. Pillon, "Thermal neutron dosimeter by synthetic single crystal diamond devices.," *Applied Radiation and Isotopes*, vol. 67, no. 7–8 Suppl, pp. S183–185, Jul. 2009.

[59] M. Marinelli, E. Milani, G. Pretopino, M. Scoccia, M. Angelone, M. Pillon, and D. Lattanzi, "High performance (Li-6)F diamond thermal neutron detectors," *Applied Physics Letters*, vol. 89, 2006.

[60] M. Angelone, M. Pillon, G. Prestopino, M. Marinelli, E. Milani, C. Verona, G. Verona-Rinati, G. Aielli, R. Cardarelli, R. Santonico, R. Bedogni, and a. Esposito, "Thermal and fast neutron dosimetry using artificial single crystal diamond detectors," *Radiation Measurements*, vol. 46, no. 12, pp. 1686–1689, Dec. 2011.

[61] D. Hussona, C. Bauerb, I. Baumannb, C. Colledani, J. Conway, P. Delpierred, F. Djamad, W. Dulinski, M. Edwardse, A. Falloud, K. K. Ganf, R. S. Gilmoreg, E. Grigorievd, G. Halewelld, S. Hanh, T. Hessingb, J. Hrubec, H. Kaganf, D. Kaniaf, R. Kassf, K. T. Knoepfleb, M. Krammer, T. J. Llewellyng, P. F. Manfredij, D. Meierk, L. S. Pan, H. Pernegger, M. Pernicka, V. Rej, S. Rock, D. Roffg, A. Rudgek, S. Schnetzerc, V. Speziallj, R. Stonec, R. J. Tapperg, R. Tesarek, W. Trischuk, R. Turchetta, G. B. Thomson, P. Weilhammerk, H. Ziockh, and M. Zoellerf, "Neutron irradiation of CVD diamond samples for tracking detectors," vol. 388, pp. 421–426, 1997.

[62]   M. Schieber, A. Zuck, G. Marom, O. Khakhan, M. Roth, and Z. B. Alfassi, "Composite polycrystalline semiconductor neutron detectors," *Nuclear Instruments and Methods in Physics Research*, vol. 579, no. 1, pp. 180–183, Aug. 2007.

[63]   B. W. Robertson, S. Adenwalla, A. Harken, P. Welsch, J. I. Brand, P. A. Dowben, and J. P. Claassen, "A class of boron-rich solid-state neutron detectors," *Applied Physics Letters*, vol. 80, no. 19, p. 3644, 2002.

[64]   D. S. McGregor, W. J. McNeil, S. L. Bellinger, T. C. Unruh, and J. K. Shultis, "Microstructured semiconductor neutron detectors," *Nuclear Instruments and Methods A*, vol. 608, no. 1, pp. 125–131, Sep. 2009.

[65]   A. N. Mabe, M. J. Urffer, S. A. Young, J. D. Auxier II, I. Sen, D. Penumadu, C. L. Melcher, G. K. Schweitzer, and L. F. Miller, "Thin Film Polystyrene Composite Scintillators for Thermal Neutron Detection and Gamma Discrimination," *To Be Published*.

[66]   L. M. Bollinger and G. E. Thomas, "Neutron Detection with Glass Scintillators," *Nuclear Instruments and Methods*, vol. 17, pp. 91–116, 1962.

[67]   R. P. Waguespack, S. M. Pelligrin, and C. G. Wilson, "Glass and Quartz Microscintillators for CMOS-Compatible Multispecies Radiation Detection," *Journal of Microelectromechanical Systems*, vol. 20, no. 5, pp. 1192–1200, 2011.

[68]   J. B. Birks, *Theory and Practice of Scintillation Counting*. Pergamon Press, 1964, pp. 554–562.

[69]   "NucSafe Products," 2013. [Online]. Available: http://www.nucsafe.com/cms/Our+Products/3.html. [Accessed: 26-Feb-2013].

[70]   A. M. Buckley and M. Greenblatt, "The Sol-Gel Preparation of Silica Gels," *Journal of Chemical Education*, vol. 71, no. 7, pp. 599–602, 1994.

[71] C. J. Brinker and G. W. Scherer, *Sol Gel Science: The Physics and Chemistry of Sol-Gel Processing*, 1st ed. Academic Press, 1990, pp. 78–83.

[72] L. Lou, D. Boyer, G. Bertrand-Chadeyron, E. Bernstein, R. Mahiou, and J. Mugnier, "Sol-Gel Waveguide thin film of YBO3: preparation and characterization," *Optical Materials*, pp. 1–6, 2000.

[73] C. Mansuy, E. Tomasella, R. Mahiou, J. Grimblot, and J. M. Nedelec, "Surface characterization of sol-gel derived scintillating rare-earth doped Lu 2 SiO 5 thin films," *Journal of Physics: Conference Series*, vol. 100, no. 1, p. 012037, Mar. 2008.

[74] B. Kesanli, K. Hong, K. Meyer, H.-J. Im, and S. Dai, "Highly Efficient solid-state neutron scintillators based on hybrid Sol-Gel nanocomposites," *Applied Physics Letters*, vol. 89, 2006.

[75] S. A. Wallace, A. C. Stephan, R. Cooper, H.-J. Im, and S. Dai, "Lithiated sol-gel based neutron scintillators," *Nuclear Instruments and Methods in Physics Research A2*, vol. 579, pp. 184–187, 2007.

[76] S. A. Wallace, A. C. Stephan, L. F. Miller, and S. Dai, "Neutron detector based on lithiated sol-gel glass," *Nuclear Instruments and Methods in Physics Research A*, pp. 764–773, 2001.

[77] P. Muralidharan, M. Ventkateswarlu, and N. Satyanarayana, "Sol-gel synthesis, characterization and impedance studies of lithium borosilicate glass," *Materials Research Bulletin*, vol. 39, 2004.

[78] T. Athar and K. R. Reddy, "Cerium Alkoxides–Synthesis, Properties and Their Use in Michael Addition Reaction," *Chinese Journal of Chemistry*, vol. 26, no. 4, pp. 751–754, Apr. 2008.

[79] A. K. Chatterjee and W. Wardlaw, "Bradley, Chatterjee, and Wardlaw : 439. Structural Chemistry of the Alkoxides. Part VI.* Primary Alkoxides," *Elements*, vol. 2025, pp. 2260–2264.

[80] P. S. Gradeff, F. G. Schreiber, K. C. Brooks, and R. E. Severs, "Simplified Method for the Synthesis of Ceric Alkoxides from Ceric Ammonium Nitrate," *Inorganic Chemistry*, vol. 24, pp. 1110–1111, 1985.

[81] H. J. Heeres, J. Renkema, M. Booij, A. Meetsma, and J. H. Teuben, "Bis(pentamethylcyclopentadienyl) Complexes of Cerium (III) Crystal Structure of (C5Me5)2CeCH(SiMe3)2," *Organometallics*, vol. 7, no. 12, pp. 2495–2502, 1988.

[82] M. Katagiri, K. Sakasai, M. Matsubayashi, T. Nakamura, Y. Kondo, Y. Chujo, H. Nanto, and T. Kojima, "Scintillation materials for neutron imaging detectors," *Nuclear Instruments and Methods in Physics Research Section A: Accelerators, Spectrometers, Detectors and Associated Equipment*, vol. 529, no. 1–3, pp. 274–279, Aug. 2004.

[83] M. Katagiri, K. Sakasai, M. Matsubayashi, and T. Kojima, "Neutron/γ-ray discrimination characteristics of novel neutron scintillators," *Nuclear Instruments and Methods A*, vol. 529, no. 1–3, pp. 317–320, Aug. 2004.

[84] N. Senguttuvan, M. Ishii, M. Shimoyama, M. Kobayashi, and N. Tsutsui, "Crystal growth and luminescence properties of Li 2 B 4 O 7 single crystals doped with Ce , In , Ni , Cu and Ti ions," *Nuclear Instruments and Methods A*, vol. 486, pp. 264–267, 2002.

[85] M. Ishii, Y. Kuwano, T. Asai, S. Asaba, M. Kawamura, N. Senguttuvan, T. Hayashi, M. Kobayashi, M. Nikl, S. Hosoya, K. Sakai, T. Adachi, T. Oku, and H. M. Shimizu, "Boron based oxide scintillation glass for neutron detection.," *Nuclear Instruments and Methods A*, vol. 537, pp. 1–5, 2005.

[86] B. I. Zadneprovski, N. V. Eremin, and A. A. Paskhalov, "New Inoragnic scintillators on the basis of LBO glass for Neutron Registration," *Functional Materials*, vol. 12, no. 2, pp. 261–268, 2005.

[87] N. Stump, G. K. Schweitzer, L. L. Pesterfield, and G. Murray, "Rare Earth Reduction Proposal." 2011.

[88] K.-I. Machida, G. Adachi, H. Hata, and J. Shiokawa, "The Crystal Structure and Magnetic Property of Europium(II) Orthoborate," *Bulletin of the Chemistry Society of Japan*, vol. 54, no. 4, pp. 1052–1055, 1980.

[89] J. H. Whang, S. Y. Sumarokov, S. W. Shin, J. M. Lee, and S. H. Choi, "Photoluminescence of lithium borate glasses doped by lanthanides," *Functional Materials*, vol. 9, no. 4, pp. 657–660, 2002.

[90] Q. Su, H. Liang, T. Hu, Y. Tao, and T. Liu, "Preparation of divalent rare earth ions in air by aliovalent substitution and spectroscopic properties of Ln 21," vol. 344, pp. 132–136, 2002.

[91] G. K. Dasmohapatra, "A spectroscopic study of cerium in lithium – alumino – borate glass," no. April, pp. 120–125, 1998.

[92] J. Anjaiah, L. C. Kanth, Y. R. Reddy, and P. Kistaiah, "Thermoluminescnence studies on Li2O-MO-B2O3 glasses doped with rare earth ions," *Asian Journal of Chemistry*, vol. 23, no. 6, pp. 2696–2700, 2011.

[93] L. R. Elias, W. S. Weaps, and W. M. Yen, "Excitation of UV Fluorescence in LaF3 Doped with Trivalent Cerium and Praesodymium," *Physical Review*, vol. 8, no. 11, pp. 4989–4995, 1973.

[94] R. Aryaeinejad, X. Y. Dardenne, J. D. Cole, and A. J. Caffrey, "Palm-Size Low-Level Neutron Sensor for Radiation Monitoring," *IEEE Transactions on Nuclear Science*, vol. 43, no. 3, pp. 1539–1543, 1996.

[95] R. Aryaeinejad and D. F. Spencer, "Pocket Dual Neutron/Gamma Radiation Detector," *IEEE Transactions on Nuclear Science*, vol. 51, no. 4, pp. 1667–1671, 2004.

[96] B. Burgkhardt and W. Schwartz, "Evaluation Techniques for Different TL Albedo Dosemeter Systems Using Automatic Readout," *Radiation Protection Dosimetry*, vol. 17, pp. 131–134, 1986.

[97]   M. Hajek, T. Berger, and N. Vana, "Thermoluminescent Detectors for Neutron Dosimetry at High Altitudes," in *IRPA*, 2004.

[98]   R. A. Murray, "Use of LiI (Li-6) as a Scintillation Detector and Spectrometer for Fast Neutrons," *Nuclear Instruments and Methods*, vol. 2, pp. 237–248, 1958.

[99]   M. Hajek, T. Berger, and N. Vana, "A TLD-Based Personal Dosemeter System for Aircrew Monitoring," *Radiation Protection Dosimetry*, vol. 110, no. 1–4, pp. 337–341, 2004.

[100]   G. M. Hale and P. G. Young, "ENDF Database," *www.nndc.bnl.gov*, 2011. [Online]. Available: http://www.nndc.bnl.gov/exfor/endf00.jsp. [Accessed: 30-Aug-2012].

[101]   W. Ge, H. Zhang, Y. Lin, X. Hao, X. Xu, J. Wang, H. Li, H. Xu, and M. Jiang, "Preparation of Li2B4O7 thin films by chemical solution decomposition method," *Materials Letters*, vol. 61, no. 3, pp. 736–740, Feb. 2007.

[102]   M. Kayhan and A. Yilmaz, "Effects of synthesis, doping methods and metal content on thermoluminescence glow curves of lithium tetraborate," *Journal of Alloys and Compounds*, vol. 509, no. 30, pp. 7819–7825, Jul. 2011.

[103]   Claisse Fluxes, "Fusion samples for XRF, AA and ICP analysis." 2013.

[104]   K. Byrappa and K. V. K. Shekar, "Phases and crystallization in the system under hydrothermal conditions," *Journal of Materials Research*, no. October 1992, pp. 2–8, 1993.

[105]   J. Krogh-Moe, "The crystal structure of lithium diborate, Li2O.2B2O3," *Acta Crystallographica*, vol. 15, no. 3, pp. 190–193, Mar. 1962.

[106]   X. Cheng, F. Dong, and C. Yu, "Bond Covalency and Electronic Structure of CaB2O4(III) crystal," *Structural Chemistry*, vol. 20, pp. 221–226, 2009.

[107] K. Binnemans, "Lanthanide-based luminescent hybrid materials.," *Chemical Reviews*, vol. 109, no. 9, pp. 4283–374, Sep. 2009.

[108] V. S. Sastri, J. C. Bunzli, V. R. Rao, G. V. S. Rayudu, and J. R. Perumareddi, *Modern Aspects of Rare Earths and their Complexes*. 2003.

[109] J. M. Roderick, D. Holland, A. P. Howes, and C. R. Scales, "Density-structure relations in mixed-alkali borosilicate glasses by 29 Si and 11 B MAS-NMR," *Analysis*, vol. 295, pp. 746–751, 2001.

[110] E. Pekpak, a. Yılmaz, and G. Özbayoğlu, "The effect of synthesis and doping procedures on thermoluminescent response of lithium tetraborate," *Journal of Alloys and Compounds*, vol. 509, no. 5, pp. 2466–2472, Feb. 2011.

[111] M. J. Urffer, "Design of a Neutron Detector Capable of Replacing He-3 Detectors Utilizing Thin Polymeric Films," University of Tennessee, Knoxville, 2012.

[112] I. Sen, D. Penumadu, M. Williamson, L. F. Miller, A. D. Green, and A. N. Mabe, "Thermal Neutron Scintillator Detectors Based on Poly (2-Vinylnaphthalene) Composite Films," *IEEE Transactions on Nuclear Science*, vol. 58, no. 3, pp. 1386–1393, Jun. 2011.

[113] R. B. Firestone and L. P. Ekstrom, "WWW Table of Radioactive Isotopes," *LBNL Isotopes Project - LUNDS Universitet*, 2004. [Online]. Available: http://ie.lbl.gov/toi/. [Accessed: 06-Oct-2012].

[114] S. Sen, Z. Xu, and J. F. Stebbins, "Temperature dependent structural changes in borate , borosilicate studies," 1998.

[115] K. J. D. MacKenzie, *Multinuclear Solid-State NMR of Inorganic Materials*, 1st ed. 2002, pp. 420–432.

[116] D. Seebach, A. Thaler, and A. K. Beck, "Solubilization of Peptides in Non-polar Organic Solvents by the Addition of Inorganic Salts '): Facts and Implications," *Helvetica Chimica Acta*, vol. 72, no. March, pp. 857–867, 1989.

[117] S. V Kuznetsov, V. V Osiko, E. A. Tkatchenko, and P. P. Fedorov, "Inorganic nanofluorides and related nanocomposites," *Russian Chemical Reviews*, vol. 75, no. 12, pp. 1065–1082, Dec. 2006.

[118] L. M. Arnbjerg, D. B. Ravnsbæk, Y. Filinchuk, R. T. Vang, Y. Cerenius, F. Besenbacher, J.-E. Jørgensen, H. J. Jakobsen, and T. R. Jensen, "Structure and Dynamics for LiBH 4 −LiCl Solid Solutions," *Chemistry of Materials*, vol. 21, no. 24, pp. 5772–5782, Dec. 2009.

[119] C.-H. Chia, Z. Wu, C.-H. Wu, R.-H. Cheng, and S. Ding, "Resolve the pore structure and dynamics of Nafion 117: application of high resolution 7Li solid state nuclear magnetic resonance spectroscopy," *Journal of Materials Chemistry*, vol. 22, no. 42, p. 22440, 2012.

[120] A. Cárdenas, J. Solans, K. Byrappa, and K. V. K. Shekar, "Structure of lithium catena-poly[3,4-dihydroxopentaborate-1:5-μ-oxo]," *Acta Crystallographica Section C Crystal Structure Communications*, vol. 49, no. 4, pp. 645–647, Apr. 1993.

[121] P. J. Bray, S. A. Feller, G. E. Jellison Jr., and Y. H. Yun, "B-10 NMR Studies of the Structure of Borate Glasses," *Journal of Non-Crystalline Solids*, vol. 39, pp. 93–98, 1980.

[122] A. Senyshyn, B. Schwarz, T. Lorenz, V. T. Adamiv, Y. V. Burak, J. Banys, R. Grigalaitis, L. Vasylechko, H. Ehrenberg, and H. Fuess, "Low-temperature crystal structure, specific heat, and dielectric properties of lithium tetraborate Li2B2O7," *Journal of Applied Physics*, vol. 108, no. 9, p. 093524, 2010.

[123] B. Chen, U. Werner-Zwanziger, M. L. F. Nascimento, L. Ghussn, E. D. Zanotto, and J. W. Zwanziger, "Structural Similarity on Multiple Length Scales and Its Relation to Devitrification Mechanism: A Solid-State NMR Study of Alkali Diborate Glasses and Crystals," *The Journal of Physical Chemistry C*, vol. 113, no. 48, pp. 20725–20732, Dec. 2009.

[124] F. Sevim, F. Demir, M. Bilen, and H. Okur, "Kinetic Analysis of Thermal Decomposition of Boric Acid from Thermogravimetric Data," *Korean Journal Chemical Engineering*, vol. 23, no. 5, pp. 736–740, 2006.

[125] J. Smolanoff, A. Eapicki, N. Kline, and S. L. Anderson, "Effects of Composition, Structure, and H Atom Addition on the Chemistry of Boron Oxide Cluster Ions with HF," *Journal of Physical Chemistry*, vol. 99, pp. 16276–16283, 1995.

[126] Z. Pei, Q. Su, and J. Zhang, "The valence change from RE 3+ to RE 2+ (RE = Eu , Sm , Yb) in S r B 4 0 7 : RE prepared in air and the spectral properties of RE 2+," *Journal of Alloys and Compounds*, vol. 198, pp. 51–53, 1993.

[127] Q. Zeng, Z. Pei, and S. Wang, "Spectroscopy Letters : An International Journal for Rapid The Reduction of Re in Srb 6 O 10 Prepared in Air and the Luminescence of Srb 6 O 10 : Re (Re = Eu , Sm , Tm)," no. December 2012, pp. 895–912, 1999.

[128] J. Sanchez-Benitez, A. de Andres, M. Marchal, E. Cordoncillo, M. V. Regi, and P. Escribano, "Optical study of SrAl1.7B0.3O4:Eu, R (R=Nd, Dy) pigments with long-lasting phosphorescence for industrial uses," *Journal of Solid State Chemistry*, vol. 171, no. 1–2, pp. 273–277, Mar. 2003.

[129] J. Qiu, Y. Shimizugawa, N. Sugimoto, and K. Hirao, "Photostimulated luminescence in borate glasses doped with Eu+2 and Sm3+ ions," *Journal of Non-Crystalline Solids1*, vol. 222, pp. 290–295, 1997.

[130] J. Holsa, M. Lastusaari, and J. Niittykoski, "Persistent luminescence of Eu 21 doped alkaline earth aluminates, MAl 2 O 4 :Eu 21 ¨ ¨," vol. 324, pp. 326–330, 2001.

[131] A. V. Sidorenko, A. J. J. Bos, P. Dorenbos, P. A. Rodnyi, C. W. E. van Eijk, I. V. Berezovskaya, and V. P. Dotsenko, "Luminescence and thermoluminescence of Sr2B5O9X:Ce3+, A+ (X = Cl, Br, A = Na + , K +)," *Journal of Physics: Condensed Matter*, vol. 3471, pp. 3471–3480, 2003.

[132] A. V. Sidorenko, A. J. J. Bos, P. Dorenbos, C. W. E. van Eijk, P. A. Rodnyi, I. V. Berezovskaya, V. P. Dotsenko, O. Guillot-Noel, and D. Gourier, "Radiation induced defects in Sr 2 B 5 O 9 Br:Ce 3+ storage phosphor," *Journal of Physics: Condensed Matter*, vol. 16, no. 23, pp. 4131–4138, Jun. 2004.

[133] V. P. Dotsenko, "Alkaline earth borates doped with lanthanides; electronic structure, and applications," in *Handbook on Borates*, 2010, pp. 59–107.

[134] N. N. Greenwood, *Ionic Crystals, Lattice Defects, and Nonstoichoimetry*, 1st ed. London: Butterworths, 1968, pp. 111–140.

[135] F. A. Kroger, *The Chemistry of Imperfect Materials*, 1st ed. Amsterdam: North-Holland Publishing Company, 1964, pp. 192–214, 606.

[136] E. G. Tsvetkov, N. a. Pylneva, and A. V. Davydov, "Some aspects of lithium–boron melts structuring," *Journal of Crystal Growth*, vol. 292, no. 2, pp. 358–363, Jul. 2006.

[137] J. Dharma, "Simple Method of Measuring the Band Gap Energy Value of TiO2 in the Powder Form using a UV-Vis-NIR Spectrometer." Perkin-Elmer, pp. 4–7, 2009.

[138] NIST, "ASTAR Database: Stopping Power and Range Tables for Helium Ions," *Physical Mass Laboratory*, 2012. .

[139] LNHB, "Nucleide-LARA on the web: http://laraweb.free.fr/," *Nucleide'*, 2007. [Online]. Available: http://laraweb.free.fr/. [Accessed: 06-Oct-2012].

[140] B. Barta, "Radiation Spectroscopy via GdBr3:Ce Glass Ceramic Scintillators," in *5th Annual Academic Research Initiatives (ARI) Grantees Conference*, 2012.

[141] B. Kahn, B. Wagner, Z. Kang, J. Nadler, R. Rosson, and B. Barta, "Gamma-Ray Spectroscopy by Nanophotonic Scintillators," in *5th Annual Academic Research Initiatives (ARI) Grantees Conference*, 2012.

[142] V. B. Brudanin, V. I. Bregadze, N. A. Gundorin, D. V. Filossofov, O. I. Kochetov, I. B. Nemtchenok, A. A. Smolnikov, and S. I. Vasiliev, "Element-loaded organic scintillators for neutron and neutrino physics," *AIP Conference Proceedings*, vol. 69, 2001.

[143] L. Ovechkina, K. Riley, S. Miller, Z. W. Bell, and V. Nagarkar, "Gadolinium loaded plastic scintillators for high efficiency neutron detection," *Physics Procedia*, vol. 2, no. 2, pp. 161–170, 2009.

[144] R. D. Breukers, C. M. Bartle, and A. Edgar, "Transparent lithium loaded plastic scintillators for thermal neutron detection," *Nuclear Instruments and Methods A*, vol. 701, no. 11, pp. 58–61, 2012.

[145] S. M. Henry, M. E. H. El-Sayed, C. M. Pirie, A. S. Hoffman, and P. S. Stayton, "pH-Responsive Poly(styrene-alt-maleic anhydride) alkylamide copolymers for intercellular drug delivery," *Biomacromolecules*, vol. 7, no. 8, pp. 2407–2414, 2006.

[146] S. D. Baruah and N. C. Laskar, "Styrene-maleic anhydride copolymers: Synthesis, characterization, and thermal properties," *Journal of Applied Polymer Science*, vol. 60, no. 5, pp. 649–656, 1998.

[147] I. P. Pozdnyakov, A. Pigliucci, N. Tkachenko, V. F. Plyusnin, E. Vauthey, and H. Lemmetyinen, "The photophysics of salicylic acid derivatives in aqueous solution," *Journal of Physical Organic Chemistry*, vol. 22, pp. 449–454, 2008.

[148] A. Quaranta, S. M. Carturan, T. Marchi, V. L. Kravchuk, F. Gramegna, G. Maggioni, and M. Degerlier, "Optical and Scintillation Properties of Polydimethyl-Diphenylsiloxane Based Organic Scintillators," *IEEE Transactions on Nuclear Science*, vol. 57, no. 2, pp. 891–900, Apr. 2010.

[149] R. K. Swank, "Characteristics of Scintillators," *Quantum*, 1954.

[150] W. S. Koski, "Scintillators in some phosphor-plastic systems," *Physical Review*, vol. 82, no. 1, 1951.

[151] I. B. Berlman, *Handbook of Fluoresncence Spectra of Aromatic Molecules*, 2nd ed. New York: Academic Press, 1971.

[152] A. Weinreb and M. Leibowitz, "On the vacuum ultraviolet excited luminscence of pure and doped polystyrene," *Molecular Crystals*, vol. 4, pp. 15–13, 1968.

[153] J. F. Ziegler, M. D. Ziegler, and J. P. Biersack, "SRIM - The stopping and range of ions in matter." 2013.

Appendices

Appendix 1 Summary of Graduate School Honors, Publications, and Presentations

Honors

- 2011 – Selected to be the LANL Chemistry Division Student Worker Safety Security Team representative.
- 2011 - Awarded the First Year Graduate Student Award for Outstanding Academic Performance at UTK.
- 2010 – Poster Session Chair and Student Volunteer for the 2010 Plutonium Futures Conference Keystone, CO.
- 2010 – Awarded Student Scholar Stipend through the Western Alliance for the Expansion of Student Opportunities (WAESO) in conjunction with Arizona State University (ASU).
    - Former the Chairman of the NACE Student Chapter at NNMC.
- 2008 – Awarded a WAESO student grant for research under Dr. Kalaiappan Chidambaram of NNMC.
- 2008 - Selected for the Who's Who in American Junior Colleges at NNMC.
- 2008 - Chosen as part of the All-American Academic Team for Two-Year Colleges for New Mexico.
- Vice-President (2007-2008) and Alumni Member of the Phi Theta Kappa Chapter of NNMC.

    2006 – Recipient of New Mexico-Alliance for Minority Participation (NM-AMP) under Dr. Ajit Hira of NNMC.

Publications

- 2013 – Mabe, A. N., J. D. Auxier II, M. J. Urffer, D. Penumadu, G. K. Schweitzer, L. F. Miller, "Transparent Lithiated Polymer Thin Films for Thermal Neutron Detection" *Nuc. Inst. Methods,*

- 2013 – Auxier, J. D. II, A. N. Mabe, S. A Young, J. P. Auxier, L. F. Miller, G. K. Schweitzer "Lithium Tetraborate as a Potential Thermal Neutron Detector", *Under Review, Nuc. Inst. Meth. A.*

- 2013 – Auxier, J. D. II, A. N. Mabe, S. A. Young, J. P. Auxier, L. F. Miller, G. K. Schweitzer, "Synthesis and Characterization of Ce^{3+} Doped Amorphous Lithium Tetraborate", *Under Review to J. Non-Cry. Sol.*

- 2011 - Auxier J. D. II "A Student's Perspective on Plutonium Futures" *Actinide Research Quarterly*

- 2009- Porterfield, D., L. Tandon, A. Plionis, D. Mercer, D. Peterson, J. D. Auxier II. (2009). "One-dimensional Mapping of Gamma Emitting Radionuclides in Support of Forensic Examination". *J. Radioanal. Nucl. Chem.*

Presentations

Technical Talks

- 2011 – "Development of a New Method for Determination of Pu and Am-241 in Aqueous Samples" – at the Radiochemical and Radiobioassay Measurements Conference, Sandestin, Fl.

- 2011 – "Scintillation Materials for Neutron and Gamma Detectors" – for LANL AAC research group meeting

- 2010 – "One-Dimensional Mapping of Gamma Emitting Radionuclides in Support of Forensic Examination" at ASC chemistry senior Seminar.

- 2009 - "Corrosion Characteristics of Steel Samples in the Rio Grande River" at ASC student research symposium

Posters

- 2012 – "Thermal Neutron Detection: Li-6/Li-7 Standard Subtraction" – Academic Research Initiatives Grantees Conference 2012 in Leesburg, VA.

- 2012 – "Investigation of Plutonium in a Borate Matrix" at Plutonium Futures – the Science 2012 at University of Cambridge, UK

- 2012 – "The Principles of 6Li-polymer Thermal Neutron Detection by Standard Subtraction" at the American Chemical Society Area Collegiate Meeting, Martin, TN.

- 2010 – "Corrosion Behavior of Mildsteel in the Rio Grande river" at the 239th ACS National Meeting in San Francisco, Ca.

- "Chaos Theory and Its Applications" at WAESO conference at Arizona State University, AZ.

- 2008 – "Improved Methods of Nuclear Spectrometry for Sample Characterization" at LANL student symposium, Los Alamos, NM.

- 2008 – "Corrosion Characteristics of Steel Samples in the Rio Grande River" at NNMC Thinko-De-Mayo student research symposium, Espanola, NM.

- 2007- "Materials and Test Equipment Database" at LANL Student Symposium, Los Alamos, NM.

- 2006- "Computational Modeling of Ga-As Clusters on a C_{60} Substrate" at New Mexico State University (NMSU) at NM-AMP Conference, Las Cruces, NM.

Vita

John D. Auxier II was born on April 29, 1989 in Aurora, Colorado and grew up in Brighton, Colorado, a suburb of Denver, Colorado. He was homeschooled throughout grade school and high school, before enrolling at Aims Community College in 2003. After two semesters, he relocated to La Madera, New Mexico where he would obtain an Associates in Science from Northern New Mexico College in 2008 graduating Summa Cum Laude. During this time, he began a student internship at Los Alamos National Laboratory in May 2007, and remained a student intern until May 2013. During the summer of 2009, Auxier was selected to be a student at the ACS/DOE Nuclear Chemistry Summer School at San Jose State University with Dr. Frank Kinard. From 2008 to 2010, Auxier attended Adams State College (now University) in Alamosa, Colorado and graduated Cum Laude in 2010 with a Bachelors of Science in Chemistry and Mathematics. Afterwards, he then enrolled at the University of Tennessee, Knoxville in pursuit of a Doctorate of Philosophy in Inorganic Chemistry under Dr. George K. Schweitzer. He graduated in May 2013.